Ab-initio study of magnons in linear and non-linear regimes

Nisha Singh
2019

im
Fachbereich Physik der
Freien Universität Berlin
eingereichte
Dissertation

zur Erlangung des akademischen Grades
Doctor rerum naturalium

Supervisor: Dr. Sangeeta Sharma
Second Examiner: Prof. Dr. Piet Brouwer

Date of defense: 25.11.2019

Abstract

Low energy excitations (< 1eV) are of utmost importance for understanding the electronic, magnetic, and thermodynamical properties of any material. The collective excitations of spin in this energy regime are magnons, which are quantized spin-waves. Recent developments in the field of spin-dynamics have opened up the world of femtomagnetism, whereby the spin degree-of-freedom is controlled using ultrafast laser pulses. Thus manipulating magnons using femtomagnetism holds great promise for future technological devices operating on ultrafast timescales. In order to reach this goal, it is vital that we are able to accurately describe these magnon excitations in order to understand, and ultimately control them.

The objective of this thesis is to study magnetic excitations using an *ab-initio* approach, namely Time Dependent Density Functional Theory (TDDFT). These studies are divided into two sections. In the first part these excitations are studied in the linear regime where a new approximation is derived. In the second part these studies are extended into the real-time, non-equilibrium, regime where the response of magnons to ultrafast laser pulses is investigated.

TDDFT encapsulates the electron-electron interactions of the many-body system in the exchange-correlation (XC) functional, which for practical applications must be approximated. Despite the plethora of approximations for the XC energy functional only a few have been used for the XC kernel. Out of these, only the Adiabatic Local Density Approximation kernel has been implemented and applied to study the magnetic excitations. The work presented first focuses on deriving the Generalized Gradient Approximation (GGA) kernel by climbing up the Jacob's ladder of functionals. Then the performance of the GGA kernel is studied by calculating the magnon spectra for ferromagnets and Heuslers. Results show that the GGA kernel generally worsens the spin-excitation spectra by overestimating the magnon energies. However, at the Brillouin Zone (BZ) boundary, suppression of the spin wave intensity is consistent with experimental findings.

In the second part of this thesis the power of real-time TDDFT is demonstrated by simulating multiple magnon modes in multi-sublattice alloys, where these modes can be visualized in real space and their response to external pulses can be investigated in real-time. The results in the case of two magnetic sublattice alloy suggests the existence of element specific decoupled magnon modes along with the coupled modes. These decoupled modes indicate that the constituent elements in the alloy respond at different timescales. Using these studies three distinct ways of ultrafast laser pulse control of magnon modes is demonstrated: (1) element selective destruction of magnon modes, (2) creation of a transient non-collinear state by destruction of specific magnon modes, (3) renormalization of the optical magnon frequency, where we found a linear dependence between the laser intensity and the decrease of the magnon frequency.

Zusammenfassung

Niederenergetische Anregungen (<1 eV) sind für das Verständnis der elektronischen, magnetischen und thermodynamischen Eigenschaften eines Materials von größter Bedeutung. Die kollektiven Anregungen des Spins in diesem Energieregime sind quantisierte Spinwellen, die man Magnonen nennt. Jüngste Entwicklungen auf dem Gebiet der Spindynamik ermöglichen den Zugang zur Kontrolle des Femtomagnetismus, wobei der Spinfreiheitsgrad mit ultraschnellen Laserpulsen gesteuert wird. Die Manipulation von Magnonen mithilfe des Femtomagnetismus ist daher vielversprechend für zukünftige technologische Geräte, die in ultraschnellen Zeitskalen arbeiten. Ein genaueres Verständnis der Magnonenanregungen ist dafür allerdings erforderlich.

Das Ziel dieser Arbeit ist es daher, magnetische Anregungen mit einem Ab-initio-Ansatz zu untersuchen, nämlich der zeitabhängigen Dichtefunktionaltheorie (TDDFT). Die Arbeit ist in zwei Abschnitte unterteilt. Im ersten Abschnitt werden Magnonenanregungen im linearen Bereich untersucht und eine neue Näherung abgeleitet. Im zweiten Abschnitt werden diese Untersuchungen auf das Echtzeit-Nichtgleichgewichtsregime ausgedehnt, in dem die Reaktion von Magnonen auf ultraschnelle Laserpulse untersucht wird.

TDDFT beschreibt die interelektronischen Wechselwirkungen des Vielteilchensystems mithilfe des Austauschkorrelationsfunktionals (XC), das für praktische Anwendungen angenähert werden muss. Trotz einer Fülle von vorhandenen Näherungen für das XC Energiefunktional wurden bisher nur wenige für den XC-Kernel verwendet. Von diesen wurde bisher nur der Kernel des lokalen Dichtefunktionals in der adiabatischen Näherung implementiert und angewendet, um die magnetischen Anregungen zu untersuchen. Der erste Abschnitt dieser Arbeit konzentriert sich daher auf die Ableitung des GGA-Kernels (Generalized Gradient Approximation). Anschließend wird die Genauigkeit des GGA-Kernels untersucht, indem die Magnonenspektren für Ferromagnete und Heuslersche Legierungen berechnet werden. Die Ergebnisse zeigen, dass der GGA-Kernel die Spinanregungsspektren im Allgemeinen verschlechtert, indem die Magnonenenergien überschätzt werden. An der Brillouin Zone (BZ)-Grenze hingegen, stimmt die berechnete Verminderung der Spinwellenintensität mit den experimentellen Ergebnissen überein.

Im zweiten Abschnitt dieser Arbeit wird die Genauigkeit der Echtzeit-TDDFT-Methode demonstriert. Mehrere Magnonenmoden in Legierungen mit mehreren Untergittern werden simuliert, wobei die Magnonenmoden im realen Raum graphisch dargestellt und die Reaktion auf externe Laserpulse in Echtzeit untersucht werden. Die Ergebnisse im Fall von zwei magnetischen Untergitterlegierungen legen die Existenz sowohl von elementspezifschen entkoppelten Magnonenmoden als aucg gekoppelter Moden nahe. Sie deuten darauf hin, dass die laserinduzierte Rückreaktion der Elemente in der Legierung auf unterschiedlichen Zeitskalen liegt. Unter Verwendung dieser Studien werden drei verschiedene Möglichkeiten der ultraschnellen Laserpulssteuerung von Magnonenmoden dargelegt: (1) Elementselektive Zerstörung von Magnonenmoden, (2) Erzeugung eines transienten nichtkollinearen Zustands durch Zerstörung spezifischer Magnonenmoden, (3) Renormierung der Magnonenfrequenz im optischen Bereich, wobei wir eine lineare Abhängigkeit zwischen der Laserintensität und der Abnahme der Magnonenfrequenz feststellten.

Dedicated to my parents,
brother,
and sister.

List of Definitions and Abbreviations:

$\hat{H}$	Many-Body Hamiltonian
$\Psi_{total}\ (\mathbf{r}_i, \mathbf{R}_\alpha)$	Total many-body wavefunction
E	Eigenvalues of the many-body system
$\Psi_{nuclei}\ (\mathbf{R}_\alpha)$	Wavefunction of nuclear system
$\Phi_e(\mathbf{r}_i \vert \mathbf{R}_\alpha); \Phi$	Wavefunction of electronic system
E_e	Eigenvalues of electronic system
$\hat{T}_{electron}$	Total kinetic energy of electronic system
$\hat{V}_{\text{ext}}(\mathbf{r})$	External potential to the electronic system
$\hat{W}(\mathbf{r})$	Coulomb potential of electrons
F	Universal functional
$\rho(\mathbf{r})$	Density
$\mathbf{m}(\mathbf{r})$	Magnetization density
$\rho_0(\mathbf{r})$	Ground state density
$\Phi_0(\mathbf{r})$	Ground state wavefunction of the electronic system
E_0	Ground state energy of the electronic system
$v_{\text{ext}}(\mathbf{r})$	Arbitrary external potential
$v_{\text{S}}(\mathbf{r})$	Effective potential of the Kohn-Sham (KS) system
$\phi_i(\mathbf{r})$	Orbitals of the KS System
ϵ_i	Eigenvalues of the KS system
$T_s[\rho]$	Non-interacting kinetic energy functional
$E_s[\rho]$	Energy functional of the KS system
$E_{\text{XC}}[\rho]$	Exchange-Correlation energy functional
$v_{\text{XC}}(\mathbf{r})$	Exchange-Correlation potential
$\mathbf{B}_{\text{XC}}(\mathbf{r})$	Exchange-Correlation magnetic field
$E_{\text{x}}[\rho]$	Exchange energy functional
$E_{\text{c}}[\rho]$	Correlation energy functional
$e_{\text{XC}}(\mathbf{r})$	Exchange-Correlation energy density per particle
$\Phi(\mathbf{r}_i, t)$	Time-dependent wavefunction of electronic system
$\hat{H}(t)$	Time-dependent Hamiltonian
$\rho(\mathbf{r}, t)$	Time-dependent density
$\mathbf{m}(\mathbf{r}, t)$	Time-dependent magnetization density
$\hat{j}(\mathbf{r})$	Current density operator
$\phi_j(\mathbf{r}, t)$	Time-dependent orbitals of the KS system
φ_0	Initial wavefunction of the KS system
Φ_0^0	Ground-state wavefunction of perturbed system
E_0^0	Ground-state eigenvalues of unperturbed system
Φ_j^0	Wavefunction of unoccupied/empty state
E_j^0	Eigenvalues of unoccupied state
$\chi(\mathbf{r}, \mathbf{r}', \omega)$	Response of interacting system in frequency regime
$\chi^{KS}(\mathbf{r}, \mathbf{r}', \omega)$	Response of KS system in frequency regime
$f_{\text{XC}}(\mathbf{r}, \mathbf{r}')$	Exchange-Correlation kernel in adiabatic approximation

LIST OF FIGURES

CONTENTS

CHAPTER 1

INTRODUCTION AND MOTIVATION

Dream, Dream, Dream
Dreams transform into thoughts
and thoughts result into action.
- Dr. APJ Abdul Kalam

An atom comprises of negatively charged electrons in quantized orbitals along with a positively charged nucleus (containing both protons and neutrons) held together by the mutual Coulomb attraction. However it took many years to reach this picture of the atom. The year 1897 witnessed the discovery of the electron by J.J. Thomson, which was soon followed by the plum pudding model of the atom. This is now known as the classical model of the atom, where the electrons are embedded in a uniform sphere of positive charge. However this model was abandoned due to the Rutherford experiment, which studied alpha particles scattering from a thin gold foil. This experiment proved that there is a positively charged core concentrated in the center of the atom and the electrons must orbit around it, just like our solar system (although the electrons and nuclei are held together by the electrostatic forces rather than by gravity). However, if this were the situation then the electrons should radiate and eventually collapse into the nuclei, making all atoms unstable.

The birth of Quantum Mechanics in the early 1900s gave a more meaningful structure of the atom. According to Neils Bohr, 1913, these electrons reside in well-defined orbitals, in complete contrast to the classical model, where the electrons are randomly and continuously distributed around the nuclei. Later Arnold Sommerfeld showed that the orientation of these orbitals is also well defined. This is an example of one of the most beautiful phenomena in physics: quantization (in this case spatial quantization or angular momentum quantization). To prove this space quantization Otto Stern and Walter Gerlach, 1922, set up an experiment to pass a collimated beam of silver atoms through an inhomogeneous magnetic field. In the Bohr-Sommerfeld model, the space quantization should cause the splitting of the beam into discrete lines. This splitting was indeed observed and the success was recorded in a postcard sent by Gerlach to Bohr, see Fig. 1.1, congratulating him on the success of his theory.

The Stern-Gerlach experiment did show the splitting of the beam but only into two states. While this confirmed that the classical model should be rejected, the results also did not agree with the Bohr-Sommerfeld model. It is now known that the splitting of the beam had, in fact, nothing to do with the orbital angular momentum, as silver has only one electron in

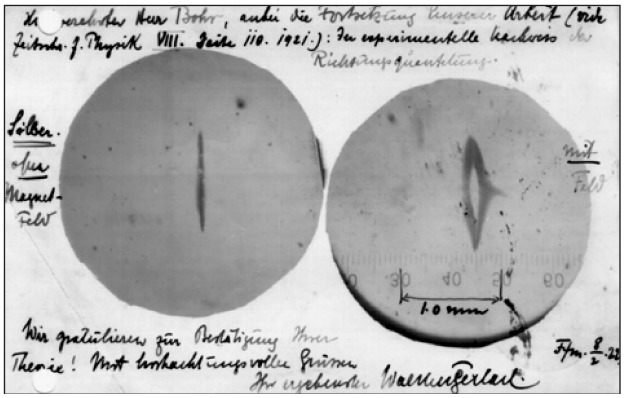

Figure 1.1: Postcard from Gerlach to Bohr.

l=0 state, i.e. the angular momentum is 0. Following the introduction of electron spin by Wolfgang Pauli, it was understood that the Stern-Gerlach experiment actually captured the quantized spin angular momentum ($= \pm\mu_B$). In summary, since 1927 it is known that the electron has two degrees of freedom associated with it, charge and spin.

The spin of the electron has proved so important to the history of electronics that it prompted the new research field of spintronics[1, 2, 3], whose goal is to exclusively utilize the spin degree of freedom. Devices working on this principle need less energy to perform, as changing spin is often less work than generating charge currents. Similarly spin states can be set quickly, making data-transfer quicker. This lead to the development of memories like MRAM which are non-volatile and can operate efficiently in high temperature and radiation environments, and are already being used in Airbus aircrafts and BMW motorbikes [4]. Additionally, it will lead to devices being smaller in size, faster in speed, and more powerful than semiconductor based electronic devices. For example, it was realized that the exploiting the electron spin increased the rate at which information could be read from a hard disk drive. This was the ground breaking discovery of the Giant-Magnetoresistance (GMR) [5, 6] effect by Albert Fert and Peter Grünberg in 2007 which led to them being awarded the Nobel prize.

If spintronics is to overcome the limits of silicon based electronics we must develop methods to:

- Manipulate spin, either to rotate and/or transfer.
- Transport spin over long distances without losing the encoded information .
- Detect and decode this information.

The control of spin by laser technology on femtosecond timescales (femtomagnetism) has emerged as a promising tool in the last two decades. It offers the possibility to alter a magnetic system on a time scale that corresponds to the (equilibrium) exchange interaction (responsible for the existence of magnetic order), while being much faster than the time scale of spin-orbit interaction (1–10 ps) or magnetic precession (100–1000 ps) The foundation stone

of this field was laid down by the observation of ultrafast demagnetization [7] in 1996. Here, it was shown that when a laser is applied to nickel, it loses its magnetization on a femtosecond timescale (see Fig. 1.2 (a)). Eventually, the spin is regained by the material but on the longer picosecond timescale. The dissipation channel of spin observed in this experiment is still an open question and attracts the attention of both theorists and experimentalists, with many experiments performed to observe and attempt to explain this intriguing behavior of spin-light interaction.

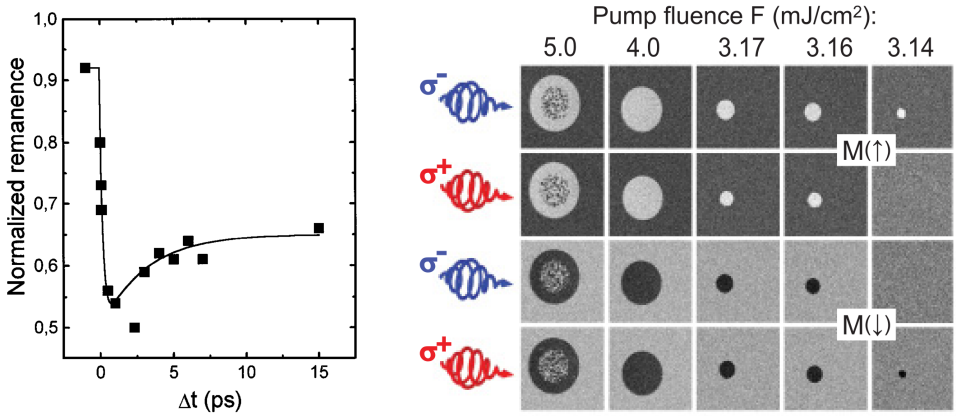

(a) (b)

Figure 1.2: (a) The demagnetization of nickel on femtosecond timescale when acted by an optical laser[7]. (b) Switching of magnetization using the circularly polarized light. The left handed light switches from up state to down and vice versa with the right handed light [8].

Another landmark event was in 2007, when a 40 fs circularly polarized laser was applied on a ferrimagnet resulting in switching of the spins. They demonstrated that controlled reversal of magnetization is achievable by femtosecond laser pulses. Further, the direction of switching is dependent on helicity of the light as can be seen in Fig. 1.2(b). This work is of particular importance to the magnetic storage industry, due to the speed with which magnetization reverses.

The control of spin by femtosecond lasers has been achieved to some extent and now the task is to control transport on femtosecond timescale. One of the means of transport is in the form of waves known as spin waves, which are formed by small disturbances in magnetically ordered materials. These were first predicted by F. Bloch and can propagate up to nanometer length scales without significant attenuation. Hence, the next leap in information processing would be to utilize these magnetic quasi-particles called spin waves or magnons to transport spin. The magnon spintronics, or magnonics[9, 10, 11], has many advantages over conventional electronics, e.g. wave-based computing, a wide frequency range from GHz to THz, contactless wiring, nonlinear-data processing, room temperature transport of spin without joule heat generation, and many more. Furthermore, spin-wave characteristics can be engineered by tuning various parameters such as choice of material, shape of sample, orientation and size of the applied magnetic field. Hence given the vast tunability and rich physics of spin-waves they are an excellent object of study in order to ultimately be able to

control them. The control of magnons by terahertz pulse is indeed feasible as was demonstrated by the experiment done by Kampfrath et al. [12]. Here a single-cycle terahertz pulse switched on and off the coherent spin waves in antiferromagnetic NiO at a frequency of 1 THz. The terahertz field addresses spin selectively by the Zeeman interaction and provides a means to control previously inaccessible magnetic excitations.

Owing to the importance of magnons from a technological point of view this thesis aims at studying them in a wide range of materials: ferromagnets, Heusler compounds, and multi-magnetic-sublattice alloys, using the fully *ab-initio* approach of time-dependent density functional theory. This was first done in the linear response regime where a new adiabatic kernel has been derived, implemented and applied to study ferromagnets and Heuslers. This formalism was extended to the real-time domain to study the high energy magnon modes present in ferromagnetic materials and $Fe_{50}Ni_{50}$ alloy. Lastly, I unite the fields of magnonics and femtomagentism and study the dynamics of these magnon modes under the effect of ultrafast, ultrastrong laser pulses. This can be shown in a nutshell by the following simple diagram (Fig. 1.3):

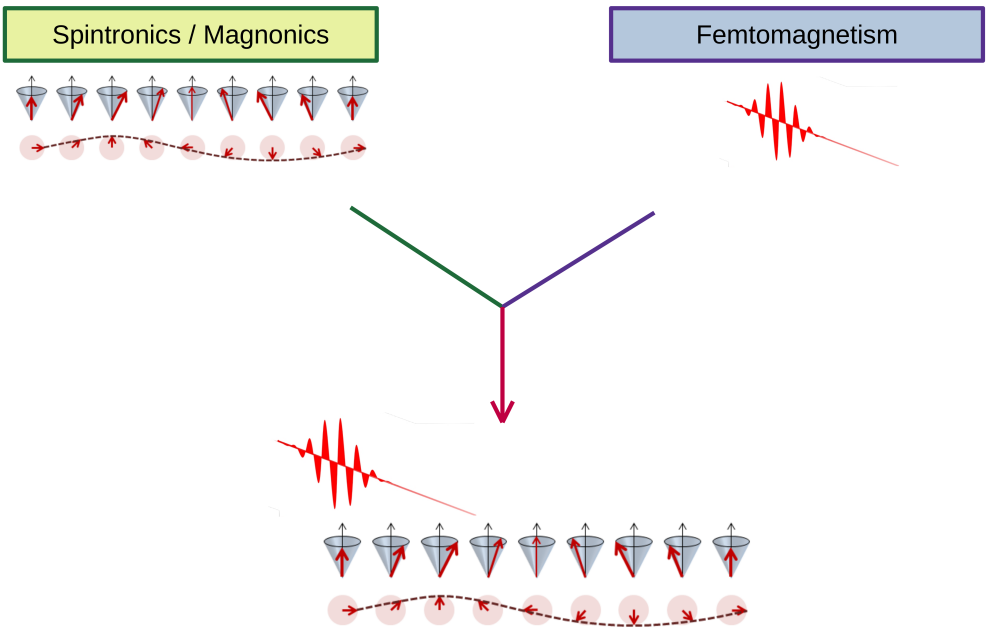

Figure 1.3: Simple diagram showing the combination of two fields : magnonics and femtomagnetism.

CHAPTER 2

TIME-DEPENDENT DENSITY FUNCTIONAL THEORY

Theory is when you understand everything but nothing works.
Practice is when everything works but you don't understand why.
Combine theory with practice: nothing works and no one knows why.
-Anonymous

Density Functional Theory (DFT), is a computational, quantum mechanical, simulation tool based on functionals of the electronic density. It is widely used by physicists, chemists, and material scientists to investigate the ground-state electronic structure of atoms, molecules, and condensed matter. Further its predictions for geometries, vibrational frequencies, and total energies are reliable and have the advantage of being faster and less memory intensive than conventional wavefunction-based methods. Time-dependent density functional theory (TDDFT) is the extension of this exact theory to the time-domain in order to capture the linear and non-linear dynamics of the electronic and magnetization densities. In this thesis TDDFT will be applied to study magnons, but first a review of DFT and TDDFT is given in this chapter. This includes the necessary theorems required to prove that the density can indeed be used instead of wavefunction to calculate all observables. Next, the approximations commonly used for all practical calculations are discussed. This is followed by equations of linear response TDDFT, including a discussion about the optical and magnetic excitation spectra and the approximations required for exchange-correlation (XC) kernel. Finally we show how the non-equilibrium response to applied laser fields may be calculated using the real-time TDDFT (RT-TDDFT) formalism. This section also discusses the techniques required to analyze and interpret the simulated dynamics.

2.1 Density Functional Theory

The quantum mechanical description of a system is given by the solutions of the many-body Hamiltonian:

$$\begin{aligned}\hat{H} &= \hat{T}_{nuclei} + \hat{T}_{electron} + \hat{V}_{nuclei-electron} + \hat{W}_{electron-electron} + \hat{V}_{nuclei-nuclei} \\ &= -\sum_{\alpha=1}^{M} \frac{\hbar^2}{2M_\alpha} \boldsymbol{\nabla}_\alpha^2 - \sum_{i=1}^{N} \frac{\hbar^2}{2m_e} \boldsymbol{\nabla}_i^2 - \sum_{i=1}^{N}\sum_{\alpha=1}^{M} \frac{1}{4\pi\epsilon_0} \frac{Z_\alpha e^2}{r_{i\alpha}} \\ &+ \sum_{i=1}^{N}\sum_{j>i}^{N} \frac{1}{4\pi\epsilon_0} \frac{e^2}{r_{ij}} + \sum_{\alpha=1}^{M}\sum_{\alpha>\beta}^{M} \frac{1}{4\pi\epsilon_0} \frac{Z_\alpha Z_\beta}{r_{\alpha\beta}}\end{aligned} \tag{2.1}$$

where M is number of nuclei labelled as α, N is number of electrons labelled as i, $\hat{T}$ is kinetic energy operator, $\hat{V}$ is the potential energy operator, M_α is mass of each nuclei, m_e is electronic mass, and r gives the separation between the electrons and/or the nuclei. The terms of Eq. (2.1) correspond to the kinetic energy of nuclei, kinetic energy of electrons, potential energy of nuclei-electron interaction, potential energy of the electron-electron interaction, and the potential energy of nuclei-nuclei interaction respectively. Solving the Schrödinger equation gives the many-body wavefunction (Ψ_{total}) and eigenvalues (E),

$$\hat{H}|\Psi_{total}\rangle = E|\Psi_{total}\rangle \tag{2.2}$$

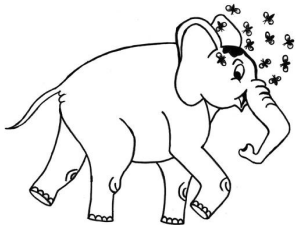

Figure 2.1: Elephant and bees analogy for Born-Oppenheimer Approximation.[13]

This equation gives us all the information we need about a particular system but only if we could solve it exactly. The Coulomb interaction terms are present in the Hamiltonian make it a difficult problem to solve, and hence we require approximations. As we know, the nuclei are heavier than electrons and hence they generally respond much slower to the changes in electronic system. This can be understood by the analogy with bees motion attracted to honey on elephant's head Fig. 2.1. The bees move faster and being lighter can instantly adjust to motion of elephant's head. Similarly, electrons being lighter their motion can be decomposed from that of the nuclei. Hence, by this approximation, the nuclear degrees of freedom can be treated classically and the many-body wavefunction factorized. This is the Born-Oppenheimer approximation in which electrons move in the external scalar potential provided by the nuclei fixed at positions $\mathbf{R}$.

$$\Psi_{total}(\mathbf{r}, \mathbf{R}) = \Psi_{nuclei}(\mathbf{R})\Phi_e(\mathbf{r}|\mathbf{R}) \tag{2.3}$$

where $\mathbf{R}$, $\mathbf{r}$ are the nuclei and electronic coordinates, respectively and $\Phi_e(\mathbf{r}|\mathbf{R})$ shows the parametric dependence of the electronic wavefunction on the nuclear coordinates. Conceptually, this means that the nuclei are fixed at their positions and electrons move with respect to them. Then the Schrödinger equation for the electronic system reads,

$$\Big[\hat{T}_{electron} + \hat{V}_{nuclei-electron} + \hat{W}_{electron-electron}\Big]|\Phi_e\rangle = E_e|\Phi_e\rangle$$

$$\Big[-\sum_{i=1}^{N}\frac{\hbar^2}{2m_e^2}\boldsymbol{\nabla}_i^2 - \frac{1}{4\pi\epsilon_0}\sum_{i=1}^{N}\sum_{\alpha=1}^{M}\frac{Z_\alpha e^2}{|\mathbf{r}_i-\mathbf{R}_\alpha|} + \frac{1}{4\pi\epsilon_0}\sum_{i=1}^{N}\sum_{j>i}^{N}\frac{e^2}{|\mathbf{r}_i-\mathbf{r}_j|}\Big]\Phi_e(\mathbf{r}) = E_e\Phi_e(\mathbf{r}) \tag{2.4}$$

which may be written in simpler form using atomic units. Since we focus on the electronic system, we will drop the 'e' subscript of the wavefunction.

$$\Big[-\sum_{i=1}^{N}\frac{1}{2}\boldsymbol{\nabla}_i^2 - \sum_{i=1}^{N}\sum_{\alpha=1}^{M}\frac{Z_\alpha}{|\mathbf{r}_i-\mathbf{R}_\alpha|} + \sum_{i=1}^{N}\sum_{j>i}^{N}\frac{1}{|\mathbf{r}_i-\mathbf{r}_j|}\Big]\Phi(\mathbf{r}) = E\Phi(\mathbf{r}) \tag{2.5}$$

$$\Big[\hat{T}_{electron} + \hat{V}_{\text{ext}} + \hat{W}\Big]|\Phi\rangle = E|\Phi\rangle \tag{2.6}$$

where the electron-nuclear interaction is often referred to as external potential, $\hat{V}_{\text{ext}}$ and electron-electron interaction by $\hat{W}$.
If we know this electronic wavefunction, we could calculate many observables of the system such as energy, geometry, magnetization . However, solving for Φ is not practical: for an Oxygen atom, which has 8 electrons, the wavefunction will depend on 3 degrees of freedom for each of these 8 electrons i.e. 3×8 spatial coordinates. If for storing one spatial coordinate we need 10 points, then to store 24 spatial coordinates we need 10^{24} points. If 1 byte of memory is used by each point then we need a total of 10^{24} bytes of memory. Usually a DVD has 10^{10} bytes for storage, which means we need 10^{14} DVD's. In terms of weight, if a DVD weighs 10g each, then we would require 10^{15} g of DVD's or 10^{14} kg of DVD. The mass of earth is 5.972×10^{24} kg, so just to store the wavefunction of Oxygen atom we would need DVD's equivalent to half the mass of our earth. To overcome this difficulty alternative methods are required.

2.2 Hohenberg-Kohn theorem:

In 1964, Hohenberg and Kohn [14] proved it is possible to obtain all the desired information of an interacting system from only the electronic density, i.e. without needing the wavefunction.

The kinetic energy and the potential energy of electron-electron interaction for a fixed number of electrons, N, can be combined to make a universal operator $\hat{F} = \hat{T}_{electron}+\hat{W}$. Therefore by specifying $\hat{V}_{\text{ext}}$ (and N), the Schrödinger equation, and hence the ground state wavefunction, $\Phi_0(\mathbf{r})$, is completely determined. From this ground state wavefunction, the ground state density can be determined

$$\rho_0(\mathbf{r}) = N\int |\Phi_0(\mathbf{r},\mathbf{r}_2,\mathbf{r}_3,....\mathbf{r}_N)|^2 d\mathbf{r}_2 d\mathbf{r}_3\cdots d\mathbf{r}_N = \langle\Phi_0|\hat{\rho}|\Phi_0\rangle \tag{2.7}$$

where $\hat{\rho}(\mathbf{r}) = \sum_{i=1}^{N} \delta(\mathbf{r} - \hat{\mathbf{r}}_i)$ is density operator. Thus the ground state wavefunction and density are both functionals of the external potential (and the number of electrons). The HK theorem proves the reverse of this, that the external potential is a unique functional of the density.

Theorem 1: There is an one-to-one mapping between the external potential, $V_{\text{ext}}(\mathbf{r})$, and the ground state density of an interacting system of electrons. In other words, the external potential is a unique functional of the density up to some additive constant.

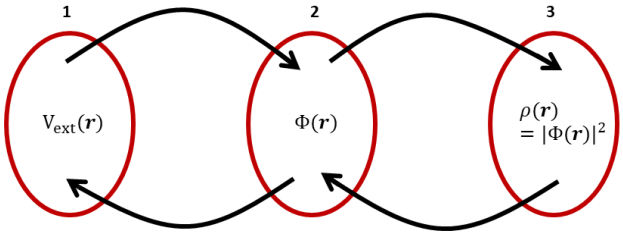

Figure 2.2: Pictorial representation of first Hohenberg-Kohn theorem.

In Fig. 2.2, the first set contains all the external potentials which describe a system. After substituting this in the Schördinger equation we get the second set which comprises of wavefunctions. As two systems can not have same set of wavefunctions which are practically indistinguishable, then for every external potential there exists only one solution. This map from external potential to wavefunctions is also invertible as implied by the Schrödinger equation. The third set is obtained by calculating the density of the wavefunctions in set 2. To prove the one-to-one correspondence it is to be shown that the map between set 3 and set 1 is invertible.

Proof: Consider that there are two different external potentials $V_{\text{ext}}(\mathbf{r})$, $V'_{\text{ext}}(\mathbf{r})$, differing more than a constant, comprising two different Hamiltonians $\hat{H}$, $\hat{H}'$ with non-degenerate ground state solutions Φ_0 and Φ'_0 satisfying the following Schrödinger equations

$$\begin{aligned} \hat{H}|\Phi_0\rangle &= E_0|\Phi_0\rangle \\ \hat{H}'|\Phi'_0\rangle &= E'_0|\Phi'_0\rangle \end{aligned} \tag{2.8}$$

where E_0 and E'_0 are the ground state energies. However assume that both give the same density, $\rho_0(\mathbf{r})$. In other words,

$$\langle\Phi'_0|\hat{\rho}|\Phi'_0\rangle = \rho_0(\mathbf{r}) = \langle\Phi_0|\hat{\rho}|\Phi_0\rangle \tag{2.9}$$

Then, we have the following inequality by the Rayleigh-Ritz principle when $\hat{H}$ acts on Φ'_0 wavefunction,

$$\begin{aligned} E_0 &< \langle \Phi_0' | \hat{H} | \Phi_0' \rangle \\ &= \langle \Phi_0' | \hat{F} + \hat{V}_{\text{ext}} + \hat{V}_{\text{ext}}' - \hat{V}_{\text{ext}}' | \Phi_0' \rangle \\ &= \langle \Phi_0' | \hat{H}' + \hat{V}_{\text{ext}} - \hat{V}_{\text{ext}}' | \Phi_0' \rangle \\ &= E_0' + \langle \Phi_0' | \hat{V}_{\text{ext}} - \hat{V}_{\text{ext}}' | \Phi_0' \rangle \end{aligned} \tag{2.10}$$

Similar inequality holds when $\hat{H}'$ acts on wavefunction Φ_0,

$$\begin{aligned} E_0' &< \langle \Phi_0 | \hat{H}' | \Phi_0 \rangle \\ &= \langle \Phi_0 | \hat{F} + \hat{V}_{\text{ext}}' + \hat{V}_{\text{ext}} - \hat{V}_{\text{ext}} | \Phi_0 \rangle \\ &= \langle \Phi_0 | \hat{H} + \hat{V}_{\text{ext}}' - \hat{V}_{\text{ext}} | \Phi_0 \rangle \\ &= E_0 + \langle \Phi_0 | \hat{V}_{\text{ext}}' - \hat{V}_{\text{ext}} | \Phi_0 \rangle \end{aligned} \tag{2.11}$$

Since both Φ_0 and Φ_0' were assumed to have the same density, adding Eq. (2.10) and (2.11) gives us the contradictory inequality

$$E_0 + E_0' < E_0' + E_0 \tag{2.12}$$

Thus by *reductio ad absurdum* we have shown that the external potential is a unique functional of the density and vice versa. In particular, the wavefunction becomes a functional of density and hence all observables become functionals of the density.

Theorem 2: This theorem establishes the variational principle for the energy functional.

Proof: As the ground-state wavefunction is a functional of the density, $\Phi_0[\rho]$, the energy of a system defined by a fixed external potential can be written as,

$$\begin{aligned} E[\rho] &= \langle \Phi_0[\rho] | \hat{H} | \Phi_0[\rho] \rangle \\ &= T[\rho] + W[\rho] + \int v_{\text{ext}}(\mathbf{r}) \rho(\mathbf{r}) d\mathbf{r} \\ &= F[\rho] + \int v_{\text{ext}}(\mathbf{r}) \rho(\mathbf{r}) d\mathbf{r} \end{aligned} \tag{2.13}$$

where $F[\rho]$ is a universal functional given by,

$$F[\rho] = \langle \Phi_0[\rho] | \hat{F} | \Phi_0[\rho] \rangle \tag{2.14}$$

Hence, the value of the energy functional is minimized for the ground state density, ρ_0, as stated by the second theorem,

$$\begin{aligned} E[\rho] = \langle \Phi_0[\rho] | \hat{H} | \Phi_0[\rho] \rangle \geq \langle \Phi_0[\rho_0] | \hat{H} | \Phi_0[\rho_0] \rangle = E_0 \\ E[\rho] \geq E_0 \end{aligned} \tag{2.15}$$

These two theorems established DFT on a firm footing however accurate approximations to the kinetic energy functional were not available. A year later Kohn and Sham derived the Kohn-Sham (KS) equations which made practical applications of DFT possible.

2.3 Kohn-Sham Equations

Kohn and Sham introduced the idea of obtaining the density of an interacting system by mapping the problem to a fictitious non-interacting system. The Schrödinger equation for this non-interacting KS system is,

$$\Big[-\frac{1}{2}\boldsymbol{\nabla}^2 + v_{\mathrm{S}}(\mathbf{r})\Big]\phi_i(\mathbf{r}) = \epsilon_i\phi_i(\mathbf{r}) \tag{2.16}$$

where $\sum_{i=1}^{N} |\phi_i(\mathbf{r})|^2 = \rho(\mathbf{r})$. Applying the Hohenberg-Kohn theorem for non-interacting systems we find that for every interacting ground state density $\rho_0(\mathbf{r})$ (assuming representability) there is a unique KS potential $v_{\mathrm{S}}(\mathbf{r})$. Therefore, solving Eq. 2.16 yields the density of the interacting system and, hence, all ground state properties are obtained.
The kinetic energy density is:

$$T_s[\rho] = -\frac{1}{2}\sum_{i=1}^{N}\int \phi_i^*(\mathbf{r})\boldsymbol{\nabla}^2\phi_i(\mathbf{r})d\mathbf{r} \tag{2.17}$$

where the orbitals are implicit functionals of the density. The energy functional can be written as

$$E_s[\rho] = T_s[\rho] + \int \rho(\mathbf{r})v_{\mathrm{S}}(\mathbf{r})d\mathbf{r} \tag{2.18}$$

Using the Euler-Lagrange method to find the ground state density, with the constraint that density integrates to the correct number of electrons.

$$\begin{aligned} \frac{\delta}{\delta\rho(\mathbf{r})}\Big[E_s[\rho] - \mu\left(\int \rho(\mathbf{r})d\mathbf{r} - N\right)\Big] &= 0 \\ \frac{\delta T_s[\rho]}{\delta\rho(\mathbf{r})} + v_s[\mathbf{r}] - \mu &= 0 \end{aligned} \tag{2.19}$$

where μ is the Lagrange multiplier. Comparing it to the energy functional of the interacting system,

$$E[\rho] = F[\rho] + \int v_{\mathrm{ext}}(\mathbf{r})\rho(\mathbf{r})d\mathbf{r} \tag{2.20}$$

and defining the XC functional as,

$$E_{\mathrm{XC}}[\rho] = F[\rho] - \frac{1}{2}\int \frac{\rho(\mathbf{r})\rho(\mathbf{r}')}{|\mathbf{r}-\mathbf{r}'|}d\mathbf{r}d\mathbf{r}' - T_s[\rho] \tag{2.21}$$

The Euler-Lagrange equation for the interacting system is then,

$$\begin{aligned} \frac{\delta}{\delta\rho(\mathbf{r})}\Big[E[\rho] - \mu\left(\int \rho(\mathbf{r})d\mathbf{r} - N\right)\Big] &= 0 \\ \frac{\delta T_s[\rho]}{\delta\rho(\mathbf{r})} + v_{\text{ext}}(\mathbf{r}) + \int \frac{\rho(\mathbf{r}')}{|\mathbf{r}-\mathbf{r}'|}d\mathbf{r}' + \frac{\delta E_{\text{XC}}[\rho]}{\delta\rho(\mathbf{r})} - \mu &= 0 \end{aligned} \tag{2.22}$$

Defining the XC potential as,

$$v_{\text{XC}}[\rho](\mathbf{r}) = \frac{\delta E_{\text{XC}}[\rho]}{\delta\rho(\mathbf{r})} \tag{2.23}$$

and the fact that the density of interacting and non-interacting systems are the same we get,

$$v_s(\mathbf{r}) = v_{\text{ext}}(\mathbf{r}) + v_{\text{H}}[\rho](\mathbf{r}) + v_{\text{XC}}[\rho](\mathbf{r}) \tag{2.24}$$

where $v_{\text{H}}[\rho](\mathbf{r}) = \int \frac{\rho(\mathbf{r}')}{|\mathbf{r}-\mathbf{r}'|}d\mathbf{r}'$ is the Hartree potential. We can therefore find the ground state density by using the following KS equations,

$$\Big[-\frac{1}{2}\boldsymbol{\nabla}^2 + v_{\text{ext}}(\mathbf{r}) + v_{\text{H}}[\rho](\mathbf{r}) + v_{\text{XC}}[\rho](\mathbf{r})\Big]\phi_i(\mathbf{r}) = \epsilon_i\phi_i(\mathbf{r}) \tag{2.25}$$

$$\sum_{i=1}^{N} |\phi_i(\mathbf{r})|^2 = \rho(\mathbf{r}) \tag{2.26}$$

Note that the kinetic energy density of the interacting system and of the non-interacting system are not equal. To solve these equation for a real system we need approximations for the XC functional.

Spin-polarized systems:

The original KS equations can be extended for the spin-polarized systems where the densities for spin up, $\rho_\uparrow(\mathbf{r})$, and spin down, $\rho_\downarrow(\mathbf{r})$, channels are defined as

$$\begin{aligned} \rho_\uparrow(\mathbf{r}) &= \sum_j |\phi_{j\uparrow}(\mathbf{r})|^2 \\ \rho_\downarrow(\mathbf{r}) &= \sum_j |\phi_{j\downarrow}(\mathbf{r})|^2 \end{aligned} \tag{2.27}$$

where the spin polarized KS orbitals are $\phi_{j\uparrow}(\mathbf{r})$ and $\phi_{j\downarrow}(\mathbf{r})$. Then the total density is given by the summation of these two densities,

$$\rho(\mathbf{r}) = \rho_\uparrow(\mathbf{r}) + \rho_\downarrow(\mathbf{r}) \tag{2.28}$$

whereas the magnetization density is given as by the difference between the two densities,

$$\mathbf{m}_z(\mathbf{r}) = \rho_\uparrow(\mathbf{r}) - \rho_\downarrow(\mathbf{r}) \tag{2.29}$$

The physical quantities under study now become a functional of these two densities and the Kohn-Sham equations are written for each spin channel separately as

$$\begin{aligned}\Big[-\frac{\boldsymbol{\nabla}^2}{2} + v_{\text{ext}}(\mathbf{r}) + v_{\text{H}}(\mathbf{r}) + v^{\uparrow}_{\text{XC}}(\mathbf{r})\Big]\phi_{j\uparrow}(\mathbf{r}) &= \epsilon_{j\uparrow}\phi_{j\uparrow}(\mathbf{r}) \\ \Big[-\frac{\boldsymbol{\nabla}^2}{2} + v_{\text{ext}}(\mathbf{r}) + v_{\text{H}}(\mathbf{r}) + v^{\downarrow}_{\text{XC}}(\mathbf{r})\Big]\phi_{j\downarrow}(\mathbf{r}) &= \epsilon_{j\downarrow}\phi_{j\downarrow}(\mathbf{r})\end{aligned} \tag{2.30}$$

where $v^{\uparrow}_{\text{XC}}(\mathbf{r})$ and $v^{\downarrow}_{\text{XC}}(\mathbf{r})$ are the XC potentials for each spin channel and are given by the functional derivatives of $E_{\text{XC}}[\rho^{\uparrow}, \rho^{\downarrow}]$,

$$v^{\uparrow}_{\text{XC}}(\mathbf{r}) = \frac{\delta E_{\text{XC}}[\rho^{\uparrow}, \rho^{\downarrow}]}{\delta \rho^{\uparrow}(\mathbf{r})} \qquad v^{\downarrow}_{\text{XC}}(\mathbf{r}) = \frac{\delta E_{\text{XC}}[\rho^{\uparrow}, \rho^{\downarrow}]}{\delta \rho^{\downarrow}(\mathbf{r})} \tag{2.31}$$

These equations describe collinear systems, where the magnetic field and magnetization are parallel to each other, along a well defined direction (say z-axis). For non-collinear systems [15], the magnetization is not necessarily parallel to the magnetic field, where the magnetization density is given by,

$$\mathbf{m}(\mathbf{r}) = \langle \Phi | \hat{\boldsymbol{\sigma}} \hat{\rho} | \Phi \rangle \tag{2.32}$$

where $\hat{\boldsymbol{\sigma}}$ are the Pauli matricies. Then the energy becomes a functional of $\mathbf{m}(\mathbf{r})$ and $\rho(\mathbf{r})$. The KS equations for such a system is written in terms of 2-component Pauli spinors, $\phi_j(\mathbf{r})$,

$$\Big[-\frac{\boldsymbol{\nabla}^2}{2} + v_{\text{S}}(\mathbf{r}) + \boldsymbol{\sigma} \cdot \mathbf{B}_{\text{S}}(\mathbf{r})\Big]\phi_j(\mathbf{r}) = \epsilon_j \phi_j(\mathbf{r}) \tag{2.33}$$

where $v_{\text{S}}(\mathbf{r})$ is given by Eq. 2.24 and $\mathbf{B}_{\text{S}}(\mathbf{r}) = \mathbf{B}_{\text{ext}}(\mathbf{r}) + \mathbf{B}_{\text{XC}}(\mathbf{r})$ is the summation of the external magnetic field (if any) and XC magnetic field which is found by functional derivative of the XC energy functional,

$$v_{\text{XC}}(\mathbf{r}) = \frac{\delta E_{\text{XC}}[\rho, \mathbf{m}]}{\delta \rho(\mathbf{r})} \qquad \mathbf{B}_{\text{XC}}(\mathbf{r}) = \frac{\delta E_{\text{XC}}[\rho, \mathbf{m}]}{\delta \mathbf{m}(\mathbf{r})} \tag{2.34}$$

Usually the functionals for collinear systems are extended for the case of non-collinear systems using the Kübler-Sandratskii method [16] (discussed in Section 3.4.1) resulting in,

$$v_{\text{XC}}(\mathbf{r}) = \frac{1}{2}\Big(v^{\uparrow}_{\text{XC}}(\mathbf{r}) + v^{\downarrow}_{\text{XC}}(\mathbf{r})\Big) \qquad \mathbf{B}_{\text{XC}}(\mathbf{r}) = \frac{1}{2}\Big(v^{\uparrow}_{\text{XC}}(\mathbf{r}) - v^{\downarrow}_{\text{XC}}(\mathbf{r})\Big)\hat{\mathbf{m}}(\mathbf{r}) \tag{2.35}$$

where $\hat{\mathbf{m}}(\mathbf{r}) = \dfrac{\mathbf{m}(\mathbf{r})}{|\mathbf{m}(\mathbf{r})|}$ is the magnetization unit vector and the XC potentials are found from collinear functionals for up/down densities $\rho_{\uparrow\downarrow}(\mathbf{r}) = (\rho(\mathbf{r}) \pm |\mathbf{m}(\mathbf{r})|)/2$.

2.4 Exchange-Correlation Functionals

The theory up to now is in principle exact, provided the exact XC functional is known. However, this functional is not known and an approximation must be made. These approximations are grouped into different rungs of a ladder known as Jacob's ladder [17] (Fig. 2.3). As we climb the ladder the level of accuracy increases along with the computational cost. The ultimate goal is to reach the topmost rung of accuracy.

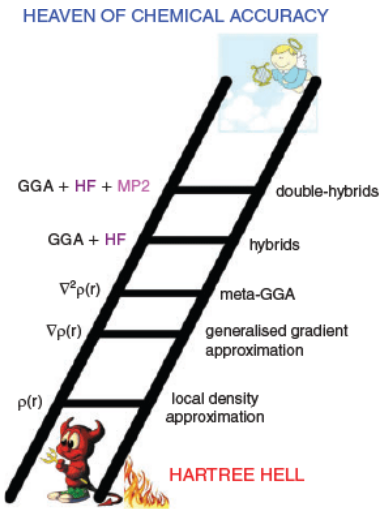

Figure 2.3: Jacob's ladder for XC functional approximations. From [18]

The total XC functional can be decomposed into the exchange and correlation parts separately and we can approximation for the whole XC energy or individually.

$$E_{\mathrm{XC}}[\rho] = E_{\mathrm{x}}[\rho] + E_{\mathrm{c}}[\rho] \tag{2.36}$$

2.4.1 Local Density Approximation (LDA)

The simplest approximation is based on the uniform electron gas. In this gas, electrons can move around freely in a positive background which is there to balance charge neutrality. In LDA, the XC energy density from each infinitesimal volume in space, $d\mathbf{r}$, is taken to be the value it would have if the whole of space were filled with a homogeneous electron gas with the same density as is found in $d\mathbf{r}$.

$$E_{\mathrm{XC}}[\rho] = \int e_{\mathrm{XC}}(\rho(\mathbf{r}))\rho(\mathbf{r})d\mathbf{r} \tag{2.37}$$

where $e_{\mathrm{XC}}(\rho)$ is the XC energy density per particle. For the exchange energy functional this can be calculated analytically and is given as,

$$E_{\mathrm{LDA}}[\rho] = -\frac{3}{4}\left(\frac{3}{\pi}\right)^{1/3}\int (\rho(\mathbf{r}))^{(4/3)}d\mathbf{r} \tag{2.38}$$

The correlation energy of the uniform electron gas on the other hand is known only in the low and high density limits which corresponds to the infinitely-weak and infinitely-strong correlation. The high-density limit of the correlation energy density is

$$\epsilon_c = A\ln(r_s) + B + r_s(C\ln r_s + D) \tag{2.39}$$

where A, B, C, and D are constants, r_s is the Weigner-Seitz radius, and is related to Fermi vector k_F, which are further related to the density as

$$\frac{4}{3}\pi r_s^3 = \frac{1}{\rho} = \frac{k_F^3}{3\pi^2} \tag{2.40}$$

The low density limit is

$$\epsilon_c = \frac{1}{2}\Big(\frac{g_0}{r_s} + \frac{g_1}{r_s^{3/2}} + \cdots\Big) \tag{2.41}$$

where g_0 and g_1 are constants. To find the values in between these density limits, Monte-Carlo simulations have been done, and the data used for interpolation. The functional form and interpolation adopted in this thesis is of Perdew-Wang [19]. This is written as,

$$\epsilon_c(r_s) = -2A(1+\alpha_1 r_s)\ln\Big[1 + \frac{1}{2A(\beta_1 r_s^{1/2} + \beta_2 r_s + \beta_3 r_s^{3/2} + \beta_4 r_s^2)}\Big] \tag{2.42}$$

where the values of the constants are given in table 2.1.

As LDA was built on data from homogeneous electron gas, but then used for inhomogeneous systems, it was not expected to give good results. However, this approximation did surprisingly well for real systems like atoms and molecules. Some of it's successes can be attributed to:

- it's XC hole satisfies the exact sum rules [20, 21, 22] and exact cusp condition [23] whereas the exchange hole also satisfies the exact negativity constraint [24, 25].
- the exchange energy obeys the exact spin scaling [26] (given in next section) and an exact uniform density scaling [27].Further the correlation energy scales properly in low-density limit [28].
- it obeys the Lieb-Oxford lower bound [28, 29, 30].
- Error cancellation exists in LDA as the exchange is typically overestimated and correlation is underestimated and the errors tend to compensate.
- Asymptotic exactness in semiclassical limit [31].

2.4.2 Spin-polarized LDA (LSDA)

The systems we treat have spins present along with the charge and hence we should have XC functionals for spin polarized systems. The known unpolarized functionals can be extended to spin polarized systems.

$$E_{\rm XC}[\rho_\alpha, \rho_\beta] = \int \rho(\mathbf{r}) e_{\rm XC}(\rho_\alpha, \rho_\beta) \tag{2.43}$$

For exchange an exact relation is known between polarized and unpolarized systems and applies for any system.

$$E_{\rm x}[\rho_\alpha, \rho_\beta] = \frac{1}{2}\Big(E_{\rm x}[2\rho_\alpha] + E_{\rm x}[2\rho_\beta]\Big) \tag{2.44}$$

No such relation exists for the much more complicated correlation energy. Functionals are then written in terms of the spin polarization,

$$\zeta(\mathbf{r}) = \frac{\rho_\alpha(\mathbf{r}) - \rho_\beta(\mathbf{r})}{\rho_\alpha(\mathbf{r}) + \rho_\beta(\mathbf{r})} \tag{2.45}$$

where $\zeta = 0$ corresponds to an unpolarized system and $\zeta = \pm 1$ corresponds to the purely ferromagnetic states where only one spin exists. The correlation energy per particle for spin-polarized system is given as,

$$\epsilon_c = \epsilon_c(r_s, 0) + \alpha_c(r_s)\frac{f(\zeta)}{f''(0)}(1 - \zeta^4) + [\epsilon_c(r_s, 1) - \epsilon_c(r_s, 0)]f(\zeta)\zeta^4 \tag{2.46}$$

where $\epsilon_c(r_s, 0)$, $\epsilon_c(r_s, 1)$, and $\alpha_c(r_s)$ are obtained by substituting the constants from Table 2.1 in Eq. 2.42 and $f(\zeta) = \dfrac{[(1+\zeta)^{4/3} + (1-\zeta)^{4/3} + 2]}{2^{4/3} - 2}$.

Table 2.1: The parameters for calculating the correlation energy based on the functional form of Eq.2.42.

	$\epsilon_c(r_s, 0)$	$\epsilon_c(r_s, 1)$	$-\alpha_c(r_s)$
A	0.031091	0.015545	0.016887
α_1	0.21370	0.20548	0.11125
β_1	7.5957	14.1189	10.357
β_2	3.5876	6.1977	3.6231
β_3	1.6382	3.3662	0.88026
β_4	0.49294	0.62517	0.49671

Despite LDA's success there are a number of systems where it performs poorly, e.g. it overestimates the lattice constants for solids, gave wrong ground state for 3d-transition metals like for iron, yields reasonable molecular geometries and vibration frequencies, but can strongly overestimate atomization energies [32]. One way to go beyond the local density approximation was by including the gradients of density in the XC functional which leads us to the next rung of the ladder.

2.4.3 Generalized Gradient Approximation (GGA)

This functional has dependency on both the density and its gradient i.e. $E_{\rm XC} = E_{\rm XC}[\rho(\mathbf{r}), \boldsymbol{\nabla}\rho(\mathbf{r})]$. There are many GGA functionals developed, to name a few Perdew-Wang 91 [33], Perdew-Burke-Ernzerhof (PBE) [34], Armiento and Mattsson (AM05) [35], Perdew-Burke-Ernzerhof revised for solids (PBEsol) [36]. In this thesis the focus is on the PBE functional. The correlation energy is given as:

$$E_c^{\rm PBE}[\rho_\alpha, \rho_\beta] = \int d\mathbf{r}\rho(\mathbf{r})[\epsilon_c^{unif}(r_s, \zeta) + H(r_s, \zeta, t)] \tag{2.47}$$

where r_s and ζ are defined previously, $t = \dfrac{|\boldsymbol{\nabla}\rho|}{2\eta k_s \rho}$ is a dimensionless density gradient. Here $k_s = \sqrt{4k_F/\pi a_0}$ is the Thomas-Fermi screening wave number. Three conditions of slowly varying ($t \to 0$), rapidly varying ($t \to \infty$) and uniform density scaling gives an expression for H as,

$$H = \gamma\eta^3 \ln\Big\{1 + \frac{\beta}{\gamma}t^2\Big[\frac{1 + At^2}{1 + At^2 + At^4}\Big]\Big\} \tag{2.48}$$

where $\eta(\zeta) = [(1+\zeta)^{2/3} + (1-\zeta)^{2/3}]/2$ is spin-scaling factor, $\beta \simeq 0.066725$, $\gamma = (1 - \ln 2)/\pi^2$ and

$$A = \frac{\beta}{\gamma}\Big[\frac{1}{exp[-\epsilon_c^{unif}/(\gamma\eta^3)] - 1}\Big] \tag{2.49}$$

The exchange energy has the following form,

$$E_{\rm x} = \int d\mathbf{r}\epsilon_{\rm x}^{unif}(\rho)F_{PBE}(s) \tag{2.50}$$

where $\epsilon_{\rm x}^{unif} = -3k_F/4\pi$, and $s = |\boldsymbol{\nabla}\rho|/2k_F\rho = r_s^{1/2}\eta t$ is another dimensionless density gradient. The exchange should obey correct uniform gas limit, spin-scaling relationship, Lieb-oxford bound, local spin density of spin-unpolarized uniform electron gas and hence the form of F_{PBE} obtained is,

$$F_{\rm PBE}(s) = 1 + \kappa - \frac{\kappa}{1 + \mu s^2/\kappa} \tag{2.51}$$

where $\kappa = 0.804$, $\mu = \beta(\pi^2/3)$.

Some of the important outcomes of using GGA functionals are:

- Improves ground state properties of light atoms, molecules, clusters and solids.
- 3d transition metals better described, e.g. gives correct bcc ferromagnetic ground state of iron unlike the LDA.

- Structural properties are generally improved with some exceptions like the 5d compounds.

The other rungs of the ladder form meta-GGA functionals, hybrids, double hybrids, exact-exchange functionals and others. As only LDA and GGA functionals are extensively used in this thesis they are explained and if the reader wishes to read more about functionals they are advised to read articles [17, 37, 38, 39].

2.5 Time-Dependent Density Functional Theory

The time-dependent extension of density functional theory to study the dynamics of the systems under time dependent electric and magnetic fields is TDDFT. These time dependent fields result in electronic excitations which drives the system away from equilibrium. The exact dynamics are given by the time-dependent Schrödinger equation for an initial wavefunction $\Phi(\mathbf{r}, 0)$, which is

$$i\frac{\partial}{\partial t}\Phi(\mathbf{r}, t) = H(\mathbf{r}, t)\Phi(\mathbf{r}, t) \tag{2.52}$$

where the Hamiltonian is time-dependent due to the time varying external potential and is written as,

$$H(\mathbf{r}, t) = -\frac{1}{2}\sum_{i}^{N}\boldsymbol{\nabla}_i^2 + \sum_{i=1}^{N}\sum_{j>i}^{N}\frac{1}{|\mathbf{r}_i - \mathbf{r}_j|} + V_{\text{ext}}(\mathbf{r}, t) \tag{2.53}$$

Similar to the ground state DFT, the idea of extracting all the observables from the one-body density (HK theorems) was extended to time-dependent regime by Runge and Gross in 1984 [40]. After the establishment of this theorem TDDFT may be used in many applications. Firstly in spectroscopy where the response of a material is studied to an external weak perturbation, for example, Magneto-Optical Kerr effect (MOKE), Faraday rotation, Electron-energy loss spectroscopy (EELS). Secondly, the real-time dynamics is used in out of equilibrium regimes where the external fields are strong as compared with the systems internal fields for example ultrastrong laser driven demagnetization and spin manipulation on femtosecond timescales.

2.5.1 Runge-Gross theorem

This theorem proves that there is one-to-one correspondence between the time-dependent external potential, $V_{\text{ext}}(\mathbf{r}, t)$, and the electronic one-body density, $\rho(\mathbf{r}, t)$, for many-body systems evolving from a fixed initial state. This is a very powerful statement in the sense that if we have knowledge about the time-dependent density originating from an initial wavefunction, then from Runge-Gross theorem we know time-dependent external potential. Substituting this potential in the Schrödinger equation gives all the information about the

interacting many-body system. Thus making all time-dependent observables functionals of the density. This is similar to the HK theorem, but with subtle difference that there is no time-dependence and no initial state dependence. The proof consists of two steps via the current densities. Additionally, it requires the time-dependent external potential to be Taylor expandable in t around t=0 for a finite time interval i.e. being time-analytic around the initial time.

$$\begin{aligned} v_{\text{ext}}(\mathbf{r},t) &= \sum_{k=0}^{\infty} \frac{1}{k!} v_{\text{ext},k}(\mathbf{r}) t^k \\ v'_{\text{ext}}(\mathbf{r},t) &= \sum_{k=0}^{\infty} \frac{1}{k!} v'_{\text{ext},k}(\mathbf{r}) t^k \end{aligned} \tag{2.54}$$

We are required to show that the two densities $\rho(\mathbf{r},t)$ and $\rho'(\mathbf{r},t)$ under the influence of external potentials $v_{\text{ext}}(\mathbf{r},t)$ and $v'_{\text{ext}}(\mathbf{r},t)$ and starting from the same initial state are always different. The potentials should differ by more than a time-dependent function.

$$v_{\text{ext}}(\mathbf{r},t) \neq v'_{\text{ext}}(\mathbf{r},t) + c(t) \tag{2.55}$$

This time-dependent function does not alter the densities as this gives wavefunctions which differ only by a time-dependent phase factor. In other words,

$$v_{\text{ext},k}(\mathbf{r}) - v'_{\text{ext},k}(\mathbf{r}) = \frac{\partial^k}{\partial t^k}[v_{\text{ext}}(\mathbf{r},t) - v'_{\text{ext}}(\mathbf{r},t)]\Big|_{t=0} \neq 0 \tag{2.56}$$

at some order k.

Step 1: In the first step it is to be shown that the current densities which originate from different potentials are different. The current definition is,

$$\hat{j}(\mathbf{r}) = \frac{1}{2i} \sum_{i=1}^{N} [\boldsymbol{\nabla}_i \delta(\mathbf{r} - \mathbf{r}_i) + \delta(\mathbf{r} - \mathbf{r}_i) \boldsymbol{\nabla}_i] \tag{2.57}$$

To prove this equation of motion for the expectation values of the currents is written as,

$$\begin{aligned} \frac{\partial}{\partial t} j(\mathbf{r},t) &= \frac{\partial}{\partial t} \Big[\langle \Phi | \hat{j}(\mathbf{r}) | \Phi \rangle \Big] = -i \langle \Phi | [\hat{j}(\mathbf{r}), \hat{H}(t)] | \Phi \rangle \\ \frac{\partial}{\partial t} j'(\mathbf{r},t) &= \frac{\partial}{\partial t} \Big[\langle \Phi' | \hat{j}(\mathbf{r}) | \Phi' \rangle \Big] = -i \langle \Phi' | [\hat{j}(\mathbf{r}), \hat{H}'(t)] | \Phi' \rangle \end{aligned} \tag{2.58}$$

Both the wave-functions evolve from the same initial state at t=0

$$\Phi(\mathbf{r},0) = \Phi'(\mathbf{r},0) = \Phi_0 \tag{2.59}$$

and the two Hamiltonians differ only in the external potentials. Now, subtracting the two current densities gives us,

$$\begin{aligned}\frac{\partial}{\partial t}[j(\mathbf{r},t)-j'(\mathbf{r},t)]\Big|_{t=0} &= -i\langle\Phi_0|[\hat{j}(\mathbf{r}),\hat{H}(t)-\hat{H}'(t)]|\Phi_0\rangle \\ &= -\rho(\mathbf{r},0)\boldsymbol{\nabla}[v_{\text{ext}}(\mathbf{r},0)-v'_{\text{ext}}(\mathbf{r},0)]\end{aligned} \tag{2.60}$$

here $\rho(\mathbf{r},0)$ is the initial density. If Eq. (2.56) is satisfied for $k=0$, the current densities j and j' become different infinitesimally later than t=0 as the right hand side of above equation can not vanish. But it could happen that at t=0 the potentials are the same and non-zero only at some later time. Then Eq. (2.56) holds for $k>0$ and the equation of motion for $-i[\hat{j}(\mathbf{r}),\hat{H}(\mathbf{r},t)]$ has to be solved k+1 times. For a given k, we have k nested commutators i.e. $(-i)^k[[[\hat{j}(\mathbf{r}),\hat{H}(\mathbf{r},t)],\hat{H}(\mathbf{r},t)]\hat{H}(\mathbf{r},t)]\cdots,\hat{H}(\mathbf{r},t)]_k$ to solve the equation of motion. After some algebra we obtain,

$$\Big(\frac{\partial}{\partial t}\Big)^k[j(\mathbf{r},t)-j'(\mathbf{r},t)] = -\rho(\mathbf{r},0)\boldsymbol{\nabla}w_k(\mathbf{r}) \neq 0 \tag{2.61}$$

where

$$w_k(\mathbf{r}) = \Big(\frac{\partial}{\partial t}\Big)^k[v_{\text{ext}}(\mathbf{r},t)-v'_{\text{ext}}(\mathbf{r},t)]\Big|_{t=0} \tag{2.62}$$

This again proves that at times infinitesimally later than the initial time yields different current densities.

$$j(\mathbf{r},t) \neq j'(\mathbf{r},t) \tag{2.63}$$

Step 2: In the second step it is to be shown that the densities coming from different current densities are different, which is achieved using the continuity equation.

$$\frac{\partial\rho(\mathbf{r},t)}{\partial t} = -\boldsymbol{\nabla}\cdot j(\mathbf{r},t) \tag{2.64}$$

doing the (k+2) derivative of the two densities and subtracting them gives,

$$\Big(\frac{\partial}{\partial t}\Big)^{k+2}[\rho(\mathbf{r},t)-\rho'(\mathbf{r},t)]\Big|_{t=0} = \boldsymbol{\nabla}\cdot[\rho(\mathbf{r},0)\boldsymbol{\nabla}w_k(\mathbf{r})] \tag{2.65}$$

now to show that the densities get different after small later time than at t=0 it is sufficient to show that the r.h.s does not vanish. For proving this consider the following expression,

$$\begin{aligned}&\int d\mathbf{r}\rho(\mathbf{r},0)[\boldsymbol{\nabla}w_k(\mathbf{r})]^2 \\ &= -\int d\mathbf{r}w_k(\mathbf{r})\boldsymbol{\nabla}\cdot[\rho(\mathbf{r},0)\boldsymbol{\nabla}w_k(\mathbf{r})] + \oint d\mathbf{S}\cdot[\rho(\mathbf{r},0)w_k(\mathbf{r})\boldsymbol{\nabla}w_k(\mathbf{r})]\end{aligned} \tag{2.66}$$

where Green's theorem is used in second part. The surface term vanishes for any physical potential. The l.h.s is positive if $\boldsymbol{\nabla}w_k(\mathbf{r}) \neq 0$, hence integrand of the first term of the r.h.s.

must also be non-zero. Therefore the r.h.s. of Eq.[2.65] can not be zero and densities must become different at an infinitesimally later time than t=0 starting from same initial state.

This completes the proof of Runge-Gross theorem and in short it can be written as

$$\Phi_0 : v_{\text{ext}} \overset{\text{1-1}}{\longleftrightarrow} \rho \tag{2.67}$$

Just like the ground state theory, we now turn to time-dependent Kohn-Sham system, designed such that it reproduces the density of true interacting system from an non-interacting system.

2.5.2 Time-dependent Kohn-Sham equations

The time-dependent Kohn-Sham equations act as a bridge connecting the interacting electrons moving in time-dependent potential, $v_{\text{ext}}(\mathbf{r}, t)$, and the non-interacting electrons moving in time-dependent effective potential, $v_{\text{S}}(\mathbf{r}, t)$.
The time-dependent Kohn-Sham equation is

$$i\frac{\partial}{\partial t}\phi_j(\mathbf{r}, t) = \Big[-\frac{1}{2}\boldsymbol{\nabla}^2 + v_{\text{S}}(\mathbf{r}, t)\Big]\phi_j(\mathbf{r}, t) \tag{2.68}$$

where $\phi_j(\mathbf{r}, t)$ are the KS eigenvectors producing the time-dependent density as,

$$\rho(\mathbf{r}, t) = \sum_{occupied} |\phi_j(\mathbf{r}, t)|^2 \tag{2.69}$$

and the effective KS potential in which the electrons move is the sum of time-dependent counterparts of external potential ($v_{\text{ext}}(\mathbf{r}, t)$), Hartree potential $\left(v_{\text{H}}(\mathbf{r}, t) = \int d\mathbf{r}' \frac{\rho(\mathbf{r}', t)}{|\mathbf{r} - \mathbf{r}'|}\right)$ and the XC potential is defined as

$$v_{\text{XC}}[\rho; \varphi_0, \Phi_0](\mathbf{r}, t) = v_{\text{S}}[\rho, \varphi_0](\mathbf{r}, t) - v_{\text{ext}}[\rho, \Phi_0](\mathbf{r}, t) - v_{\text{H}}[\rho](\mathbf{r}, t) \tag{2.70}$$

As can be seen, the XC potential depends on the entire history of the density, and the initial wavefuctions of both the interacting, $\Phi_0(\mathbf{r}, t)$, and non-interacting systems, $\varphi_0(\mathbf{r}, t)$. However, if we start from the non-degenerate ground state for both the interacting and KS system, then the initial state dependence is subsumed into the density due to the HK theorem. This is generally how the TDDFT is used, i.e. on top of a ground state calculation. Even after removing this dependence the potential still depends on the density's past or has memory i.e. at a particular time, t, and point, $\mathbf{r}$, in space it depends on the density at all previous times, t', for any arbitrary point, $\mathbf{r}'$, in space. This past dependence is ignored in what is known as the adiabatic approximation and only instantaneous density dependence is allowed. This makes the functional local in time.

$$v_{\text{XC}}^{adia}[\rho](\mathbf{r}, t) = v_{\text{XC}}^{approx}[\rho(t)](\mathbf{r}) \tag{2.71}$$

This approximation will be valid if the time-dependent potential changes very slowly or adiabatically and the electrons always stay in their instantaneous ground state. The systems for which this approximation can be made exact requires,

$$v_{\mathrm{XC}}^{adia}[\rho](\mathbf{r},t) = v_{\mathrm{XC}}^{GS}[\rho_{GS}](\mathbf{r})\Big|_{\rho_{GS}(\mathbf{r}')=\rho(\mathbf{r}',t)} \tag{2.72}$$

where $v_{\mathrm{XC}}^{GS}[\rho_{GS}](\mathbf{r})$ is the exact ground state XC potential for the ground state density $\rho_{GS}(\mathbf{r})$. Since the form of exact XC energy functional is unknown even in static case the spatial nonlocality is also approximated. Using this approximation, in principle, any ground state functional such as a GGA or hybrid or meta-GGA can be automatically used in TDDFT calculations.

2.6 Linear Response TDDFT

To study a system of interacting charges and spins, we generally perturb it externally with some stimulus, e.g. electrons (used in Scanning Electron Microscope(SEM), Transmission Electron Microscope(TEM), optical absorption spectra, etc.), photons (used in X-ray Diffraction(XRD), Ellipsometry, etc.), electric fields (all systems have charges present in them and hence the effect of electric field can be used to study electrical conductivity; number and type of charge carriers through Hall coefficient etc.), and magnetic fields (Nuclear Magnetic Resonance (NMR), Quantum Oscillators, de Haas-van Alphen (dHvA) effect, etc.) etc. To calculate such properties, we may use linear-response TDDFT (LR-TDDFT), where we similarly perturb the KS system which must, by definition, reproduce the exact response of the density. We now calculate the linear response of a spin unpolarized system to a small perturbation to the Hamiltonian of $\delta v(\mathbf{r},t)$ (following the derivation of Pines and Nozières [PN66]),

$$\begin{aligned}
\delta\hat{H}(t) &= e^{\Upsilon t}\sum_{i=1}^{N}\delta v(\mathbf{r}_i,t) \qquad\qquad 0<\Upsilon<<1 \\
&= \int d\mathbf{r}e^{\Upsilon t}\sum_{i=1}^{N}\delta v(\mathbf{r},t)\delta(\mathbf{r}-\mathbf{r}_i) \\
&= \int e^{\Upsilon t}\delta v(\mathbf{r},t)\hat{n}(\mathbf{r})d\mathbf{r}
\end{aligned} \tag{2.73}$$

where $e^{\Upsilon t}$ is to insure that the perturbation is slow and stays within the adiabatic regime. Also as $t\to-\infty$, $e^{\Upsilon t}=0$ and 1 for t=0. Writing this perturbation in frequency space,

$$\delta\hat{H}(t) = \int d\mathbf{r}\int\frac{d\omega}{2\pi}e^{-i\breve{\omega}t}\delta v(\mathbf{r},\omega)\hat{n}(\mathbf{r}) \tag{2.74}$$

where $\breve{\omega}=\omega+i\Upsilon$. Hence the time-dependent Hamiltonian can be written as,

$$\hat{H}(t) = \hat{H}^0 + \delta\hat{H}(t) \tag{2.75}$$

where the first term is the Hamiltonian corresponding to the static case and the second is the time-dependent perturbation. The wavefunctions, $|\Phi^0\rangle$, and the eigenvalues, E^0, of the unperturbed system are obtained by solving the Schrödinger equation,

$$\hat{H}^0|\Phi^0\rangle = E^0|\Phi^0\rangle \tag{2.76}$$

Denoting the ground state and excited states by $|\Phi_0^0\rangle$ and $|\Phi_j^0\rangle$ with energies E_0^0 and E_j^0 respectively. The time evolution of ground state is $|\Phi_0^0(t)\rangle = e^{-iE_0^0 t}|\Phi_0^0\rangle$. For the time-dependent perturbation the Schrödinger equation becomes,

$$i\frac{\partial|\Phi(t)\rangle}{\partial t} = \Big(\hat{H}^0 + \delta\hat{H}(t)\Big)|\Phi(t)\rangle \tag{2.77}$$

Within first order perturbation theory we can write the wavefunction as,

$$|\Phi(t)\rangle = e^{-iE_0^0 t}|\Phi_0^0\rangle + \sum_{j\neq 0} a_j(t)|\Phi_j^0\rangle e^{-iE_j^0 t} \tag{2.78}$$

where the first term is the unperturbed time-dependent solution and the second term is admixture of components resulting from excited states of the unperturbed Schrödinger equation excluding the ground state ($j \neq 0$). As it is performed on top of ground state calculation, the response depends on time difference and not on it's absolute value. The coefficients, $a_j(t)$, can be found as

$$\begin{aligned} a_j(t) &= -i\int_{-\infty}^{t} dt' e^{i\omega_{0j}t'}\langle\Phi_j^0|\delta\hat{H}(t')|\Phi_0^0\rangle \\ &= -i\int d\mathbf{r}\int\frac{d\omega}{2\pi}\int_{-\infty}^{t} dt' e^{i(\omega_{0j}-\breve{\omega})t'}\delta v(\mathbf{r}',\omega)\langle\Phi_j^0|\delta\hat{n}(\mathbf{r}')|\Phi_0^0\rangle \\ &= -\int d\mathbf{r}\int\frac{d\omega}{2\pi}\delta v(\mathbf{r}',\omega)\langle\Phi_j^0|\delta\hat{n}(\mathbf{r}')|\Phi_0^0\rangle\frac{e^{i(\omega_{0j}-\breve{\omega})t}}{\omega_{0j}-\breve{\omega}} \end{aligned} \tag{2.79}$$

$\omega_{0j} = E_j - E_0$ is the excitation energy. The change in the density can also be calculated to lowest order.

$$
\begin{aligned}
\rho_{ind}(\mathbf{r},t) &= \delta\rho(\mathbf{r},t) \\
&= \langle\Phi(t)|\hat{n}(\mathbf{r})|\Phi(t)\rangle - \langle\Phi_0(t)|\hat{n}(\mathbf{r})|\Phi_0(t)\rangle \\
&= \Big\{e^{iE_0^0t}\langle\Phi_0^0| + \sum_{j\neq 0} a_j^*(t)e^{iE_j^0t}\langle\Phi_j^0|\Big\}|\hat{n}(\mathbf{r})|\Big\{e^{-iE_0^0t}|\Phi_0^0\rangle + \sum_{j\neq 0} a_j(t)e^{-iE_j^0t}|\Phi_j^0\rangle\Big\} \\
&- e^{iE_0^0t}\langle\Phi_0^0|\hat{n}(\mathbf{r})|\Phi_0^0\rangle e^{-iE_0^0t} \\
&= \langle\Phi_0^0|\hat{n}(\mathbf{r})|\Phi_0^0\rangle + e^{iE_0^0t}\sum_{j\neq 0}\langle\Phi_0^0|\hat{n}(\mathbf{r})|\Phi_j^0\rangle a_j(t)e^{-iE_j^0t} + \sum_{j\neq 0} a_j^*(t)e^{iE_j^0t}\langle\Phi_j^0|\hat{n}(\mathbf{r})|\Phi_0^0\rangle e^{-iE_j^0t} \\
&+ \sum_{j\neq 0} a_j^*(t)a_j(t)e^{iE_j^0t - iE_j^0t}\langle\Phi_j^0|\hat{n}(\mathbf{r})|\Phi_j^0\rangle - \langle\Phi_0^0|\hat{n}(\mathbf{r})|\Phi_0^0\rangle \\
&= \sum_{j\neq 0}\Big[a_j(t)\langle\Phi_0^0|\hat{n}(\mathbf{r})|\Phi_j^0\rangle e^{-i\omega_{0j}t} + a_j^*(t)\langle\Phi_j^0|\hat{n}(\mathbf{r})|\Phi_0^0\rangle e^{i\omega_{0j}t}\Big] \\
&= -\int d\mathbf{r}'\int\frac{d\omega}{2\pi}\delta v(\mathbf{r}',\omega)e^{i(\omega_{0j}-\breve{\omega})t - i\omega_{0j}t}\sum_{j\neq 0}\Big[\frac{\langle\Phi_j^0|\hat{n}(\mathbf{r}')|\Phi_0^0\rangle\langle\Phi_0^0|\hat{n}(\mathbf{r})|\Phi_j^0\rangle}{\omega_{0j}-\breve{\omega}} \\
&+ \frac{\langle\Phi_0^0|\hat{n}(\mathbf{r})|\Phi_j^0\rangle\langle\Phi_j^0|\hat{n}(\mathbf{r})|\Phi_0^0\rangle}{\omega_{0j}+\breve{\omega}}\Big]
\end{aligned}
\tag{2.80}
$$

The induced density in frequency space becomes

$$
\rho_{ind}(\mathbf{r},\omega) = -\int d\mathbf{r}'\delta v(\mathbf{r}',\omega)\sum_{j\neq 0}\Big[\frac{\langle\Phi_j^0|\hat{n}(\mathbf{r}')|\Phi_0^0\rangle\langle\Phi_0^0|\hat{n}(\mathbf{r})|\Phi_j^0\rangle}{\omega_{0j}-\breve{\omega}} + \frac{\langle\Phi_0^0|\hat{n}(\mathbf{r})|\Phi_j^0\rangle\langle\Phi_j^0|\hat{n}(\mathbf{r})|\Phi_0^0\rangle}{\omega_{0j}+\breve{\omega}}\Big]
\tag{2.81}
$$

Now the linear response function can be calculated, defined as the change induced in the density by the change in the external potential,

$$
\begin{aligned}
\frac{\delta\rho(\mathbf{r},\omega)}{\delta v_{\text{ext}}(\mathbf{r}',\omega)} &= \chi(\mathbf{r},\mathbf{r}',\omega) \\
&= -\sum_{j\neq 0}\Big[\frac{\langle\Phi_j^0|\hat{n}(\mathbf{r}')|\Phi_0^0\rangle\langle\Phi_0^0|\hat{n}(\mathbf{r})|\Phi_j^0\rangle}{\omega_{0j}-\breve{\omega}} + \frac{\langle\Phi_0^0|\hat{n}(\mathbf{r})|\Phi_j^0\rangle\langle\Phi_j^0|\hat{n}(\mathbf{r})|\Phi_0^0\rangle}{\omega_{0j}+\breve{\omega}}\Big]
\end{aligned}
\tag{2.82}
$$

This is the response of the fully interacting system in frequency space when the system is acted upon by $\delta v(\mathbf{r},t)$ and the poles correspond to the excitation energy of interacting system. In the non-interacting KS system the ground state wavefunction, Φ_0^0, can be written as a product of orthonormal KS one-particle wavefunctions, ϕ_n

$$\Phi_0^0(\mathbf{r}_1, \mathbf{r}_2, \cdots, \mathbf{r}_{N/2}) = \frac{1}{\sqrt{N}} \begin{vmatrix} \phi_1(\mathbf{r}_1) & \phi_2(\mathbf{r}_1) & \cdots & \phi_n(\mathbf{r}_1) & \cdots & \phi_{N/2}(\mathbf{r}_1) \\ \phi_1(\mathbf{r}_2) & \phi_2(\mathbf{r}_2) & \cdots & \phi_n(\mathbf{r}_2) & \cdots & \phi_{N/2}(\mathbf{r}_2) \\ \vdots & \vdots & \vdots & \vdots & \vdots & \vdots \\ \phi_1(\mathbf{r}_{N/2}) & \phi_2(\mathbf{r}_{N/2}) & \cdots & \phi_n(\mathbf{r}_{N/2}) & \cdots & \phi_{N/2}(\mathbf{r}_{N/2}) \end{vmatrix}$$

When electron moves from an occupied state to an unoccupied state, then we get excited states of the system represented by the following wavefunction,

$$\Phi_j^0(\mathbf{r}_1, \mathbf{r}_2, \cdots, \mathbf{r}_{N/2}) = \frac{1}{\sqrt{N}} \begin{vmatrix} \phi_1(\mathbf{r}_1) & \phi_2(\mathbf{r}_1) & \cdots & \phi_m(\mathbf{r}_1) & \cdots & \phi_{N/2}(\mathbf{r}_1) \\ \phi_1(\mathbf{r}_2) & \phi_2(\mathbf{r}_2) & \cdots & \phi_m(\mathbf{r}_2) & \cdots & \phi_{N/2}(\mathbf{r}_2) \\ \vdots & \vdots & \vdots & \cdots & \vdots & \vdots \\ \phi_1(\mathbf{r}_{N/2}) & \phi_2(\mathbf{r}_{N/2}) & \cdots & \phi_m(\mathbf{r}_{N/2}) & \cdots & \phi_{N/2}(\mathbf{r}_{N/2}) \end{vmatrix}$$

where $m > N/2$. Then the expectation value of $\langle \Phi_0^0 | \hat{n}(\mathbf{r}) | \Phi_j^0 \rangle$ is,

$$\sum_k \langle \phi_1(\mathbf{r}_1)\phi_2(\mathbf{r}_2)\cdots\phi_n(\mathbf{r}_i)\cdots\phi_{N/2}(\mathbf{r}_{N/2}) | \delta(\mathbf{r}-\mathbf{r}_k) | \phi_1(\mathbf{r}_1)\phi_2(\mathbf{r}_2)\cdots\phi_m(\mathbf{r}_i)\cdots\phi_{N/2}(\mathbf{r}_{N/2}) \rangle = \phi_n^*(\mathbf{r})\phi_m^*(\mathbf{r}) \tag{2.83}$$

Also the one-particle energies are $\omega_{nm} = \epsilon_m - \epsilon_n$. Thus the response of the KS system is,

$$\chi^{KS}(\mathbf{r}, \mathbf{r}', \omega) = -\sum_{n_{occ}} \sum_{m_{unocc}} 2\Big(\frac{\phi_m^*(\mathbf{r}')\phi_n(\mathbf{r}')\phi_n^*(\mathbf{r})\phi_m(\mathbf{r})}{\omega_{nm} - \breve{\omega}} + \frac{\phi_n^*(\mathbf{r}')\phi_m(\mathbf{r}')\phi_m^*(\mathbf{r})\phi_n(\mathbf{r})}{\omega_{nm} + \breve{\omega}} \Big) \tag{2.84}$$

where 2 is to account for the unpolarized system. The transition will take place from an occupied level to an unoccupied level. Hence writing in terms of Fermi distribution function, f with values of 1 for occupied and 0 for unoccupied.

$$\chi^{KS}(\mathbf{r}, \mathbf{r}', \omega) = -\sum_{n_{all}} \sum_{m_{all}} 2f_n(1-f_m)\Big(\frac{\phi_m^*(\mathbf{r}')\phi_n(\mathbf{r}')\phi_n^*(\mathbf{r})\phi_m(\mathbf{r})}{\epsilon_m - \epsilon_n - \breve{\omega}} + \frac{\phi_n^*(\mathbf{r}')\phi_m(\mathbf{r}')\phi_m^*(\mathbf{r})\phi_n(\mathbf{r})}{\epsilon_m - \epsilon_n + \breve{\omega}} \Big) \tag{2.85}$$

The Fourier transform of $\chi(\mathbf{r}, \mathbf{r}', \omega)$ is $\chi(\mathbf{q}, \mathbf{q}', \omega)$ and for periodic systems having translational invariance, $\chi(\mathbf{r}+\mathbf{R}, \mathbf{r}'+\mathbf{R}) = \chi(\mathbf{r}, \mathbf{r}')$ will be non zero only when $\mathbf{q}$ and $\mathbf{q}'$ (within the first brillouin zone) differ by a reciprocal lattice vector, $\mathbf{G}$. Also by Bloch's theorem the sum of states can be relabelled by k-points and states n, m. Then the response in momentum space is given by,

$$\chi^{KS}_{\mathbf{G}\mathbf{G}'}(\mathbf{q},\omega) = -\frac{1}{\Omega}\sum_{nk}\sum_{mk'} 2f_{nk}(1-f_{mk')}\Big(\frac{\langle\phi_{mk'}|e^{i(\mathbf{q}+\mathbf{G})\cdot\mathbf{r}}|\phi_{nk}\rangle\langle\phi_{nk}|e^{-i(\mathbf{q}+\mathbf{G}')\cdot\mathbf{r}}|\phi_{mk'}\rangle}{\epsilon_{mk'}-\epsilon_{nk}-\breve{\omega}} + \frac{\langle\phi_{nk}|e^{i(\mathbf{q}+\mathbf{G})\cdot\mathbf{r}}|\phi_{mk'}\rangle\langle\phi_{mk'}|e^{-i(\mathbf{q}+\mathbf{G}')\cdot\mathbf{r}}|\phi_{nk}\rangle}{\epsilon_{mk'}-\epsilon_{nk}-\breve{\omega}}\Big) \tag{2.86}$$

where Ω is unit cell volume

$$\begin{aligned}\langle\phi_{mk'}|e^{i(\mathbf{q}+\mathbf{G})\cdot\mathbf{r}}|\phi_{nk}\rangle &= \int d\mathbf{r}\phi^*_{mk'}(\mathbf{r})e^{i(\mathbf{q}+\mathbf{G})\cdot\mathbf{r}}\phi_{nk}(\mathbf{r}) \\ &= \delta(\mathbf{k}'-\mathbf{q}-\mathbf{k})\int_\Omega d\mathbf{r}u^*_{mk'}(\mathbf{r})e^{i\mathbf{G}\cdot\mathbf{r}}u_{nk}(\mathbf{r})\end{aligned} \tag{2.87}$$

where the KS states are Bloch states consisting of lattice periodic part, $u(\mathbf{r})$, and the oscillating part, $e^{i\mathbf{k}\cdot\mathbf{r}}$. By changing the summation index in second term we can combine both terms of Eq. (2.86) and get,

$$\chi^{KS}_{\mathbf{G},\mathbf{G}'}(\mathbf{q},\omega) = \frac{1}{\Omega}\sum_{nk}\sum_{mk'} 2(f_{mk'}-f_{nk})\frac{\langle\phi_{mk'}|e^{i(\mathbf{q}+\mathbf{G})\cdot\mathbf{r}}|\phi_{nk}\rangle\langle\phi_{nk}|e^{-i(\mathbf{q}+\mathbf{G}')\cdot\mathbf{r}'}|\phi_{mk'}\rangle}{\epsilon_{mk'}-\epsilon_{nk}-\breve{\omega}} \tag{2.88}$$

Now the aim in TDDFT is to use this information of the KS system and obtain the response of the fully interacting system. Writing again the responses of the interacting and non-interacting system in the time domain,

Interacting system:

$$\begin{aligned}\delta\rho(\mathbf{r},t) &= \int dt'\int d\mathbf{r}'\chi(\mathbf{r},\mathbf{r}',t-t')\delta v_{\text{ext}}(\mathbf{r}',t') \\ \chi(\mathbf{r},\mathbf{r}',t-t') &= \frac{\delta\rho(\mathbf{r},t)}{\delta v_{\text{ext}}(\mathbf{r}',t')}\end{aligned} \tag{2.89}$$

Non-interacting system:

$$\begin{aligned}\delta\rho(\mathbf{r},t) &= \int dt'\int d\mathbf{r}'\chi^{KS}(\mathbf{r},\mathbf{r}',t-t')\delta v_{\text{S}}(\mathbf{r}',t') \\ \chi^{KS}(\mathbf{r},\mathbf{r}',t-t') &= \frac{\delta\rho(\mathbf{r},t)}{\delta v_{\text{S}}(\mathbf{r}',t')}\end{aligned} \tag{2.90}$$

To bridge these two systems we use the fact that the density change arising from both is, by definition, the same. Hence,

$$\begin{aligned}\int dt' \int d\mathbf{r}' \chi(\mathbf{r},\mathbf{r}',t-t')\delta v_{\text{ext}}(\mathbf{r}',t') &= \int dt' \int d\mathbf{r}' \chi^{KS}(\mathbf{r},\mathbf{r}',t-t')\delta v_{\text{S}}(\mathbf{r}',t') \\ &= \int dt' \int d\mathbf{r}' \chi^{KS}(\mathbf{r},\mathbf{r}',t-t')[\delta v_{\text{ext}}(\mathbf{r}',t') + \delta v_{\text{H}}(\mathbf{r}',t') + \delta v_{\text{XC}}(\mathbf{r}',t')]\end{aligned} \tag{2.91}$$

Applying the chain rule we get,

$$\begin{aligned}\delta v_{\text{H}}(\mathbf{r}',t') &= \int dt_1 \int dt_2 \int d\mathbf{r}_1 \int d\mathbf{r}_2 \frac{\delta v_{\text{H}}(\mathbf{r}',t')}{\delta\rho(\mathbf{r}_1,t_1)} \frac{\delta\rho(\mathbf{r}_1,t_1)}{\delta v_{\text{ext}}(\mathbf{r}_2,t_2)} \delta v_{\text{ext}}(\mathbf{r}_2,t_2) \\ &= \int dt_1 \int dt_2 \int d\mathbf{r}_1 \int d\mathbf{r}_2 \frac{1}{|\mathbf{r}_1-\mathbf{r}'|} \chi(\mathbf{r}_1,\mathbf{r}_2,t_1-t_2)\delta v_{\text{ext}}(\mathbf{r}_2,t_2) \\ \delta v_{\text{XC}}(\mathbf{r}',t') &= \int dt_1 \int dt_2 \int d\mathbf{r}_1 \int d\mathbf{r}_2 \frac{\delta v_{\text{XC}}(\mathbf{r}',t')}{\delta\rho(\mathbf{r}_1,t_1)} \frac{\delta\rho(\mathbf{r}_1,t_1)}{\delta v_{\text{ext}}(\mathbf{r}_2,t_2)} \delta v_{\text{ext}}(\mathbf{r}_2,t_2) \\ &= \int dt_1 \int dt_2 \int d\mathbf{r}_1 \int d\mathbf{r}_2 f_{\text{XC}}(\mathbf{r}',\mathbf{r}_1,t'-t_1)\chi(\mathbf{r}_1,\mathbf{r}_2,t_1-t_2)\delta v_{\text{ext}}(\mathbf{r}_2,t_2)\end{aligned} \tag{2.92}$$

where f_{XC} is the XC kernel obtained from the Taylor series expansion of the XC potential up to first order,

$$\begin{aligned} v_{\text{XC}}[\rho_0+\delta\rho](\mathbf{r},t) &= v_{\text{XC}}[\rho_0](\mathbf{r}) + \int dt' \int d\mathbf{r}' f_{\text{XC}}[\rho_0](\mathbf{r},\mathbf{r}',t-t')\delta\rho(\mathbf{r}',t') \\ f_{\text{XC}}[\rho_0](\mathbf{r},\mathbf{r}',t-t') &= \frac{\delta v_{\text{XC}}(\mathbf{r},t)}{\delta\rho(\mathbf{r}',t')}\Big|_{\rho=\rho_0}\end{aligned} \tag{2.93}$$

Substituting Eq. (2.92) in Eq. (2.91), an equation for χ is obtained, in frequency space it reads:

$$\chi(\mathbf{r},\mathbf{r}',\omega) = \chi^{KS}(\mathbf{r},\mathbf{r}',\omega) + \int d\mathbf{r}_1 d\mathbf{r}_2 \chi^{KS}(\mathbf{r},\mathbf{r}_1,\omega)\Big[\frac{1}{|\mathbf{r}_1-\mathbf{r}_2|} + f_{\text{XC}}(\mathbf{r}_1,\mathbf{r}_2,\omega)\Big]\chi(\mathbf{r}_2,\mathbf{r}',\omega) \tag{2.94}$$

This is known as the Dyson-like equation and can be used to obtain the fully interacting response of a system from the non-interacting KS system. Dropping the dependencies it may be written in the following compact form

$$\chi = \chi^{KS} + \chi^{KS}[f_{\text{H}} + f_{\text{XC}}]\chi \tag{2.95}$$

For non-collinear spin-polarized systems this can be generalized,

$$\begin{aligned}\chi_{\mu\nu}(\mathbf{r},\mathbf{r}',\omega) = \chi^{KS}_{\mu\nu}(\mathbf{r},\mathbf{r}',\omega) + \sum_{\delta\gamma} \int d^3r'' \int d^3r''' \chi^{KS}_{\mu\delta}(\mathbf{r},\mathbf{r}'',\omega)\Big[f_{\text{H}}^{\delta\gamma}(\mathbf{r}'',\mathbf{r}''') \\ + f_{\text{XC}}^{\delta\gamma}(\mathbf{r}'',\mathbf{r}''',\omega)\Big]\chi_{\gamma\nu}(\mathbf{r}''',\mathbf{r}',\omega)\end{aligned} \tag{2.96}$$

where $\mu = [0, 1 \cdots 3]$ and $f_{\text{H}} = \dfrac{\delta_{0\mu}\delta_{0\nu}}{|\mathbf{r} - \mathbf{r}'|}$ is Hartree kernel, the density becomes a 4-vector given as $\rho^{\mu} = [\rho^0, \mathbf{m}]$, also the XC potential becomes $v^{\mu}_{\text{XC}} = [v_{\text{XC}}, \mathbf{B}_{\text{XC}}]$. The non-interacting KS linear response functions can easily be calculated in terms of the KS spinors, $\phi(\mathbf{r})$:

$$\chi^{KS}_{\mu\nu}(\mathbf{r}, \mathbf{r}', \omega) = \lim_{\Upsilon \to 0} \sum_{p} \sum_{q} \sigma^{\mu}\sigma^{\nu}(f_p - f_q) \frac{\phi^*_p(\mathbf{r})\phi_q(\mathbf{r})\phi_p(\mathbf{r}')\phi^*_q(\mathbf{r}')}{\omega + (\varepsilon_p - \varepsilon_q) + i\Upsilon} \tag{2.97}$$

where f_p, f_q denote the occupation number of the p^{th}, q^{th} band, respectively, and $\sigma^{\mu} = [\text{I}, \sigma]$ are the four-dimensional counterparts of Pauli spin matrices, σ, with the identity matrix, I.

For practical applications approximations are needed for the XC kernel. In principle, we can have as many kernels as XC potentials, as any approximations may be used within the adiabatic approximations. However, the level of complexity increases as we climb up the Jacob's ladder of approximations. The simplest approximation which is widely adopted for these linear-response calculations is the Adiabatic LSDA (ALSDA). Before discussing the XC approximations for the kernel, we should look at the response and it's encoded information. The structure of response is a 4×4 matrix:

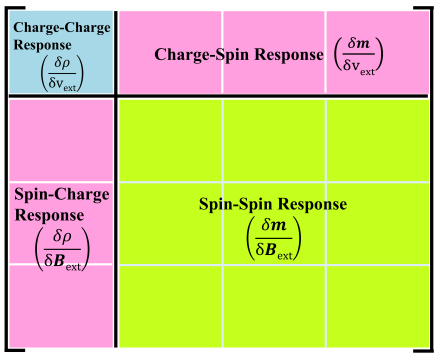

Figure 2.4: The structure of the fully interacting and non-interacting response functions

where the different blocks give the different responses. First is the charge-charge response which is how the charge responds to the scalar potential, second is charge-spin which tells how charge responds to a magnetic field, third is spin-charge giving information about spin response to scalar potential, and lastly the spin-spin response gives spin response to an applied magnetic fields.

Conventionally, the excitations are studied in the decoupled limit where the off-diagonal terms of Fig. 2.4 are set to zero (i.e. $\delta\mathbf{m}/\delta v_{\text{ext}} = \delta\rho/\delta\mathbf{B}_{\text{ext}}$=0). This allows us to separate and study the charge-charge response and spin-spin response independently.

2.6.1 Charge-Charge response

In the linear regime an electron is excited from an occupied state to an unoccupied state when it absorbs a photon (see Fig. 2.5). The relation between the absorbed energy as a function of photon frequency gives the absorption spectra and can be calculated for molecules, atoms or solids. For periodic systems, it is given by imaginary part of the dielectric constant. It contains information about both the density of states that take part in the absorptive processes and the frequency of the excitation. All this information is embedded in the charge-charge part of the matrix Fig. 2.4, and extensive work [41, 42, 43, 44] has been done to study these electronic and optical excitations using TDDFT.

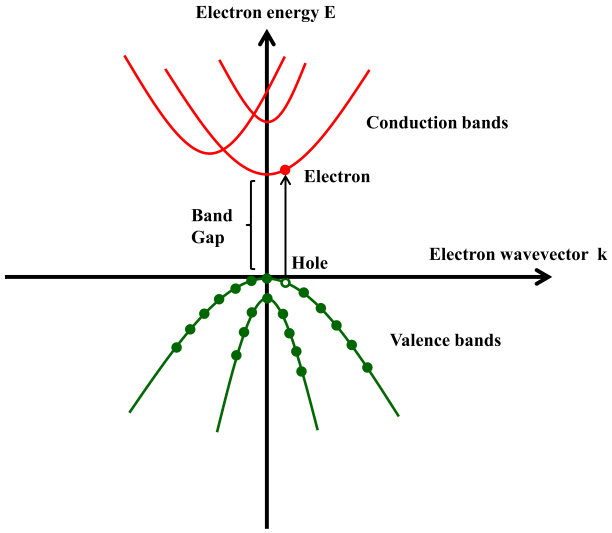

Figure 2.5: A cartoon of excitation of electron from valence band to conduction band.

Experimental observables may then be extracted from the response functions, for example, the inverse dielectric function is

$$\begin{aligned} \epsilon^{-1} &= 1 + v\Big(\frac{\delta\rho}{\delta v}\Big) \\ &= 1 + v\chi \end{aligned} \tag{2.98}$$

where v is the bare Coulomb potential. The imaginary part of ϵ^{-1} gives the EELS whereas the imaginary part of ϵ gives the absorption spectrum in long wavelength limit.
As stated above to study these optical excitations an approximation for the kernel is needed and in charge-charge response many kernels have been developed. These kernels were required to correct the interesting physics of excitons, which are bound electron hole pairs, and can be seen as a peak below the bandgap in the absorption spectra (see Fig. 2.6). To produce these peaks it was found that the XC kernel should have the correct long-wavelength limit, it must go as $1/\mathbf{q}^2$ as $\mathbf{q} \to 0$. This behavior of the kernel is missing in the Random Phase

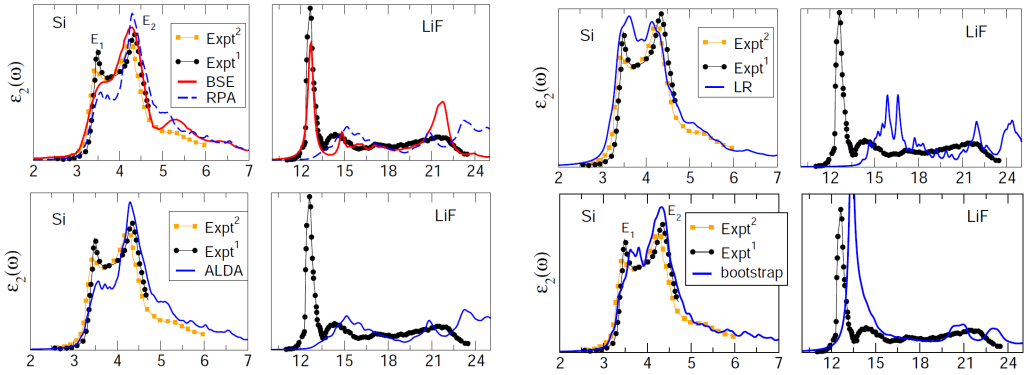

Figure 2.6: The absorption spectra for Silicon and LiF (taken from [41]) for various kernels and compared to experiments. The reference for the experimental data can be found in the cited chapter.

Approximation [45, 46] and Adiabatic LDA kernels, hence new kernels were developed, such as Long Range kernel [47, 48], Bootstrap kernel [49, 50], Nanoquanta kernel[47, 51].

The EELS at finite q-values can be accurately treated by ALDA kernel, in contrast to the absorption spectra in the long-wavelength limit. This indicates that away from Γ-point the $1/\mathbf{q}^2$ dependence of kernel is less relevant. Outside the first Brillouin Zone (BZ) the EELS is suppressed which is captured by all the kernel qualitatively (Fig. 2.7). The BSE kernel reproduces the experiment quite well whereas the bootstrap data is blue-shifted by ≈ 0.75eV. The ALDA kernel is an improvement over the RPA kernel but not significantly.

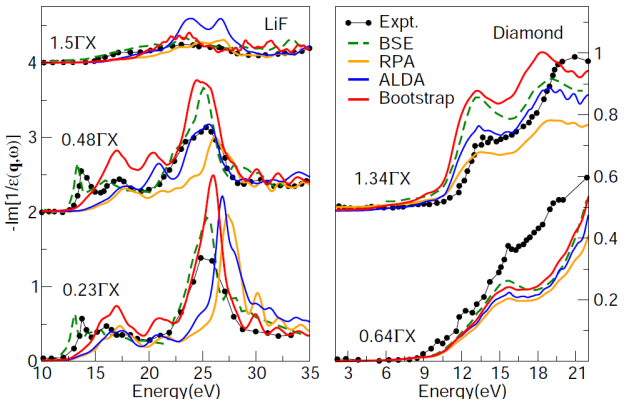

Figure 2.7: The EELS for LiF and Diamond (taken from [41]) for various kernel used and compared to experiments. The reference for the experimental data can be found in the cited chapter.

2.6.2 Spin-Spin response

A magnetic system is formed when spins align in a particular direction breaking the rotational symmtery. Whenever a symmetry is broken it leads to excitations of zero energy known as

Goldstone excitations. Finite energy excitations are possible and can be studied as a function of wavevector $\mathbf{q}$. Thus, this dispersion spectrum must go to zero as $\mathbf{q}$ goes to zero, satisfying the Goldstone theorem. However, in real systems having magnetic anisotropy these zero-energy excitations do not exist and we get finite energy at $\mathbf{q} = 0$. The spin ordered systems can be excited in two ways by an external perturbation, which can be understood with the example of a ferromagnetic system (shown in Fig. 2.8). For this system a ground state of spins is formed when they spontaneously align with each other in one direction. One of the ways a spin can be excited is when it completely flips, reducing the angular momentum of the system by $\hbar$. This spin reversal costs high energy as it has overcome the Heisenberg interaction of its neighboring spins (see Fig. 2.101). However low energy excitations are possible, where this spin reversal is spread over many spins like a waveform. The quanta of this excitation is called a magnon.

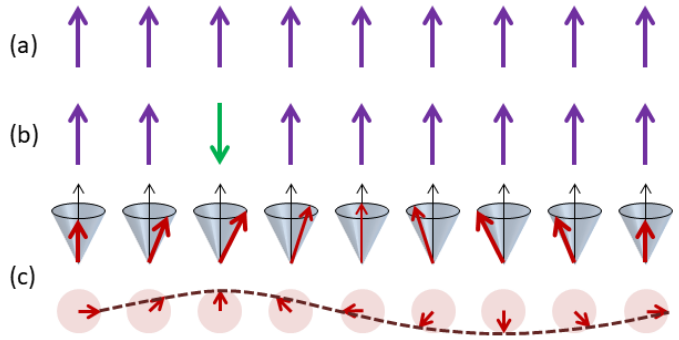

Figure 2.8: (a) Ground state of a ferromagnetic material. (b) High energy single particle spin flip. (c) Low energy spin-waves.

In realistic systems, the magnetic excitation where a single electron of a given spin is excited from an occupied state below the Fermi level into an empty state with opposite spin, leaving a hole behind is known as a stoner excitation. These excitations are described by the Stoner model, but it neglects the interactions between the excited electron and hole. This leads to high energies of magnetic excitations which then lead to wrong curie temperatures. To explain the experimentally observed Curie temperatures the itinerant electron model is needed, which considers the low-energy excitations. These are collective excitations whose nature can be described by the superposition of single-particle states and the correlated motion of the spin-reversed electron and hole left behind in the sea of aligned electrons. This was introduced by Slater [52] for an itinerant electron insulator and was extended by Herring and Kittel [53, 54]. The general finding was that these collective excitations in the itinerant model are identical to the well-defined spin waves in the localized model of Fig. 2.8(c), in the limit of low wave vectors and low energies. For a ferromagnet, in this limit the dispersion relation is quadratic in nature and at high wave-vectors the magnon energies become comparable to the Stoner excitations. The region in which Stoner excitations are possible, the collective excitations get damped and they are not well defined. The reason behind this is that the correlated electron-hole pair decays into uncorrelated states.

To understand this picture a cartoon of exchange-split bands is shown in Fig. 2.9 for

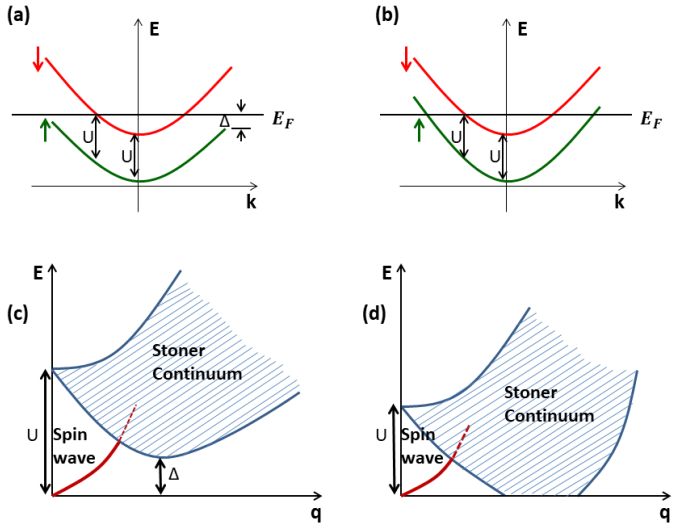

Figure 2.9: The exchange split bands with majority band (a) completely below the Fermi level representing strong ferromagnet and (b) for a weak ferromagnet when majority band is half filled. The excitation spectra for both the cases is shown in (c) and (d) respectively.

two situations: (a) when the majority band is completely filled, i.e. completely below the Fermi level and (b) when it is half filled. The first case corresponds to a strong ferromagnet while the second one to a weak ferromagnet. Here, the exchange splitting , U, is taken to be identical over the whole BZ which is not the case in real material. At low and high wave vectors the energy required to excite an electron from an occupied band to an unoccupied band is shown in Fig. 2.9 (c) and (d) as the shaded area. This represents the single particle stoner excitations. The minimum energy required for stoner excitation is the difference between the top of majority band and the Fermi level called the Stoner gap Δ. At $\mathbf{q} = 0$ this excitation costs U amount of energy while the minimum energy for such an excitations lies at some high $\mathbf{q}$ vector. The spin wave is also shown in the figure which gets damped when it interacts with the stoner continuum.

The single-particle stoner excitations are collinear excitations while the spin waves are non-collinear excitations. Stoner excitations change the magnetization along a preferential direction hence collinear. Whereas, spin waves excites the moment off this preferential axis, leading to non-collinear state. The linear-response TDDFT formalism can be applied to study these collinear and non-collinear excitations. Both these excitations can be seen from the x, y components of the spin-spin response function. While, the longitudinal response does not contain spin-flips excitations.
The spin-spin response is a 3×3 matrix given by,

$$\chi_{ij} = \begin{bmatrix} \chi_{xx} & \chi_{xy} & \chi_{xz} \\ \chi_{yx} & \chi_{yy} & \chi_{yz} \\ \chi_{zx} & \chi_{zy} & \chi_{zz} \end{bmatrix}$$

For collinear initial states, it takes a simpler form, and incorporating the symmetries due to

Pauli spin matricies, it becomes:

$$\chi_{ij} = \begin{bmatrix} \chi_{xx} & \chi_{xy} & 0 \\ -\chi_{xy} & \chi_{yy} & 0 \\ 0 & 0 & \chi_{zz} \end{bmatrix}$$

Instead of working in this basis for the transversal excitations it is better to utilize the ladder operators,

$$\begin{aligned} \chi^{-+} &= 2\chi_{xx} + 2i\chi_{xy} \\ \chi^{+-} &= 2\chi_{xx} - 2i\chi_{xy} \end{aligned} \tag{2.99}$$

The magnon spectra of a system can be calculated from the transverse response function $\chi^{-+}(\mathbf{q},\omega)$, which is found using the Dyson-like equation, Eq. (2.96). The excitations in $\chi^{-+}(\mathbf{q},\omega)$ originate from two sources: (1) renormalized poles of the KS response χ_0 corresponding to the Stoner continuum of single-particle spin-flips and (2) additional peaks created by the XC kernel corresponding to spin-wave excitations.

Experimentally, the transverse magnetic response is proportional to the neutron scattering cross-section [55]

$$\begin{aligned} \frac{d^2\sigma}{d\Omega d\omega} \propto \Big\{ &(1-\kappa_z^2) Im[\chi^{zz}(\mathbf{q},\omega)] \\ &+ \frac{1}{4}(1-\kappa_z^2) Im[\chi^{-+}(\mathbf{q},\omega) + \chi^{+-}(\mathbf{q},\omega)] \Big\} \end{aligned} \tag{2.100}$$

where $\kappa_z = (\mathbf{k}_f - \mathbf{k}_i)_z / |\mathbf{k}_f - \mathbf{k}_i|$ is related to the $\mathbf{q}$-vector through $\mathbf{q} = \mathbf{k}_f - \mathbf{k}_i$ and is folded back into the first BZ.

Magnons in the Heisenberg model:

Magnons are usually studied using the Heisenberg Hamiltonian which can be written as,

$$H = \frac{1}{2} \sum_{i,j} J_{ij} \mathbf{S}_i \cdot \mathbf{S}_j \tag{2.101}$$

here the exchange interaction between spins $\mathbf{S}_i$ and $\mathbf{S}_j$ at sites i and j is J_{ij}. Only small perturbations in the transverse components ($S_j^{\pm} = S_j^x \pm S_j^y$) are considered such that $\langle S_j^z \rangle = S$. Then the equation of motion can be written for the transverse components which contain magnon excitations.

$$\begin{aligned} \frac{dS_i^x}{dt} &= \sum_j J_{ij} \Big(\mathbf{S}_i \times \mathbf{S}_j \Big)_x \\ &= \Big(\mathbf{S}_i \times \mathbf{B}_i^{eff} \Big)_x \end{aligned} \tag{2.102}$$

Here B^{eff} can be understood as an effective magnetic field felt by a single spin due to exchange interactions with its neighbors. Making an ansatz for $S_i^x = \mathrm{A}\cos(\mathbf{q}\cdot\mathbf{R}_i - \omega_{\mathbf{q}}t)$ and $S_i^y = \mathrm{A}\sin(\mathbf{q}\cdot\mathbf{R}_i - \omega_{\mathbf{q}}t)$ the frequency/energy of the $\mathbf{q}$ magnon mode can be derived:

$$\begin{aligned} -A\omega_{\mathbf{q}}e^{i(\mathbf{q}\cdot\mathbf{R}_i-\omega_{\mathbf{q}}t)} &= \sum_{ij} J_{ij}\Big(S_i^y S_j^z - S_i^z S_j^y\Big) \\ &= \sum_{j} J_{ij}\Big(SAe^{i(\mathbf{q}\cdot\mathbf{R}_i-\omega_{\mathbf{q}}t)} - SAe^{i(\mathbf{q}\cdot\mathbf{R}_j-\omega_{\mathbf{q}}t)}\Big) \\ \omega_{\mathbf{q}} &= S\sum_{j} J_{ij}\Big(1 - e^{i(\mathbf{q}\cdot(\mathbf{R}_j-\mathbf{R}_i))}\Big) \end{aligned} \tag{2.103}$$

As can be seen, the magnon energy is dependent on the Fourier transform of the exchange coupling. These exchange parameters are usually extracted from DFT ground state calculations using the frozen magnon approach [56, 57, 58].

2.7 Real-time TDDFT

In non-collinear systems, Eq. (2.52) must be extended, where the Kohn-Sham orbitals for a spin system are treated as 2-component Pauli spinors and propagated using the following equation:

$$\begin{aligned} i\frac{\partial\phi_j(\mathbf{r},t)}{\partial t} = \Big[\frac{1}{2}\Big(-i\boldsymbol{\nabla} + \frac{1}{c}\mathbf{A}_{\mathrm{ext}}(t)\Big)^2 + v_{\mathrm{S}}(\mathbf{r},t) + \frac{1}{2c}\boldsymbol{\sigma}\cdot\mathbf{B}_{\mathrm{S}}(\mathbf{r},t) \\ + \frac{1}{4c^2}\boldsymbol{\sigma}\cdot(\boldsymbol{\nabla}v_{\mathrm{S}}(\mathbf{r},t)\times -i\boldsymbol{\nabla})\Big]\phi_j(\mathbf{r},t) \end{aligned} \tag{2.104}$$

where the last represents the spin-orbit coupling term. A time-dependent DOS can be used to see how the states in each spin channel are being occupied above the Fermi level as time propagates. This becomes a very useful tool when the interaction of the laser with a system is investigated. It can be obtained from the following formula,

$$\rho(\omega,t) = \sum_{i=1}^{\infty}\int_{BZ}\delta(\omega-\epsilon_{i\mathbf{k}})g_{i\mathbf{k}}(t) \tag{2.105}$$

with

$$g_{i\mathbf{k}}(t) = \sum_j f_{j\mathbf{k}}|O_{ij}^{\mathbf{k}}(t)|^2 \tag{2.106}$$

where $f_{j\mathbf{k}}$ is the occupation number of the j^{th} evolving orbital and

$$O_{ij}^{\mathbf{k}}(t) = \int d\mathbf{r}(\phi_{i\mathbf{k}}^0)^*(\mathbf{r})\phi_{j\mathbf{k}}(\mathbf{r},t) \tag{2.107}$$

with $\phi^0_{i\mathbf{k}}(\mathbf{r})$ the ground state KS orbitals. In the absence of any time-dependent perturbation, $\phi_{j\mathbf{k}}(\mathbf{r},t) = \phi^0_{j\mathbf{k}}(\mathbf{r})$ and one correctly obtains the ground state density of states.

To study magnons in real-time TDDFT, the oscillations in the magnetization density may be analyzed. The Fourier transform of these oscillations is done to obtain the power spectrum (defined below), which is peaked at the magnon frequency.

$$\left|\tilde{m}(\omega)\right| = \left| \int e^{-i\omega t} m(t) f(t) dt \right| \tag{2.108}$$

However, as the magnetization simulations has a finite time period (T) due to computational limitations one obtains noise in the Fourier transform. This noise can be smoothed out by introducing a damping function before the Fourier transform is performed. One choice for this damping function is the third order polynomial in time [59] given by,

$$f(t) = 1 - 3\Big(\frac{t}{T}\Big)^2 + 2\Big(\frac{t}{T}\Big)^3 \tag{2.109}$$

The properties of this function makes the Fourier transform of magnetization smooth. However, the width of any peak in the spectrum can be artificially increased if the simulation time is not sufficiently long.

All these equations either in the static regime or in time-dependent regime are implemented in the ELK code. Hence a look at the code is done next.

2.8 The ELK code

The ELK code is an all-electron code based on a linearized augmented plane-wave (LAPW) basis or APW+l.o. basis, where l.o. stands for local orbital. Here the space is divided into muffin tin (MT), regions around each atom, and the rest known as the interstitial region (IR), as can be seen in Fig. 2.10.

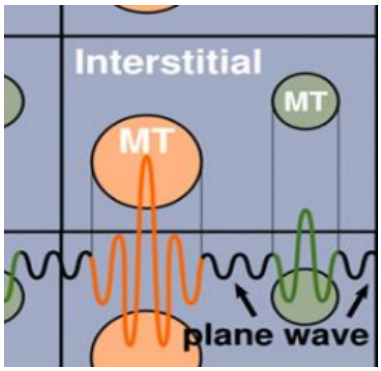

Figure 2.10: Representation of the LAPW basis set. (From [60])

The KS orbitals within the MT are expanded using spherical harmonics and in the IR region, where the potential is nearly constant, using plane waves. The wavefunctions, formed

with suitable basis functions, in the two regions (MT and IR) are matched at the boundary of the two. Deeper lying electrons (≈100 eV below the Fermi energy) are treated as core electrons. These are treated by solving the Dirac equation, as the core electrons feel strong potential and can be regarded as having relativistic speeds.

As the unit cell gets divided into MT and IR region all the physical quantities are also divided into MT and IR region. For example the time-dependent magnetic moments in the MT and IR regions can be obtained from:

$$\mathbf{m}(t)^{MT/IR} = \int_{MT/IR} \mathbf{m}(\mathbf{r}, t) d\mathbf{r} \tag{2.110}$$

The dynamics of the MT moments has been plotted in all the calculations done in the following chapters.

CHAPTER 3

ADIABATIC GGA (AGGA) KERNEL

If you have a derivation with some approximation,
I recommend "Assume a spherical cow ····· "
-Anonymous

There are many different flavors of XC energy functionals in ground-state DFT as discussed in Chapter 2. These comprise the so called *Jacob's ladder* [17] of approximations, where the level of accuracy increases as we climb from LDA to hybrids. The performance of these approximations in static ground-state DFT has been well-studied, however much less is known about their behavior in TDDFT. This is an active research field, involving development of functionals, including those within the adiabatic approximation, and those going beyond the adiabatic approximation [61, 62, 63, 64]. Most of the research concerns the optical absorption spectra, and, in particular, the failure of simple XC kernels to predict bound excitons. From these studies, we know the importance of describing the long wavelength limit of the XC kernel correctly in order to obtain reasonable exciton binding energies, leading to a number of new approximations [65, 49, 66, 67, 47, 48, 68, 69, 70]. However for magnetic excitations, only the ALDA XC kernel within the framework of TDDFT has been properly studied, e.g. for calculations of the magnon spectra [71, 72, 73], where for many cases it overestimates magnon energies as compared to experiments. Besides TDDFT, many-body perturbation theory can be used [74, 75] to calculate magnon spectra. Additionally, time-dependent generalization of all-electron Sternheimer approach [76] or exchange parameters [57, 56] extracted from ground state DFT calculations can also be used to calculate the magnon spectra using DFT/TDDFT.

In this chapter we will derive the XC kernel for GGA functionals within the adiabatic approximation, which is semi-local in space and local in time. It will be reviewed firstly for unpolarized systems, and then derived for spin-polarized systems. Extension to non-collinear systems is done by using Kubler's method which utilizes the kernel derived for collinear systems. Lastly, the implementation of the kernel in the all-electron ELK code is discussed.

3.1 Unpolarized kernel

For the spin unpolarized case, the XC energy functional, E_{XC}, depends not only on the density, $\rho(\mathbf{r})$, but also on its gradient, $\nabla\rho(\mathbf{r})$, at each point in space. The XC potential and kernel can be obtained from first and second order functional derivatives, respectively, of E_{XC} with respect to density i.e.,

$$v_{\mathrm{XC}}[\rho](\mathbf{r}) = \frac{\delta E_{\mathrm{XC}}[\rho]}{\delta\rho(\mathbf{r})} \tag{3.1}$$

$$f_{\mathrm{XC}}[\rho](\mathbf{r},\mathbf{r}') = \frac{\delta^2 E_{\mathrm{XC}}[\rho]}{\delta\rho(\mathbf{r})\delta\rho(\mathbf{r}')} \tag{3.2}$$

where $E_{\mathrm{XC}}[\rho] = \int e_{\mathrm{XC}}(\rho, \boldsymbol{\nabla}\rho)(\vec{r})d^3r$ and e_{XC} is the XC energy density per particle.

The variation of the XC energy w.r.t. the density is defined by:

$$\begin{aligned}\delta E_{\mathrm{XC}} = E_{\mathrm{XC}}[\rho+\delta\rho] - E_{\mathrm{XC}}[\rho] = &\int v_{\mathrm{XC}}[\rho](\mathbf{r})\delta\rho(\mathbf{r})d^3r \\ &+ \frac{1}{2}\int\int f_{\mathrm{XC}}[\rho](\mathbf{r},\mathbf{r}')\delta\rho(\mathbf{r})\delta\rho(\mathbf{r}')d^3r d^3r' + \cdots\end{aligned} \tag{3.3}$$

Taylor expanding the energy density around the ground state density up to first order gives

$$\begin{aligned}e_{\mathrm{XC}}(\rho+\delta\rho, \boldsymbol{\nabla}\rho + \boldsymbol{\nabla}\delta\rho)(\mathbf{r}) = &\, e_{\mathrm{XC}}(\rho, \boldsymbol{\nabla}\rho)(\mathbf{r}) + \frac{\partial e_{\mathrm{XC}}(\rho, \boldsymbol{\nabla}\rho)}{\partial\rho}(\mathbf{r})\delta\rho(\mathbf{r}) \\ &+ \frac{\partial e_{\mathrm{XC}}(\rho, \boldsymbol{\nabla}\rho)}{\partial\boldsymbol{\nabla}\rho}(\mathbf{r})\cdot\boldsymbol{\nabla}\delta\rho(\mathbf{r})\end{aligned} \tag{3.4}$$

This expansion then leads to the following expression for the XC energy,

$$\begin{aligned}E_{\mathrm{XC}}[\rho+\delta\rho, \boldsymbol{\nabla}\rho + \boldsymbol{\nabla}\delta\rho] = &\, E_{\mathrm{XC}}[\rho, \boldsymbol{\nabla}\rho] + \int d^3r \frac{\partial e_{\mathrm{XC}}(\rho, \boldsymbol{\nabla}\rho)}{\partial\rho}(\mathbf{r})\delta\rho(\mathbf{r}) \\ &+ \int d^3r \frac{\partial e_{\mathrm{XC}}(\rho, \boldsymbol{\nabla}\rho)}{\partial\boldsymbol{\nabla}\rho}(\mathbf{r})\cdot\boldsymbol{\nabla}\delta\rho(\mathbf{r})\end{aligned} \tag{3.5}$$

and

$$\delta E_{\mathrm{XC}} = \int d^3r \Big[\frac{\partial e_{\mathrm{XC}}(\rho, \boldsymbol{\nabla}\rho)}{\partial\rho}(\mathbf{r})\delta\rho(\mathbf{r}) + \frac{\partial e_{\mathrm{XC}}(\rho, \boldsymbol{\nabla}\rho)}{\partial\boldsymbol{\nabla}\rho}(\mathbf{r})\cdot\boldsymbol{\nabla}\delta\rho(\mathbf{r})\Big] \tag{3.6}$$

Carrying out integration by parts of the second term (the surface term is 0 for physical systems with finite or periodic boundary conditions) gives us:

$$\delta E_{\mathrm{XC}} = \int d^3r \Big[\frac{\partial e_{\mathrm{XC}}(\rho, \boldsymbol{\nabla}\rho)}{\partial\rho}(\mathbf{r}) - \Big\{\boldsymbol{\nabla}\cdot\frac{\partial e_{\mathrm{XC}}(\rho, \boldsymbol{\nabla}\rho)}{\partial\boldsymbol{\nabla}\rho}(\mathbf{r})\Big\}\Big]\delta\rho(\mathbf{r}) \tag{3.7}$$

Comparing Eq. (3.7) and Eq. (3.3) leads to the following XC potential

$$\begin{aligned} v_{\mathrm{XC}}[\rho](\mathbf{r}) &= \frac{\partial e_{\mathrm{XC}}(\rho,\boldsymbol{\nabla}\rho)}{\partial\rho}(\mathbf{r}) - \Big\{\boldsymbol{\nabla}\cdot\frac{\partial e_{\mathrm{XC}}(\rho,\boldsymbol{\nabla}\rho)}{\partial\boldsymbol{\nabla}\rho}(\mathbf{r})\Big\} \\ &= \frac{\partial e_{\mathrm{XC}}(\rho,\boldsymbol{\nabla}\rho)}{\partial\rho}(\mathbf{r}) - 2\Big\{\boldsymbol{\nabla}\cdot\Big(\frac{\partial e_{\mathrm{XC}}(\rho,\boldsymbol{\nabla}\rho)}{\partial\sigma}(\mathbf{r})\boldsymbol{\nabla}\rho\Big)\Big\} \end{aligned} \tag{3.8}$$

where $\sigma = \boldsymbol{\nabla}\rho\cdot\boldsymbol{\nabla}\rho$ is often used in practice. Variation of this potential to first order will give the kernel:

$$\begin{aligned} \delta v_{\mathrm{XC}}(\mathbf{r}) &= \int f_{\mathrm{XC}}(\mathbf{r},\mathbf{r}')\delta\rho(\mathbf{r}')d\mathbf{r}' \\ &= v_{\mathrm{XC}}[\rho+\delta\rho,\boldsymbol{\nabla}\rho+\boldsymbol{\nabla}\delta\rho](\mathbf{r}) - v_{\mathrm{XC}}[\rho,\boldsymbol{\nabla}\rho](\mathbf{r}) \\ &= \frac{\partial v_{\mathrm{XC}}}{\partial\rho}(\mathbf{r})\delta\rho(\mathbf{r}) + \frac{\partial v_{\mathrm{XC}}}{\partial\boldsymbol{\nabla}_j\rho}(\mathbf{r})\boldsymbol{\nabla}_j\delta\rho(\mathbf{r}) \\ &= \frac{\partial}{\partial\rho}\Big[\frac{\partial e_{\mathrm{XC}}(\rho,\boldsymbol{\nabla}\rho)}{\partial\rho}(\mathbf{r})\Big]\delta\rho(\mathbf{r}) - \boldsymbol{\nabla}_k\Big[\frac{\partial}{\partial\rho}\Big\{\frac{\partial e_{\mathrm{XC}}(\rho,\boldsymbol{\nabla}\rho)}{\partial\boldsymbol{\nabla}_k\rho}(\mathbf{r})\Big\}\delta\rho(\mathbf{r})\Big] \\ &+ \frac{\partial}{\partial\boldsymbol{\nabla}_j\rho}\Big[\frac{\partial e_{\mathrm{XC}}(\rho,\boldsymbol{\nabla}\rho)}{\partial\rho}(\mathbf{r})\Big]\boldsymbol{\nabla}_j\delta\rho(\vec{r}) - \boldsymbol{\nabla}_k\Big[\frac{\partial}{\partial\boldsymbol{\nabla}_j\rho}\Big\{\frac{\partial e_{\mathrm{XC}}(\rho,\boldsymbol{\nabla}\rho)}{\partial\boldsymbol{\nabla}_k\rho}(\mathbf{r})\Big\}\boldsymbol{\nabla}_j\delta\rho(\vec{r})\Big] \end{aligned} \tag{3.9}$$

where the subscripts j and k denote the dot product summation. Expanding the second and third terms further gives,

$$\begin{aligned} \delta v_{\mathrm{XC}}(\mathbf{r}) &= \frac{\partial^2 e_{\mathrm{XC}}}{\partial\rho^2}(\mathbf{r})\delta\rho(\mathbf{r}) + \frac{\partial^2 e_{\mathrm{XC}}}{\partial\boldsymbol{\nabla}_j\rho\partial\rho}(\mathbf{r})\boldsymbol{\nabla}_j\delta\rho(\mathbf{r}) - \boldsymbol{\nabla}_k\Big[\frac{\partial^2 e_{\mathrm{XC}}}{\partial\rho\partial\boldsymbol{\nabla}_k\rho}(\mathbf{r})\delta\rho(\mathbf{r}) \\ &+ \frac{\partial^2 e_{\mathrm{XC}}}{\partial\boldsymbol{\nabla}_j\rho\partial\boldsymbol{\nabla}_k\rho}(\mathbf{r})\boldsymbol{\nabla}_j\delta\rho(\mathbf{r})\Big] \\ &= \frac{\partial^2 e_{\mathrm{XC}}}{\partial\rho^2}(\mathbf{r})\delta\rho(\mathbf{r}) + \frac{\partial^2 e_{\mathrm{XC}}}{\partial\boldsymbol{\nabla}_j\rho\partial\rho}(\mathbf{r})\boldsymbol{\nabla}_j\delta\rho(\mathbf{r}) - [\boldsymbol{\nabla}_k\frac{\partial^2 e_{\mathrm{XC}}}{\partial\rho\partial\boldsymbol{\nabla}_k\rho}(\mathbf{r})]\delta\rho(\mathbf{r}) \\ &- \frac{\partial^2 e_{\mathrm{XC}}}{\partial\rho\partial\boldsymbol{\nabla}_k\rho}(\mathbf{r})\boldsymbol{\nabla}_k\delta\rho(\mathbf{r}) - \boldsymbol{\nabla}_k\Big[\frac{\partial^2 e_{\mathrm{XC}}}{\partial\boldsymbol{\nabla}_j\rho\partial\boldsymbol{\nabla}_k\rho}(\mathbf{r})\boldsymbol{\nabla}_j\delta\rho(\mathbf{r})\Big] \end{aligned} \tag{3.10}$$

here second and fourth terms cancel. Integrating the other terms individually by introducing a delta function and performing integration by parts gives,

$$\frac{\partial^2 e_{\mathrm{XC}}}{\partial\rho^2}(\mathbf{r})\delta\rho(\mathbf{r}) = \int d\mathbf{r}\delta(\mathbf{r}-\mathbf{r}')\frac{\partial^2 e_{\mathrm{XC}}}{\partial\rho^2}(\mathbf{r}')\delta\rho(\mathbf{r}') \tag{3.11}$$

$$-\Big[\boldsymbol{\nabla}_k\frac{\partial^2 e_{\mathrm{XC}}}{\partial\rho\partial\boldsymbol{\nabla}_k\rho}(\mathbf{r})\Big]\delta\rho(\mathbf{r}) = -\int d\mathbf{r}'\delta(\mathbf{r}-\mathbf{r}')\Big[\boldsymbol{\nabla}'_k\frac{\partial^2 e_{\mathrm{XC}}}{\partial\rho\partial\boldsymbol{\nabla}_k\rho}(\mathbf{r}')\Big]\delta\rho(\mathbf{r}') \tag{3.12}$$

$$
\begin{aligned}
-\boldsymbol{\nabla}_k\Big[\frac{\partial^2 e_{\mathrm{XC}}}{\partial\boldsymbol{\nabla}_j\rho\partial\boldsymbol{\nabla}_k\rho}(\mathbf{r})\boldsymbol{\nabla}_j\delta\rho(\mathbf{r})\Big] &= -\int d\mathbf{r}'\delta(\mathbf{r}-\mathbf{r}')\boldsymbol{\nabla}'_k\Big[\frac{\partial^2 e_{\mathrm{XC}}}{\partial\boldsymbol{\nabla}_j\rho\partial\boldsymbol{\nabla}_k\rho}(\mathbf{r}')\boldsymbol{\nabla}'_j\delta\rho(\mathbf{r}')\Big] \\
&= \int d\mathbf{r}'[\boldsymbol{\nabla}'_k\delta(\mathbf{r}-\mathbf{r}')]\Big[\frac{\partial^2 e_{\mathrm{XC}}}{\partial\boldsymbol{\nabla}_j\rho\partial\boldsymbol{\nabla}_k\rho}(\mathbf{r}')\boldsymbol{\nabla}'_j\delta\rho(\mathbf{r}')\Big] \\
&= -\int d\mathbf{r}'\boldsymbol{\nabla}'_j\Big[[\boldsymbol{\nabla}'_k\delta(\mathbf{r}-\mathbf{r}')]\frac{\partial^2 e_{\mathrm{XC}}}{\partial\boldsymbol{\nabla}_j\rho\partial\boldsymbol{\nabla}_k\rho}(\mathbf{r}')\Big]\delta\rho(\mathbf{r}')
\end{aligned}
\tag{3.13}
$$

Collecting all coefficients of $\delta\rho(\mathbf{r})$ together results in the unpolarized kernel for GGA functional [70, 77, 78]

$$
\begin{aligned}
f_{\mathrm{XC}}(\mathbf{r},\mathbf{r}') = \delta(\mathbf{r}-\mathbf{r}')\Big[\frac{\partial^2 e_{\mathrm{XC}}}{\partial\rho\partial\rho}(\mathbf{r}') - \boldsymbol{\nabla}'_j\frac{\partial^2 e_{\mathrm{XC}}}{\partial\boldsymbol{\nabla}_j\rho\partial\rho}(\mathbf{r}')\Big] \\
- \boldsymbol{\nabla}'_j\Big[[\boldsymbol{\nabla}'_k\delta(\mathbf{r}-\mathbf{r}')]\frac{\partial^2 e_{\mathrm{XC}}}{\partial\boldsymbol{\nabla}_j\rho\partial\boldsymbol{\nabla}_k\rho}(\mathbf{r}')\Big]
\end{aligned}
\tag{3.14}
$$

3.2 Implementation of unpolarized kernel

Libxc [79, 80] is a library which is continuously updated with the inclusion of most of the known XC functionals. The functionals it provides depends locally on the density, gradients of density and the kinetic energy density. Hence, this library was used in providing the derivatives of the XC fucntionals with respect to the density and its gradients for the GGA kernel. The derivatives that libxc returns are in terms of density (ρ) and sigma ($\sigma = \boldsymbol{\nabla}\rho\cdot\boldsymbol{\nabla}\rho$). These derivatives are then used to obtain the kernel by using the following expressions,

$$
\begin{aligned}
\frac{\partial e_{\mathrm{XC}}}{\partial\boldsymbol{\nabla}\rho} &= \frac{\partial e_{\mathrm{XC}}}{\partial\sigma}\frac{\partial\sigma}{\partial\boldsymbol{\nabla}\rho} = \frac{\partial e_{\mathrm{XC}}}{\partial\sigma}2\boldsymbol{\nabla}\rho \\
\frac{\partial^2 e_{\mathrm{XC}}}{\partial\rho\partial\boldsymbol{\nabla}\rho} &= \frac{\partial^2 e_{\mathrm{XC}}}{\partial\rho\partial\sigma}\frac{\partial\sigma}{\partial\boldsymbol{\nabla}\rho} = 2\frac{\partial^2 e_{\mathrm{XC}}}{\partial\rho\partial\sigma}\boldsymbol{\nabla}\rho \\
\frac{\partial}{\partial\boldsymbol{\nabla}_j\rho}\Big(\frac{\partial e_{\mathrm{XC}}}{\partial\boldsymbol{\nabla}_k\rho}\Big) = 2\frac{\partial}{\partial\boldsymbol{\nabla}_j\rho}\Big(\frac{\partial e_{\mathrm{XC}}}{\partial\sigma}\boldsymbol{\nabla}_k\rho\Big) &= 2\frac{\partial^2 e_{\mathrm{XC}}}{\partial\boldsymbol{\nabla}_j\rho}\boldsymbol{\nabla}_k\rho + 2\frac{\partial e_{\mathrm{XC}}}{\partial\sigma}\delta_{jk} \\
&= 4\frac{\partial^2 e_{\mathrm{XC}}}{\partial\sigma\partial\sigma}\boldsymbol{\nabla}_j\rho\boldsymbol{\nabla}_k\rho + 2\frac{\partial e_{\mathrm{XC}}}{\partial\sigma}\delta_{jk}
\end{aligned}
\tag{3.15}
$$

3.3 Spin-Polarized kernel

For the spin polarized case we have two spin channels: spin-up denoted by α and spin-down denoted by β. The XC energy functional, E_{XC}, depends on spin-up, $\rho_\alpha(\mathbf{r})$, spin-down, $\rho_\beta(\mathbf{r})$, densities and their gradients, $\boldsymbol{\nabla}\rho_\alpha(\mathbf{r}), \boldsymbol{\nabla}\rho_\beta(\mathbf{r})$. The XC potential, v_{XC}, and the kernel, f_{XC}, can be obtained by the first and second order functional derivative of E_{XC} with respect to these densities.

Now adding variation in the two densities and their gradients, and Taylor expanding, one gets the XC energy density, $e_{\rm XC}$, (up to first order).

$$\begin{aligned} e_{\rm XC}(\rho_\alpha(\mathbf{r})+\delta\rho_\alpha(\mathbf{r}),&\rho_\beta(\mathbf{r})+\delta\rho_\beta(\mathbf{r}),\boldsymbol{\nabla}\rho_\alpha(\mathbf{r})+\boldsymbol{\nabla}\delta\rho_\alpha(\mathbf{r}),\boldsymbol{\nabla}\rho_\beta(\mathbf{r})+\boldsymbol{\nabla}\delta\rho_\beta(\mathbf{r})) \\ &= e_{\rm XC}(\rho_\alpha(\mathbf{r}),\rho_\beta(\mathbf{r}),\boldsymbol{\nabla}\rho_\alpha(\mathbf{r}),\boldsymbol{\nabla}\rho_\beta(\mathbf{r})) + \frac{\partial e_{\rm XC}}{\partial\rho_\alpha}(\mathbf{r})\delta\rho_\alpha(\mathbf{r}) + \frac{\partial e_{\rm XC}}{\partial\rho_\beta}(\mathbf{r})\delta\rho_\beta(\mathbf{r}) \\ &+ \frac{\partial e_{\rm XC}}{\partial\boldsymbol{\nabla}\rho_\alpha}(\mathbf{r})\boldsymbol{\nabla}\delta\rho_\alpha(\mathbf{r}) + \frac{\partial e_{\rm XC}}{\partial\boldsymbol{\nabla}\rho_\beta}(\mathbf{r})\boldsymbol{\nabla}\delta\rho_\beta(\mathbf{r}) \end{aligned} \tag{3.16}$$

integrating this gives,

$$\begin{aligned} E_{\rm XC}[\rho_\alpha(\mathbf{r})+\delta\rho_\alpha(\mathbf{r}),&\rho_\beta(\mathbf{r})+\delta\rho_\beta(\mathbf{r}),\boldsymbol{\nabla}\rho_\alpha(\mathbf{r})+\boldsymbol{\nabla}\delta\rho_\alpha(\mathbf{r}),\boldsymbol{\nabla}\rho_\beta(\mathbf{r})+\boldsymbol{\nabla}\delta\rho_\beta(\mathbf{r})] \\ &= E_{\rm XC}[\rho_\alpha(\mathbf{r}),\rho_\beta(\mathbf{r}),\boldsymbol{\nabla}\rho_\alpha(\mathbf{r}),\boldsymbol{\nabla}\rho_\beta(\mathbf{r})] \\ &+ \int d^3r\Big[\frac{\partial e_{\rm XC}}{\partial\rho_\alpha}(\mathbf{r})\delta\rho_\alpha(\mathbf{r}) + \frac{\partial e_{\rm XC}}{\partial\rho_\beta}(\mathbf{r})\delta\rho_\beta(\mathbf{r}) \\ &+ \frac{\partial e_{\rm XC}}{\partial\boldsymbol{\nabla}\rho_\alpha}(\mathbf{r})\boldsymbol{\nabla}\delta\rho_\alpha(\mathbf{r}) + \frac{\partial e_{\rm XC}}{\partial\boldsymbol{\nabla}\rho_\beta}(\mathbf{r})\boldsymbol{\nabla}\delta\rho_\beta(\mathbf{r})\Big] \end{aligned}$$

the variation of XC energy functional w.r.t. density gives,

$$\delta E_{\rm XC} = \int d^3r\Big[\frac{\partial e_{\rm XC}}{\partial\rho_\alpha}(\mathbf{r})\delta\rho_\alpha(\mathbf{r}) + \frac{\partial e_{\rm XC}}{\partial\rho_\beta}(\mathbf{r})\delta\rho_\beta(\mathbf{r}) + \frac{\partial e_{\rm XC}}{\partial\boldsymbol{\nabla}\rho_\alpha}(\mathbf{r})\boldsymbol{\nabla}\delta\rho_\alpha(\mathbf{r}) + \frac{\partial e_{\rm XC}}{\partial\boldsymbol{\nabla}\rho_\beta}(\mathbf{r})\boldsymbol{\nabla}\delta\rho_\beta(\mathbf{r})\Big] \tag{3.17}$$

This will give the spin-polarized potential. To obtain the kernel we could either expand Eq. (3.16) to 2^{nd} order or do variational of the potential, $v^{\alpha,\beta}_{\rm XC}$. The expansion of XC energy functional leads to,

$$\begin{aligned} \delta E_{\rm XC} = &\int d^3r v^\alpha_{\rm XC}(\mathbf{r})\delta\rho_\alpha(\mathbf{r}) + \int d^3r v^\beta_{\rm XC}(\mathbf{r})\delta\rho_\beta(\mathbf{r}) + \frac{1}{2}\int\int d^3r d^3r' f^{\alpha\alpha}_{\rm XC}(\mathbf{r},\mathbf{r}')\delta\rho_\alpha(\mathbf{r})\delta\rho_\alpha(\mathbf{r}') \\ &+ \frac{1}{2}\int\int d^3r d^3r' f^{\alpha\beta}_{\rm XC}(\mathbf{r},\mathbf{r}')\delta\rho_\beta(\mathbf{r})\delta\rho_\alpha(\mathbf{r}') + \frac{1}{2}\int\int d^3r d^3r' f^{\beta\alpha}_{\rm XC}(\mathbf{r},\mathbf{r}')\delta\rho_\alpha(\mathbf{r})\delta\rho_\beta(\mathbf{r}') \\ &+ \frac{1}{2}\int\int d^3r d^3r' f^{\beta\beta}_{\rm XC}(\mathbf{r},\mathbf{r}')\delta\rho_\beta(\mathbf{r})\delta\rho_\beta(\mathbf{r}'), \end{aligned} \tag{3.18}$$

and the variation of the potential leads to,

$$\begin{aligned} \delta v^\alpha_{\rm XC}[\rho_\alpha,\rho_\beta,\boldsymbol{\nabla}\rho_\alpha,\boldsymbol{\nabla}\rho_\beta](\mathbf{r}) &= \int f^{\alpha\alpha}_{\rm XC}(\mathbf{r},\mathbf{r}')\delta\rho_\alpha(\mathbf{r}')d\mathbf{r}' + \int f^{\alpha\beta}_{\rm XC}(\mathbf{r},\mathbf{r}')\delta\rho_\beta(\mathbf{r}')d\mathbf{r}' \\ \delta v^\beta_{\rm XC}[\rho_\alpha,\rho_\beta,\boldsymbol{\nabla}\rho_\alpha,\boldsymbol{\nabla}\rho_\beta](\mathbf{r}) &= \int f^{\beta\beta}_{\rm XC}(\mathbf{r},\mathbf{r}')\delta\rho_\beta(\mathbf{r}')d\mathbf{r}' + \int f^{\beta\alpha}_{\rm XC}(\mathbf{r},\mathbf{r}')\delta\rho_\alpha(\mathbf{r}')d\mathbf{r}' \end{aligned} \tag{3.19}$$

where $f_{\rm XC}^{\alpha\alpha}$ is the change in $v_{\rm XC}^{\alpha}$ when ρ_α changes while $f_{\rm XC}^{\alpha\beta}$ is change in $v_{\rm XC}^{\alpha}$ when ρ_β changes, and similarly for the other spin channel. Using integration by parts in Eq.(3.17), we obtain the XC potential for the two spin densities as:

$$v_{\rm XC}^{\alpha}[\rho_\alpha,\rho_\beta,\boldsymbol{\nabla}\rho_\alpha,\boldsymbol{\nabla}\rho_\beta](\mathbf{r}) = \frac{\partial e_{\rm XC}}{\partial \rho_\alpha}(\mathbf{r}) - \boldsymbol{\nabla}_j\Big[\frac{\partial e_{\rm XC}}{\partial \boldsymbol{\nabla}_j\rho_\alpha}(\mathbf{r})\Big] \tag{3.20}$$

and

$$v_{\rm XC}^{\beta}[\rho_\alpha,\rho_\beta,\boldsymbol{\nabla}\rho_\alpha,\boldsymbol{\nabla}\rho_\beta](\mathbf{r}) = \frac{\partial e_{\rm XC}}{\partial \rho_\beta}(\mathbf{r}) - \boldsymbol{\nabla}_j\Big[\frac{\partial e_{\rm XC}}{\partial \boldsymbol{\nabla}_j\rho_\beta}(\mathbf{r})\Big] \tag{3.21}$$

Now variation of $v_{\rm XC}^{\alpha}$ w.r.t. ρ_α gives the kernels $f_{\rm XC}^{\alpha\alpha}(\mathbf{r},\mathbf{r}')$ and $f_{\rm XC}^{\alpha\beta}(\mathbf{r},\mathbf{r}')$

$$\begin{aligned}
\delta v_{\rm XC}^{\alpha}(\mathbf{r}) &= v_{\rm XC}^{\alpha}[\rho_\alpha(\mathbf{r})+\delta\rho_\alpha(\mathbf{r}),\rho_\beta(\mathbf{r})+\delta\rho_\beta(\mathbf{r}),\boldsymbol{\nabla}\rho_\alpha(\mathbf{r})+\boldsymbol{\nabla}\delta\rho_\alpha(\mathbf{r}),\boldsymbol{\nabla}\rho_\beta(\mathbf{r})+\boldsymbol{\nabla}\delta\rho_\beta(\mathbf{r})] \\
&\quad - v_{\rm XC}^{\alpha}[\rho_\alpha(\mathbf{r}),\rho_\beta(\mathbf{r}),\boldsymbol{\nabla}\rho_\alpha(\mathbf{r}),\boldsymbol{\nabla}\rho_\beta(\mathbf{r})] \\
&= \Big[\frac{\partial v_{\rm XC}^{\alpha}}{\partial\rho_\alpha}(\mathbf{r})\delta\rho_\alpha(\mathbf{r}) + \frac{\partial v_{\rm XC}^{\alpha}}{\partial\boldsymbol{\nabla}\rho_\alpha}(\mathbf{r})\boldsymbol{\nabla}\delta\rho_\alpha(\mathbf{r})\Big] + \Big[\frac{\partial v_{\rm XC}^{\alpha}}{\partial\rho_\beta}(\mathbf{r})\delta\rho_\beta(\mathbf{r}) + \frac{\partial v_{\rm XC}^{\alpha}}{\partial\boldsymbol{\nabla}\rho_\beta}(\mathbf{r})\boldsymbol{\nabla}\delta\rho_\beta(\mathbf{r})\Big] \\
&= \Big\{\frac{\partial}{\partial\rho_\alpha}\Big(\frac{\partial e_{\rm XC}}{\partial\rho_\alpha}\Big)\delta\rho_\alpha(\mathbf{r}) - \boldsymbol{\nabla}_j\Big[\frac{\partial}{\partial\rho_\alpha}\Big(\frac{\partial e_{\rm XC}}{\partial\boldsymbol{\nabla}_j\rho_\alpha}\Big)\delta\rho_\alpha(\mathbf{r})\Big] + \frac{\partial}{\partial\boldsymbol{\nabla}_k\rho_\alpha}\Big(\frac{\partial e_{\rm XC}}{\partial\rho_\alpha}\Big)\boldsymbol{\nabla}_k\delta\rho_\alpha(\mathbf{r}) \\
&\quad - \boldsymbol{\nabla}_j\Big[\frac{\partial}{\partial\boldsymbol{\nabla}_k\rho_\alpha}\Big(\frac{\partial e_{\rm XC}}{\partial\boldsymbol{\nabla}_j\rho_\alpha}\Big)\boldsymbol{\nabla}_k\delta\rho_\alpha(\mathbf{r})\Big]\Big\} \\
&\quad + \Big\{\frac{\partial}{\partial\rho_\beta}\Big(\frac{\partial e_{\rm XC}}{\partial\rho_\alpha}\Big)\delta\rho_\beta(\mathbf{r}) - \boldsymbol{\nabla}_j\Big[\frac{\partial}{\partial\rho_\beta}\Big(\frac{\partial e_{\rm XC}}{\partial\boldsymbol{\nabla}_j\rho_\alpha}\Big)\delta\rho_\beta(\mathbf{r})\Big] + \frac{\partial}{\partial\boldsymbol{\nabla}_k\rho_\beta}\Big(\frac{\partial e_{\rm XC}}{\partial\rho_\alpha}\Big)\boldsymbol{\nabla}_k\delta\rho_\beta(\mathbf{r}) \\
&\quad - \boldsymbol{\nabla}_j\Big[\frac{\partial}{\partial\boldsymbol{\nabla}_k\rho_\beta}\Big(\frac{\partial e_{\rm XC}}{\partial\boldsymbol{\nabla}_j\rho_\alpha}\Big)\boldsymbol{\nabla}_k\delta\rho_\beta(\mathbf{r})\Big]\Big\} \\
&= \Big\{\frac{\partial^2 e_{\rm XC}}{\partial\rho_\alpha^2}(\mathbf{r})\delta\rho_\alpha(\mathbf{r}) + \Big(\frac{\partial^2 e_{\rm XC}}{\partial\boldsymbol{\nabla}_k\rho_\alpha\partial\rho_\alpha}(\mathbf{r})\Big)\boldsymbol{\nabla}_k\delta\rho_\alpha(\mathbf{r}) - \boldsymbol{\nabla}_j\Big[\Big(\frac{\partial^2 e_{\rm XC}}{\partial\rho_\alpha\partial\boldsymbol{\nabla}_j\rho_\alpha}(\mathbf{r})\Big)\delta\rho_\alpha(\mathbf{r})\Big] \\
&\quad - \boldsymbol{\nabla}_j\Big[\Big(\frac{\partial^2 e_{\rm XC}}{\partial\boldsymbol{\nabla}_k\rho_\alpha\partial\boldsymbol{\nabla}_j\rho_\alpha}(\mathbf{r})\Big)\boldsymbol{\nabla}_k\delta\rho_\alpha(\mathbf{r})\Big]\Big\} + \Big\{\frac{\partial^2 e_{\rm XC}}{\partial\rho_\beta\partial\rho_\alpha}(\mathbf{r})\delta\rho_\beta(\mathbf{r}) + \Big(\frac{\partial^2 e_{\rm XC}}{\partial\boldsymbol{\nabla}_k\rho_\beta\partial\rho_\alpha}(\mathbf{r})\Big)\boldsymbol{\nabla}_k\delta\rho_\beta(\mathbf{r}) \\
&\quad - \boldsymbol{\nabla}_j\Big[\Big(\frac{\partial^2 e_{\rm XC}}{\partial\rho_\beta\partial\boldsymbol{\nabla}_j\rho_\alpha}(\mathbf{r})\Big)\delta\rho_\beta(\mathbf{r})\Big] - \boldsymbol{\nabla}_j\Big[\Big(\frac{\partial^2 e_{\rm XC}}{\partial\boldsymbol{\nabla}_k\rho_\beta\partial\boldsymbol{\nabla}_j\rho_\alpha}(\mathbf{r})\Big)\boldsymbol{\nabla}_k\delta\rho_\beta(\mathbf{r})\Big]\Big\} \\
&= A+B+C+D+F+G+H+I
\end{aligned} \tag{3.22}$$

Solving each term separately by introducing an integration with a delta function, we obtain the kernels $f_{\rm XC}^{\alpha\alpha}(\mathbf{r},\mathbf{r}')$ and $f_{\rm XC}^{\alpha\beta}(\mathbf{r},\mathbf{r}')$

$$A = \int \delta(\mathbf{r}-\mathbf{r}')\frac{\partial^2 e_{\rm XC}}{\partial\rho_\alpha\partial\rho_\alpha}(\mathbf{r}')\delta\rho_\alpha(\mathbf{r}')d\mathbf{r}' \tag{3.23}$$

$$
\begin{aligned}
B &= \int \delta(\mathbf{r}-\mathbf{r}')\Big(\frac{\partial^2 e_{\mathrm{XC}}}{\partial \boldsymbol{\nabla}_k \rho_\alpha \partial \rho_\alpha}(\mathbf{r}')\Big)\boldsymbol{\nabla}'_k \delta\rho_\alpha(\mathbf{r}')d\mathbf{r}' \\
&= -\int \boldsymbol{\nabla}'_k\Big[\delta(\mathbf{r}-\mathbf{r}')\Big(\frac{\partial^2 e_{\mathrm{XC}}}{\partial \boldsymbol{\nabla}_k \rho_\alpha(\mathbf{r}') \partial \rho_\alpha(\mathbf{r}')}\Big)\Big]\delta\rho_\alpha(\mathbf{r}')d\mathbf{r}' \\
&= -\int \Big\{\Big[\boldsymbol{\nabla}'_k \delta(\mathbf{r}-\mathbf{r}')\Big]\Big(\frac{\partial^2 e_{\mathrm{XC}}}{\partial \boldsymbol{\nabla}_k \rho_\alpha \partial \rho_\alpha}(\mathbf{r}')\Big) + \delta(\mathbf{r}-\mathbf{r}')\Big(\boldsymbol{\nabla}'_k \frac{\partial^2 e_{\mathrm{XC}}}{\partial \boldsymbol{\nabla}_k \rho_\alpha \partial \rho_\alpha}(\mathbf{r}')\Big)\Big\}\delta\rho_\alpha(\mathbf{r}')d\mathbf{r}'
\end{aligned}
\tag{3.24}
$$

$$
\begin{aligned}
C &= -\int \delta(\mathbf{r}-\mathbf{r}')\boldsymbol{\nabla}'_j\Big[\Big(\frac{\partial^2 e_{\mathrm{XC}}}{\partial \rho_\alpha \partial \boldsymbol{\nabla}_j \rho_\alpha}(\mathbf{r}')\Big)\delta\rho_\alpha(\mathbf{r}')\Big]d\mathbf{r}' \\
&= \int \Big[\boldsymbol{\nabla}'_j \delta(\mathbf{r}-\mathbf{r}')\Big]\Big(\frac{\partial^2 e_{\mathrm{XC}}}{\partial \rho_\alpha \partial \boldsymbol{\nabla}_j \rho_\alpha}(\mathbf{r}')\Big)\delta\rho_\alpha(\mathbf{r}')d\mathbf{r}'
\end{aligned}
\tag{3.25}
$$

$$
B + C = -\int \delta(\mathbf{r}-\mathbf{r}')\Big(\boldsymbol{\nabla}'_k \frac{\partial^2 e_{\mathrm{XC}}}{\partial \boldsymbol{\nabla}_k \rho_\alpha \partial \rho_\alpha}(\mathbf{r}')\Big)\delta\rho_\alpha(\mathbf{r}')d\mathbf{r}' \tag{3.26}
$$

$$
\begin{aligned}
D &= -\int \delta(\mathbf{r}-\mathbf{r}')\boldsymbol{\nabla}'_j\Big[\Big(\frac{\partial^2 e_{\mathrm{XC}}}{\partial \boldsymbol{\nabla}_k \rho_\alpha \partial \boldsymbol{\nabla}'_j \rho_\alpha}(\mathbf{r}')\Big)\boldsymbol{\nabla}_k \delta\rho_\alpha(\mathbf{r}')\Big]d\mathbf{r}' \\
&= \int \Big[\boldsymbol{\nabla}'_j \delta(\mathbf{r}-\mathbf{r}')\Big]\Big(\frac{\partial^2 e_{\mathrm{XC}}}{\partial \boldsymbol{\nabla}_k \rho_\alpha \partial \boldsymbol{\nabla}_j \rho_\alpha}(\mathbf{r}')\Big)\boldsymbol{\nabla}'_k \delta\rho_\alpha(\mathbf{r}')d\mathbf{r}' \\
&= -\int \boldsymbol{\nabla}'_k\Big[[\boldsymbol{\nabla}'_j \delta(\mathbf{r}-\mathbf{r}')]\Big(\frac{\partial^2 e_{\mathrm{XC}}}{\partial \boldsymbol{\nabla}_k \rho_\alpha \partial \boldsymbol{\nabla}_j \rho_\alpha}(\mathbf{r}')\Big)\Big]\delta\rho_\alpha(\mathbf{r}')d\mathbf{r}'
\end{aligned}
\tag{3.27}
$$

substituting all the terms in Eq. 3.22 leads to,

$$
f^{\alpha\alpha}_{\mathrm{XC}}(\mathbf{r},\mathbf{r}') = \delta(\mathbf{r}-\mathbf{r}')\Big[\frac{\partial^2 e_{xc}}{\partial \rho_\alpha \partial \rho_\alpha}(\mathbf{r}') - \Big(\boldsymbol{\nabla}'_k \frac{\partial^2 e_{xc}}{\partial \boldsymbol{\nabla}'_k \rho_\alpha \partial \rho_\alpha}(\mathbf{r}')\Big)\Big] - \boldsymbol{\nabla}'_k\Big[[\boldsymbol{\nabla}'_j \delta(\mathbf{r}-\mathbf{r}')]\Big(\frac{\partial^2 e_{xc}}{\partial \boldsymbol{\nabla}_k \rho_\alpha \partial \boldsymbol{\nabla}_j \rho_\alpha}(\mathbf{r}')\Big)\Big] \tag{3.28}
$$

Following the similar steps to solve for F, G, H, I one can obtain the expression for $f^{\alpha\beta}_{\mathrm{XC}}(\mathbf{r},\mathbf{r}')$,

$$
F = \int \delta(\mathbf{r}-\mathbf{r}')\frac{\partial^2 e_{\mathrm{XC}}}{\partial \rho_\beta \partial \rho_\alpha}(\mathbf{r}')\delta\rho_\beta(\mathbf{r}')d\mathbf{r}' \tag{3.29}
$$

$$
\begin{aligned}
G &= \int \delta(\mathbf{r}-\mathbf{r}')\Big(\frac{\partial^2 e_{\mathrm{XC}}}{\partial \boldsymbol{\nabla}_k \rho_\beta \partial \rho_\alpha}(\mathbf{r})\Big)\boldsymbol{\nabla}'_k \delta\rho_\beta(\mathbf{r}')d\mathbf{r}' \\
&= -\int \boldsymbol{\nabla}'_k\Big[\delta(\mathbf{r}-\mathbf{r}')\Big(\frac{\partial^2 e_{\mathrm{XC}}}{\partial \boldsymbol{\nabla}_k \rho_\beta \partial \rho_\alpha}(\mathbf{r})\Big)\Big]\delta\rho_\beta(\mathbf{r}')d\mathbf{r}' \\
&= -\int \Big\{\Big[\boldsymbol{\nabla}'_k \delta(\mathbf{r}-\mathbf{r}')\Big]\Big(\frac{\partial^2 e_{\mathrm{XC}}}{\partial \boldsymbol{\nabla}_k \rho_\beta \partial \rho_\alpha}(\mathbf{r})\Big)\Big\}\delta\rho_\beta(\mathbf{r}')d\mathbf{r}'
\end{aligned}
\tag{3.30}
$$

$$
\begin{aligned}
H &= -\int \delta(\mathbf{r}-\mathbf{r}')\boldsymbol{\nabla}'_j\Big[\Big(\frac{\partial^2 e_{\mathrm{XC}}}{\partial\rho_\beta\partial\boldsymbol{\nabla}_j\rho_\alpha}(\mathbf{r}')\Big)\delta\rho_\beta(\mathbf{r}')\Big]d\mathbf{r}' \\
&= \int \Big[\boldsymbol{\nabla}'_j\delta(\mathbf{r}-\mathbf{r}')\Big]\Big(\frac{\partial^2 e_{\mathrm{XC}}}{\partial\rho_\beta\partial\boldsymbol{\nabla}_j\rho_\alpha}(\mathbf{r}')\Big)\delta\rho_\beta(\mathbf{r}')d\mathbf{r}'
\end{aligned}
\tag{3.31}
$$

$$
\begin{aligned}
I &= -\int \delta(\mathbf{r}-\mathbf{r}')\boldsymbol{\nabla}'_j\Big[\Big(\frac{\partial^2 e_{\mathrm{XC}}}{\partial\boldsymbol{\nabla}_k\rho_\beta\partial\boldsymbol{\nabla}_j\rho_\alpha}(\mathbf{r}')\Big)\boldsymbol{\nabla}'_k\delta\rho_\beta(\mathbf{r}')\Big]d\mathbf{r}' \\
&= \int \Big[\boldsymbol{\nabla}'_j\delta(\mathbf{r}-\mathbf{r}')\Big]\Big(\frac{\partial^2 e_{\mathrm{XC}}}{\partial\boldsymbol{\nabla}_k\rho_\beta\partial\boldsymbol{\nabla}_j\rho_\alpha}(\mathbf{r}')\Big)\boldsymbol{\nabla}'_k\delta\rho_\beta(\mathbf{r}')d\mathbf{r}' \\
&= -\int \boldsymbol{\nabla}'_k\Big[[\boldsymbol{\nabla}'_j\delta(\mathbf{r}-\mathbf{r}')]\Big(\frac{\partial^2 e_{\mathrm{XC}}}{\partial\boldsymbol{\nabla}_k\rho_\beta\partial\boldsymbol{\nabla}_j\rho_\alpha}(\mathbf{r}')\Big)\Big]\delta\rho_\beta(\mathbf{r}')d\mathbf{r}'
\end{aligned}
\tag{3.32}
$$

Collecting the terms together we get,

$$
\begin{aligned}
f^{\alpha\beta}_{\mathrm{XC}}(\mathbf{r},\mathbf{r}') = \delta(\mathbf{r}-\mathbf{r}')\Big\{\frac{\partial^2 e_{\mathrm{XC}}}{\partial\rho_\beta\partial\rho_\alpha}(\mathbf{r}')\Big\} - \Big\{[\boldsymbol{\nabla}'_j\delta(\mathbf{r}-\mathbf{r}')]\Big(\frac{\partial^2 e_{\mathrm{XC}}}{\partial\rho_\alpha\partial\boldsymbol{\nabla}^r_j\rho_\beta}(\mathbf{r})\Big)\Big\} \\
+ \Big\{[\boldsymbol{\nabla}'_j\delta(\mathbf{r}-\mathbf{r}')]\Big(\frac{\partial^2 e_{\mathrm{XC}}}{\partial\rho_\beta\partial\boldsymbol{\nabla}_j\rho_\alpha}(\mathbf{r}')\Big)\Big\} - \boldsymbol{\nabla}'_k\Big\{[\boldsymbol{\nabla}'_j\delta(\mathbf{r}-\mathbf{r}')]\Big(\frac{\partial^2 e_{\mathrm{XC}}}{\partial\boldsymbol{\nabla}_k\rho_\beta\partial\boldsymbol{\nabla}_j\rho_\alpha}(\mathbf{r}')\Big)\Big\}.
\end{aligned}
\tag{3.33}
$$

solving the equation in the similar way for v^{β}_{XC} we will get,

$$
f^{\beta\beta}_{\mathrm{XC}}(\mathbf{r},\mathbf{r}') = \delta(\mathbf{r}-\mathbf{r}')\Big[\frac{\partial^2 e_{xc}}{\partial\rho_\beta\partial\rho_\beta}(\mathbf{r}) - \Big(\boldsymbol{\nabla}_k\frac{\partial^2 e_{xc}}{\partial\boldsymbol{\nabla}_k\rho_\beta\partial\rho_\beta}(\mathbf{r})\Big)\Big] - \boldsymbol{\nabla}'_k\Big[[\boldsymbol{\nabla}'_j\delta(\mathbf{r}-\mathbf{r}')]\Big(\frac{\partial^2 e_{xc}}{\partial\boldsymbol{\nabla}_k\rho_\beta\partial\boldsymbol{\nabla}_j\rho_\beta}(\mathbf{r}')\Big)\Big]
\tag{3.34}
$$

$$
\begin{aligned}
f^{\beta\alpha}_{\mathrm{XC}}(\mathbf{r},\mathbf{r}') = \delta(\mathbf{r}-\mathbf{r}')\Big\{\frac{\partial^2 e_{\mathrm{XC}}}{\partial\rho_\alpha\partial\rho_\beta}(\mathbf{r}')\Big\} - \Big\{[\boldsymbol{\nabla}'_j\delta(\mathbf{r}-\mathbf{r}')]\Big(\frac{\partial^2 e_{\mathrm{XC}}}{\partial\rho_\beta\partial\boldsymbol{\nabla}^r_j\rho_\alpha}(\mathbf{r})\Big)\Big\} \\
+ \Big\{[\boldsymbol{\nabla}'_j\delta(\mathbf{r}-\mathbf{r}')]\Big(\frac{\partial^2 e_{\mathrm{XC}}}{\partial\rho_\alpha\partial\boldsymbol{\nabla}_j\rho_\beta}(\mathbf{r}')\Big)\Big\} - \boldsymbol{\nabla}'_k\Big\{[\boldsymbol{\nabla}'_j\delta(\mathbf{r}-\mathbf{r}')]\Big(\frac{\partial^2 e_{\mathrm{XC}}}{\partial\boldsymbol{\nabla}_k\rho_\alpha\partial\boldsymbol{\nabla}_j\rho_\beta}(\mathbf{r}')\Big)\Big\}.
\end{aligned}
\tag{3.35}
$$

3.4 Non-Collinear kernel

3.4.1 Kubler's method

For many systems, the spins do not align along one direction, for example the frustrated anti-ferromagnetism seen in a Cr monolayer [81]. Hence the functionals known for collinear

systems need to be extended for non-collinear systems in order to be applied to such systems. One solution to this problem is the Kübler method [16], where the potentials are transformed from the $(\rho_\uparrow, \rho_\downarrow)$ to the (ρ, m) basis. We may use the Kübler method to extend our kernel to treat non-collinear excitations.

Note: In the following method the $\rho_\uparrow(\mathbf{r})$ density corresponds to the spin-up density, $\rho_\alpha(\mathbf{r})$, and $\rho_\downarrow(\mathbf{r})$ to the spin-down density, $\rho_\beta(\mathbf{r})$. Similarly, the spin-up and spin-down potentials are represented as $v^\alpha_{\mathrm{XC}}(\mathbf{r}) = v^\uparrow_{\mathrm{XC}}(\mathbf{r})$ and $v^\beta_{\mathrm{XC}}(\mathbf{r}) = v^\downarrow_{\mathrm{XC}}(\mathbf{r})$.

The kernel for non-collinear systems can be written as:

$$\left[\begin{array}{c|c} Charge- \\ Charge & Charge-Spin \\ \hline Spin- \\ Charge & Spin-Spin \end{array}\right] \Longrightarrow \left[\begin{array}{c|ccc} \frac{\delta v^0_{\mathrm{XC}}}{\delta\rho} & \frac{\delta v^0_{\mathrm{XC}}}{\delta m_x} & \frac{\delta v^0_{\mathrm{XC}}}{\delta m_y} & \frac{\delta v^0_{\mathrm{XC}}}{\delta m_z} \\ \hline \frac{\delta B^x_{\mathrm{XC}}}{\delta\rho} & \frac{\delta B^x_{\mathrm{XC}}}{\delta m_x} & \frac{\delta B^x_{\mathrm{XC}}}{\delta m_y} & \frac{\delta B^x_{\mathrm{XC}}}{\delta m_z} \\ \frac{\delta B^y_{\mathrm{XC}}}{\delta\rho} & \frac{\delta B^y_{\mathrm{XC}}}{\delta m_x} & \frac{\delta B^y_{\mathrm{XC}}}{\delta m_y} & \frac{\delta B^y_{\mathrm{XC}}}{\delta m_z} \\ \frac{\delta B^z_{\mathrm{XC}}}{\delta\rho} & \frac{\delta B^z_{\mathrm{XC}}}{\delta m_x} & \frac{\delta B^z_{\mathrm{XC}}}{\delta m_y} & \frac{\delta B^z_{\mathrm{XC}}}{\delta m_z} \end{array}\right] \tag{3.36}$$

The Kübler's method defines effective spin up/spin down densities using

$$\rho^\uparrow(\mathbf{r}) = \frac{1}{2}\Big(\rho(\mathbf{r}) + |\mathbf{m}(\mathbf{r})|\Big), \qquad \rho^\downarrow(\mathbf{r}) = \frac{1}{2}\Big(\rho(\mathbf{r}) - |\mathbf{m}(\mathbf{r})|\Big) \tag{3.37}$$

leading to scalar, $v^0_{\mathrm{XC}}(\mathbf{r})$, and vectors potentials, $\mathbf{B}_{\mathrm{XC}}(\mathbf{r})$,

$$v^0_{\mathrm{XC}}(\mathbf{r}) = \frac{1}{2}(v^\uparrow_{\mathrm{XC}}(\mathbf{r}) + v^\downarrow_{\mathrm{XC}}(\mathbf{r})), \qquad \mathbf{B}_{\mathrm{XC}}(\mathbf{r}) = \frac{1}{2}(v^\uparrow_{\mathrm{XC}}(\mathbf{r}) - v^\downarrow_{\mathrm{XC}}(\mathbf{r}))\hat{\mathbf{m}}(\mathbf{r}) \tag{3.38}$$

where the chain rule is used to find the potentials from the energy functionals. In the same manner the kernel terms can be obtained using the above relations.

- Charge-Charge:

$$\frac{\delta v^0_{\mathrm{XC}}}{\delta\rho}\Big|_{\mathbf{m}} = \Big(\frac{\delta v^0_{\mathrm{XC}}}{\delta\rho_\uparrow}\Big)\Big(\frac{\delta\rho_\uparrow}{\delta\rho}\Big)\Big|_{\mathbf{m}} + \Big(\frac{\delta v^0_{\mathrm{XC}}}{\delta\rho_\downarrow}\Big)\Big(\frac{\delta\rho_\downarrow}{\delta\rho}\Big)\Big|_{\mathbf{m}} \tag{3.39}$$

$$\begin{aligned} \frac{\delta v^0_{\mathrm{XC}}}{\delta\rho}\Big|_{\mathbf{m}} &= \frac{1}{2}\Big(\frac{\delta v^\uparrow_{\mathrm{XC}}}{\delta\rho^\uparrow} + \frac{\delta v^\downarrow_{\mathrm{XC}}}{\delta\rho^\uparrow}\Big)\frac{\delta\rho^\uparrow}{\delta\rho}\Big|_{\mathbf{m}} + \frac{1}{2}\Big(\frac{\delta v^\uparrow_{\mathrm{XC}}}{\delta\rho^\downarrow} + \frac{\delta v^\downarrow_{\mathrm{XC}}}{\delta\rho^\downarrow}\Big)\frac{\delta\rho^\downarrow}{\delta\rho}\Big|_{\mathbf{m}} \\ &= \frac{1}{2}(f^{\uparrow\uparrow}_{\mathrm{XC}} + f^{\downarrow\uparrow}_{\mathrm{XC}})\frac{1}{2} + (f^{\uparrow\downarrow}_{\mathrm{XC}} + f^{\downarrow\downarrow}_{\mathrm{XC}})\frac{1}{2} \\ &= \frac{1}{4}\Big(f^{\uparrow\uparrow}_{\mathrm{XC}} + f^{\uparrow\downarrow}_{\mathrm{XC}} + f^{\downarrow\uparrow}_{\mathrm{XC}} + f^{\downarrow\downarrow}_{\mathrm{XC}}\Big) \end{aligned} \tag{3.40}$$

- Charge-Spin: The Charge-Spin term of the kernel is a vector with 3 elements for each direction of moment. It is also equivalent to the spin-charge term of the kernel matrix. Hence it is sufficient to obtain any one of the terms.

$$\frac{\delta v^0_{\text{XC}}}{\delta \mathbf{m}}\Big|_\rho = \Big(\frac{\delta v^0_{\text{XC}}}{\delta \rho_\uparrow}\Big)\Big(\frac{\delta \rho_\uparrow}{\delta \mathbf{m}}\Big)\Big|_\rho + \Big(\frac{\delta v^0_{\text{XC}}}{\delta \rho_\downarrow}\Big)\Big(\frac{\delta \rho_\downarrow}{\delta \mathbf{m}}\Big)\Big|_\rho \tag{3.41}$$

$$\begin{aligned}\frac{\delta \rho^\uparrow}{\delta \mathbf{m}} &= \frac{\delta \rho^\uparrow}{\delta |\mathbf{m}|}\frac{\delta |\mathbf{m}|}{\delta \mathbf{m}}\Big|_\rho \\ &= \frac{\delta \rho^\uparrow}{\delta |\mathbf{m}|}\hat{\mathbf{m}}\Big|_\rho \\ &= \frac{1}{2}\hat{\mathbf{m}}\Big|_\rho\end{aligned} \tag{3.42}$$

Similarly, for the spin down channel we have,

$$\begin{aligned}\frac{\delta \rho^\downarrow}{\delta \mathbf{m}} &= \frac{\delta \rho^\downarrow}{\delta |\mathbf{m}|}\frac{\delta |\mathbf{m}|}{\delta \mathbf{m}}\Big|_\rho \\ &= \frac{\delta \rho^\downarrow}{\delta |\mathbf{m}|}\hat{\mathbf{m}}\Big|_\rho \\ &= -\frac{1}{2}\hat{\mathbf{m}}\Big|_\rho\end{aligned} \tag{3.43}$$

Substituting in Eq. (3.41) leads to,

$$\begin{aligned}\frac{\delta v^0_{\text{XC}}}{\delta \mathbf{m}}\Big|_\rho &= \frac{1}{2}\Big(\frac{\delta v^\uparrow_{\text{XC}}}{\delta \rho^\uparrow} + \frac{\delta v^\downarrow_{\text{XC}}}{\delta \rho^\uparrow}\Big)\frac{\delta \rho^\uparrow}{\delta \mathbf{m}}\Big|_\rho + \frac{1}{2}\Big(\frac{\delta v^\uparrow_{\text{XC}}}{\delta \rho^\downarrow} + \frac{\delta v^\downarrow_{\text{XC}}}{\delta \rho^\downarrow}\Big)\frac{\delta \rho^\downarrow}{\delta \mathbf{m}}\Big|_\rho \\ &= \frac{1}{2}\Big(f^{\uparrow\uparrow}_{\text{XC}} + f^{\downarrow\uparrow}_{\text{XC}}\Big)\Big(\frac{1}{2}\hat{\mathbf{m}}\Big) + \Big(f^{\uparrow\downarrow}_{\text{XC}} + f^{\downarrow\downarrow}_{\text{XC}}\Big)\Big(-\frac{1}{2}\hat{\mathbf{m}}\Big) \\ &= \frac{1}{4}\Big(f^{\uparrow\uparrow}_{\text{XC}} + f^{\downarrow\uparrow}_{\text{XC}} - f^{\uparrow\downarrow}_{\text{XC}} - f^{\downarrow\downarrow}_{\text{XC}}\Big)\hat{\mathbf{m}}\end{aligned} \tag{3.44}$$

- Spin-Spin: The last 3×3 matrix comprises the spin-spin term. The XC magnetic field can be written as $\mathbf{B}_{\text{XC}} = |\mathbf{B}_{\text{XC}}|\hat{\mathbf{m}}$. Then,

$$\begin{aligned}\frac{\delta \mathbf{B}_{\text{XC}}}{\delta \mathbf{m}}\Big|_\rho &= \frac{\delta}{\delta \mathbf{m}}\Big(|\mathbf{B}_{\text{XC}}|\hat{\mathbf{m}}\Big)\Big|_\rho \\ &= \frac{\delta |\mathbf{B}_{\text{XC}}|}{\delta \mathbf{m}} \otimes \hat{\mathbf{m}} + |\mathbf{B}_{\text{XC}}|\frac{\delta \hat{\mathbf{m}}}{\delta \mathbf{m}}\Big|_\rho\end{aligned} \tag{3.45}$$

derivative the unit vector, $\hat{\mathbf{m}}$, gives,

$$\begin{aligned}\frac{\delta\hat{\mathbf{m}}}{\delta\mathbf{m}} &= \Big(\frac{\delta\mathbf{m}}{\delta\mathbf{m}}\Big)\frac{1}{\delta|\mathbf{m}|} + \Big(-\frac{1}{|\mathbf{m}|^2}\Big)\hat{\mathbf{m}}\otimes\frac{\delta|\mathbf{m}|}{\delta\mathbf{m}} \\ &= \frac{I_3}{|\mathbf{m}|} - \frac{1}{|\mathbf{m}|^2}\mathbf{m}\otimes\hat{\mathbf{m}}\end{aligned} \tag{3.46}$$

Substituting Eq. (3.46) in Eq. (3.45) gives

$$\frac{\delta\mathbf{B}_{\mathrm{XC}}}{\delta\mathbf{m}}\Big|_\rho = \frac{\delta|\mathbf{B}_{\mathrm{XC}}|}{\delta\mathbf{m}}\otimes\hat{\mathbf{m}} + |\mathbf{B}_{\mathrm{XC}}|\Big(\frac{I_3}{|\mathbf{m}|} - \frac{1}{|\mathbf{m}|}\hat{\mathbf{m}}\otimes\hat{\mathbf{m}}\Big) \tag{3.47}$$

From the knowledge of spin-DFT we have $|\mathbf{B}_{\mathrm{XC}}| = \frac{1}{2}(v^{\uparrow}_{\mathrm{XC}} - v^{\downarrow}_{\mathrm{XC}})$, which gives

$$\begin{aligned}\frac{\delta|\mathbf{B}_{\mathrm{XC}}|}{\delta\mathbf{m}}\Big|_\rho &= \frac{\delta|\mathbf{B}_{\mathrm{XC}}|}{\delta\rho^{\uparrow}}\frac{\delta\rho^{\uparrow}}{\delta\mathbf{m}}\Big|_\rho + \frac{\delta|\mathbf{B}_{\mathrm{XC}}|}{\delta\rho^{\downarrow}}\frac{\delta\rho^{\downarrow}}{\delta\mathbf{m}}\Big|_\rho \\ &= \frac{1}{2}\Big(\frac{\delta v^{\uparrow}_{\mathrm{XC}}}{\delta\rho^{\uparrow}} - \frac{\delta v^{\downarrow}_{\mathrm{XC}}}{\delta\rho^{\uparrow}}\Big)\Big(\frac{1}{2}\hat{\mathbf{m}}\Big) + \frac{1}{2}\Big(\frac{\delta v^{\uparrow}_{\mathrm{XC}}}{\delta\rho^{\downarrow}} - \frac{\delta v^{\downarrow}_{\mathrm{XC}}}{\delta\rho^{\downarrow}}\Big)\Big(-\frac{1}{2}\hat{\mathbf{m}}\Big) \\ &= \frac{1}{4}\Big(f^{\uparrow\uparrow}_{\mathrm{XC}} - f^{\uparrow\downarrow}_{\mathrm{XC}} - f^{\downarrow\uparrow}_{\mathrm{XC}} + f^{\downarrow\downarrow}_{\mathrm{XC}}\Big)\end{aligned} \tag{3.48}$$

Putting all of the terms together we get,

$$\frac{\delta|\mathbf{B}_{\mathrm{XC}}|}{\delta\mathbf{m}}\Big|_\rho = \Big[\frac{1}{4}\Big(f^{\uparrow\uparrow}_{\mathrm{XC}} - f^{\uparrow\downarrow}_{\mathrm{XC}} - f^{\downarrow\uparrow}_{\mathrm{XC}} + f^{\downarrow\downarrow}_{\mathrm{XC}}\Big) - \frac{|\mathbf{B}_{\mathrm{XC}}|}{|\mathbf{m}|}\Big]\hat{\mathbf{m}}\otimes\hat{\mathbf{m}} + \frac{|\mathbf{B}_{\mathrm{XC}}|}{|\mathbf{m}|}I_3 \tag{3.49}$$

For the LDA functional the terms $f^{\downarrow\uparrow}_{\mathrm{XC}}(\mathbf{r},\mathbf{r}') = f^{\uparrow\downarrow}_{\mathrm{XC}}(\mathbf{r},\mathbf{r}')$ and the above expressions are reduced to a simpler form, but this cancellation may not be true in general.
In conclusion, we may use the kernels derived in Eqs. (3.28), (3.33), and (3.35) in the following equations to calculate the charge-charge, f^{00}_{XC}, charge-spin, f^{0i}_{XC}, and spin-spin, f^{ij}_{XC}, non-collinear parts of the full kernel:

$$f^{00}_{\mathrm{XC}}(\mathbf{r},\mathbf{r}') = \frac{1}{4}\Big[f^{\uparrow\uparrow}_{\mathrm{XC}}(\mathbf{r},\mathbf{r}') + f^{\uparrow\downarrow}_{\mathrm{XC}}(\mathbf{r},\mathbf{r}') + f^{\downarrow\uparrow}_{\mathrm{XC}}(\mathbf{r},\mathbf{r}') + f^{\downarrow\downarrow}_{\mathrm{XC}}(\mathbf{r},\mathbf{r}')\Big] \tag{3.50}$$

$$f^{0i}_{\mathrm{XC}}(\mathbf{r},\mathbf{r}') = \frac{1}{4}\Big[f^{\uparrow\uparrow}_{\mathrm{XC}}(\mathbf{r},\mathbf{r}') - f^{\uparrow\downarrow}_{\mathrm{XC}}(\mathbf{r},\mathbf{r}') + f^{\downarrow\uparrow}_{\mathrm{XC}}(\mathbf{r},\mathbf{r}') - f^{\downarrow\downarrow}_{\mathrm{XC}}(\mathbf{r},\mathbf{r}')\Big]\hat{m}_i(\mathbf{r}') \tag{3.51}$$

$$\begin{aligned}f^{ij}_{\mathrm{XC}}(\mathbf{r},\mathbf{r}') = \frac{1}{4}\Big[f^{\uparrow\uparrow}_{\mathrm{XC}}(\mathbf{r},\mathbf{r}') - f^{\uparrow\downarrow}_{\mathrm{XC}}(\mathbf{r},\mathbf{r}') - f^{\downarrow\uparrow}_{\mathrm{XC}}(\mathbf{r},\mathbf{r}') + f^{\downarrow\downarrow}_{\mathrm{XC}}(\mathbf{r},\mathbf{r}') - \frac{|\mathbf{B}_{\mathrm{XC}}(\mathbf{r})|}{|\mathbf{m}(\mathbf{r})|}\Big]\hat{\mathbf{m}}_i(\mathbf{r})\hat{\mathbf{m}}_j(\mathbf{r}') \\ + \frac{|\mathbf{B}_{\mathrm{XC}}(\mathbf{r})|}{|\mathbf{m}(\mathbf{r})|}I_3\end{aligned} \tag{3.52}$$

where I_3 is the 3×3 Identity matrix, $\hat{m}$ is the unit magnetization vector, $|\mathbf{B}_{\mathrm{XC}}|$ is the magnitude of XC magnetic field, and $|\mathbf{m}|$ is the magnitude of the magnetization.

3.5 Implementation of spin-polarized kernel

Again, in libxc the XC functionals are expressed in terms of density ($\rho = \rho_\alpha + \rho_\beta$) and sigmas ($\sigma_{\alpha\alpha}, \sigma_{\alpha\beta}, \sigma_{\beta\beta}$), where,

$$\begin{aligned}\sigma &= \boldsymbol{\nabla}\rho \cdot \boldsymbol{\nabla}\rho \\ &= \boldsymbol{\nabla}(\rho_\alpha + \rho_\beta) \cdot \boldsymbol{\nabla}(\rho_\alpha + \rho_\beta) \\ &= \boldsymbol{\nabla}\rho_\alpha \cdot \boldsymbol{\nabla}\rho_\alpha + 2\boldsymbol{\nabla}\rho_\alpha \cdot \boldsymbol{\nabla}\rho_\beta + \boldsymbol{\nabla}\rho_\beta \cdot \boldsymbol{\nabla}\rho_\beta \\ &= \sigma_{\alpha\alpha} + 2\sigma_{\alpha\beta} + \sigma_{\beta\beta}\end{aligned} \tag{3.53}$$

For any GGA functional, $g[\rho, \boldsymbol{\nabla}\rho]$, libxc returns the energy, potential and their derivatives up to second order (shown here):

- exc$[\rho, \boldsymbol{\nabla}\rho] \rightarrow$ energy per particle
- vrho$[\rho, \boldsymbol{\nabla}\rho] \rightarrow$ 2 components for each spin density i.e. $[\frac{\delta g}{\delta \rho_\alpha}, \frac{\delta g}{\delta \rho_\beta}]$
- vsigma$[\rho, \boldsymbol{\nabla}\rho] \rightarrow$ 3 components i.e. $[\frac{\delta g}{\delta \sigma_{\alpha\alpha}}, \frac{\delta g}{\delta \sigma_{\alpha\beta}}, \frac{\delta g}{\delta \sigma_{\beta\beta}}]$
- v2rho2$[\rho, \boldsymbol{\nabla}\rho] \rightarrow$ 3 components i.e. $[\frac{\delta^2 g}{\delta \rho_\alpha \delta \rho_\alpha}, \frac{\delta^2 g}{\delta \rho_\alpha \delta \rho_\beta}, \frac{\delta^2 g}{\delta \rho_\beta \delta \rho_\beta}]$
- v2rhosigma$[\rho, \boldsymbol{\nabla}\rho] \rightarrow$ 6 components

  i.e. $[\frac{\delta^2 g}{\delta \rho_\alpha \delta \sigma_{\alpha\alpha}}, \frac{\delta^2 g}{\delta \rho_\alpha \delta \sigma_{\alpha\beta}}, \frac{\delta^2 g}{\delta \rho_\alpha \delta \sigma_{\beta\beta}}, \frac{\delta^2 g}{\delta \rho_\beta \delta \sigma_{\alpha\alpha}}, \frac{\delta^2 g}{\delta \rho_\beta \delta \sigma_{\alpha\beta}}, \frac{\delta^2 g}{\delta \rho_\beta \delta \sigma_{\beta\beta}}]$
- v2sigma2$[\rho, \boldsymbol{\nabla}\rho] \rightarrow$ 6 components

  i.e. $[\frac{\delta^2 g}{\delta \sigma_{\alpha\alpha} \delta \sigma_{\alpha\alpha}}, \frac{\delta^2 g}{\delta \sigma_{\alpha\alpha} \delta \sigma_{\alpha\beta}}, \frac{\delta^2 g}{\delta \sigma_{\alpha\alpha} \delta \sigma_{\beta\beta}}, \frac{\delta^2 g}{\delta \sigma_{\alpha\beta} \delta \sigma_{\alpha\beta}}, \frac{\delta^2 g}{\delta \sigma_{\beta\beta} \delta \sigma_{\alpha\beta}}, \frac{\delta^2 g}{\delta \sigma_{\beta\beta} \delta \sigma_{\beta\beta}}]$

For implementation each of the terms in the spin polarized kernels, $f_{\mathrm{XC}}^{\alpha\alpha}(\mathbf{r}, \mathbf{r}')$ and $f_{\mathrm{XC}}^{\alpha\beta}(\mathbf{r}, \mathbf{r}')$, have to be converted in the above libxc expressions. The first terms of Eqs. (3.28) and (3.33) need no conversion, as it is one of the terms of v2rho2. But for the other terms in the kernel a conversion is needed. The first order derivatives of the functional w.r.t. $\boldsymbol{\nabla}\rho_\alpha$ gives,

$$\frac{\delta g}{\delta \boldsymbol{\nabla}\rho_\alpha} = 2\Big[\frac{\delta g}{\delta \sigma_{\alpha\alpha}} \boldsymbol{\nabla}\rho_\alpha + \frac{1}{2}\frac{\delta g}{\delta \sigma_{\alpha\beta}} \boldsymbol{\nabla}\rho_\beta\Big] \tag{3.54}$$

$$\frac{\delta}{\delta \rho_\alpha}\Big(\frac{\delta g}{\delta \boldsymbol{\nabla}\rho_\alpha}\Big) = 2\Big[\frac{\delta^2 g}{\delta \rho_\alpha \delta \sigma_{\alpha\alpha}} \boldsymbol{\nabla}\rho_\alpha + \frac{1}{2}\frac{\delta^2 g}{\delta \rho_\alpha \delta \sigma_{\alpha\beta}} \boldsymbol{\nabla}\rho_\beta\Big] \tag{3.55}$$

$$\frac{\delta}{\delta\rho_\beta}\Big(\frac{\delta g}{\delta\boldsymbol{\nabla}\rho_\alpha}\Big) = 2\Big[\frac{\delta^2 g}{\delta\rho_\beta\delta\sigma_{\alpha\alpha}}\boldsymbol{\nabla}\rho_\alpha + \frac{1}{2}\frac{\delta^2 g}{\delta\rho_\beta\delta\sigma_{\alpha\beta}}\boldsymbol{\nabla}\rho_\beta\Big] \tag{3.56}$$

The second order derivatives will be,

$$\begin{aligned}
\frac{\delta}{\delta\boldsymbol{\nabla}_j\rho_\alpha}\Big(\frac{\delta g}{\delta\boldsymbol{\nabla}_k\rho_\alpha}\Big) &= 2\frac{\delta}{\delta\boldsymbol{\nabla}_j\rho_\alpha}\Big[\frac{\delta g}{\delta\sigma_{\alpha\alpha}}\boldsymbol{\nabla}_k\rho_\alpha + \frac{1}{2}\frac{\delta g}{\delta\sigma_{\alpha\beta}}\boldsymbol{\nabla}_k\rho_\beta\Big] \\
&= 2\Big[\frac{\delta^2 g}{\delta\sigma_{\alpha\alpha}\delta\sigma_{\alpha\alpha}}\frac{\delta\sigma_{\alpha\alpha}}{\delta\boldsymbol{\nabla}_j\rho_\alpha}\boldsymbol{\nabla}_k\rho_\alpha + \frac{\delta g}{\delta\sigma_{\alpha\alpha}}\delta_{jk} + \frac{\delta^2 g}{\delta\sigma_{\alpha\beta}\delta\sigma_{\alpha\alpha}}\frac{\delta\sigma_{\alpha\beta}}{\delta\boldsymbol{\nabla}_j\rho_\alpha}\boldsymbol{\nabla}_k\rho_\alpha \\
&+ \frac{1}{2}\frac{\delta^2 g}{\delta\sigma_{\alpha\alpha}\delta\sigma_{\alpha\beta}}\frac{\delta\sigma_{\alpha\alpha}}{\delta\boldsymbol{\nabla}_j\rho_\alpha}\boldsymbol{\nabla}_k\rho_\beta + \frac{1}{2}\frac{\delta^2 g}{\delta\sigma_{\alpha\beta}\delta\sigma_{\alpha\beta}}\frac{\delta\sigma_{\alpha\beta}}{\delta\boldsymbol{\nabla}_j\rho_\alpha}\boldsymbol{\nabla}_k\rho_\beta\Big] \\
&= 4\frac{\delta^2 g}{\delta\sigma_{\alpha\alpha}\delta\sigma_{\alpha\alpha}}\boldsymbol{\nabla}_j\rho_\alpha\boldsymbol{\nabla}_k\rho_\alpha + 2\frac{\delta^2 g}{\delta\sigma_{\alpha\beta}\delta\sigma_{\alpha\alpha}}\boldsymbol{\nabla}_j\rho_\beta\boldsymbol{\nabla}_k\rho_\alpha + 2\frac{\delta^2 g}{\delta\sigma_{\alpha\beta}\delta\sigma_{\alpha\alpha}}\boldsymbol{\nabla}_j\rho_\alpha\boldsymbol{\nabla}_k\rho_\beta \\
&+ \frac{\delta^2 g}{\delta\sigma_{\alpha\beta}\delta\sigma_{\alpha\beta}}\boldsymbol{\nabla}_j\rho_\beta\boldsymbol{\nabla}_k\rho_\beta + 2\frac{\delta g}{\delta\sigma_{\alpha\alpha}}\delta_{jk}
\end{aligned} \tag{3.57}$$

$$\begin{aligned}
\frac{\delta}{\delta\boldsymbol{\nabla}_j\rho_\beta}\Big(\frac{\delta g}{\delta\boldsymbol{\nabla}_k\rho_\alpha}\Big) &= 2\frac{\delta}{\delta\boldsymbol{\nabla}_j\rho_\beta}\Big[\frac{\delta g}{\delta\sigma_{\alpha\alpha}}\boldsymbol{\nabla}_k\rho_\alpha + \frac{1}{2}\frac{\delta g}{\delta\sigma_{\alpha\beta}}\boldsymbol{\nabla}_k\rho_\beta\Big] \\
&= 2\Big[\frac{\delta^2 g}{\delta\sigma_{\beta\beta}\delta\sigma_{\alpha\alpha}}\frac{\delta\sigma_{\beta\beta}}{\delta\boldsymbol{\nabla}_j\rho_\beta}\boldsymbol{\nabla}_k\rho_\alpha + \frac{\delta^2 f}{\delta\sigma_{\alpha\beta}\delta\sigma_{\alpha\alpha}}\frac{\delta\sigma_{\alpha\beta}}{\delta\boldsymbol{\nabla}_j\rho_\beta}\boldsymbol{\nabla}_k\rho_\alpha \\
&+ \frac{1}{2}\frac{\delta^2 g}{\delta\sigma_{\beta\beta}\delta\sigma_{\alpha\beta}}\frac{\delta\sigma_{\beta\beta}}{\delta\boldsymbol{\nabla}_j\rho_\beta}\boldsymbol{\nabla}_k\rho_\beta + \frac{1}{2}\frac{\delta^2 g}{\delta\sigma_{\alpha\beta}\delta\sigma_{\alpha\beta}}\frac{\delta\sigma_{\alpha\beta}}{\delta\boldsymbol{\nabla}_j\rho_\beta}\boldsymbol{\nabla}_k\rho_\beta + \frac{1}{2}\frac{\delta g}{\delta\sigma_{\alpha\beta}}\delta_{jk}\Big] \\
&= 4\frac{\delta^2 g}{\delta\sigma_{\beta\beta}\delta\sigma_{\alpha\alpha}}\boldsymbol{\nabla}_j\rho_\beta\boldsymbol{\nabla}_k\rho_\alpha + 2\frac{\delta^2 g}{\delta\sigma_{\alpha\beta}\delta\sigma_{\alpha\alpha}}\boldsymbol{\nabla}_j\rho_\beta\boldsymbol{\nabla}_k\rho_\alpha + 2\frac{\delta^2 g}{\delta\sigma_{\beta\beta}\delta\sigma_{\alpha\beta}}\boldsymbol{\nabla}_j\rho_\beta\boldsymbol{\nabla}_k\rho_\beta \\
&+ \frac{\delta^2 g}{\delta\sigma_{\alpha\beta}\delta\sigma_{\alpha\beta}}\boldsymbol{\nabla}_j\rho_\alpha\boldsymbol{\nabla}_k\rho_\beta + \frac{\delta g}{\delta\sigma_{\alpha\beta}}\delta_{jk}
\end{aligned} \tag{3.58}$$

Using the above conversion equations from libxc, the GGA kernel was implemented in the all-electron ELK code [82].

The kernel is transformed in Fourier space for it's implementation. The third term of the kernel involves a gradient of a delta function in real space whose Fourier transform is difficult numerically and hence is carried out explicitly. First the property of delta function $\boldsymbol{\nabla}^{\mathbf{r}}\delta(\mathbf{r}-\mathbf{r}') = -\boldsymbol{\nabla}^{\mathbf{r}'}\delta(\mathbf{r}-\mathbf{r}')$ is used to simplify the third term:

$$\boldsymbol{\nabla}_j^{\mathbf{r}'}\Big[\frac{\partial^2 e_{\mathrm{XC}}}{\partial\boldsymbol{\nabla}_j\rho_\alpha\boldsymbol{\nabla}_k\rho_\beta}(\mathbf{r}')[\boldsymbol{\nabla}_k^{\mathbf{r}}\delta(\mathbf{r}-\mathbf{r}')]\Big] \tag{3.59}$$

Assuming,

$$f_3^{jk}(\mathbf{r}') = \frac{\partial^2 e_{\mathrm{XC}}}{\partial \boldsymbol{\nabla}_j \rho_\alpha \boldsymbol{\nabla}_k \rho_\beta}(\mathbf{r}') \tag{3.60}$$

Then performing a Fourier transform gives

$$\int\int e^{-i(\mathbf{q}+\mathbf{G})\cdot\mathbf{r}} \Big[\boldsymbol{\nabla}_j^{\mathbf{r}'} \Big(f_3^{jk}(\mathbf{r}')\boldsymbol{\nabla}_k^{\mathbf{r}}\delta(\mathbf{r}-\mathbf{r}')\Big)\Big] e^{i(\mathbf{q}+\mathbf{G}')\cdot\mathbf{r}'} d\mathbf{r} d\mathbf{r}' \tag{3.61}$$

Doing Integration by parts twice we get,

$$\begin{aligned}
&-\int\int \boldsymbol{\nabla}_j^{\mathbf{r}'} \Big[e^{-i(\mathbf{q}+\mathbf{G})\cdot\mathbf{r}} e^{i(\mathbf{q}+\mathbf{G}')\cdot\mathbf{r}'}\Big] f_3^{jk}(\mathbf{r}') \Big[\boldsymbol{\nabla}_k^{\mathbf{r}}\delta(\mathbf{r}-\mathbf{r}')\Big] d\mathbf{r} d\mathbf{r}' \\
&= -\int\int (i(\mathbf{q}+\mathbf{G}')_j) e^{-i(\mathbf{q}+\mathbf{G})\cdot\mathbf{r}} e^{i(\mathbf{q}+\mathbf{G}')\cdot\mathbf{r}'} f_3^{jk}(\mathbf{r}') \Big[\boldsymbol{\nabla}_k^{\mathbf{r}}\delta(\mathbf{r}-\mathbf{r}')\Big] d\mathbf{r} d\mathbf{r}' \\
&= \int\int (i(\mathbf{q}+\mathbf{G}')_j)(-i(\mathbf{q}+\mathbf{G})_k) e^{-i(\mathbf{q}+\mathbf{G})\cdot\mathbf{r}} e^{i(\mathbf{q}+\mathbf{G}')\cdot\mathbf{r}'} f_3^{jk}(\mathbf{r}')\delta(\mathbf{r}-\mathbf{r}') d\mathbf{r} d\mathbf{r}' \\
&= \int (\mathbf{q}+\mathbf{G}')_j (\mathbf{q}+\mathbf{G})_k f_3^{jk}(\mathbf{r}) e^{-i(\mathbf{G}-\mathbf{G}')\cdot\mathbf{r}} d^3r \\
&= (\mathbf{q}+\mathbf{G}')_j (\mathbf{q}+\mathbf{G})_k \int \Big[\frac{\partial^2 e_{\mathrm{XC}}}{\partial \boldsymbol{\nabla}_j \rho_\alpha \boldsymbol{\nabla}_k \rho_\beta}(\mathbf{r})\Big] e^{-i(\mathbf{G}-\mathbf{G}')\cdot\mathbf{r}} d\mathbf{r} \\
&= (\mathbf{q}+\mathbf{G}')_j (\mathbf{q}+\mathbf{G})_k \tilde{f}_3(\mathbf{G}-\mathbf{G}')
\end{aligned} \tag{3.62}$$

where $\tilde{f}_3(\mathbf{G}-\mathbf{G}')$ is Fourier transform of $f_3^{jk}(\mathbf{r})$. Hence we write $\Big[\frac{\partial^2 e_{\mathrm{XC}}}{\partial \boldsymbol{\nabla}_j \rho_\alpha \boldsymbol{\nabla}_k \rho_\beta}\Big]$ in terms of the libxc terms, do Fourier transform of it and then multiply it with $-(\mathbf{q}+\mathbf{G}')_j(\mathbf{q}+\mathbf{G})_k$ to get the third term of the kernel. The Fourier transform of rest of the terms is quite straightforward and can be written as,

a)

$$\begin{aligned}
&\int\int e^{-i(\mathbf{q}+\mathbf{G})\cdot\mathbf{r}} \Big[\delta(\mathbf{r}-\mathbf{r}') \frac{\partial^2 e_{\mathrm{XC}}}{\partial \rho_\beta \partial \rho_\alpha}(\mathbf{r}')\Big] e^{i(\mathbf{q}+\mathbf{G}')\cdot\mathbf{r}'} d\mathbf{r} d\mathbf{r}' \\
&= \int e^{-i(\mathbf{G}-\mathbf{G}')\cdot\mathbf{r}} d\mathbf{r} \frac{\partial^2 e_{\mathrm{XC}}}{\partial \rho_\beta \partial \rho_\alpha}(\mathbf{r})
\end{aligned} \tag{3.63}$$

b)

$$\begin{aligned}
&-\int\int e^{-i(\mathbf{q}+\mathbf{G})\cdot\mathbf{r}} \Big[\boldsymbol{\nabla}_j^{\mathbf{r}'}\delta(\mathbf{r}-\mathbf{r}') \frac{\partial^2 e_{\mathrm{XC}}}{\partial \rho_\alpha \partial \boldsymbol{\nabla}_j^{\mathbf{r}} \rho_\beta}(\mathbf{r})\Big] e^{i(\mathbf{q}+\mathbf{G}')\cdot\mathbf{r}'} d\mathbf{r} d\mathbf{r}' \\
&= i(\mathbf{q}+\mathbf{G})_j \int\int e^{-i(\mathbf{q}+\mathbf{G})\cdot\mathbf{r}} e^{i(\mathbf{q}+\mathbf{G}')\cdot\mathbf{r}'} \Big[\delta(\mathbf{r}-\mathbf{r}') \frac{\partial^2 e_{\mathrm{XC}}}{\partial \rho_\alpha \partial \boldsymbol{\nabla}_j^{\mathbf{r}} \rho_\beta}(\mathbf{r})\Big] d\mathbf{r} d\mathbf{r}' \\
&= i(\mathbf{q}+\mathbf{G})_j \int e^{-i(\mathbf{G}-\mathbf{G}')\cdot\mathbf{r}} \Big[\frac{\partial^2 e_{\mathrm{XC}}}{\partial \rho_\alpha \partial \boldsymbol{\nabla}_j^{\mathbf{r}} \rho_\beta}(\mathbf{r})\Big] d\mathbf{r}
\end{aligned} \tag{3.64}$$

c)

$$\begin{aligned}
&\int\int e^{-i(\mathbf{q}+\mathbf{G})\cdot\mathbf{r}}\Big[\boldsymbol{\nabla}_j^{\mathbf{r}'}\delta(\mathbf{r}-\mathbf{r}')\frac{\partial^2 e_{\mathrm{XC}}}{\partial\rho_\beta\partial\boldsymbol{\nabla}_j^{\mathbf{r}'}\rho_\alpha}(\mathbf{r}')\Big]e^{i(\mathbf{q}+\mathbf{G}')\cdot\mathbf{r}'}d\mathbf{r}d\mathbf{r}' \\
&= -i(\mathbf{q}+\mathbf{G})_j\int\int e^{-i(\mathbf{q}+\mathbf{G})\cdot\mathbf{r}}e^{i(\mathbf{q}+\mathbf{G}')\cdot\mathbf{r}'}\Big[\delta(\mathbf{r}-\mathbf{r}')\frac{\partial^2 e_{\mathrm{XC}}}{\partial\rho_\beta\partial\boldsymbol{\nabla}_j^{\mathbf{r}'}\rho_\alpha}(\mathbf{r})\Big]d\mathbf{r}d\mathbf{r}' \\
&= -i(\mathbf{q}+\mathbf{G})_j\int e^{-i(\mathbf{G}-\mathbf{G}')\cdot\mathbf{r}}\Big[\frac{\partial^2 e_{\mathrm{XC}}}{\partial\rho_\beta\partial\boldsymbol{\nabla}_j^{\mathbf{r}}\rho_\alpha}(\mathbf{r})\Big]d\mathbf{r}
\end{aligned} \tag{3.65}$$

For noncollinear systems the implementation of the third term gets even more complicated as one ends up with terms which include gradients of magnetization. The spin-spin part of the kernel is given by Eq. 3.52 and writing only the first part here, $f_{\mathrm{XC}}^{\uparrow\uparrow}$, but it is to be done with each term of the kernel, $f_{\mathrm{XC}}^{\downarrow\downarrow}, f_{\mathrm{XC}}^{\uparrow\downarrow}, f_{\mathrm{XC}}^{\downarrow\uparrow}$.

$$\begin{aligned}
f_{\mathrm{XC}}^{ij}(\mathbf{r},\mathbf{r}') &= \frac{1}{4}\Big[f_{\mathrm{XC}}^{\uparrow\uparrow}(\mathbf{r},\mathbf{r}') - \frac{|\mathbf{B}_{\mathrm{XC}}(\mathbf{r})|}{|\mathbf{m}(\mathbf{r})|}\Big]\hat{\mathbf{m}}_a(\mathbf{r})\hat{\mathbf{m}}_b(\mathbf{r}') + \frac{|\mathbf{B}_{\mathrm{XC}}(\mathbf{r})|}{|\mathbf{m}(\mathbf{r})|}I_3 \\
&= \frac{1}{4}\Big[\delta(\mathbf{r}-\mathbf{r}')\Big[\frac{\partial^2 e_{xc}}{\partial\rho_\alpha\partial\rho_\alpha}(\mathbf{r}') - \Big(\boldsymbol{\nabla}'_k\frac{\partial^2 e_{xc}}{\partial\boldsymbol{\nabla}_k\rho_\alpha\partial\rho_\alpha}(\mathbf{r}')\Big)\Big] \\
&- \boldsymbol{\nabla}'_k\Big[[\boldsymbol{\nabla}'_j\delta(\mathbf{r}-\mathbf{r}')]\Big(\frac{\partial^2 e_{xc}}{\partial\boldsymbol{\nabla}_k\rho_\alpha\partial\boldsymbol{\nabla}_j\rho_\alpha}(\mathbf{r}')\Big)\Big] - \frac{|\mathbf{B}_{\mathrm{XC}}(\mathbf{r})|}{|\mathbf{m}(\mathbf{r})|}\Big]\hat{\mathbf{m}}_a(\mathbf{r})\hat{\mathbf{m}}_b(\mathbf{r}') + \frac{|\mathbf{B}_{\mathrm{XC}}(\mathbf{r})|}{|\mathbf{m}(\mathbf{r})|}I_3
\end{aligned} \tag{3.66}$$

The Fourier transform of all the terms is simple except the one which involves gradient of delta function. Let,

$$B = \boldsymbol{\nabla}'_k\Big[[\boldsymbol{\nabla}_j\delta(\mathbf{r}-\mathbf{r}')]f_4^{jk}(\mathbf{r}')\Big]\hat{\mathbf{m}}_a(\mathbf{r})\hat{\mathbf{m}}_b(\mathbf{r}') \tag{3.67}$$

where

$$f_4^{jk}(\mathbf{r}') = \frac{1}{4}\Big(\frac{\partial^2 e_{xc}}{\partial\boldsymbol{\nabla}_k\rho_\alpha\partial\boldsymbol{\nabla}_j\rho_\alpha}(\mathbf{r}')\Big) \tag{3.68}$$

Then doing the Fourier transform gives

$$\int\int e^{-i(\mathbf{q}+\mathbf{G})\cdot\mathbf{r}}\Big[\boldsymbol{\nabla}'_k\Big([\boldsymbol{\nabla}_j\delta(\mathbf{r}-\mathbf{r}')]f_4(\mathbf{r}')\Big)\Big]\hat{\mathbf{m}}_a(\mathbf{r})\hat{\mathbf{m}}_b(\mathbf{r}')e^{i(\mathbf{q}+\mathbf{G}')\cdot\mathbf{r}'}d\mathbf{r}d\mathbf{r}' \tag{3.69}$$

doing integration by parts,

$$
\begin{aligned}
-\int\int \boldsymbol{\nabla}'_k \Big[e^{-i(\mathbf{q}+\mathbf{G})\cdot\mathbf{r}} e^{i(\mathbf{q}+\mathbf{G}')\cdot\mathbf{r}'} \hat{\mathbf{m}}_a(\mathbf{r})\hat{\mathbf{m}}_b(\mathbf{r}') \Big] [\boldsymbol{\nabla}_j \delta(\mathbf{r}-\mathbf{r}')] f_4^{jk}(\mathbf{r}') d\mathbf{r} d\mathbf{r}' \\
= -\int\int \Big[(i(\mathbf{q}+\mathbf{G}')_k) e^{-i(\mathbf{q}+\mathbf{G})\cdot\mathbf{r}} e^{i(\mathbf{q}+\mathbf{G}')\cdot\mathbf{r}'} \hat{\mathbf{m}}_a(\mathbf{r})\hat{\mathbf{m}}_b(\mathbf{r}') \\
+ e^{-i(\mathbf{q}+\mathbf{G})\cdot\mathbf{r}} e^{i(\mathbf{q}+\mathbf{G}')\cdot\mathbf{r}'} [\boldsymbol{\nabla}'_k \hat{\mathbf{m}}_b(\mathbf{r}')] \hat{\mathbf{m}}_a(\mathbf{r}) \Big] \Big\{ \boldsymbol{\nabla}_j \delta(\mathbf{r}-\mathbf{r}') \Big\} f_4^{jk}(\mathbf{r}') d\mathbf{r} d\mathbf{r}' \\
= \int\int \Big[(i(\mathbf{q}+\mathbf{G}')_k)(-i(\mathbf{q}+\mathbf{G})_j) + (i(\mathbf{q}+\mathbf{G}')_k) [\boldsymbol{\nabla}_j \hat{\mathbf{m}}_a(\mathbf{r})] \hat{\mathbf{m}}_b(\mathbf{r}') \\
+ (-i(\mathbf{q}+\mathbf{G})_j) [\boldsymbol{\nabla}'_k \hat{\mathbf{m}}_b(\mathbf{r}')] \hat{\mathbf{m}}_a(\mathbf{r}) + [\boldsymbol{\nabla}'_k \hat{\mathbf{m}}_b(\mathbf{r}')][\boldsymbol{\nabla}_j \hat{\mathbf{m}}_a(\mathbf{r})] \Big] \\
e^{-i(\mathbf{q}+\mathbf{G})\cdot\mathbf{r}} e^{i(\mathbf{q}+\mathbf{G}')\cdot\mathbf{r}'} f_4^{jk}(\mathbf{r}') \delta(\mathbf{r}-\mathbf{r}') d\mathbf{r} d\mathbf{r}' \\
= \int \Big[(i(\mathbf{q}+\mathbf{G}')_k)(-i(\mathbf{q}+\mathbf{G})_j) + (i(\mathbf{q}+\mathbf{G}')_k) [\boldsymbol{\nabla}_j \hat{\mathbf{m}}_a(\mathbf{r})] \hat{\mathbf{m}}_b(\mathbf{r}) \\
+ (-i(\mathbf{q}+\mathbf{G})_j) [\boldsymbol{\nabla}_k \hat{\mathbf{m}}_b(\mathbf{r})] \hat{\mathbf{m}}_a(\mathbf{r}) + [\boldsymbol{\nabla}_k \hat{\mathbf{m}}_b(\mathbf{r})][\boldsymbol{\nabla}_j \hat{\mathbf{m}}_a(\mathbf{r})] \Big] e^{-i(\mathbf{G}-\mathbf{G}')\cdot\mathbf{r}} f_4^{jk}(\mathbf{r}) d\mathbf{r}
\end{aligned}
\tag{3.70}
$$

Hence the kernel for non-collinear systems becomes complicated to calculate and implement. For collinear systems the $\boldsymbol{\nabla}\mathbf{m}$ terms are zero.
As part of our analysis of the XC kernel a new exact condition of kernel was derived which may be useful for developing new kernels for non-collinear systems in the future.

3.6 Zero force and Zero torque theorem

We first review the zero-force theorem for the XC kernel. In the ground-state or dynamical situation the XC potential or XC magnetic field can not exert a net force or torque on the electrons [27, 83]. In the presence of an external perturbation there can be a net force or torque on the system, however, the internal forces must still vanish and hence one can write,

$$
\int d\mathbf{r}\, \rho(\mathbf{r},t) \boldsymbol{\nabla} v_{\mathrm{XC}}(\mathbf{r},t) = 0 \tag{3.71}
$$

Considering a small perturbation leads to

$$
\begin{aligned}
\rho(\mathbf{r},t) &= \rho_0(\mathbf{r}) + \rho_1(\mathbf{r},t) \\
v_{\mathrm{XC}}(\mathbf{r},t) &= v^0_{\mathrm{XC}}(\mathbf{r}) + v^1_{\mathrm{XC}}(\mathbf{r},t)
\end{aligned}
\tag{3.72}
$$

substituting Eq. 3.72 in Eq. 3.71 we get,

$$
\begin{aligned}
&\int d\mathbf{r} \Big[\Big\{ \rho_0(\mathbf{r}) + \rho_1(\mathbf{r},t) \Big\} \Big\{ v^0_{\mathrm{XC}}(\mathbf{r}) + v^1_{\mathrm{XC}}(\mathbf{r},t) \Big\} \Big] = 0 \\
&\int d\mathbf{r} \Big[\rho_0(\mathbf{r}) \boldsymbol{\nabla} v^0_{\mathrm{XC}}(\mathbf{r}) + \rho_0(\mathbf{r}) \boldsymbol{\nabla} v^1_{\mathrm{XC}}(\mathbf{r},t) + \rho_1(\mathbf{r},t) \boldsymbol{\nabla} v^0_{\mathrm{XC}}(\mathbf{r}) + \rho_1(\mathbf{r},t) \boldsymbol{\nabla} v^1_{\mathrm{XC}}(\mathbf{r},t) \Big] = 0
\end{aligned}
\tag{3.73}
$$

here the first term is zero as it is the zero-force theorem itself and considering only the linear terms i.e. ignoring second order terms in perturbation we get,

$$\int d\mathbf{r}\Big[\rho_0(\mathbf{r})\boldsymbol{\nabla} v^1_{\mathrm{XC}}(\mathbf{r}) + \rho_1(\mathbf{r},t)\boldsymbol{\nabla} v^0_{\mathrm{XC}}(\mathbf{r})\Big] = 0 \tag{3.74}$$

the linearized XC potential gives the f_{XC} term,

$$\begin{aligned} v^1_{\mathrm{XC}}(\mathbf{r},t) &= \int dt' \int d\mathbf{r}' \, \frac{\delta v_{\mathrm{XC}}[\rho](\mathbf{r},t)}{\delta\rho(\mathbf{r}',t')}\Big|_{\rho_0(\mathbf{r})} \rho_1(\mathbf{r}',t') \\ &= \int dt' \int d\mathbf{r}' \, f_{\mathrm{XC}}(\mathbf{r},t,\mathbf{r}',t')\rho_1(\mathbf{r}',t') \end{aligned} \tag{3.75}$$

then,

$$\int d\mathbf{r}\, \rho_0(\mathbf{r})\boldsymbol{\nabla} \int dt' \int d\mathbf{r}' \, f_{\mathrm{XC}}(\mathbf{r},t,\mathbf{r}',t')\rho_1(\mathbf{r}',t') + \int d\mathbf{r}\, \rho_1(\mathbf{r},t)\boldsymbol{\nabla} v^0_{\mathrm{XC}}(\mathbf{r},t) = 0 \tag{3.76}$$

as this holds for arbitrary density $\rho_1(\mathbf{r},t)$ one gets,

$$\int dt' \int d\mathbf{r}' \, \rho_1(\mathbf{r}',t')\Big\{ \int d\mathbf{r}\, \rho_0(\mathbf{r})\boldsymbol{\nabla} f_{\mathrm{XC}}(\mathbf{r},t,\mathbf{r}',t') + \boldsymbol{\nabla}' v^0_{\mathrm{XC}}(\mathbf{r}')\delta(t-t')\Big\} = 0 \tag{3.77}$$

$$\int d\mathbf{r}\, \rho_0(\mathbf{r})\boldsymbol{\nabla} f_{\mathrm{XC}}(\mathbf{r},t,\mathbf{r}',t') = -\boldsymbol{\nabla}' v^0_{\mathrm{XC}}(\mathbf{r}')\delta(t-t') \tag{3.78}$$

performing the Fourier transform,

$$\int d\mathbf{r}\, \rho_0(\mathbf{r})\boldsymbol{\nabla} f_{\mathrm{XC}}(\mathbf{r},\mathbf{r}',\omega) = -\boldsymbol{\nabla}' v^0_{\mathrm{XC}}(\mathbf{r}') \tag{3.79}$$

as f_{XC} is symmetric in $\mathbf{r}$ and $\mathbf{r}'$,

$$\int d\mathbf{r}'\, \rho_0(\mathbf{r}')\boldsymbol{\nabla}' f_{\mathrm{XC}}(\mathbf{r},\mathbf{r}',\omega) = -\boldsymbol{\nabla} v^0_{\mathrm{XC}}(\mathbf{r}) \tag{3.80}$$

multiplying by $\rho_0(\mathbf{r})$ and integrating it

$$\int d\mathbf{r} \int d\mathbf{r}' \, \rho_0(\mathbf{r})\rho_0(\mathbf{r}')\boldsymbol{\nabla}' f_{\mathrm{XC}}(\mathbf{r},\mathbf{r}',\omega) = -\int d\mathbf{r}\rho_0(\mathbf{r})\boldsymbol{\nabla} v^0_{\mathrm{XC}}(\mathbf{r}) \tag{3.81}$$

the right hand side is zero because of the zero-force theorem,

$$\int d\mathbf{r} \int d\mathbf{r}' \, \rho_0(\mathbf{r})\rho_0(\mathbf{r}')\boldsymbol{\nabla}' f_{\mathrm{XC}}(\mathbf{r},\mathbf{r}',\omega) = 0 \tag{3.82}$$

This is the zero-force theorem for the kernel.

After reviewing the zero-force theorem for the kernel the zero-torque theorem [84] for the kernel is now derived for spin polarized systems. It begins with the zero-torque theorem for the XC magnetic field, i.e. the XC magnetic field cannot exert a net torque on the spin system in the ground-state:

$$\int d\mathbf{r}\, \mathbf{m}(\mathbf{r},t) \times \mathbf{B}_{\mathrm{XC}}(\mathbf{r},t) = 0 \tag{3.83}$$

Proceeding in the similar way, as done in the above review, we consider a small perturbation and linearize the magnetization and magnetic field.

$$\begin{aligned} \mathbf{m}(\mathbf{r},t) &= \mathbf{m}_0(\mathbf{r}) + \mathbf{m}_1(\mathbf{r},t) \\ \mathbf{B}_{\mathrm{XC}}(\mathbf{r},t) &= \mathbf{B}_0(\mathbf{r}) + \mathbf{B}_1(\mathbf{r},t) \end{aligned} \tag{3.84}$$

substituting Eq. (3.84) in Eq. (3.83) we get,

$$\begin{aligned} \int d\mathbf{r}\Big\{\mathbf{m}_0(\mathbf{r}) + \mathbf{m}_1(\mathbf{r},t)\Big\} \times \Big\{\mathbf{B}_0(\mathbf{r}) + \mathbf{B}_1(\mathbf{r},t)\Big\} = 0 \\ \int d\mathbf{r}\Big\{\mathbf{m}_0(\mathbf{r}) \times \mathbf{B}_0(\mathbf{r}) + \mathbf{m}_0(\mathbf{r}) \times \mathbf{B}_1(\mathbf{r},t) + \mathbf{m}_1(\mathbf{r},t) \times \mathbf{B}_0(\mathbf{r}) + \mathbf{m}_1(\mathbf{r},t) \times \mathbf{B}_1(\mathbf{r},t)\Big\} = 0 \end{aligned} \tag{3.85}$$

the first term is zero by the zero-torque theorem and last term is dropped as it is second order in perturbation. Then,

$$\int d\mathbf{r}\Big\{\mathbf{m}_0(\mathbf{r}) \times \mathbf{B}_1(\mathbf{r},t) + \mathbf{m}_1(\mathbf{r},t) \times \mathbf{B}_0(\mathbf{r})\Big\} = 0 \tag{3.86}$$

now the linearized magnetic field term is the magnetic kernel (written as $\overleftrightarrow{f}_{\mathrm{XC}}(\mathbf{r},t,\mathbf{r}',t')$ tensor),

$$\begin{aligned} \mathbf{B}_1(\mathbf{r},t) &= \int dt' \int d\mathbf{r}'\, \frac{\delta \mathbf{B}_{\mathrm{XC}}[\rho,\mathbf{m}](\mathbf{r},t)}{\delta \mathbf{m}(\mathbf{r}',t')}\Big|_{\mathbf{m}_0(\mathbf{r})} \mathbf{m}_1(\mathbf{r}',t') \\ &= \int dt' \int d\mathbf{r}'\, \overleftrightarrow{f}_{\mathrm{XC}}(\mathbf{r},t,\mathbf{r}',t') \mathbf{m}_1(\mathbf{r}',t') \end{aligned} \tag{3.87}$$

then,

$$\begin{aligned} \int d\mathbf{r}\Big\{\mathbf{m}_0(\mathbf{r}) \times \int dt' \int d\mathbf{r}'\, \overleftrightarrow{f}_{\mathrm{XC}}(\mathbf{r},t,\mathbf{r}',t') \cdot \mathbf{m}_1(\mathbf{r}',t')\Big\} + \int d\mathbf{r}'\, \mathbf{m}_1(\mathbf{r}',t') \times \mathbf{B}_0(\mathbf{r}') = 0 \\ \int d\mathbf{r}\Big\{ \int dt' \int d\mathbf{r}'\, \mathbf{m}_0(\mathbf{r}) \times \overleftrightarrow{f}_{\mathrm{XC}}(\mathbf{r},t,\mathbf{r}',t') \cdot \mathbf{m}_1(\mathbf{r}',t')\Big\} + \int d\mathbf{r}'\, \mathbf{m}_1(\mathbf{r}',t') \times \mathbf{B}_0(\mathbf{r}') = 0 \\ \int d\mathbf{r}\Big\{ \int dt' \int d\mathbf{r}'\, \mathbf{m}_0(\mathbf{r}) \cdot \overleftrightarrow{f}_{\mathrm{XC}}(\mathbf{r},t,\mathbf{r}',t') \times \mathbf{m}_1(\mathbf{r}',t')\Big\} - \int d\mathbf{r}'\, \mathbf{B}_0(\mathbf{r}') \times \mathbf{m}_1(\mathbf{r}',t') = 0 \end{aligned} \tag{3.88}$$

this should be true for arbitrary magnetization density. Hence,

$$\int dt' \int d\mathbf{r}' \, \mathbf{m}_0(\mathbf{r}) \cdot \overleftrightarrow{f}_{\mathrm{XC}}(\mathbf{r}, t, \mathbf{r}', t') = \mathbf{B}_0(\mathbf{r}')\delta(t - t') \tag{3.89}$$

performing Fourier transform,

$$\int d\mathbf{r} \, \mathbf{m}_0(\mathbf{r}) \cdot \overleftrightarrow{f}_{\mathrm{XC}}(\mathbf{r}, \mathbf{r}', \omega) = \mathbf{B}_0(\mathbf{r}') \tag{3.90}$$

again, the kernel is symmetric in $\mathbf{r}$ and $\mathbf{r}'$,

$$\int d\mathbf{r}' \, \mathbf{m}_0(\mathbf{r}') \cdot \overleftrightarrow{f}_{\mathrm{XC}}(\mathbf{r}, \mathbf{r}', \omega) = \mathbf{B}_0(\mathbf{r}) \tag{3.91}$$

take cross product with $\mathbf{m}_0(\mathbf{r})$ and integrate,

$$\int d\mathbf{r} \int d\mathbf{r}' \, \mathbf{m}_0(\mathbf{r}) \times \left\{ \mathbf{m}_0(\mathbf{r}') \cdot \overleftrightarrow{f}_{\mathrm{XC}}(\mathbf{r}, \mathbf{r}', \omega) \right\} = \int \mathbf{m}_0(\mathbf{r}) \times \mathbf{B}_0(\mathbf{r}) \, d\mathbf{r} \tag{3.92}$$

the right hand side is zero due to zero-torque theorem,

$$\int d\mathbf{r} \int d\mathbf{r}' \, \mathbf{m}_0(\mathbf{r}) \times \left\{ \mathbf{m}_0(\mathbf{r}') \cdot \overleftrightarrow{f}_{\mathrm{XC}}(\mathbf{r}, \mathbf{r}', \omega) \right\} = 0 \tag{3.93}$$

This is zero-torque theorem of the kernel for spin-polarized system. The kernel obtained by using the Kübler method by extending the collinear kernels trivially satisfies this zero-torque theorem. However, for functionals derived explicitly for non-collinear systems e.g. Ref. [85] should satisfy this exact condition. Hence such conditions are useful for developing kernels applicable to non-collinear systems.

CHAPTER 4

AGGA KERNEL APPLICATIONS

Success isn't about end result,
It's about what you learn along the way.
- Vera Wang

In this chapter the AGGA kernel derived in the previous chapter has been used to calculate response function of materials. First the optical response of LiF and diamond are studied. For this the unpolarized form of the kernel is utilized and we explore how the $\mathbf{q}^2$ dependence (as seen in Eq. 3.62) of the kernel affects the spectra. Next we study the magnetic response of ferromagnets Fe, Ni and Co, and two heusler compounds NiMnSb and Co_2MnSi. Results for magnon spectra show that the AGGA kernel doesn't provide an improvement over the traditional ALSDA kernel.

4.1 Brillouin Zone and high symmetry points

The real-space and reciprocal-space primitive lattice vectors for the fcc and bcc structures are given as,

$$A_{fcc} = \frac{a}{2}\begin{bmatrix} 0 & 1 & 1 \\ 1 & 0 & 1 \\ 1 & 1 & 0 \end{bmatrix} \qquad B_{fcc} = \frac{2\pi}{a}\begin{bmatrix} -1 & 1 & 1 \\ 1 & -1 & 1 \\ 1 & 1 & -1 \end{bmatrix}$$

$$A_{bcc} = \frac{a}{2}\begin{bmatrix} -1 & 1 & 1 \\ 1 & -1 & 1 \\ 1 & 1 & -1 \end{bmatrix} \qquad B_{bcc} = \frac{2\pi}{a}\begin{bmatrix} 0 & 1 & 1 \\ 1 & 0 & 1 \\ 1 & 1 & 0 \end{bmatrix}$$

where a denotes the lattice constant and A_{fcc} is the matrix formed of the real-space lattice vectors while B_{fcc} corresponds to the matrix of reciprocal vectors. This lattice constant can be either taken from experiments or an equilibrium value of this constant can be found for each functional. The shape of the BZ along with the high-symmetry points is shown in Fig. 4.1.
The $\mathbf{q}$-vectors of some of the high symmetry points in Cartesian coordinates are,

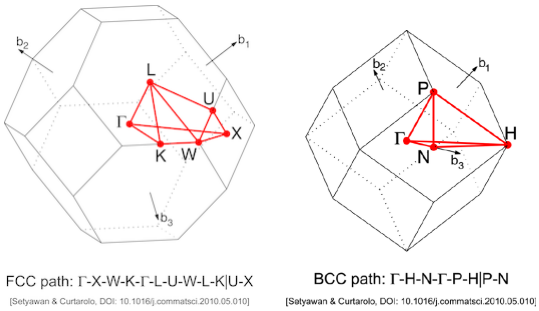

(a) (b)

Figure 4.1: The shape of the first Brillouin zone of (a) fcc and (b) bcc lattice [86].

$$\begin{aligned} &\text{fcc:} && X = \frac{2\pi}{a}\Big(0,0,1\Big) && K = \frac{\pi}{a}\Big(0,\frac{3}{2},\frac{3}{2}\Big) && L = \frac{\pi}{a}\Big(1,1,1\Big) \\ &\text{bcc:} && H = \frac{2\pi}{a}\Big(0,0,1\Big) && N = \frac{\pi}{a}\Big(0,1,1\Big) && P = \frac{\pi}{a}\Big(1,1,1\Big) \end{aligned} \tag{4.1}$$

The point $\Gamma = (0,0,0)$ is the center of the BZ and is same for all the lattices. These vectors in lattice coordinates, $\mathbf{q}'$, can be obtained from the use of Reciprocal matrix (B)

$$\mathbf{q} = B\mathbf{q}' \tag{4.2}$$

Then the obtained vectors are,

$$\begin{aligned} &\text{fcc:} && X' = \frac{1}{2}\Big(1,1,0\Big) && K' = \frac{3}{8}\Big(2,1,1\Big) && L = \frac{1}{2}\Big(1,1,1\Big) \\ &\text{bcc:} && H' = \frac{1}{2}\Big(1,1,-1\Big) && N' = \frac{1}{2}\Big(1,0,0\Big) && P' = \frac{1}{4}\Big(1,1,1\Big) \end{aligned} \tag{4.3}$$

The spectra is plotted along the path formed by joining the Γ point to any one of these high symmetry points.

4.2 Optical Response

It is well known that the correct $\mathbf{q}$-dependent behavior of the XC kernel is crucial for predicting the optical response of materials. For example, the XC kernel must go as $1/\mathbf{q}^2$ [47, 69, 41, 87, 88, 50] in the long-wavelength limit ($\mathbf{q} \to 0$). This property is needed for capturing the excitonic response of the material. However, the first rung on *Jacob's ladder*, the ALDA, does not display any $\mathbf{q}$-dependence, owing to the local approximation for the XC energy. This explains why ALDA does not yield any excitonic peaks in the optical spectra (see Chapter 2). The second rung consists of semi-local functionals which include information not just about the density but also its gradients. In chapter 3 the AGGA kernel for spin unpolarized system was derived and it shows weak $\mathbf{q}^2$ behavior [89] and here we explore the effect of this on the optical spectra.

4.2.1 Computational details:

All calculations are performed using the all-electron full-potential linearized augmented plane wave electronic structure code ELK [82] with PW91 (LDA) [19] and PBE (GGA) [34] functionals. The materials chosen for study are diamond which is small bandgap semiconductor and LiF which is large bandgap insulator. A fcc unit cell with experimental lattice spacings of 3.56 Å and 4.02 Å, respectively, is used. A dense k-point grid is required to obtain the response functions, hence the BZ is sampled on a k-point grid of $25 \times 25 \times 25$ for both. The interstitial density and potential are expanded on a **G**-point grid of size $36 \times 36 \times 36$ and the response is calculated using **G**-vectors of length 4 Bohr^{-1}. The number of conduction bands included in the response calculation are 20 for LiF and 36 for diamond. The method to obtain response functions is a two-step procedure, firstly a ground-state calculation is done to obtain the converged density and potentials. These ground state calculations give wrong band gaps due to the shortcomings of XC functionals and hence have to be corrected. Here, a scissor operator has been used to shift the band gap to the correct band-gap by 1.306 eV and 5.06 eV for diamond and LiF, respectively. Then the absorption and EELS spectra of LiF and diamond are obtained from the LDA and GGA kernels using the scissor corrected band structure.

4.2.2 Spectra:

Absorption spectroscopy is the technique which measures absorption of radiation as a function of frequency. Within LR-TDDFT this absorption spectra can be obtained from the imaginary part of the dielectric tensor. This is shown for diamond and LiF for several values of **q** using the ALDA and AGGA kernels respectively and, the results are plotted in Fig. 4.2 (a and b). As can been seen from the figure that the AGGA kernel does not improve upon the absorption spectra for diamond obtained using ALDA. The situation is different for LiF, where the AGGA kernel reduces the spectral weight of the first peak seen around 15 eV as compared with the ALDA kernel, but has negligible effect for **q**'s outside the zone boundary.

Another technique is the Electron Energy Loss Spectroscopy (EELS), where a beam of electrons with a known, narrow range of kinetic energies are incident on a material. These electrons will undergo inelastic scattering processes, implying loss of their energy and deflection of their path of motion. The amount of energy loss can be measured and the processes which lead to the energy loss can be studied such as phonon excitations, inter- and intra- band transitions, plasmon excitations, etc. This energy loss spectrum can be roughly divided into two regions: the low-loss spectrum which contains the zero-energy peak and the plasmon peaks and the high-loss spectrum which contains the inner-shell ionization edges. The presence of bound exciton appears as a peak in the bandgap of the material in the low loss part of the spectrum. A shift in the spectral weight towards lower energies is observed for an unbound exciton. The **q**-resolved EELS can be studied from the dielectric response obtained by LR-TDDFT formalism.

The EELS for (i) LiF, which is a large bandgap material with a bound exciton, and (ii) diamond which is a medium bandgap material with excitonic effects appearing as a shift

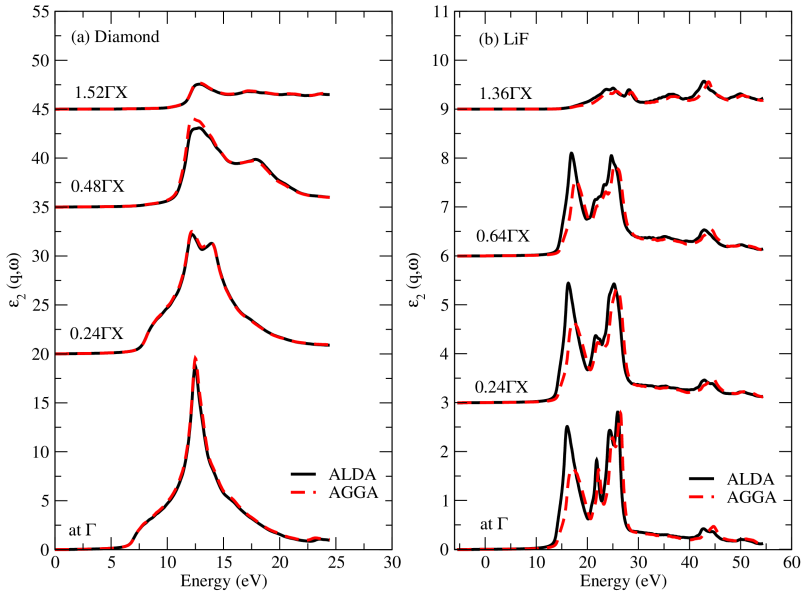

Figure 4.2: The absorption spectra given by imaginary part of the dielectric tensor as a function of photon energy for (a) Diamond and (b) LiF, using the AGGA kernel (red dashed) and the ALDA kernel (black line). The **q**-values used in calculations for LiF are 0.24ΓX, 0.48ΓX, and 1.52ΓX while for diamond they are 0.24ΓX, 0.64ΓX and 1.36ΓX as **q** must be commensurate with **k**-grid ($25 \times 25 \times 25$).

in the spectral weight towards lower energies is plotted in Fig. 4.3. For LiF, the AGGA shifts the spectra towards lower energies for $\mathbf{q} = 0.24\ \mathbf{X}, 0.48\ \mathbf{X}$ and makes the peaks more pronounced, as compared to ALDA (Fig. 4.3(a)). Although, the shifting of the spectra is towards the correct experimental values, both ALDA and AGGA fail to capture the excitonic peak at 13 eV as neither kernel has the correct **q**-dependence. Outside the first BZ ($\mathbf{q} = 1.52\ \mathbf{X}$), ALDA and AGGA exhibit similar behavior; for diamond, neither AGGA nor ALDA captures the shift in spectral weight as can be seen in Fig. 4.3(b). In fact there is little difference between the results obtained using the two approximations.

Hence, the **q**-dependence of the AGGA kernel slightly improves upon the ALDA results, although neither captures the excitonic effects.

4.3 Magnetic response

4.3.1 Background

In 1960s inelastic neutron scattering was used to study magnetic excitations of ferromagnetic 3d transition metals and their alloys. Nickel was one of the first elements to be studied in the low-energy region. In the 1980s Mook et. al [55] performed precise experiments with special emphasis on the high-energy region up to 240 meV energies. They measured the spin-wave dispersion at several temperatures ranging from 4.2 K till $2T_c$ where T_c=631 K. It was found that spin-wave dispersion is isotropic in **q** upto 100 meV and then the intensities dropped by

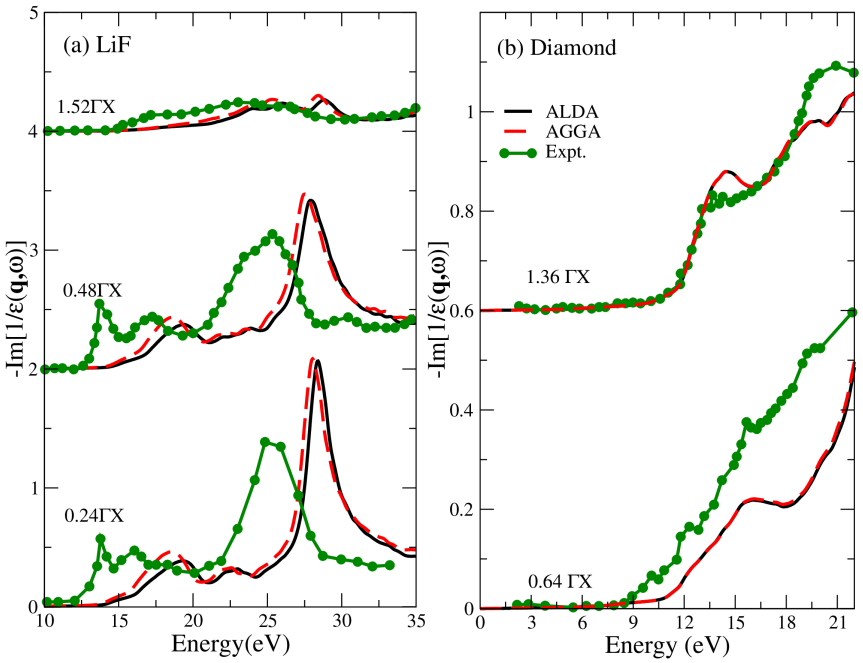

Figure 4.3: Electron energy loss spectra given by imaginary part of the inverse dielectric tensor for different experimental values of **q** (indicated in the figure) as a function of photon energy for (a) LiF and (b) Diamond, using the AGGA kernel (red dashed), the ALDA kernel (black line) and the experimental data [90] (green dots). The **q**-values used in calculations for LiF are 0.24ΓX, 0.48ΓX, and 1.52ΓX while for diamond they are 0.64ΓX and 1.36ΓX as **q** must be commensurate with **k**-grid ($25 \times 25 \times 25$).

an order of magnitude. Further along the [111] direction the reduction in spin-wave intensity was more pronounced when compared to other directions. These high energy excitations were strongly damped at some wave vector close to the zone boundary of the first BZ. The reason was attributed to their interaction with the Stoner continuum. Another interesting feature was detection of an optical branch in nickel inspite of it having a single atom in its unit cell. It was observed along [100] direction around 125 meV. As the inelastic neutron scattering does not scan the whole BZ, SPEELS was used in 1989 by Abraham and Hopster [91]. They did long wave vector studies but could capture only the stoner excitations inspite having a resolution of 17 meV. Later Hong and Mills [92] explained why the spin-waves were not observed with SPEELS; they showed that the spin waves can only be observed by SPEELS when the exchange splitting of 3d bands is large in comparison with the spin-wave energies. In Fe and Co the spin-waves up to the BZ boundary were indeed observed by SPEELS as they have substantially larger value of exchange-splittings than nickel.

Theoretically, Lowde and Windsor [93] made the first attempt to study these magnetic excitations. They examined the magnetic susceptibility using the random phase approximation for spin-split bands. But, the agreement with the experimental data was poor. Then in 1973 Cooke [94] used the tight-binding model with two adjustable parameters one for the electronic energy bands and the other for the on-site Coulombic interaction between the *d* electrons. It was not an *ab-initio* study as the parameters were chosen to produce the

correct experimentally observed magnetic moment as well as the correct t_{2g} and e_g character of the bands. As a result, these calculations yielded the correct dispersion relation of nickel including the optical branch along [100] direction. Further it also correctly described the damping of the spin-waves in the presence of the stoner modes. A similar approach of scaling the Coulomb interaction being form-invariant under spin rotations was adopted by Hong and Mills in 2000 [92]. However, they failed to find the optical-mode in nickel. In 1998, Savrasov [76] used the spin-polarized version of *ab-initio* DFT for ground state and TDDFT for transverse spin susceptibility calculations. He attributed the discrepancies in his observations to the lack of approximations which encapsulate the dynamical exchange and correlation. In 2000, Karlsson and Aryasetiawan [74] used Many-Body Perturbation theory (MBPT) to calculate spin-waves in ferromagnetic transition metals. They obtained two branches in nickel dispersion relation along [100] with an optical branch at higher energies. Also a good agreement between theory and experiment was found when the exchange splitting of 3d bands was manually reduced to half. Additionally they observed an optical branch along [111] direction. In 2010, Şaşıoğlu et. al [95] again used the MBPT formalism to obtain the excitation energies by approximating the dynamic correlations between the electrons and holes as a summation over ladder diagrams. They found that LSDA overestimates the exchange-splitting of nickel by a factor of 2 and hence overestimates the magnon energies. The spin waves also have dimensionality effects as was seen by Buczek et. al [71] using the Korringa-Kohn-Rostoker Green's function method which again utilized the ALSDA kernel within the TDDFT formalism. The dispersion relations obtained in all these TDDFT calculations used the ALSDA kernel. Here we use the AGGA kernel derived in Chapter 3.

4.3.2 Convergence Parameters:

To speed-up practical calculations of the magnetic excitation energies, various numerical parameters can be optimized. However, the response function, as given by Eq. (2.88), should be independent of the choice of these parameters and hence their convergence must be tested. Moreover the convergence of these parameters depend on the choice of XC functional used for calculations. As the GGA functional involves gradient of density, which are numerically delicate, extra care has to be taken while performing convergence tests.

The most important parameters which affect the excitations are the number of unoccupied bands, the number of **G**-vectors, the length of $|\mathbf{G}+\mathbf{k}|$-vectors, and the **k**-point grid used for sampling the BZ. Further, these parameters are material dependent and the convergence tests must be performed for each of them. This process will be illustrated now for nickel:

Unoccupied bands:

The summation over states in Eq. (2.88), may be cut-off for faster convergence and is controlled by the parameter `emaxrf` such that $|\epsilon_{nk} - \epsilon_{Fermi}| <$ `emaxrf`. In other words, the value of energy set by this parameter decides the number of conduction bands included in the calculation. Hence, the spectra was calculated using the ALSDA kernel for various

values of `emaxrf` see Fig. 4.4. It was found that for `emaxrf` $\geq$ 1.1 a.u., we get converged (overlapping) response functions and hence 1.2 a.u. was chosen for calculating the magnetic response function. This resulted in inclusion of all bands 1.2 a.u. above the Fermi energy.

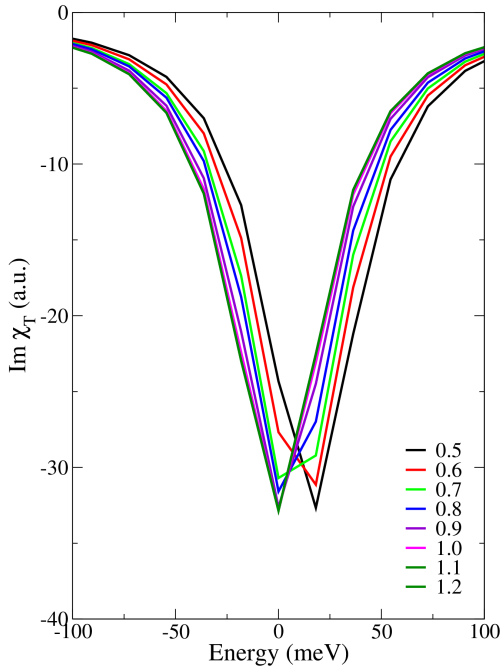

Figure 4.4: The Imaginary part of the response for nickel with different values of the `emaxrf` parameter.

Number of G-vectors for response function:
LDA:
The matrix size of the response depends on the number of **G**-vectors as was seen in Eq. (2.88). This matrix size is controlled by the parameter `gmaxrf` which determines the maximum length of **G**-vectors used in calculation. Keeping the `emaxrf` value fixed to 1.2 a.u., `gmaxrf` value was changed from 4 a.u. to 7 a.u. along with the kmesh used for BZ sampling (Fig. 4.5). It was found that with `gmaxrf` $>$ 6 a.u. the response remains unchanged. This corresponds to a matrix size of 283 $\times$ 283 in **G**-space.

GGA:
The convergence of `gmaxrf` was checked with three different values of k-point mesh. As can be seen from Fig. 4.6 that for values of 6 a.u. and 7 a.u. it gives overlapping results. Hence the value 6 a.u. was taken for all the GGA functional calculations. Also this variation was checked with respect to the BZ sampling and the mesh greater than 20 $\times$ 20 $\times$ 20 gave the same result. Hence a 20 $\times$ 20 $\times$ 20 k-point mesh was used along with `emaxrf`=1.1 a.u. and `gmaxrf`=6 a.u.

The GGA functional involves gradient of density along with density and the presence of gra-

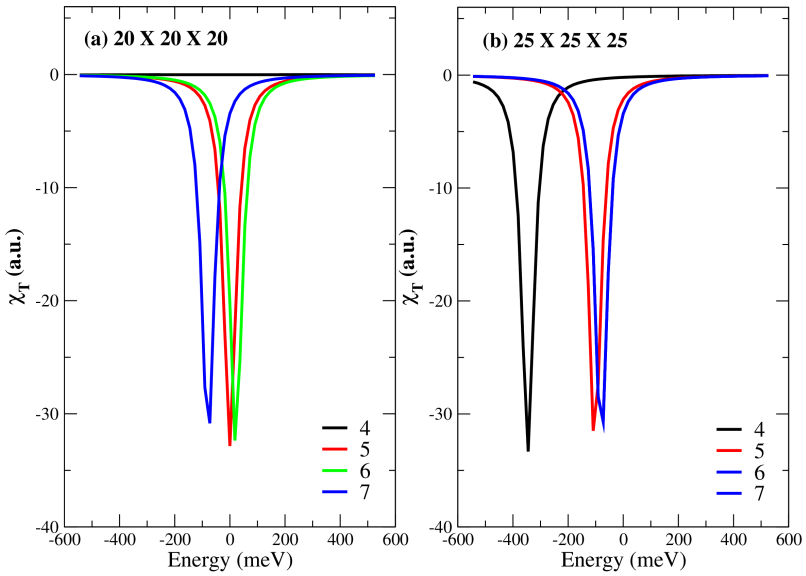

Figure 4.5: The imaginary part of transverse response for nickel with different values of the `gmaxrf` parameter keeping `emaxrf` fixed to 1.2 a.u. and their convergence with respect to the (a) $20 \times 20 \times 20$ kpoints mesh and (b) $25 \times 25 \times 25$ kpoints mesh for LDA functional.

dients makes the computations difficult. To obtain smooth variation of the gradients ground state should be well converged, hence convergence is to be performed regarding the length of **G**-vectors required for the expansion of density and potentials in the interstitial region, product of muffin-tin radius (R^{MT}) and length of $|\mathbf{G}+\mathbf{k}|$-vectors needed to solve the KS functions. Therefore to obtain a well converged ground state by using the GGA functionals the following parameters have to be tested for convergence:

Number of G-vectors for ground state:
The parameter used for expanding the density and potentials in the interstitial region is `gmaxvr`. Our test showed that 20 **G**-vectors were needed for convergence (see Fig. 4.7).

$R^{MT} \times |\mathbf{G}+\mathbf{k}|$ vectors:
This product decides the maximum length of $|\mathbf{G}+\mathbf{k}|$ vectors required for minimum muffin radius (if more than one species) to expand the KS functions. This product is controlled by the parameter `rgkmax`. Hence, it's value was varied keeping all the above parameters fixed and the results are shown in Fig. 4.8. The value 8 was chosen as the results overlapped with 9 and it also gave minimum Goldstone error; the error which arises due to numerical computations and gives a finite excitation energy for $\mathbf{q} = 0$. This violates the Goldstone theorem which says $w = 0$ for $\mathbf{q} = 0$. For the numerical calculations this error is subtracted, from the entire spectrum to satisfy the Goldstone theorem.

Smearing width:

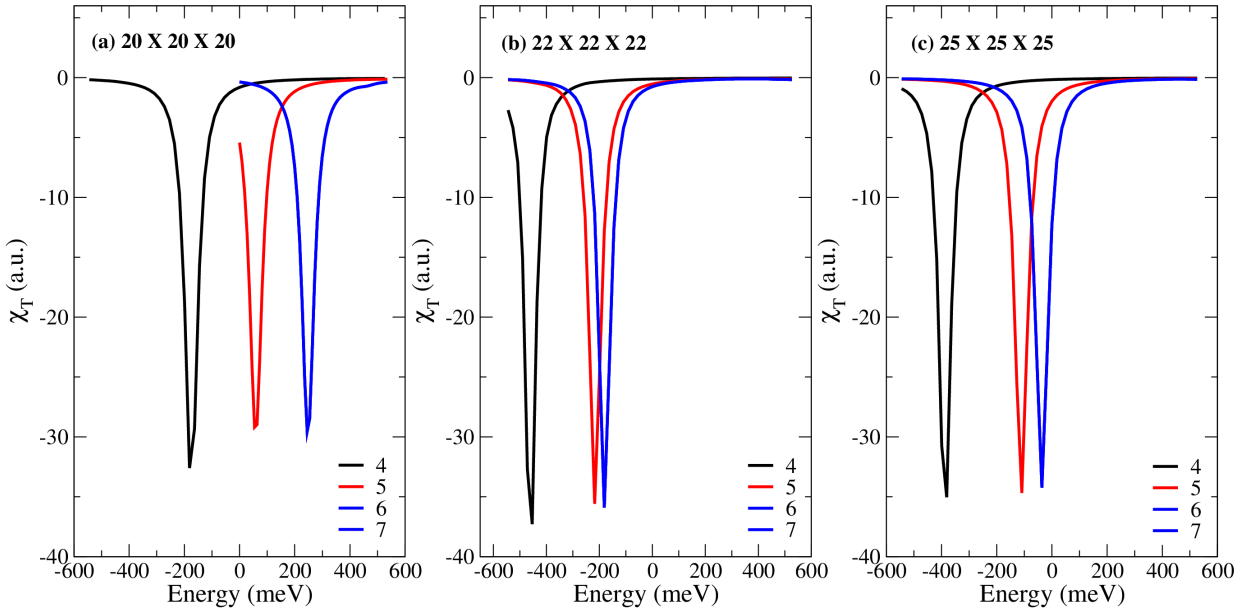

Figure 4.6: The imaginary part of transverse response for nickel with different values of the `gmaxrf` parameter keeping `emaxrf` fixed to 1.1 a.u. and their convergence with respect to the (a) $20 \times 20 \times 20$, (b) $22 \times 22 \times 22$ and (c) $25 \times 25 \times 25$ k-point grid for GGA functional.

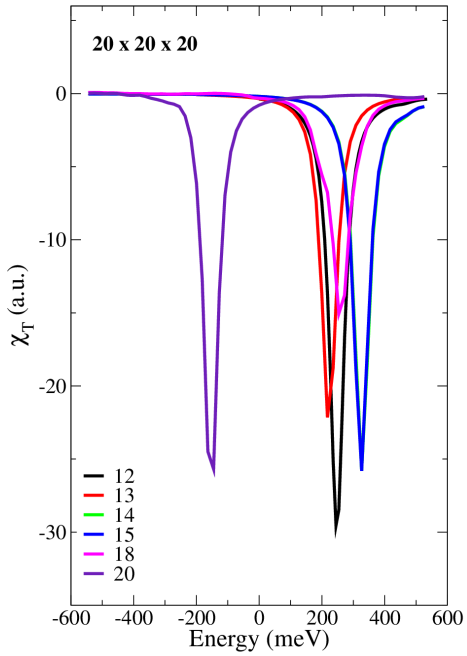

Figure 4.7: The imaginary part of transverse response for nickel with different values of the `gmaxvr` parameter keeping `emaxrf`(1.1 a.u.) and `gmaxrf` fixed(6 a.u.) k-point mesh of $20 \times 20 \times 20$.

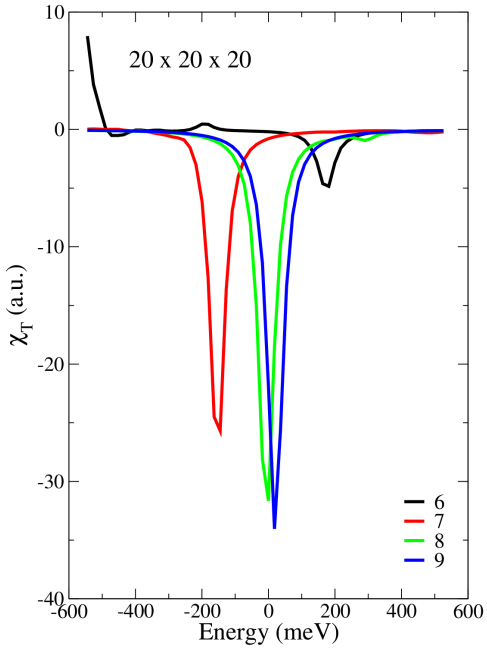

Figure 4.8: The imaginary part of transverse response for nickel with different values of the `rgkmax` parameter keeping `emaxrf`(1.1 a.u.), `gmaxrf`(6 a.u.), `gmaxvr`(20 a.u.) and fixed kpoints mesh of $20 \times 20 \times 20$.

The response function also depends on the usage of the smearing parameter as seen in Eq. (2.97). The value of this smearing parameter used in all the calculations is 0.027 eV.

4.3.3 Spectra

To find the magnon spectra, $\mathrm{Im}\{\chi^{-+}(\mathbf{q},\omega)\}$ for each $\mathbf{q}$ value is calculated, then the magnon peak position was extracted and plotted as a function of $\mathbf{q}$. This is shown in Fig. 4.9 for nickel, cobalt, and iron (at $a_0(exp.)$ from Table 4.1). For Ni, Fig. 4.9(a), both the ALSDA and the AGGA show quantitatively the same behavior from the BZ center to $|\mathbf{q}| = 0.4$. As one moves further away from the zone center along ΓX direction, the AGGA kernel tends to deviate from ALSDA until it becomes $\approx$ 80 meV higher in energy at the zone boundary. For Co, Fig. 4.9(b), the experimental results are well captured by both ALDA and AGGA calculations. For Fe, Fig. 4.9(c), in contrast to ALSDA which reproduces the experimental values, the AGGA dispersion overestimates the magnon energies. Beyond half ΓN, the transverse response function obtained using AGGA becomes too broad to assign a single energy to the excitation peaks although some features are still present, as can be seen in Fig. 4.12.

The strength and width of the peak in $\mathrm{Im}\{\chi^{-+}(\mathbf{q},\omega)\}$ is related to the scattering amplitude and lifetime of the magnon, respectively. To visualize how these properties change throughout the BZ, a 2D contour plot of $\mathrm{Im}\{\chi^{-+}(\mathbf{q},\omega)\}$ is made. These are shown for both ALSDA and AGGA in Fig. 4.10 for Ni, Co and Fe along with the experimental data. Beginning again with Ni, one can see that the peaks in $\mathrm{Im}\{\chi^{-+}(\mathbf{q},\omega)\}$ obtained by using ALSDA

Table 4.1: The experimental lattice (in Å) constants used in magnon spectra calculations. Also the experimental magnetic moments (in μ_B) are listed.

	a_0 (exp.)	$m_{exp.}$
Ni(fcc)	3.524 [96]	0.60 [97]
Co(fcc)	3.539 [98]	1.52 [99]
Fe(bcc)	2.8665 [100]	2.08 [101]

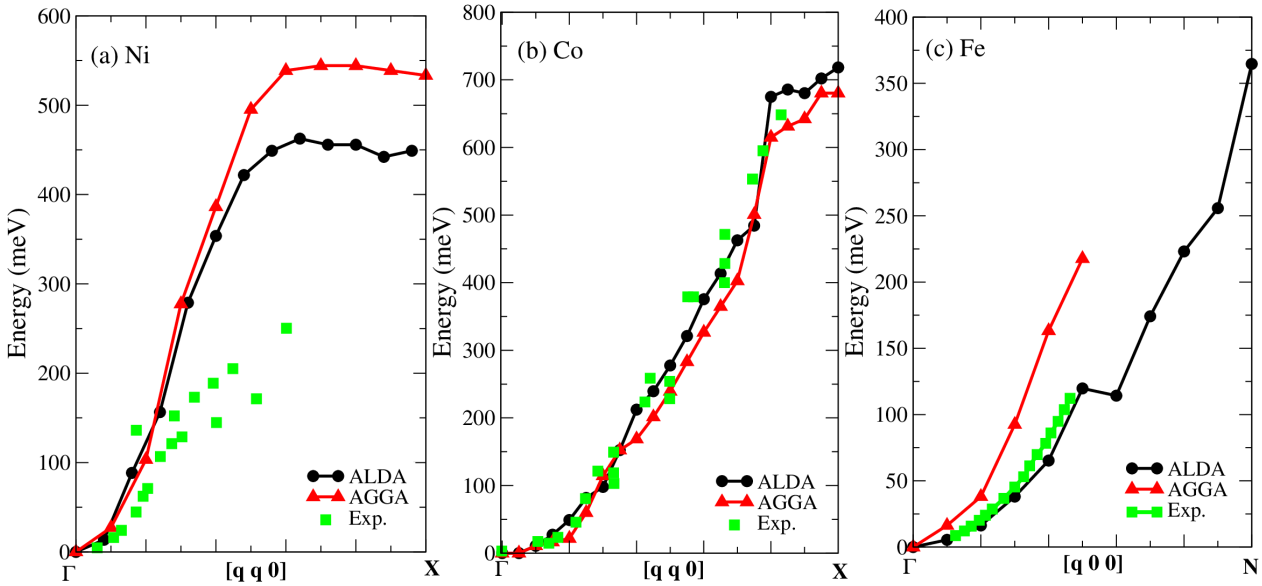

Figure 4.9: Magnon dispersion spectrum for (a) fcc nickel, (b) fcc cobalt along the ΓX direction and (c) bcc iron along the ΓN direction calculated using the ALSDA kernel (black dots) and AGGA kernel (red triangles). A comparison is made with the experimental result (green squares) taken from Mook et al. [55, 102] for nickel, Balashov et al. [103] for cobalt, and Lynn [104] for iron.

(Fig. 4.10(a)) are stronger in intensity and better resolved than AGGA (Fig. 4.10(b)). There exists a high probability of observing a magnon at the BZ boundary with ALSDA whereas it is suppressed significantly beyond $\mathbf{q} = 0.5\,\mathbf{X}$ with AGGA. A strong suppression in the magnon intensity between $|\mathbf{q}| = 0.1$ and 0.2 for both AGGA and ALSDA (see Figs. 4.10(a) and (b)) is also observed. Experimentally, Paul et. al [102] measured a disruption to the magnon dispersion at $|\mathbf{q}| = 0.2$, which they attributed to a split into optical and acoustic branches. While neither ALSDA nor AGGA shows two branches, both correctly predict an abrupt change in the magnon dispersion around this value of $\mathbf{q}$. This is due to the Stoner spin-flip transitions (Eq. 2.97) having energy comparable to the magnon energy causing strong interference and intensity suppression [107] at these values of $\mathbf{q}$ (see Fig. 4.11 (a) and (b)).

In contrast to Ni, the experimental dispersion for fcc Co, obtained by Balashov et al. [103], along [100] does not show any optical branches. Both ALSDA and AGGA behave the same and show good agreement with experiment, with AGGA being slightly lower in energy.

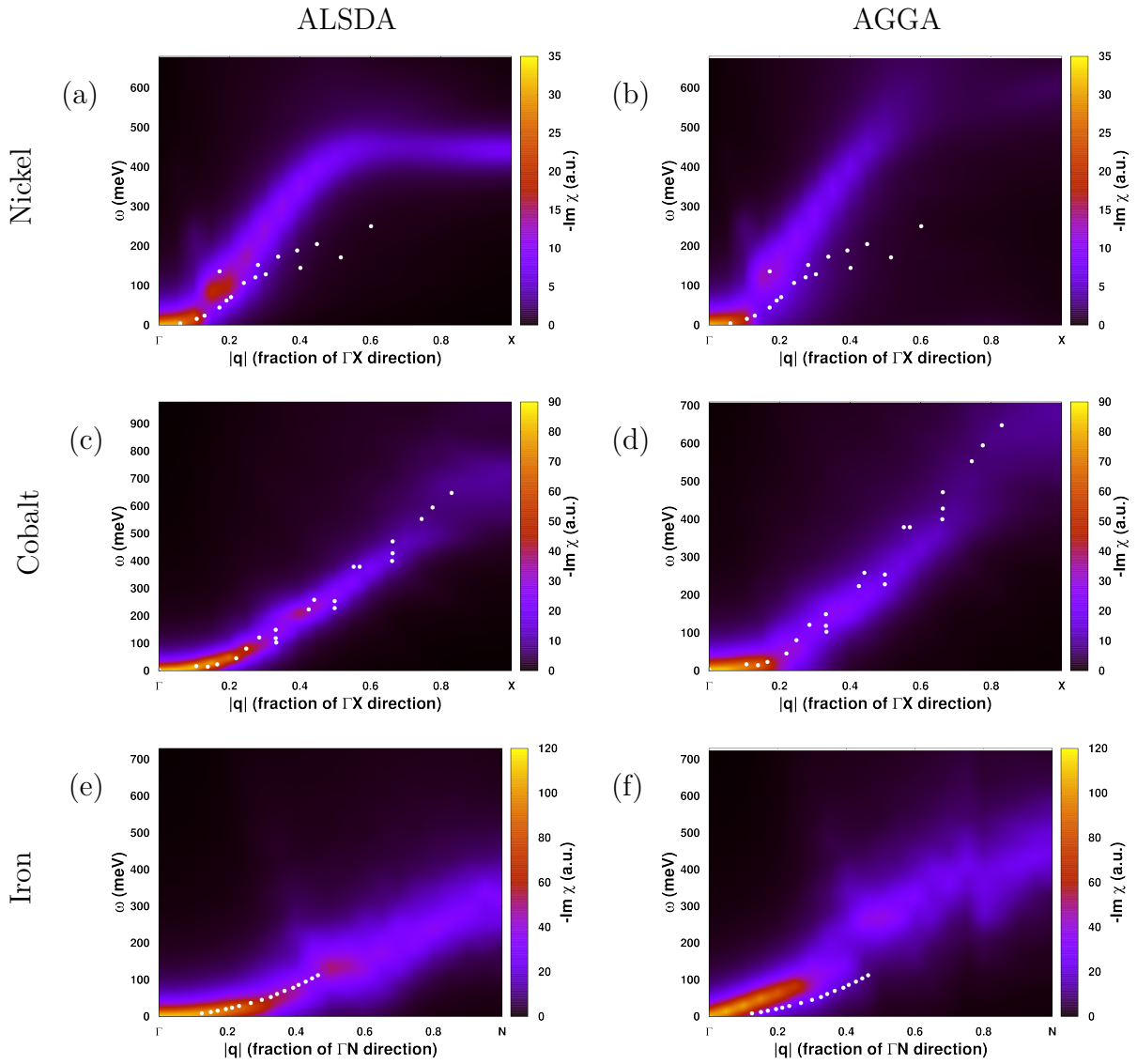

Figure 4.10: The imaginary part of the interacting response of nickel, cobalt, and iron using the ALSDA kernel (a,c,e) and the AGGA kernel (b,d,f), and the experimental results [102, 103, 104] (white dots).

Observing the full transverse response function over the whole BZ (Figs. 4.10(c) and (d)) one can see a reduction in the peak strength and suppression of the magnons by AGGA as compared to ALSDA. Qualitatively, AGGA also reproduces the jump in magnon energy witnessed in experiments around $|\mathbf{q}| = 0.6$, although at a higher $|\mathbf{q}|$ value of 0.8. Also the Stoner spin-flip transitions for Co are relatively high in energy (see Fig. 4.11 (c) and (d)) as compared to Ni and hence there is no reduction in intensity.

For Fe, significant broadening in the AGGA transverse response for $|\mathbf{q}| > 0.5$ (Fig. 4.10 (f) and 4.12 (b)) is seen. This broadening is to such an extent that it becomes impossible to assign a single peak position. We note that in Ref. [74] a jump to a higher branch occurs in this region. Experimental data reported in Ref. [108] sees magnon excitations in this

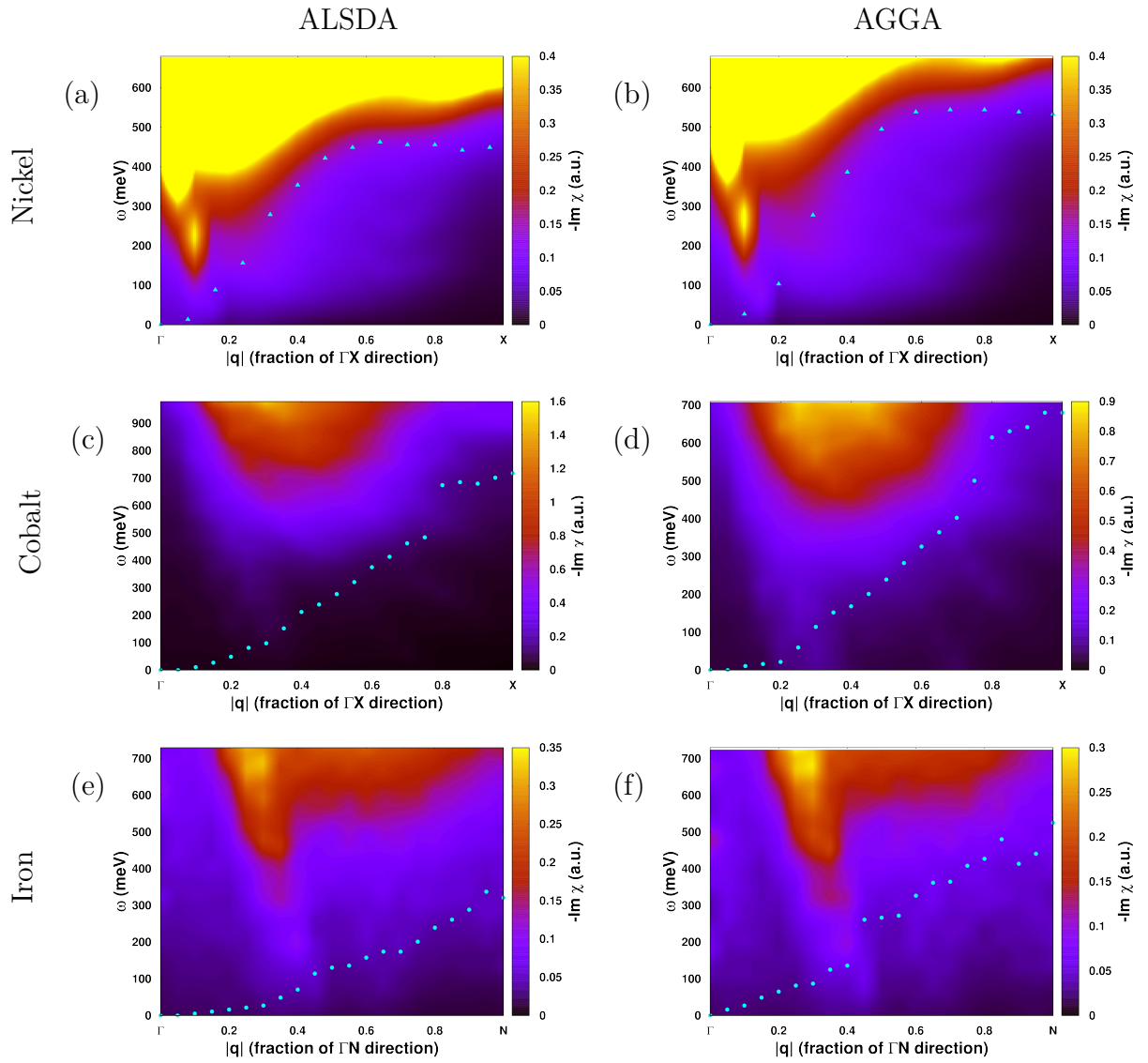

Figure 4.11: Imaginary part of the non-interacting response function for nickel, cobalt and Iron using the ALSDA kernel (a,c,e) and the AGGA kernel (b,d,f), and also the corresponding theoretical magnon spectra for comparison (cyan triangles).

region, although with a large full width at half maximum indicating strong suppression. This suppression can also be seen in these results due to interaction with the Stoner continuum (Fig. 4.11 (e) and (f)).

A comparison is done of the magnon spectra obtained here with the past ALSDA results obtained within TDDFT or MBPT approach [71, 95, 75, 57, 74, 75, 76] and the experimental data. This is shown in Fig. 4.13 and from these two important facts can be inferred; the ALSDA results are consistent with previously reported data, and most importantly the AGGA kernel does not offer any improvement over ALSDA spin excitation spectra.

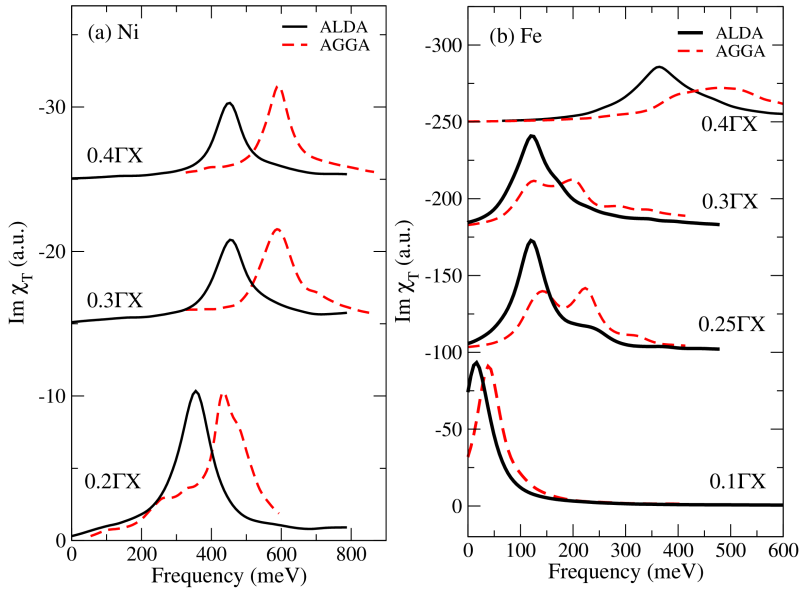

Figure 4.12: The transverse response at certain **q**-values for (a) nickel and (b) iron using ALSDA (black lines) and AGGA (red dashed) kernels.

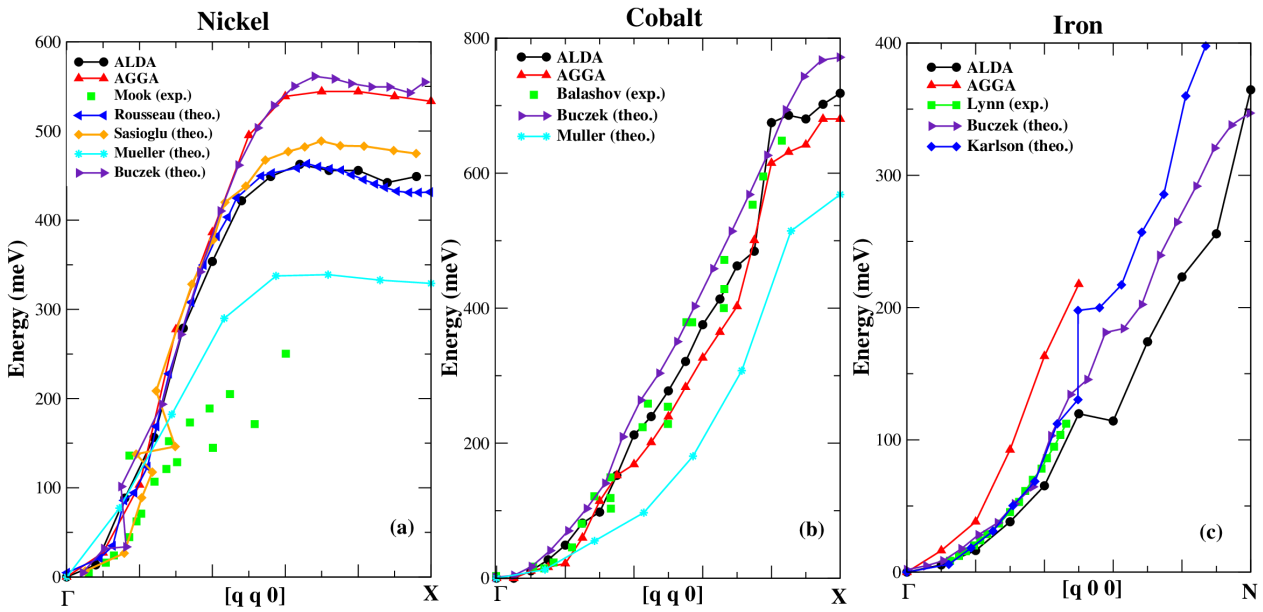

Figure 4.13: Magnon dispersion spectrum for (a) fcc nickel, (b) fcc cobalt along the ΓX direction and (c) bcc iron along the ΓN direction calculated using the ALSDA kernel (black dots) and AGGA kernel (red triangles). A comparison is made with reported theoretical work [71, 72, 95, 74, 105, 106] and also the experimental result (green squares) taken from Mook et al. [55, 102] for nickel, Balashov et al. [103] for cobalt, and Lynn [104] for iron. For Ref. [[75]], the ALSDA corrected values have been taken.

Effect of equilibrium lattice constant:

An *ab-initio* computational method, given the atomic composition, should be able to predict the equilibrium geometry. After finding the minimum energy crystal structure from ground-state calculations, one can then calculate the excited state properties, all without reference to experimental data. Only those methods which follow this prescription can be considered fully predictive. Hence, we will study if the magnon dispersion changes if the equilibrium lattice constant values are used. These are obtained by using the Birch-Murnaghan 3^{rd}-order equation of state (EOS). The energy vs volume curves for all the three elements with different volume are plotted in Fig. 4.14. These are then fitted to the EOS expression to find the lattice constants corresponding to both the LDA and GGA functionals.

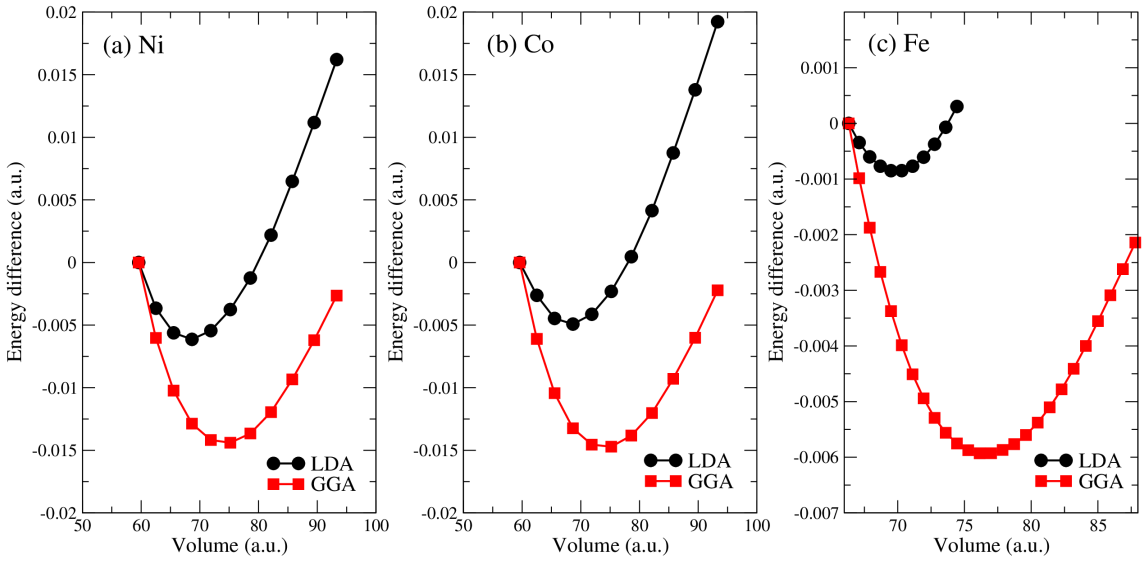

Figure 4.14: The equilibrium lattice constant obtained by solving the Birch-Murnaghan 3rd order equation of state for (a) nickel, (b) cobalt and (c) iron using the LDA and GGA functionals.

The ground-state DFT calculations with experimental and optimized lattice parameters are summarized in Table 4.2. From this one can conclude that (i) GGA is very good in reproducing the structures of materials whereas (ii) LDA is better in predicting the magnetic moments.

Next the predictive power of LDA and GGA is tested by comparing the magnon energies for Ni, Co, and Fe at the experimental and optimized lattice parameters (see Fig. 4.15). From the figure it can inferred that the AGGA magnon spectra are more sensitive to the lattice parameters than the ALSDA. In most cases, the AGGA results at the corresponding GGA parameter $(a_0)_{theo}$ are lower in energy than at $(a_0)_{exp}$, although still overestimated w.r.t. experiment.

Table 4.2: Equilibrium lattice parameters, a_0 Å(LDA or GGA), calculated using the 3^{rd} order Birch-Murnaghan equation of state and the experimental lattice constants. The experimental magnetic moments, $m_{exp.}$ (in μ_B), compared with the magnetic moments obtained at the equilibrium lattice parameters.

	a_0 (exp.)	a_0 (LDA)	a_0 (GGA)	$m_{exp.}$	m_{LDA}	m_{GGA}
Ni(fcc)	3.524 [96]	3.436	3.527	0.60 [97]	0.591	0.636
Co(fcc)	3.539 [98]	3.429	3.525	1.52 [99]	1.525	1.641
Fe(bcc)	2.8665 [100]	2.743	2.836	2.08 [101]	1.996	2.174

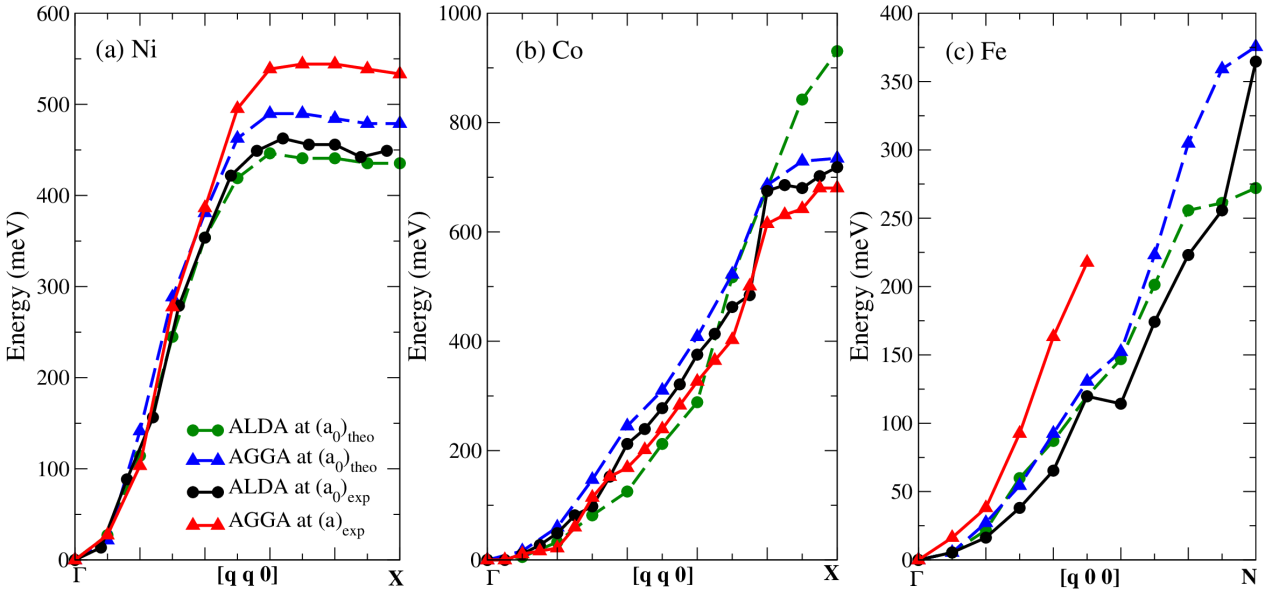

Figure 4.15: The magnon spectrum with the theoretical and experimental lattice parameters for (a) fcc nickel, (b) fcc cobalt along the ΓX direction and (c) bcc iron along the ΓN direction calculated using the ALSDA kernel (dots) and AGGA kernel (triangles). The lattice parameters are given in Table 4.2.

Heuslers:

Next, Heusler and half-Heusler compounds Co_2MnSi and NiMnSb are studied which, due to their geometry of interlocking magnetic fcc lattices, can (in principle) have multiple magnon branches [109, 111]. The experimental lattice constant used for Co_2MnSi is 5.640 [112] Å and for NiMnSb [113] is 5.897 Å. In Fig. 4.16, the AGGA magnon spectra of Co_2MnSi and NiMnSb are plotted along with the experimental and ALSDA results (as reported by Buczek et. al)

For Co_2MnSi (see Fig. 4.16(a)) both, an acoustic branch and an optical branch are observed. An increase in the energies of acoustic branch is noted when compared with earlier ALSDA results [109], based on loss function. However, energies of the optical branch with AGGA are within the same range as reported by Buczek[109] using ALSDA.

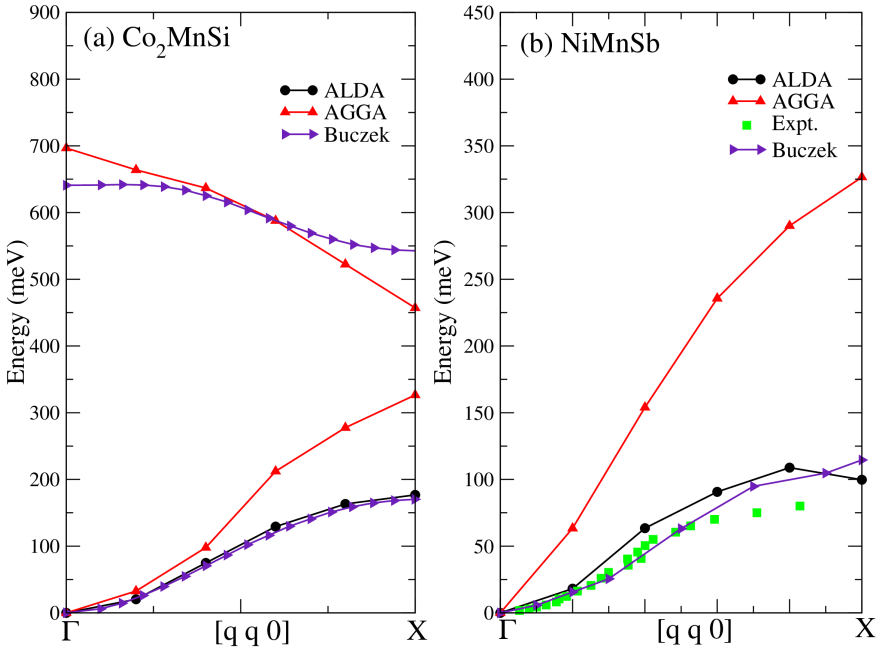

Figure 4.16: (a) The magnon spectra of Co_2MnSi using the ALSDA (black dots) and AGGA (red triangles) kernels and compared with Buczek calculations [109] with the ALSDA kernel (violet triangle left). (b) The magnon spectra of NiMnSb using ALSDA and AGGA kernel and the experimental results [110] (green squares).

For NiMnSb (Fig. 4.16(b)), both ALSDA and AGGA predict only an acoustic branch, as is also the case experimentally. This is likely due to Ni not possessing a strong local moment as most of the total moment is localized on the Mn atoms. In this case AGGA severely overestimates the magnon energies.

4.4 Exchange-Splitting

The underlying explanation as to why AGGA tends to overestimate the magnon energies is explored. The role of the XC kernel is to transform the excitation structure of $\mathrm{Im}\{\chi_0^{-+}\}$ into the true response. From the Stoner single-particle excitations, contained in $\mathrm{Im}\{\chi_0^{-+}\}$, it must create the magnon peak.

At $\mathbf{q} = 0$, the gap (U) in $\mathrm{Im}\{\chi_0^{-+}\}$ (see Fig. 2.9) is related to the exchange splitting between spin-up and spin-down states. This splitting dictates the position of the Stoner continuum across the BZ. In Figs. 4.11(a) and (b), the $\mathrm{Im}\{\chi_0^{-+}\}$ for LDA and GGA is plotted, and it can be seen that the this gap increases by approximately 60 meV for nickel. This increment stems from the fact that GGA increases the exchange splitting in Ni by 59.9 meV compared to LDA as can also be seen in the density of states shown in Fig. 4.17 (a), leading to the shift in Stoner continuum towards higher energies. At $\mathbf{q} = 0$, the symmetries of the response equation will enforce Goldstone's theorem, however the increase in the exchange

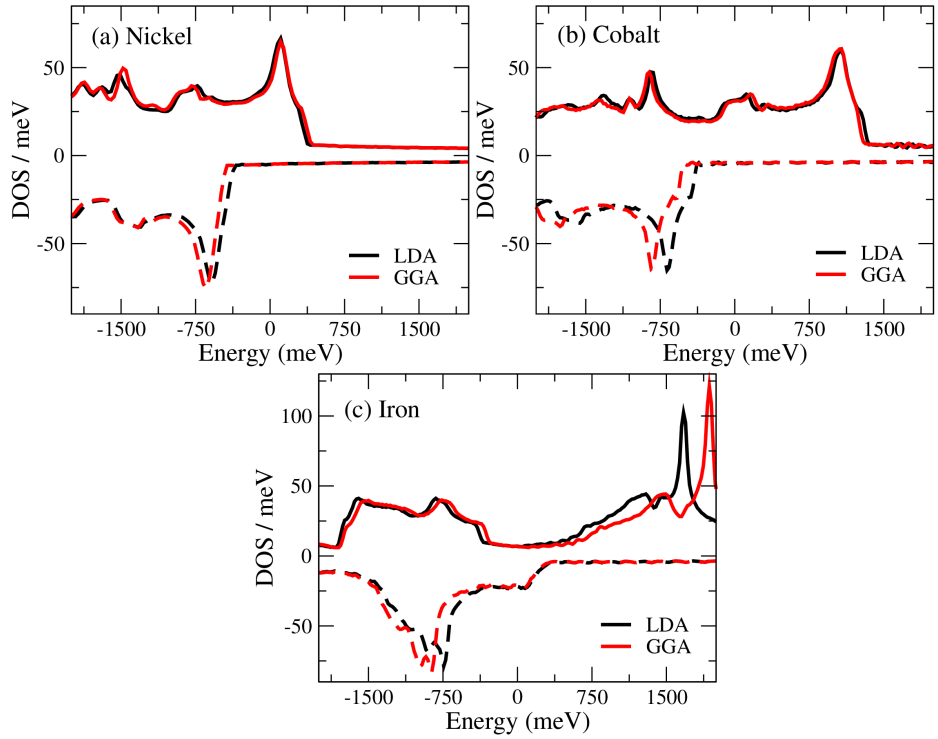

Figure 4.17: The density of states using LDA (black solid line) and GGA (red dashed line) functional for (a) nickel, (b) cobalt and (c) iron.

splitting will cause the magnon energies also to increase as we move across the zone. This can be seen in Fig. 4.11 where both ALSDA and AGGA have a similar behavior relative to the background Stoner excitations. Similar behavior was also observed for other materials, e.g for Fe there is $\approx$ 150 meV increase (see Fig. 4.17 (c)), and even a 50% increase of the LDA Stoner gap in χ_0^{-+} for the half-metal NiMnSb. The connection between the exchange splitting and the magnon energies was previously reported in Ref. [74] where the LDA value was artificially reduced leading to lower magnon energies. Given that LDA is well-known to overestimate the exchange splitting, a further enhancement on going from LDA to GGA leads to large overestimation of the magnon energies. To establish this fact the exchange splitting for nickel was reduced from 680 meV to 355 meV by hand in both LDA and GGA calculations of the response and the magnon spectra. This is shown in Fig. 4.18. As can be seen the exchange splitting effects the spectrum at higher $\mathbf{q}$-values, give reasonable values as compared to experiment and the lower $\mathbf{q}$-values are unaffected. Further changing the exchange splitting by hand does not lead to good ground-state hence the shape of the curves is not well defined.

To summarize this chapter, the AGGA kernel was derived for unpolarized systems was applied to study the absorption spectra and EELS of diamond and LiF. The results obtained did not improve upon the results obtained by using ALDA kernel. The situation became worse when AGGA kernel was applied to study magnon dispersion relation. Here, the magnon energies predicted by AGGA kernel were worse than the ALSDA kernel. This reason

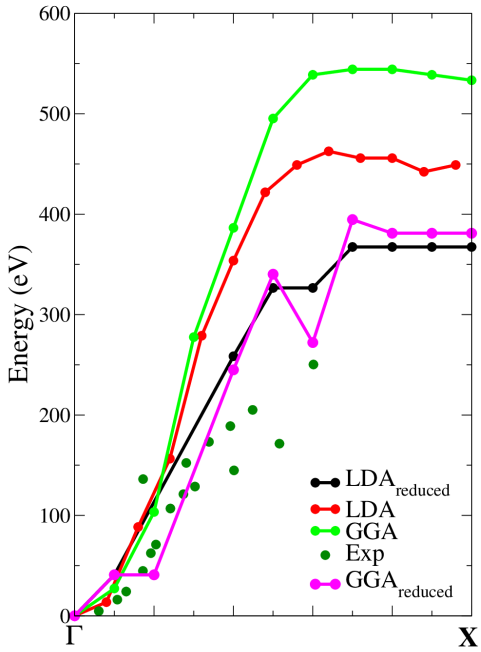

Figure 4.18: The magnon spectra of nickel with exchange splitting reduced ($LDA_{reduced}$ and $GGA_{reduced}$) along with the LDA, GGA and experimental results.

for these results was due to high exchange splitting value obtained with GGA functional. Unlike many properties, climbing up the *Jacob's ladder* for XC kernel did not lead to better accuracy in magnon calculations.

CHAPTER 5

REAL-TIME MAGNON DYNAMICS

Today's oscillations are for a stable tomorrow.
- Unknown

In chapters 3 and 4, TDDFT was used in the linear response regime to extract excitation energies and associated properties in frequency space. However, to study the response of a system to strong external fields, linear response is inappropriate and one requires the explicit time evolution of occupied KS orbitals, as is done in RT-TDDFT. Note that for small fields, the density obtained with RT-TDDFT is the same (to first order) as that obtained from LR-TDDFT. Hence in this limit the spectrum obtained from both these methods must agree. The RT-TDDFT method yields a full time-resolved, potentially non-linear, solution which can be used to compute not only spectroscopic properties (e.g. absorption, polarizabilities, etc.) but also the time and space resolved electronic response to arbitrary stimuli (e.g. laser excitation of charge dynamics). RT-TDDFT is one of the few *ab-initio* yet computationally affordable ways to study electron dynamics and laser-matter interaction.

In this chapter the RT-TDDFT method is employed to study magnons in real-time and real-space. It is a powerful tool to study magnon dynamics as atoms can be observed and analyzed individually and element specific dynamics of moments can be discovered. Furthermore, the behavior of several $\mathbf{q}$-vectors magnon modes can be studied together, as for practical calculations a supercell is constructed. The dimensions of this supercell determine the $\mathbf{q}$- vectors under study. However, this does require significant computational resources, which limits the supercell size, and hence the number of magnon modes that can be studied. Bound by this restriction we study the high energy, or high $\mathbf{q}$, modes, although it should be noted that these are often difficult to study experimentally, due to their shorter life times. After constructing the supercell, the KS orbitals are propagated using Eq. (2.104) and the transverse moments of each atom are plotted as a function of time.

To demonstrate RT-TDDFT as a tool to study magnon dynamics, we first benchmark the frequency of various magnon modes against linear response calculations. Then we show how several modes may be studied simultaneously by preparing initial states in superpositions of many modes. Lastly a system with two magnetic sublatticies is studied, namely $Fe_{50}Ni_{50}$ alloy, and test whether there exist coupled and un-coupled dynamics of the Ni and Fe transverse magnetic moments.

5.1 Iron

In the previous chapter LR-TDDFT was utilized to obtain the magnon energies along the ΓN direction for bcc Fe. Here we will study fcc Fe, with the unit cell extended along the c axis to obtain a supercell consisting of four atoms. We change to a fcc lattice for Fe as it will be useful for understanding the behavior of iron atomic moments in the $Fe_{50}Ni_{50}$ alloy studied later. The number of modes which can be investigated is equivalent to the number of atoms in the supercell, this is known from normal mode analysis of the Heisenberg Hamiltonian. Therefore, as there are four atoms one would expect to observe four modes (each mode must have a $\mathbf{q}$ vector commensurate with the supercell size). These are shown in Fig. (5.1).

To obtain these modes by TDDFT simulations a two step procedure is followed. Firstly a ground state calculation is done to obtain the converged densities and potentials. Then small perturbations are done via a single additional ground state iteration, now including small magnetic fields along x and y directions. This initial state is then propagated in time. From this we obtain the time varying magnetization density and time-varying atomic moments, defined in Eq. (2.32) and Eq. (2.110) respectively. These applied magnetic fields mimic the effect of an external perturbation that excites the magnon modes. The Fourier transform of the oscillations in $m_x(t)$ and $m_y(t)$ will result in a power spectrum (Section 2.7) having a peaked structure with the peak position corresponding to the magnon frequency.

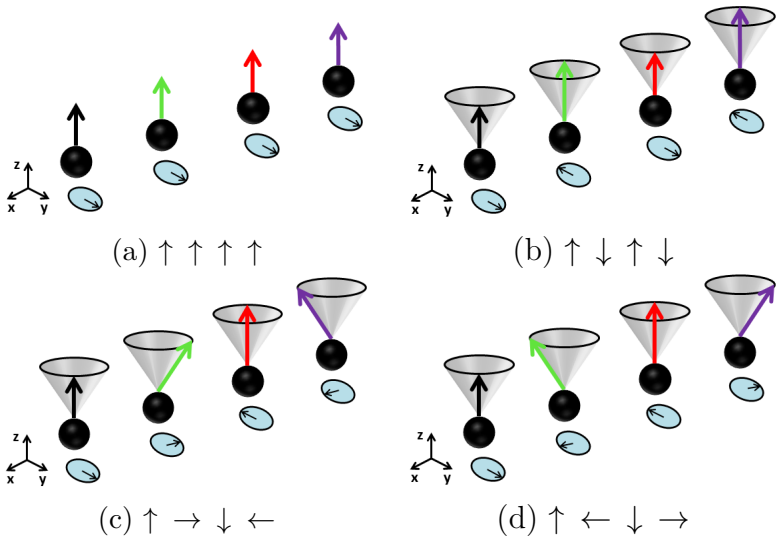

Figure 5.1: The four modes (along with their projections in xy plane) which exist in a four atom supercell of iron. (a) Goldstone mode, (b) Optical mode, (c) $+\mathbf{Q} = \Gamma X/2$, and (d) $-\mathbf{Q} = -\Gamma X/2$

.

Computational details: The KS orbitals are time-propagated with a time-step of 1.209 attoseconds unless explicitly stated. A $8\times8\times8$ k-point grid is used and the ALDA functional is used to approximate the XC potential. The lattice constants used for constructing the supercell are a= 7.2902 a.u. (3.85Å) and c= 14.57 a.u. (15.423Å). The length of $\mathbf{G}+\mathbf{k}$ vectors is set to 2.917 a.u. and the length of $\mathbf{G}$-vectors used for expanding the interstitial

density and potentials is 12 a.u. A typical 4-atom supercell simulation requires 16000 CPU hours to obtain magnetization oscillations up to 48.2 femtoseconds.

The arrangement of spin for all the four modes after the initial perturbation can be represented in the xy plane using $\uparrow$, $\rightarrow$ for $+y$, $+x$ and $\downarrow$, $\leftarrow$ for $-y$, $-x$ directions respectively. As the time evolves these spins will precess in the counterclockwise direction (note that in these simulations the z-moment points in the negative z-direction). We will now tailor the initial state to excite each mode individually:

- Goldstone mode: $\uparrow\ \uparrow\ \uparrow\ \uparrow$

  The initial state required to excite the Goldstone mode is all spins pointing in same direction. This is created by perturbing each atom with the same magnetic field. Propagating in time, we do not see any precession of the spins (Fig. 5.2(a)) as these are excitations of zero energy. This can also be seen from the Fourier transform of y-moments in the Fig. 5.2(b). The y moments of all the atoms stay fixed to its initial value ($0.044\mu_B$) which is the moment induced by the applied magnetic field. As discussed in chapter 4, the Goldstone mode is simply a tilting of the ground-state magnetization along a new direction, this therefore costs no energy when the system has magnetic isotropy. Note, for systems with magnetic anisotropy, where the spins align in a preferential direction, this mode will no longer be a zero energy mode, as tilting of spins off the easy axis will cost a small amount of energy.

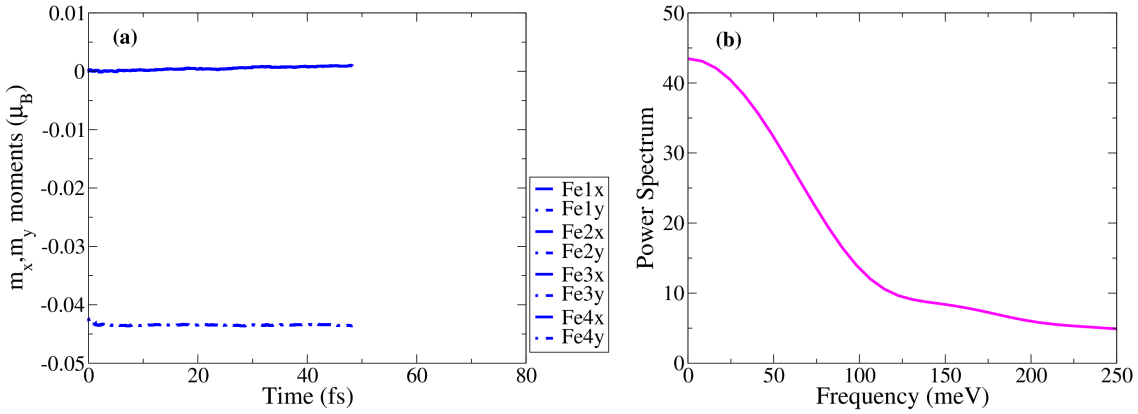

Figure 5.2: (a) Oscillations of the transverse moments for 4 atom supercell of iron in the Goldstone mode and the (b) Fourier transform of y moments.

- Optical mode: $\uparrow\ \downarrow\ \uparrow\ \downarrow$

  Next an initial state for studying the optical mode is prepared by applying magnetic fields in alternating y and -y directions on the neighboring atoms. The time propagation of orbitals is performed and transverse moments as a function of time are obtained, as shown in Fig. 5.3(a). Here the neighboring atoms oscillate 180° out of phase with each other, but the first and third atoms, and second and fourth atoms behave identically. The wavevector for this excitation is **q**-vector = **X**, where X corresponds to the zone boundary of the primitive unit cell.

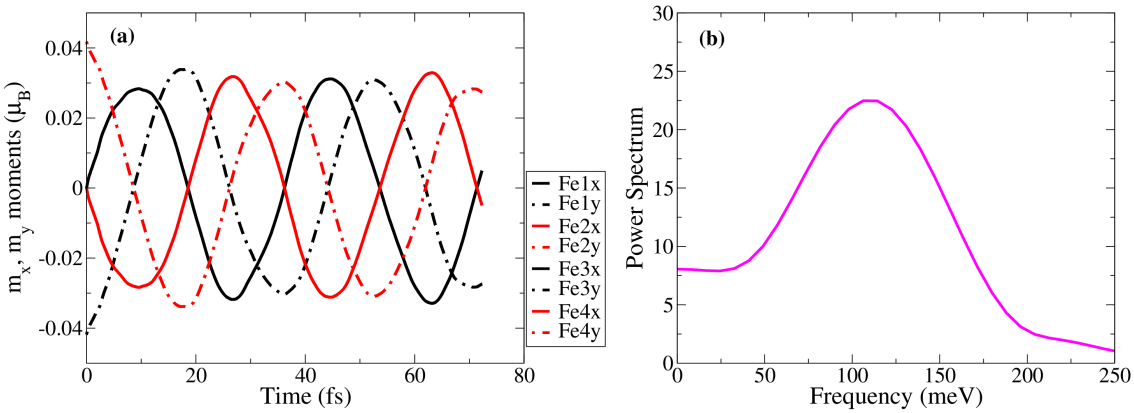

Figure 5.3: (a) Oscillations of the transverse moments for 4 atom supercell of iron in the optical mode and it's (b) Fourier transform.

At any instant of time, as we can see in Fig. 5.3(a) that the x and y moments of each atom are 90° out of phase with each other and they precess counterclockwise. The frequency of oscillation of this mode is 110 meV, as can be obtained by performing a Fourier transform of x or y moments, see Fig. 5.3(b).

- $+\mathbf{Q} = \Gamma X/2$ mode: $\uparrow \rightarrow \downarrow \leftarrow$

  In the case of $+\mathbf{Q}$ mode the neighboring atoms have a 90° phase with each other. This implies that the y moment of first atom and x moment of second atom will be in phase with each other during the time propagation, which can be seen in Fig. 5.4 (a).

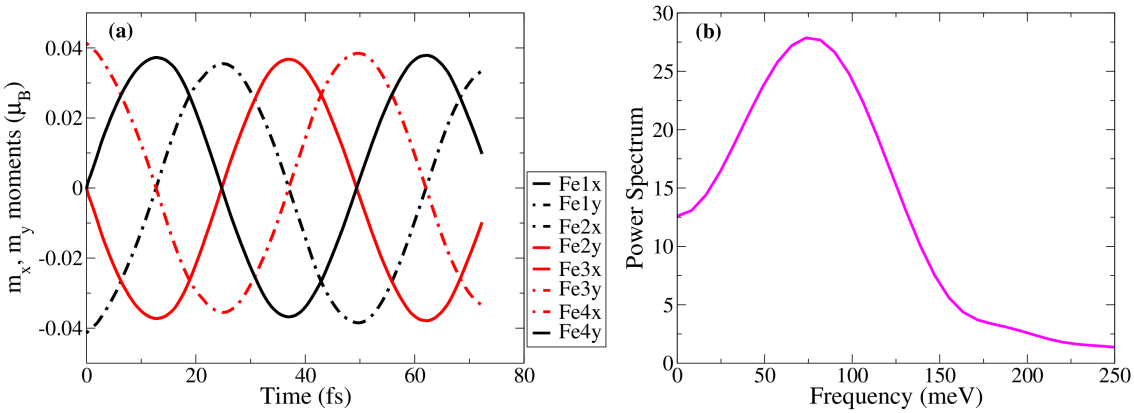

Figure 5.4: (a) Oscillations of the transverse moments for 4 atom iron supercell in the $+\mathbf{Q}$ mode and it's (b) Fourier transform.

These oscillations correspond to a frequency of 76 meV as seen in Fig. 5.4(b). This mode has lower frequency when compared with the frequency of the optical mode.

- $-\mathbf{Q} = -\Gamma X/2$ mode: $\uparrow \leftarrow \downarrow \rightarrow$

The dynamics of $-\mathbf{Q}$ mode can be seen in Fig. 5.5 (a). Similar to $+\mathbf{Q}$ mode the neighboring atoms are $-90°$ (or $270°$) out of phase with each other. The $+\mathbf{Q}$ and $-\mathbf{Q}$ modes are degenerate modes and oscillate with the same frequency of 76 meV (see Fig. 5.5(b)).

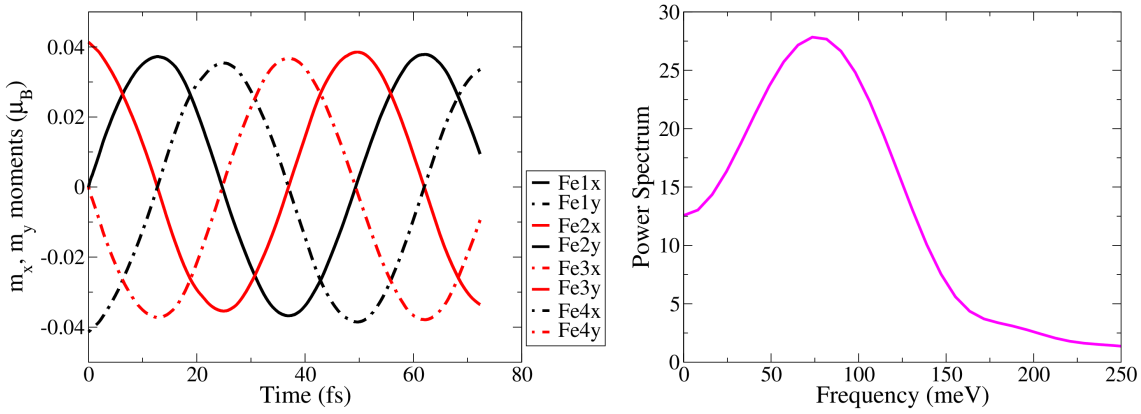

Figure 5.5: (a) Oscillations of the transverse moments for 4 atom iron supercell in the $-\mathbf{Q}$ mode and it's (b) Fourier transform.

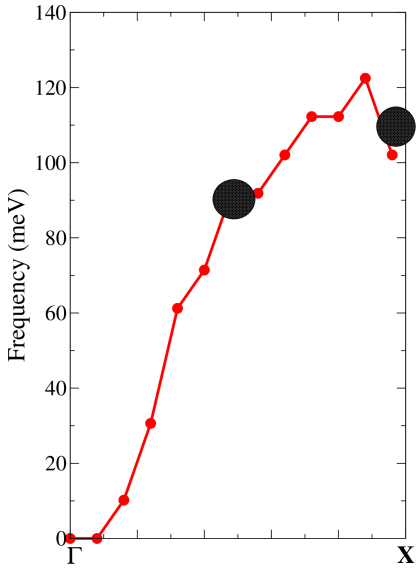

Figure 5.6: The magnon spectra of fcc Fe obtained from linear response TDDFT using LDA functional with particular modes under study highlighted.

After obtaining these normal modes for fcc iron using RT-TDDFT simulations, a linear response calculation was done to confirm the predictions of RT-TDDFT. The energies obtained with LR-TDDFT of these modes along ΓX direction are in good agreement with the real-time calculations as shown in Fig. 5.6. Here, the optical mode is the mode at the zone boundary and the $\pm\mathbf{Q}$ modes are at half ΓX shown by the two black dots in the Fig. 5.6.

One note on the lifetimes of these magnons: In linear response, the width of the peaks is inversely proportional to the lifetime of the magnon. As real-time propagation is computationally demanding, the total simulation time is not long enough to obtain accurate Fourier transforms, and hence the peaks are also broadened numerically. Hence, the peak widths have both the finite lifetimes and numerical errors embedded in them, which makes it difficult to extract magnon lifetimes accurately. The errors arising due to numerical calculations can be removed by propagating the modes for longer time.

Hence, by preparing initial states with particular symmetries, we can control the occupation of individual modes and study the dynamics of a individual modes. Such selective excitation was recently achieved in NiO[12].

We will now demonstrate an advantage of RT-TDDFT over LR-TDDFT, as we can observe and study several magnon modes together in real-space. As the excitation of modes is dependent on the initial perturbation given to the atoms, several examples of different initial states and their decomposition in terms of the normal modes are discussed. Here the left hand spin arrangement corresponds to the perturbation given to the atoms and the right hand side gives the decomposition of the state in terms of normal modes.

(a) No Goldstone mode

$$\uparrow\downarrow\cdots = \uparrow\ \downarrow\ \uparrow\ \downarrow + \nearrow\ \searrow\ \swarrow\ \nwarrow + \nwarrow\ \swarrow\ \searrow\ \nearrow$$

where $\nearrow\ \searrow\ \swarrow\ \nwarrow$ and $\nwarrow\ \swarrow\ \searrow\ \nearrow$ are the $+\mathbf{Q}$ and $-\mathbf{Q}$ modes respectively with a phase factor. The dynamics of this state is shown in Fig. 5.7(a). As this state does not have overlap with Goldstone mode, no shift along x or y-axis of the moments is observed, and all moments oscillate about zero axis. The Fourier transform of the moments should yield two peaks, due to the mixture of the optical mode and the $\pm\mathbf{Q}$ modes. However, these two peaks are not well resolved and only a single peak centered between the two mode frequencies is observed. Recall the numerical error in the width of the peaks is inversely proportional to the total propagation time, hence a longer simulation would be required to resolve the two peaks. However, by duplicating the data before performing the Fourier transform , we can confirm that the dynamics is dominated by just two frequencies. This is also included in Fig. 5.7(b), where the two peak structure is clearly visible and the frequencies exactly match the mode energies found previously, thus demonstrating the superposition of modes.

(b) No optical mode

$$\uparrow\uparrow\cdots = \uparrow\ \uparrow\ \uparrow\ \uparrow + \nwarrow\ \nearrow\ \searrow\ \swarrow + \nearrow\ \nwarrow\ \swarrow\ \searrow$$

Here, the Goldstone mode and combinations of $+\mathbf{Q}$ mode and $-\mathbf{Q}$ mode with a phase factor result in a state where the optical mode is absent. The dynamics of this resultant

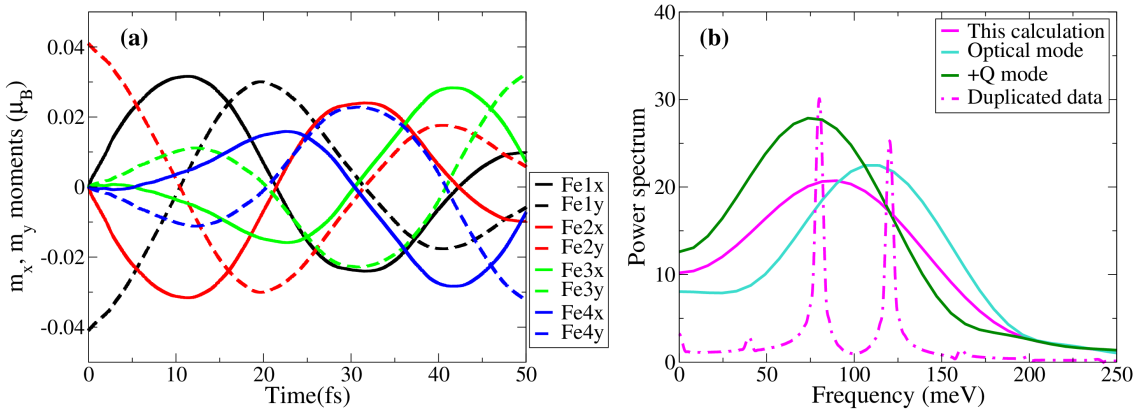

Figure 5.7: (a) Oscillations of the transverse moments for 4 atom supercell of iron. (b) Comparison between frequencies obtained after the Fourier transform for the optical mode, the $+\mathbf{Q}$ mode and the state excited in (a).

state can be seen in Fig. 5.8 (a). Note that the $+\mathbf{Q}$ mode and $-\mathbf{Q}$ mode are degenerate modes. The y moments of the four atoms oscillate about -0.02 instead of 0 signifying the presence of Goldstone mode. This can also be seen in the Fourier transform of the y-moments which has a peak at 0 frequency. Further the oscillations correspond to the state formed by the combination of $+\mathbf{Q}$ and $-\mathbf{Q}$ mode and hence the frequency of this state should be near the frequency of $+\mathbf{Q}$ mode as can be seen in the Fourier transform of x- and y-moments (Fig. 5.8 (b)).

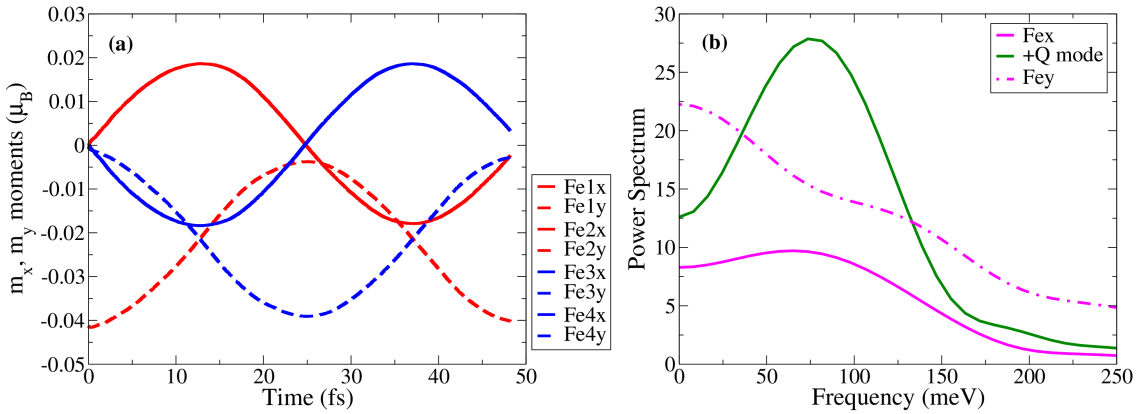

Figure 5.8: (a) Oscillations of the transverse moments for 4 atom supercell of iron. (b) Comparison between frequencies of $+\mathbf{Q}$ mode and the state excited in (a).

(c) No optical and no Goldstone modes

$$\uparrow \cdot \downarrow \cdot \quad = \quad \uparrow \rightarrow \downarrow \leftarrow$$
$$+ \quad \uparrow \leftarrow \downarrow \rightarrow$$

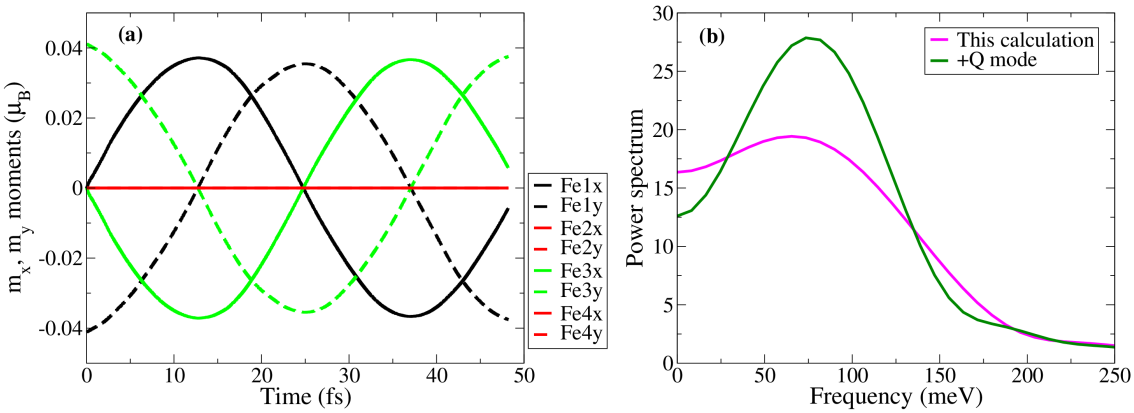

Figure 5.9: (a) Oscillations of the transverse moments for 4 atom supercell of iron. (b) Comparison between frequencies of $+\mathbf{Q}$ mode and the state excited in (a).

In this state both the Goldstone mode and the optical mode are absent as can be seen from moments oscillations in Fig. 5.9(a). It is formed by the combination of $+\mathbf{Q}$ and $-\mathbf{Q}$ mode and hence its frequency should also be equal to these modes as can be seen in Fig. 5.9 (b). Also the first and third atoms respond opposite to each other while second and fourth atom do not oscillate. This is because the net moment on these atoms is zero as can be seen from the decomposition of initial state (shown above) and will remain zero at all times, as the mode frequencies are degenerate.

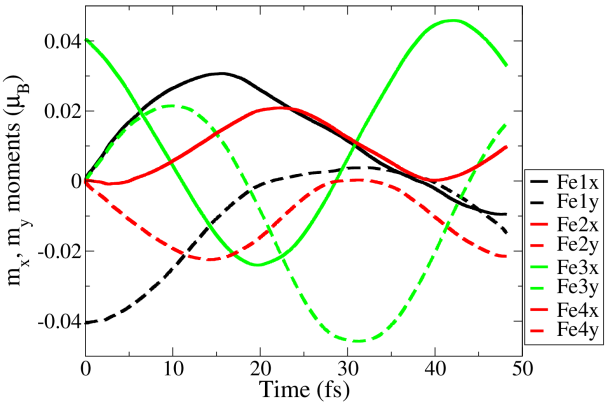

Figure 5.10: Oscillations of the transverse moments for 4 atom supercell of iron.

(d) complex mode

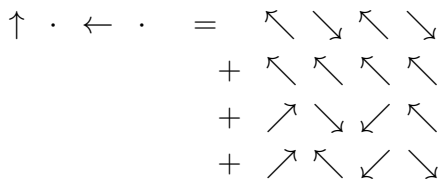

Here all the four modes in iron combine with phases to give rise to a complex state whose dynamics is shown in Fig. 5.10. The Fourier transform can not be performed due to limited data points and oscillations of low frequency.

To summarize this section, these simulations showcase the power of RT-TDDFT to study multiple magnon modes together, in contrast to linear response TDDFT where only a single $\mathbf{q}$ can be studied at a time. It has been shown how the choice of initial state can be exploited to choose which magnon modes are excited and how this can induce complex spin dynamics. The phase and amplitude of each mode is uniquely determined by the initial state. The energies obtained from RT-TDDFT and LR-TDDFT are in good agreement with each other, confirming the accuracy and validity of the supercell approach.

Next we study the system comprising of two magnetic sublattice, namely the ferromagnetic state of $Fe_{50}Ni_{50}$ alloy. As it consists of two magnetic species it is a good candidate for optical control via tailored laser pulses. However, before this can be tested, one needs to know how the unperturbed modes behave in such a system.

5.2 $Fe_{50}Ni_{50}$ alloy

To study the unperturbed magnon modes in $Fe_{50}Ni_{50}$ alloy, a 4 atom supercell is again constructed. Thus the allowed magnon wavevectors are $\mathbf{\Gamma}$, $\pm 1/2\mathbf{\Gamma X}$, and $\mathbf{X}$, where $\mathbf{X} = (0, 0, 2\pi/a)$ in Cartesian coordinates. This supercell is formed by extending the $L1_0$ primitive cell along the c-axis with lattice parameters $a = 3.85$Å and $c = 7.71$Å. The Brillouin zone is sampled on a $\mathbf{k}$-grid of $8 \times 8 \times 8$ and a time step of 1.209 attoseconds was used for time-propagating the orbitals. The other computational parameters were the same as in the iron case.

In the $Fe_{50}Ni_{50}$ multisublattice ferromagnet one could expect coupled modes between the iron and nickel atoms. Hence we performed RT-TDDFT calculations to see the behavior of the Fe and Ni atoms and test the existence of these modes. The results are summarized in Fig. 5.11, obtained after analyzing the moments of Fig. 5.12. In fact, both coupled and uncoupled modes are found. As discussed in section 2.6, we can think in terms of the Heisenberg Hamiltonian to aid our understanding of these modes. The form and frequency of these modes are dictated by the intersite Heisenberg-exchange interaction between the Ni-Ni, Fe-Fe, and Fe-Ni atoms.

As was done in Fe, we can study the dynamics of these modes by preparing the spin system of Fe-Ni-Fe-Ni in the following initial states:

(a) Pure Ni mode

$$\cdot \ \rightarrow \ \cdot \ \leftarrow$$

(b) Pure Fe mode

$$\uparrow \ \cdot \ \downarrow \ \cdot$$

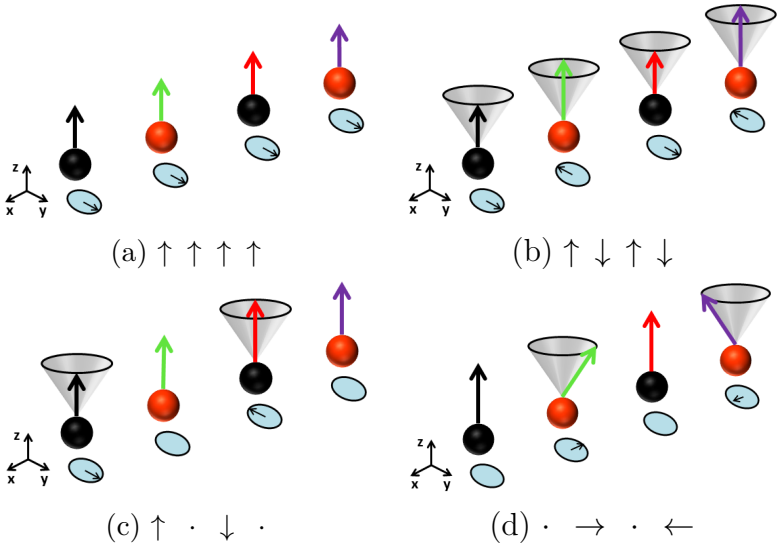

Figure 5.11: The four modes which exist in the ferromagnetic alloy, $Fe_{50}Ni_{50}$. (a) Goldstone mode, (b) Optical mode, (c) Pure iron mode, and (d) Pure nickel mode.

(c) Optical and Goldstone mode

$$\begin{array}{cccccccccc} \uparrow & \cdot & \uparrow & \cdot & = & \uparrow & \uparrow & \uparrow & \uparrow \\ & & & & & + & \uparrow & \downarrow & \uparrow & \downarrow \end{array}$$

(d) All four modes

$$\begin{array}{cccccccccc} \uparrow & \leftarrow & \cdot & \cdot & = & \nwarrow & \nwarrow & \nwarrow & \nwarrow \\ & & & & & + & \nearrow & \swarrow & \nearrow & \swarrow \\ & & & & & + & \uparrow & \cdot & \downarrow & \cdot \\ & & & & & + & \cdot & \leftarrow & \cdot & \rightarrow \end{array}$$

Their dynamics were obtained and plotted in Fig. 5.12. First, the coupled Goldstone and optical modes are discussed, which are shown in Fig. 5.12 (c). In both of these modes, the Ni atoms behave identically to each other, as do the Fe atoms. In these simulations we do not include the spin-orbit coupling shown in Eq. (2.104), and thus there is no magnetic anisotropy as previously discussed. As was the case for iron, the Goldstone mode is a zero frequency mode where the spins do not precess in time and the moment remains fixed at the initial value. In a multi sublattice system this mode can be seen as the invariant ratio of the induced x or y moments, and the z moments in the ground state. In the ground state the z moments ratio of Ni ($0.64\mu_B$) and Fe ($2.88\mu_B$) atoms is 4:1. In Fig. 5.12 (c) we find the ratio, $m^y_{Fe} : m^y_{Ni} = 4{:}1$, of y moments is equal to the ground state moment ratio. This is just the ground state along new axis and hence the ratio must remain the same. On top of the Goldstone mode, the optical mode, signified by the Ni and Fe atoms oscillating 180° out-of-phase with each other, also is seen in the same figure. The frequency of this mode is

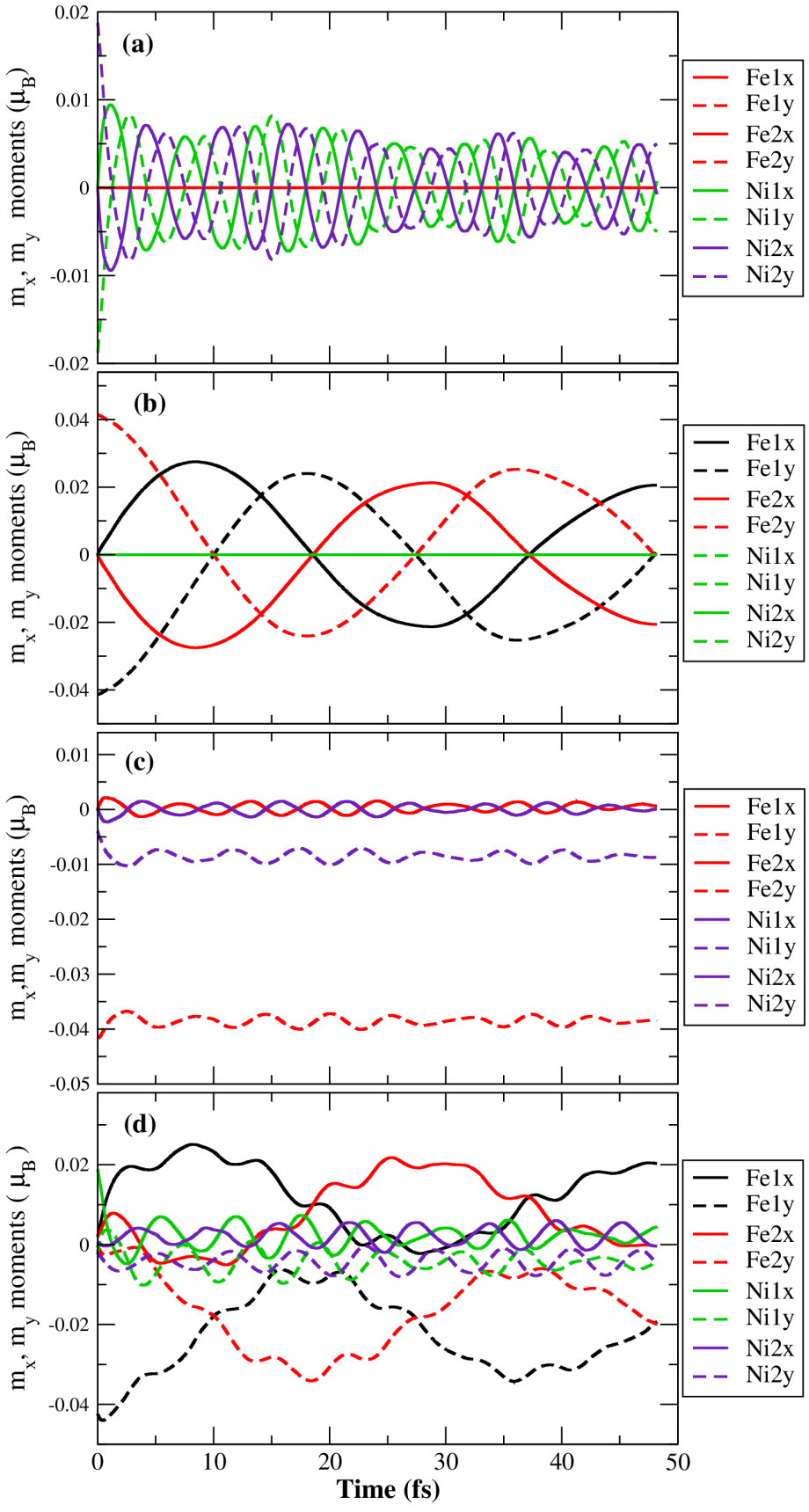

Figure 5.12: Oscillation of the transverse (x,y) magnetic moments of the individual nickel and iron atoms in a 4-atom supercell of $Fe_{50}Ni_{50}$ for different initial states. These magnons correspond to momenta q = Γ, $\pm\frac{1}{2}$ΓX, and X. Decoupled, element specific magnon modes can be seen for (a) nickel and (b) iron. Coupled Goldstone and optical modes can be seen in (c) and (d). All 4 modes are excited in (d).

760 meV, much higher than the $\mathbf{q} = \mathbf{X}$ mode in either Fe or Ni indicating strong exchange coupling between neighboring Fe and Ni atoms.

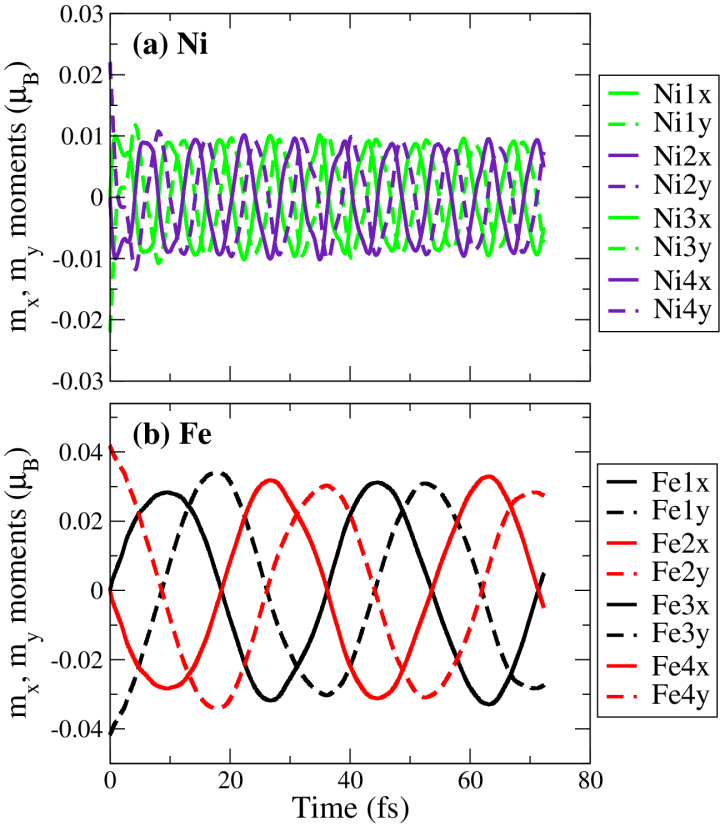

Figure 5.13: Oscillation of the transverse (x,y) magnetic moments of the individual nickel and iron atoms in a 4-atom supercell of (a) nickel and (b) iron for optical mode.

At wavevector $\mathbf{q} = \pm 1/2\mathbf{\Gamma X}$, the effective exchange fields acting on each atom from their nearest neighbors of the other species cancel. This allows decoupled element-specific modes to form, which are indeed observed, as can be seen in Figs. 5.12 (a) and (b). If coupled modes existed, one would see the same frequency in both Ni and Fe perturbations, however very different behavior of the two elements is observed. In Fig. 5.12 (a), only the Ni atoms show transverse oscillations which are 180° out-of-phase with each other, and the x and y moments on each atom are 90° out-of-phase. The frequency of this pure Ni mode obtained by Fourier transform is 710 meV. To check how this frequency differs from the bulk nickel, a 4 atom supercell was again build and calculations were done. The dynamics of the same initial state in bulk Ni as of the pure Ni mode in $Fe_{50}Ni_{50}$ alloy can be seen in Fig. 5.13(a), whose Fourier transform gives a frequency of 390 meV. This is much lower in frequency than the pure Ni mode in $Fe_{50}Ni_{50}$ implying the present of Fe has increased the beyond-nearest-neighbor exchange interactions. The same behavior is observed for the Fe atoms in Fig. 5.12 (b) except the frequency of this pure Fe mode is 90 meV, also higher than the corresponding

mode in bulk Fe 65 meV (as was seen in the previous section - Fig. 5.13(b)). The vast difference between the frequencies of these two modes may also indicate their reluctance to form coupled modes in $Fe_{50}Ni_{50}$.

All four modes can also be excited at once by choosing particular perturbation fields, such as the case shown in Fig. 5.12(d). Here, the Goldstone mode can be seen as a constant-shift in iron and nickel oscillations. The optical mode oscillations can be seen on top of iron oscillations. Similarly, due to the presence of optical mode, the oscillations of nickel atoms are affected but the difference from Fig. 5.12 (a) is more subtle as the frequencies are very close.

The decoupled modes obtained in the case of two magnetic sublattice alloy suggests their response to external fields, such as a laser, would be on different timescales. For example, the lower energy pure Fe modes will be more strongly occupied in the case of laser-induced heating, and thus we would expect Fe to demagnetize faster than Ni, as was observed in Ref. [114]. As we saw in chapter 4, TDDFT is known to overestimate the magnon frequencies, especially in the case of Ni. However this error is smaller than the difference between the pure Ni and Fe modes and thus will not change this conclusion.

5.3 Real-time GGA

In chapter 4, we found that the excitation energies obtained using the GGA functional in LR-TDDFT equation are higher, when compared with LDA, although, they showed better agreement in capturing the interaction with the Stoner continuum. Here, we confirm these results using RT-TDDFT. Note in real-time TDDFT no explicit expression for the kernel is required, only the XC potential is required to time propagate the KS equations. A two atom supercell of nickel is constructed having a commensurate $\mathbf{q}$ vector equal to $\mathbf{X}$. The dynamics of the transverse moments of nickel are shown in Fig. 5.14 for both LDA (a), and GGA (b) and their Fourier transform in (c).

By comparing Fig. 5.14(a) and (b) several observations can be made: (1) The frequency difference at this wavevector obtained by using GGA functional is approximately 80 meV higher in energy than LDA functional, which agrees well with LR-TDDFT calculations ($\approx$ 100 meV) of Chapter 4. (2) The decay in moment oscillation is also stronger with GGA than with LDA functional, which is consistent with the suppression seen in Fig. 4.10. This manifests itself as a broader peak in Fourier transform, representing higher decay and also more interaction the with Stoner continuum. (3) As the GGA functional is sensitive to the gradients, numerical instability appears in GGA moment oscillations and slowly builds up in time, (Fig. 5.14(b)). This instability arises due to unphysical core level excitations from 3p to 3d. More demanding calculations with higher convergence parameters would be required to prevent this instability.

Hence, the results obtained with RT-TDDFT calculations are mutually verified with the LR-TDDFT calculations. Although RT-TDDFT is computationally expensive, it helps in visualizing different magnon-modes and how the coupling between the atoms affect these modes. Another mechanism by which magnons can be coupled is by spin-orbit coupling, which is explored in next section.

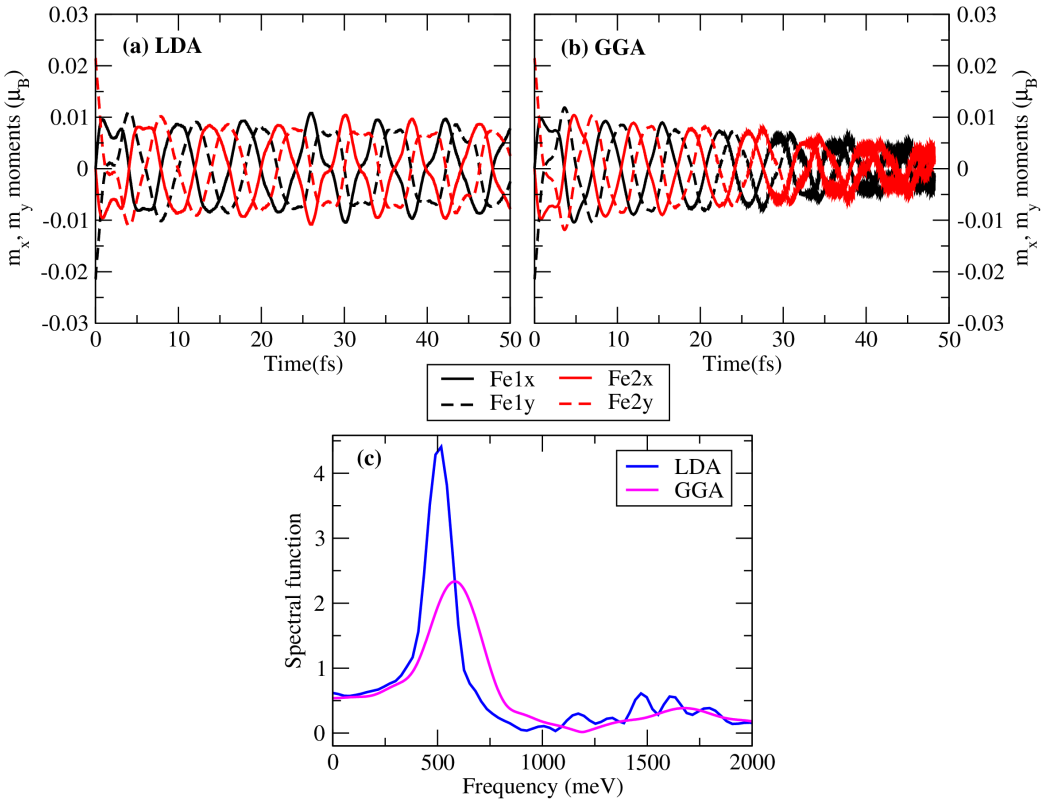

Figure 5.14: Oscillations in transverse moments of nickel atoms using (a) LDA and (b) GGA functional. (c) The Fourier transform of the oscillations obtained using the LDA and GGA functional.

5.4 Spin-orbit Coupling

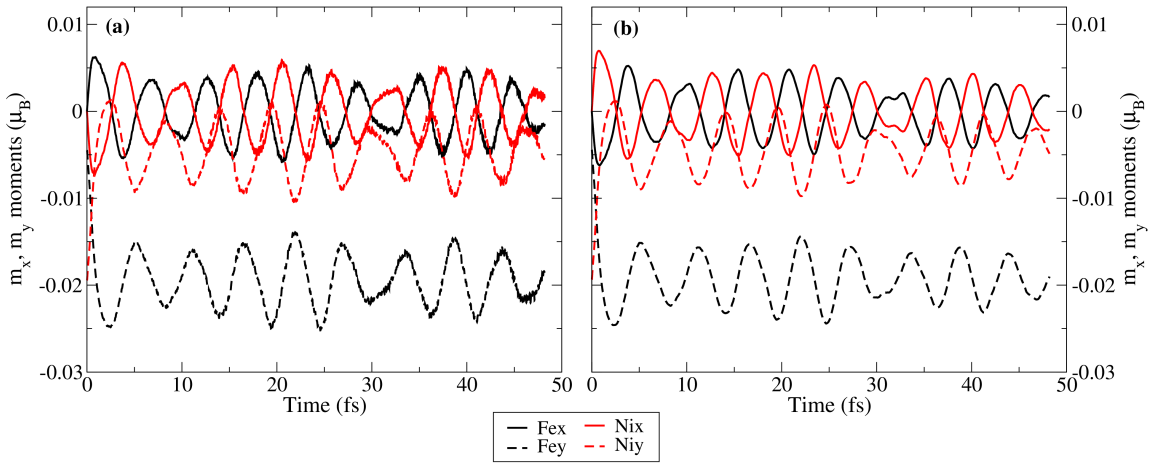

Figure 5.15: The optical mode of $Fe_{50}Ni_{50}$ (a) without spin-orbit coupling and (b) with spin-orbit coupling.

The phenomena of spin-orbit coupling (SOC) is the underlying reason behind many fascinating physical observations, such as ultrafast demagnetization, magnetic anisotropy energy (MAE), Dzyaloshinskii Moriya Interaction (DMI), Quantum Spin Hall Effect (QSHE), and many more. This raises the question of whether the SOC could affect the magnon modes and if this can be addressed using RT-TDFT simulations. To partially answer this question the optical mode of $Fe_{50}Ni_{50}$ is studied. In Fig. 5.15 the dynamics with and without spin-orbit interaction is shown. As can be seen from the figure, spin-orbit coupling does not affect the optical magnon mode. Although if the affect of SOC on magnon modes is to change the frequency by a small amount then longer timescales would be required in order to resolve this small change.

Although SOC did not affect the magnon modes in this case, we propose an application of RT-TDDFT including SOC to extract DMI parameters. By time-propagating $+\mathbf{Q}$ and $-\mathbf{Q}$ magnon modes, the frequency of these modes could be found, and the energy difference between them extracted, which is known to depend on the DMI interaction strength. However, generally these modes can have very small energy differences (μeV-meV), and thus need to be propagated for a very long time. Further the range of energies is very small which again limits the studies due to numerical noise. Due to computational limitations they have not been performed in this thesis, but the method is proposed.

To summarize this chapter, it is shown that TDDFT can be used to study the dynamics of magnon modes in real-space and real-time. This allowed us to see the TDDFT prediction of decoupled element-specific magnon modes in FeNi, with vastly different energies, information not easily accessible in LR-TDDFT. With knowledge of how the unperturbed modes behave, we can now study if they may be manipulated using laser pulses.

CHAPTER 6

OPTICAL CONTROL OF MAGNON

The urge to destroy is also a creative urge.
- Pablo Picasso

The emerging field of controlling magnetism with femtosecond laser pulses is both exciting and challenging from a technological point of view. Uniting this new field of femtomagnetism with magnonics opens up a new range of possibilites for the next generation of spintronic devices. In this chapter we investigate how the magnon dynamics respond to ultrafast, ultra-strong, laser pulses. One of the fastest responses of spins in multi-sublattice magnets to applied laser pulses is due to Optical Inter site Spin TRansfer (OISTR). Hence, we will study $Fe_{50}Ni_{50}$ alloy which consists of two magnetic sublattices making OISTR possible excitations. Here, we examine how these excitations affect the magnon modes and whether they can be used to control the magnons.

6.1 OISTR in $Fe_{50}Ni_{50}$

Ultrashort laser pulses hold the capability to dramatically change the magnetic structures, including switching from antiferromagnetic to transient ferromagnetic magnetic order by inducing spin-selective charge flow using a laser pulse [115, 116]. The microscopic mechanism responsible for the ultrafast switching is governed by transfer of spin from one magnetic sublattice to another, often driven by the minority spin electrons, known as OISTR transitions. It has been experimentally observed in a wide range of materials and geometries, such as bulk Heusler compounds [117], Co/Cu interfaces [118], and Ni/Pt multilayers [119]. As these excitations are induced by direct optical excitation of lasers, they take place on the timescale of the laser pulse duration. This promises extremely fast manipulation of spin which is perfect for future technology.

To demonstrate OISTR in $Fe_{50}Ni_{50}$, a laser with intensity 9.6807 mJ/cm^2, frequency 2.19 eV and Full Width at Half Maximum (FWHM) 2.41 fs is used. The frequency of the pulse is chosen in such a way that it favors maximum optical excitations or in other words maximizes OISTR. The evolution of z-moment of iron and nickel in FeNi is plotted in Fig. 6.1. As can be seen the moment of iron reduces while that of nickel increases due to the laser application, hence moment is transferred between the Fe and Ni sublattices. Also the delocalized states

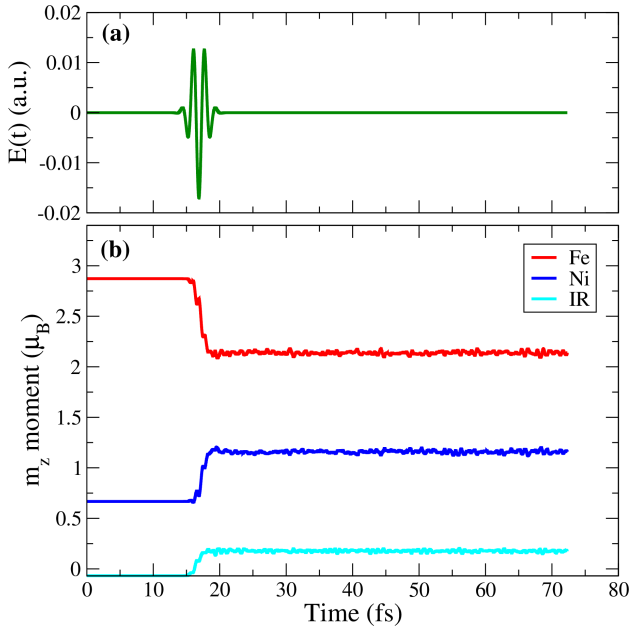

Figure 6.1: (a) The electric field of incident laser with intensity 9.6807 mJ/cm^2, frequency 2.19 eV and FWHM 2.41 fs. (b) The evolution of z-moment of iron and nickel atoms in FeNi.

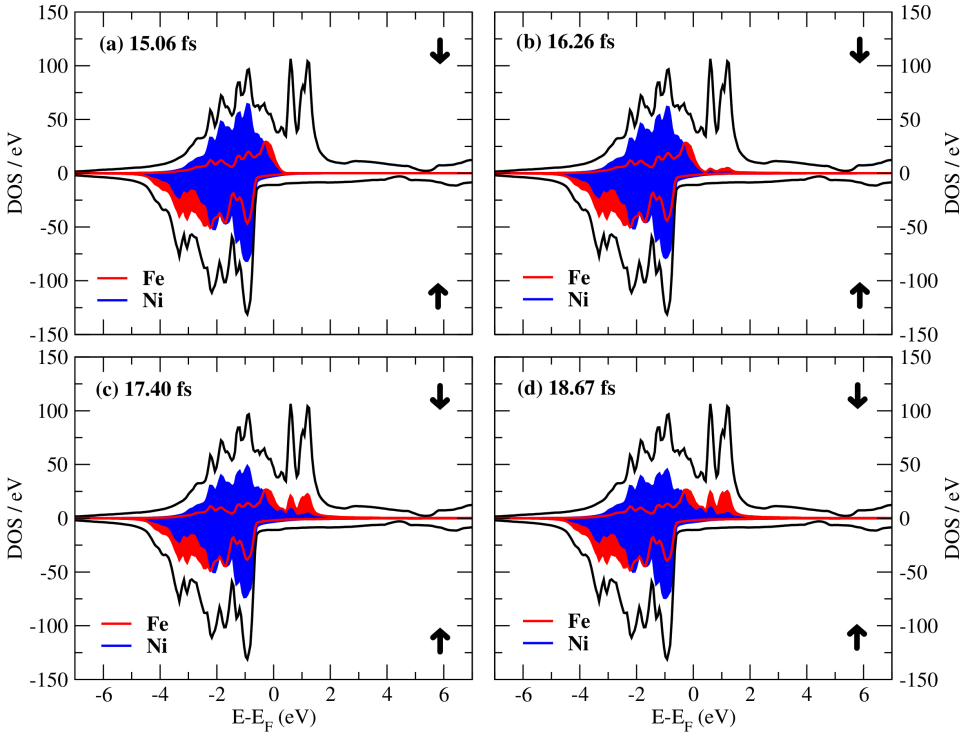

Figure 6.2: The d-orbitals TD-DOS of iron and nickel for the minority and majority spin channels when acted upon by a laser at (a) 15.06 fs, (b) 16.26 fs, (c) 17.40 fs, and (d) 18.67 fs .

(IR region) gains moment.

To study the reason behind this reduction of moment the time-dependent density of states (TDDOS) (defined in Section 2.7) for iron (red) and nickel (blue) at different times: (a) 15.06, (b) 16.26, (c) 17.40, and (d) 18.67 fs is plotted in Fig. 6.2. It can be seen that as the laser reaches its peak intensity, the minority spins from nickel *d*-bands flow into the unoccupied states of iron above Fermi level. As the minority spins move out of nickel to iron, the Ni magnetic moment increases. Similarly for iron, it loses majority to nickel and gains minority spin from nickel, both of which result in the reduction of the Fe moment.

The intensity of the laser pulse is then varied to see the affect on the moment gained by nickel or the moment lost by iron (see Fig. 6.3). From the figure, it can be seen that the amount of moment transferred depends linearly on the laser intensity until it reaches saturation. Similar linear dependence on laser intensity was also found for the change in moment of the delocalized states. This implies there is a cut-off value of the laser intensity above which the transfer of moment is unaffected. Hence, we find that the amount of moment transferred can be controlled using the laser intensity.

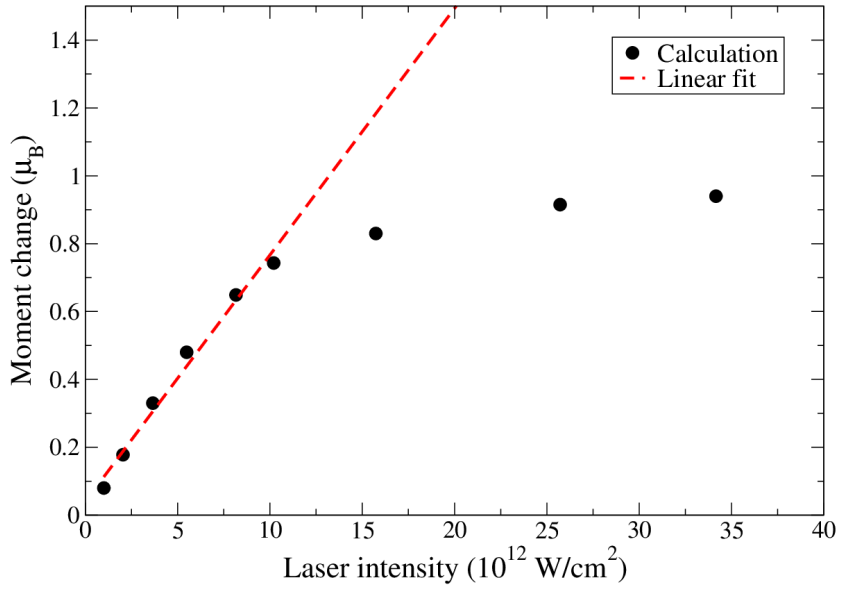

Figure 6.3: The linear dependence of moment transferred due to OISTR to the laser intensity.

6.2 Iron

As a first step towards controlling the magnons in $Fe_{50}Ni_{50}$ alloy, we look at the case of pure iron. The four normal modes which exist in a four atom supercell of fcc iron were discussed in chapter 5. To recap, these modes were the zero frequency Goldstone mode, the optical mode with energy 110 meV, and two degenerate $\pm\mathbf{Q}$ modes both with energy 76 meV. As a prototype to study magnon-light interaction, we excite the $+\mathbf{Q}$ magnon mode and calculate

the response of this mode (as shown in Fig. 5.4(a)) to three laser pulses of different intensities.

Case 1:

Here a laser with fluence 9.6807 mJ/cm^2, frequency 2.19 eV and FWHM of 2.41 fs is used. As can be seen in Fig. 6.4 when this intense laser is applied to the +**Q** magnon mode of iron the amplitude of magnon is quickly damped and the mode is destroyed.

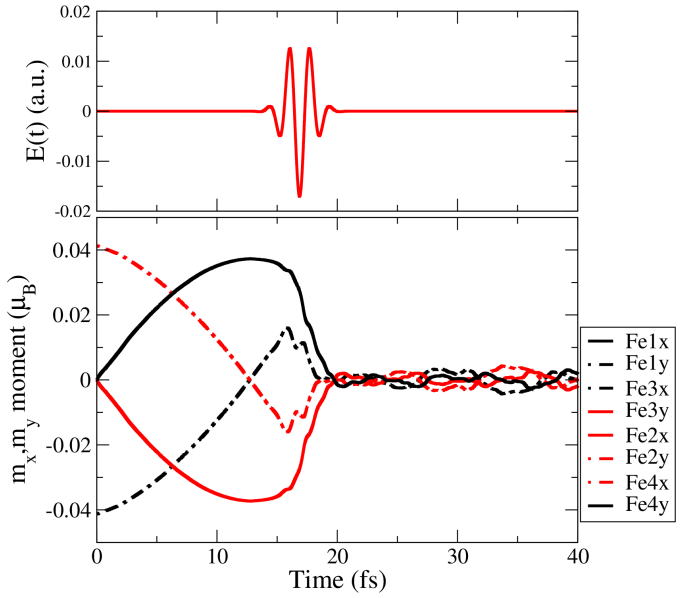

Figure 6.4: The oscillations of moments in +**Q** mode and its response to the laser of fluence 9.6807 mJ/cm^2, frequency 2.19 eV and FWHM 2.41 fs.

Case 2:

A pulse which is 10 times weaker in fluence (= 0.953 mJ/cm^2) was applied (the frequency and FWHM were kept the same). The response of the mode to this pulse was surprising, (see Fig. 6.5). At time t=0 the spins are in the following arrangement,

$$\downarrow \leftarrow \uparrow \rightarrow$$

and then precess counterclockwise. However, at the peak of the laser pulse at t = 16.8 fs a transient static non-collinear state is formed where the magnon oscillations are destroyed and the spins are frozen into the following spin spiral state,

$$\nearrow \searrow \swarrow \nwarrow$$

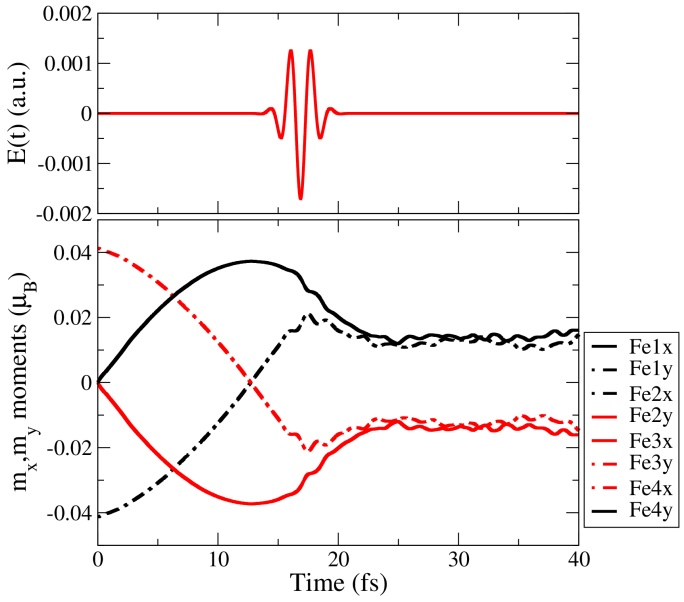

Figure 6.5: The oscillations of moments in +**Q** mode and its response to the laser of fluence 0.953 mJ/cm^2, frequency 2.19 eV and FWHM 2.41 fs.

Case 3:

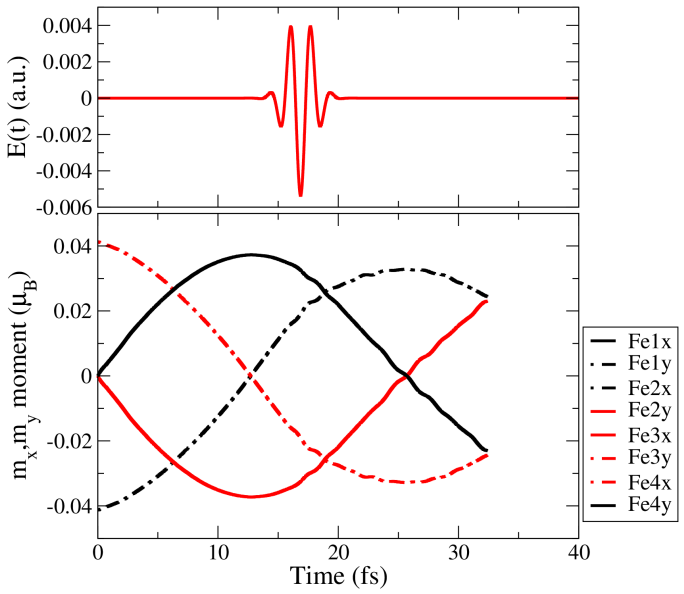

Figure 6.6: The oscillations of moments in +**Q** mode and its response to the laser of fluence 96 μJ/cm^2, frequency 2.19 eV and FWHM 2.41 fs.

Again we reduce the pulse to one 10 times weaker (96 μJ/cm^2) than case 2, while keeping

the other parameters the same. In this case the magnon mode is not destroyed and it precesses with the same frequency of 76 meV (see Fig. 6.6). Although some oscillations at the pump frequency are observed due to a weak oscillating charge current induced by the laser.

From the above three cases it can be inferred that there is a window of laser pulse intensity (at this frequency) where the magnons can be manipulated. To find the reason behind these different responses, the dynamics of the majority and minority spins [117] local to each atom are plotted in Fig. 6.7. It can be seen that as the intensity of the laser increases, the transfer of charge from localized to highly delocalized states also increase. As magnetic moment is the difference between the majority (solid lines) and minority (dashed lines), it will lead to decrease in magnetic moment of iron. This affects the magnon excitations and destroys the magnon which by definition are magnetic excitations of localized moments.

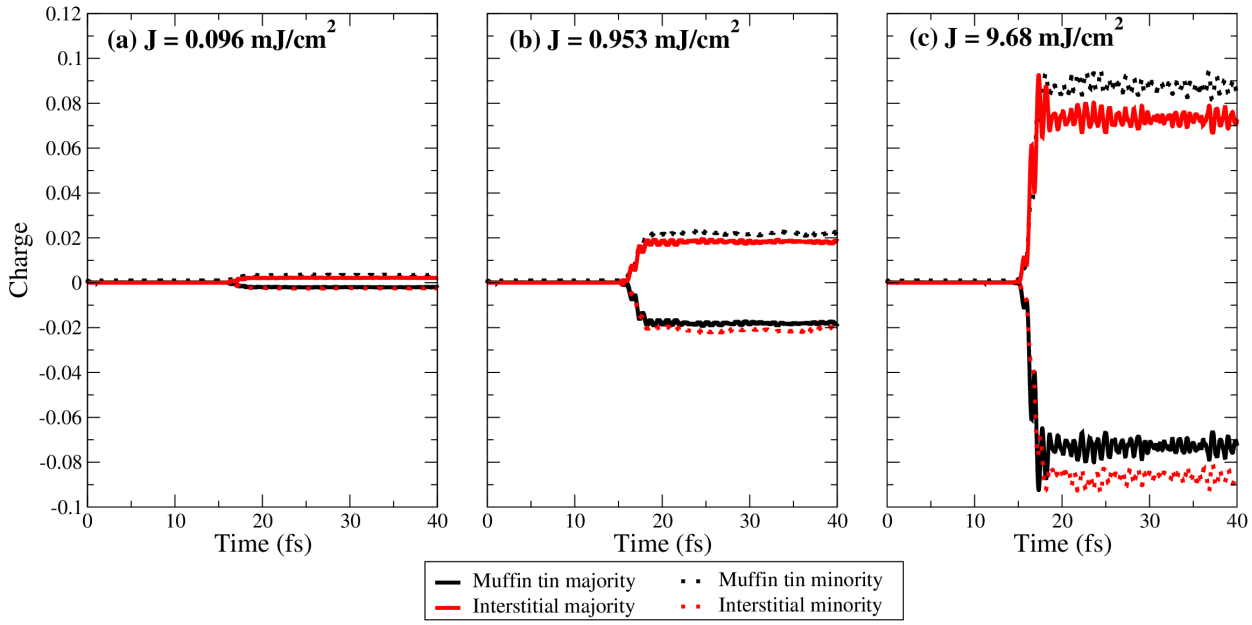

Figure 6.7: The charge transfer in the interstitial region and muffin tin per atom when acted upon by laser of fluence (a) 0.096 mJ/cm^2, (b) 0.953 mJ/cm^2 and (c) 9.6807 mJ/cm^2, frequency 2.19 eV and FWHM 2.41 fs. The solid line is majority charges and dashed is minority charges.

After studying the interaction of laser with the magnon modes in a bulk ferromagnet, the case of two magnetic sublatticies is undertaken. Here the presence of two magnetic sublattices and element specific modes (as seen in chapter 5) gives rise to interesting magnon dynamics.

6.3 $Fe_{50}Ni_{50}$ magnon dynamics

In order to be able to manipulate magnons at ultrafast time scales we now investigate the behavior of magnon modes under short laser pulses. One of the fastest possible spin response to lasers is via OISTR. In this section the material, as well as the laser pulses, are chosen

to maximize OISTR: in the $Fe_{50}Ni_{50}$ alloy the magnetic moment on the Fe sub-lattice (2.88 μ_B) is much higher than on the Ni sub-lattice (0.64 μ_B). As seen in Section 6.1, this causes laser induced optical excitations to transfer minority spin electrons from Ni to Fe, which in turn leads to a increase in the moment on the Ni site, while a corresponding decrease on the Fe site (see Fig. 6.8 (c and d)). The frequency of the laser pulse (2.19 eV) is tuned to optimize this charge transfer. Here, the question of how OISTR excitation affects the four magnon modes previously studied (Chapter 5) in $Fe_{50}Ni_{50}$ is explored. To address this question, different initial states are created and then the laser parameters such as intensity, frequency, time delay, and duration are varied to see their affect on the different magnon modes.

6.3.1 Four modes + laser

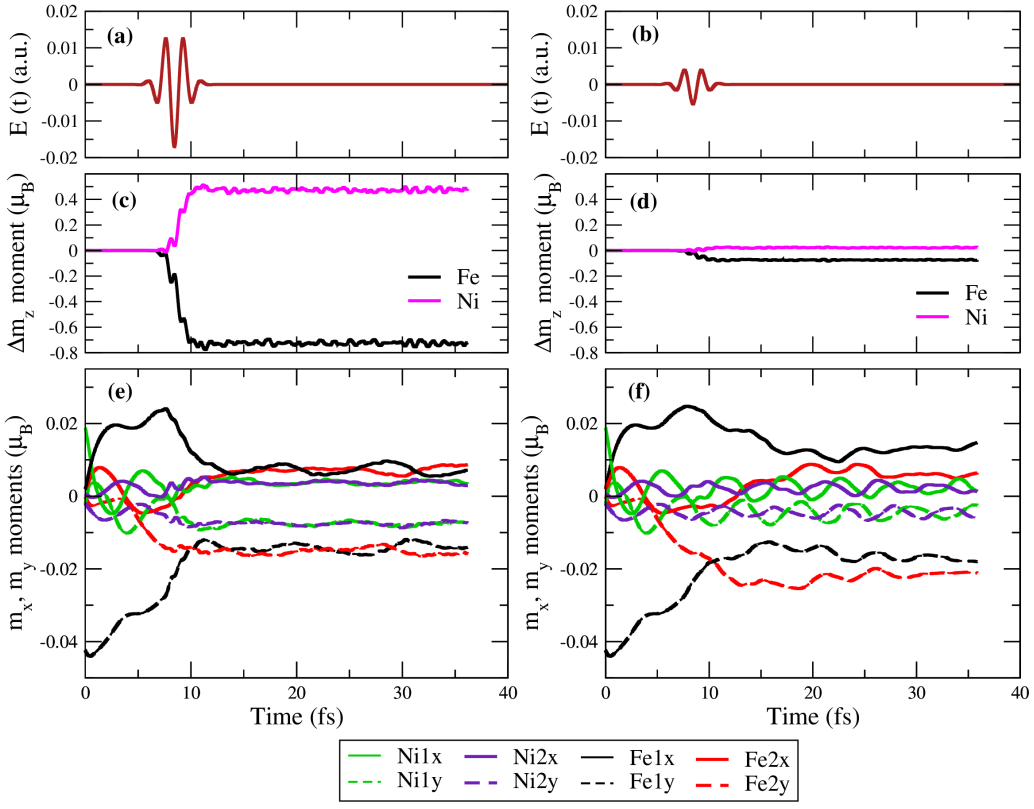

Figure 6.8: The electric fields of two laser pulses designed to induce OISTR transitions in FeNi, with frequency 2.19eV, FWHM 2.41 fs, and fluences (a) 9.6807 mJ/cm^2 and (b) 0.9537 mJ/cm^2. The change in magnetic moments of Fe and Ni corresponding to the pulse is shown in (c) and (d). Next, the reaction of all magnon modes to the laser pulses is shown. In (e) the pure Fe mode is destroyed while the pure Ni persists, while in (f) only the Goldstone and optical modes survive.

The effect of OISTR on magnon modes can be seen in Fig. 6.8– strong laser pulse (incident fluences of 9.6807 mJ/cm^2 and FWHM of 2.41 fs) effectively destroy both decoupled modes (see Fig. 6.8 (e)); the amplitude of the pure Fe magnon mode collapses with only

small oscillations remaining which are also quickly damped. Looking at the Ni moments, which initially are a superposition of the pure Ni mode and the optical mode, we see that now only the optical mode exists as the two Ni atoms behave identically (recall that in the pure Ni mode, the two are 180° out-of-phase).

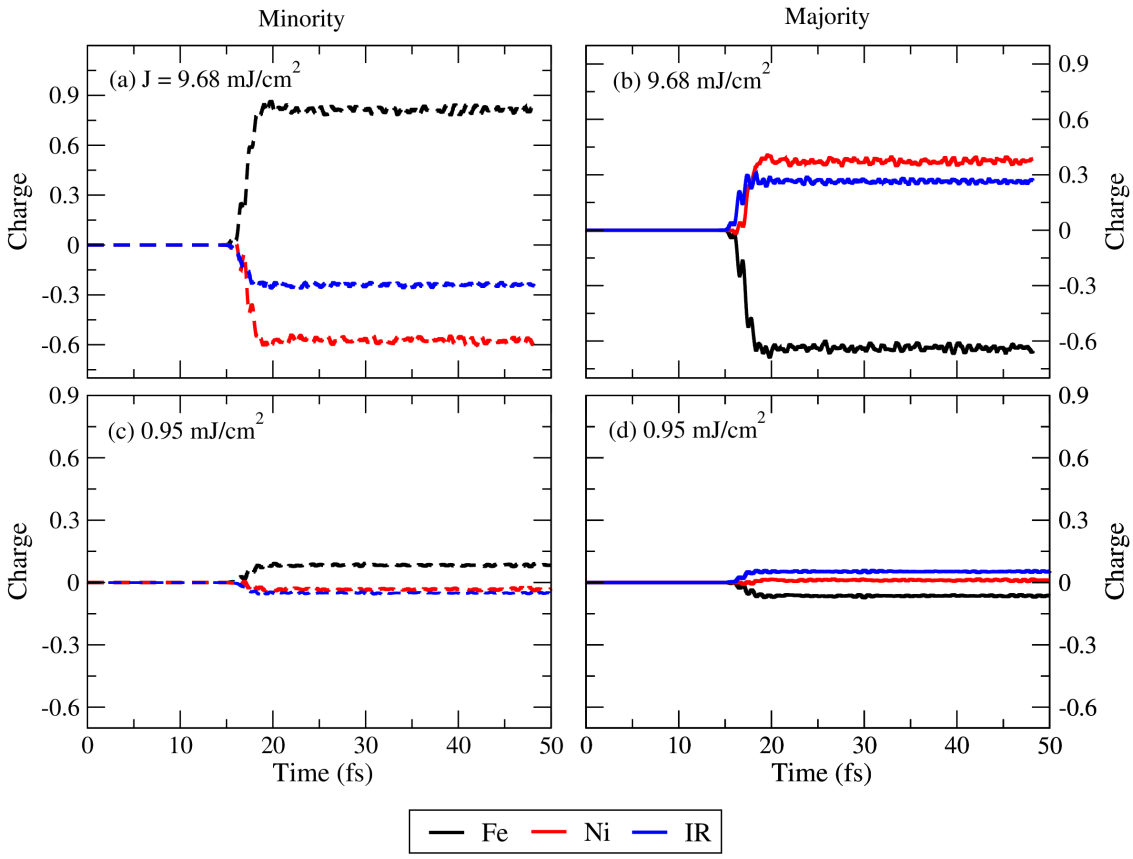

Figure 6.9: The evolution of minority charges (a,c) and majority charges (b,d) for nickel, iron and interstitial region with 9.6807 mJ/cm^2 (a,b) and 0.9537 mJ/cm^2 laser (c,d).

These magnon modes show a different dynamics when subjected to a weaker laser pulse of incident fluence 0.9537 mJ/cm^2; the pure nickel mode now survives while the Fe mode is still destroyed (see in Fig. 6.8 (f)). In this case the Fe atoms cant with respect to each other with a new, but much reduced, pure Fe mode oscillating about this new configuration. By examining the amount of majority/minority electrons excited on each atom, we find that the Fe atoms have significantly more local optical excitations than Ni (see Fig. 6.9). This causes the Fe-Fe exchange coupling to be modified more strongly than the Ni-Ni coupling, explaining the difference in behavior between the two modes. Thus we have found a method by which we can selectively destroy either both Fe and Ni modes or just the Fe mode, on a femtosecond timescale by tuning the fluence of the laser pulse.

In the following section combinations of other normal modes are investigated to gain insight into their response to optical laser.

6.3.2 Goldstone mode + Optical mode + laser

In this case a state is chosen which consists of only the Goldstone mode and optical mode. The dynamics of the moments obtained is shown in Fig. 6.10 under the affect of three different pulses all having the same frequency and FWHM. The strength of pulse in decreasing order is 9.6807 mJ/cm^2, 0.95377 mJ/cm^2, and 0.0966 mJ/cm^2.

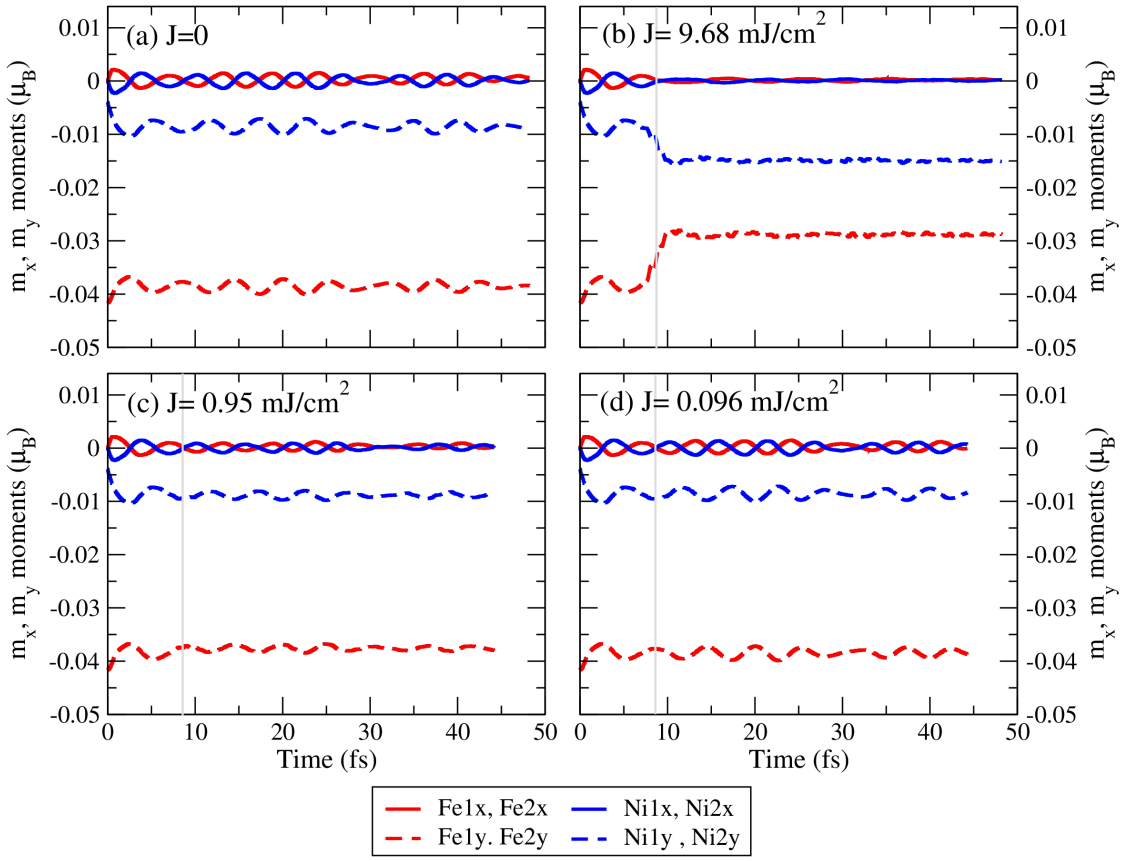

Figure 6.10: Oscillations of transverse moments when (a) no pulse is applied, (b) the strongest pulse of 9.6807 mJ/cm^2, (c) intermediate pulse of strength 0.95377 mJ/cm^2, and (d) the weakest pulse 0.0966 mJ/cm^2. The vertical lines correspond to the peak of the laser. The weakest pulse does not destroy the modes, the intermediate pulse changes the amplitude of oscillation while the strongest pulse changes the frequency of optical mode as well as the Goldstone mode.

As can be seen from the figure the most intense pulse changes both the frequency of the optical mode as well as the Goldstone mode. The ratio between the iron and nickel moments of the Goldstone mode changes from 4:1 to 2:1 due to OISTR, as seen in Fig.6.10 (b). Also, the pulse with fluence 0.95377 mJ/cm^2 reduces the amplitude of oscillation of the moments but has very little affect on the frequency of the optical mode. Additionally, this pulse does not affect the Goldstone mode and the ratio of iron nickel moments remain unchanged at 4:1. Hence, both the modes remain unaffected by the weakest pulse. From this it can be inferred that there exists a threshold value of the pulse strength which affects the optical

magnon mode.

6.3.3 Element specific mode + laser

Next, the idea of exciting the coupled modes following application of the laser while starting from any one of the uncoupled modes was explored. The laser with fluence 0.9537 mJ/cm^2 was applied on the pure iron mode in $Fe_{50}Ni_{50}$ alloy. Since OISTR will transfer moment between iron and nickel, we explore the possibility of exciting a coupled Fe-Ni mode or even a pure Ni mode, starting from a pure Fe mode and vice-versa.

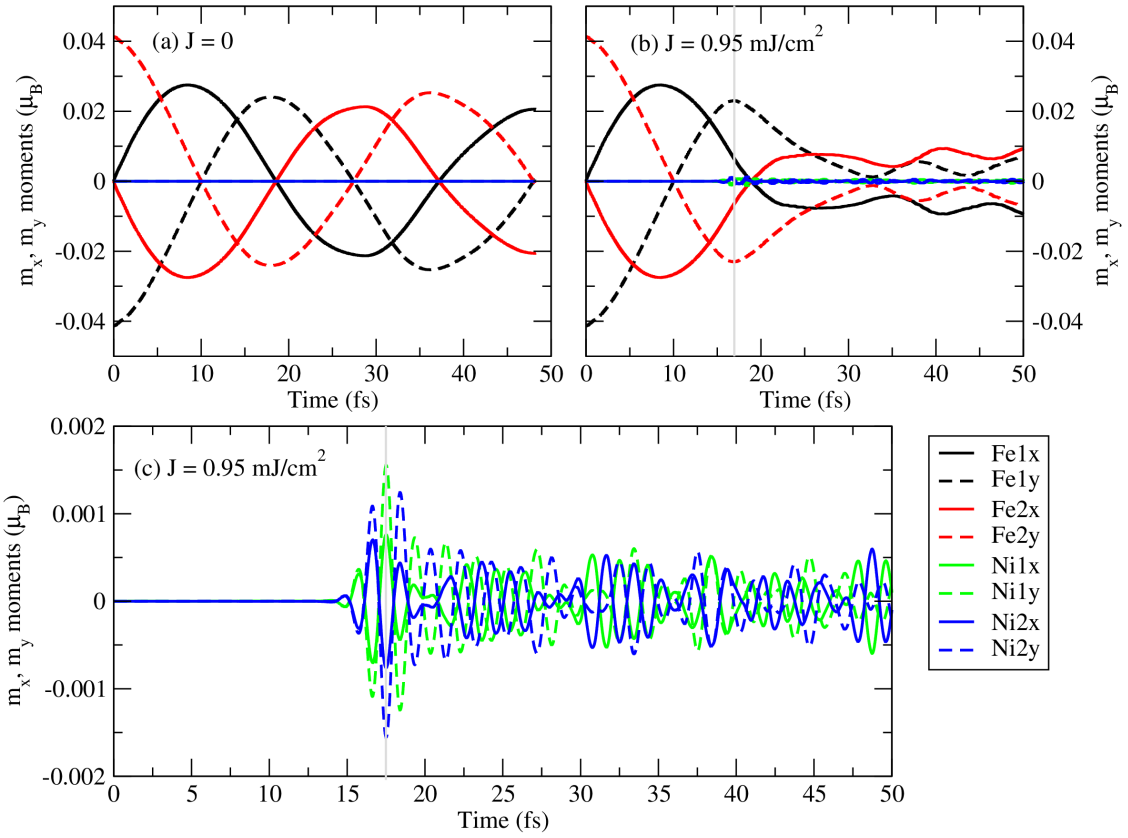

Figure 6.11: Oscillations of transverse moments of Ni and Fe in (a) unperturbed mode and with a laser of fluence (b) 0.9537 mJ/cm^2. (c) A magnified image of the nickel moments in (b) when acted by the laser. The vertical lines correspond to the peak of the laser.

The unperturbed pure iron mode in $Fe_{50}Ni_{50}$ is shown in Fig. 6.12(a) and after pumping with laser in (b). This laser fluence resulted in a non-collinear spin spiral state in pure bulk iron moments (Section 6.2) and is again observed in iron moments in the alloy. However, the nickel moments also start to oscillate upon pumping with the laser which is shown in Fig. 6.10(c). This appears to be arising due to the charge oscillations happening in nickel at the laser frequency.

The laser interaction with the pure nickel mode in the alloy was also studied and is shown in Fig. 6.12. Similar to the results obtained for pure iron mode, the strong laser (fluence = 9.6807 mJ/cm^2) also destroys the magnon modes and weak laser pulse (fluence = 96 μJ/cm^2) does not affect the mode. While there is a weak response of the iron moments, this is likely numerical noise due to intense laser pulse. We conclude that exciting a magnon mode with different dynamics on the two Fe atoms is forbidden by symmetry

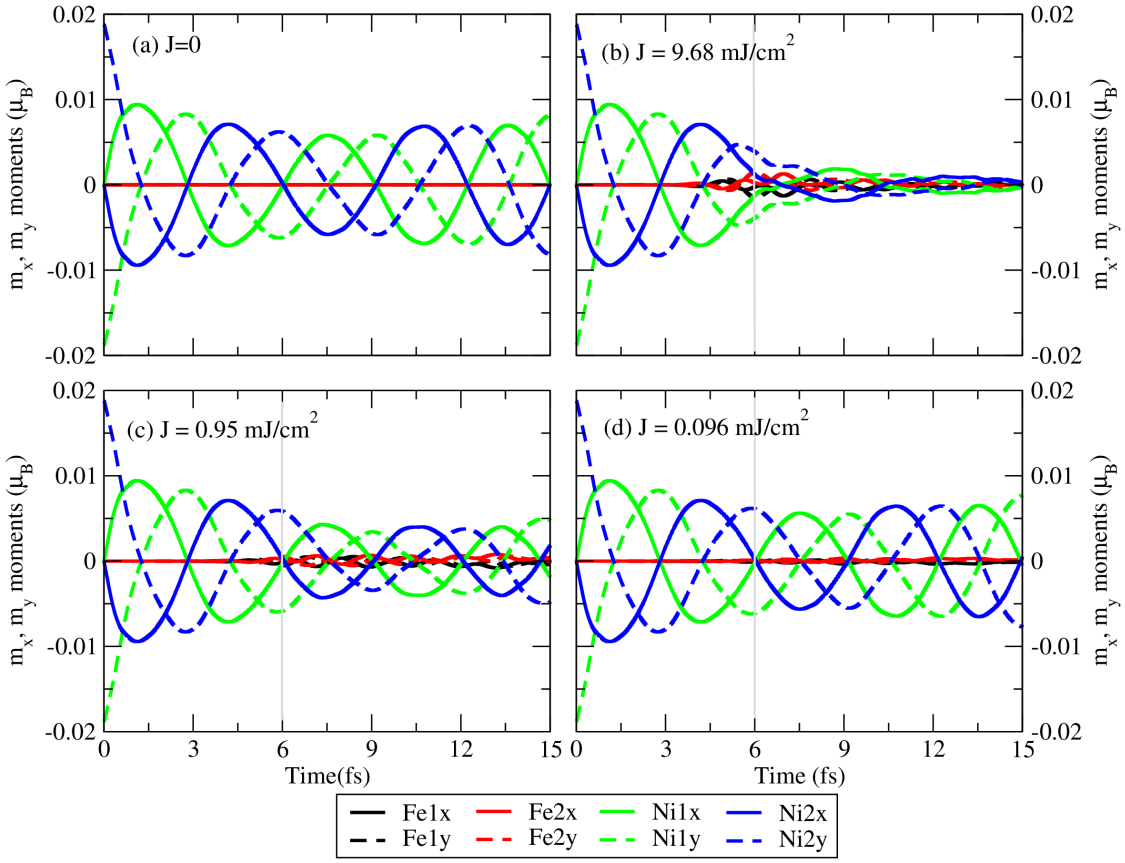

Figure 6.12: Oscillations of transverse moments of Ni and Fe in (a) unperturbed mode and with laser of fluence (b) 9.6807 mJ/cm^2, (c) 0.9537 mJ/cm^2 and (d) 0.0966 mJ/cm^2. The vertical lines correspond to the peak of laser.

6.3.4 Frequency dependence

The above calculations were done by keeping the frequency of the laser pulse fixed at 2.19 eV (which was chosen to maximize the OISTR transitions). In this section, the laser frequency is modified in order to examine how this affects the magnon dynamics. In the following calculations the laser frequency was increased to 3.26 eV and two pulses with fluences (a) 1.73 mJ/cm^2 and (b) 20.87 mJ/cm^2 were used. For efficiency, the initial state comprising of all four magnon modes was chosen. As can been seen in Fig. 6.13(a), following application of the weaker pulse, all four modes precess without disruption. This is in contrast to the

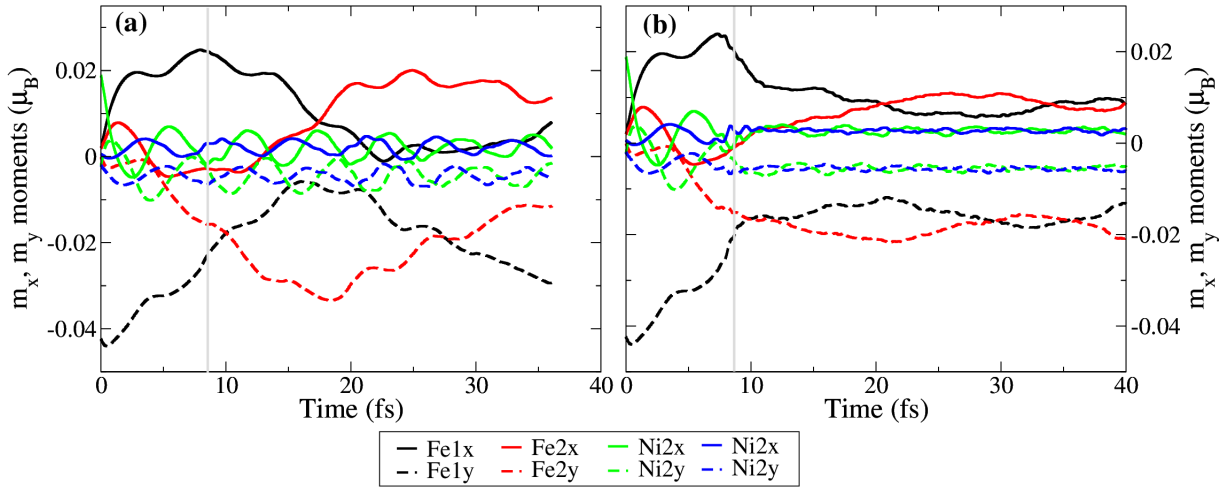

Figure 6.13: Oscillations of transverse moments under the laser with frequency of 3.26 eV and fluence of (a) 1.73 mJ/cm^2 and (b) 20.87 mJ/cm^2. The peak of laser denoted by vertical lines.

previous case of Fig. 6.8(f), where the pure iron mode was destroyed by a pulse with similar fluence. Thus we observe dependence of the response of the magnon modes on the laser frequency.

This dependence can be understood by considering Fig. 6.9, which showed that the destruction of the pure Fe mode strongly depends on the number of electrons transferred between the atoms and the delocalized states. This transfer is proportional to the degree of optical excitation of the system, which itself is proportional to the number of unoccupied states available for excitation. In this case, we see in Fig. (6.2) that the unoccupied density of states available for excitations at a frequency of 3.26 eV is lower than that available at 2.19 eV, hence less excitation, leading to less spin transfer and the survival of the pure iron mode. When the laser with higher fluence was applied, the amplitude of all four modes were reduced, as can be seen in Fig. 6.13(b), similar to Fig. 6.8(e) except requiring twice the fluence.

6.3.5 Time delay dependence

As seen in Figs. 6.8(f) and 6.11(b) a static non-collinear state could be seen following destruction of the pure Fe mode by the laser. In this section it is shown that the canting vector, $\mathbf{m}^{\mathrm{Fe1}}(t) - \mathbf{m}^{\mathrm{Fe2}}(t)$ between neighboring atoms, can be controlled using the time delay of the laser pulse. More precisely, we find that the relative phase between the magnon mode and the laser determines in which direction the Fe moments eventually point, and thus determines the direction of the canting vector. Recall that this canting of the spins was also seen in the case of 4-atom iron (Fig. 6.5) where the amplitude of both the x and y moments were equal. To keep the total moment in the x or y direction zero while keeping the amplitudes of x and y moments the same, there are only 4 possible canting vector configurations:

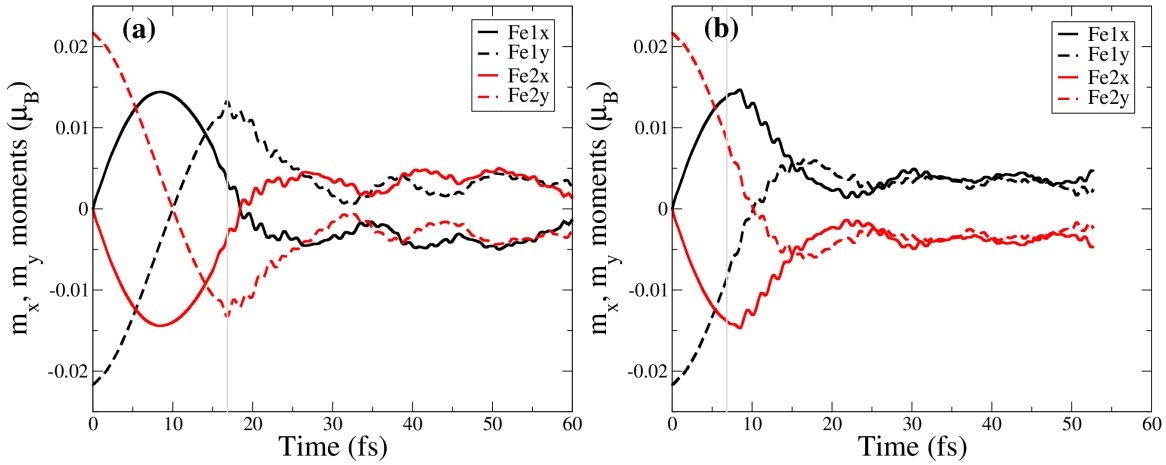

Figure 6.14: The canting vector is dependent on the delay time of the laser and is shown relative to the pure Fe mode oscillations. A laser of fluence 0.9537 mJ/cm^2 is applied at (a) 16.8 fs and (b) 8.4 fs on the pure iron mode.

Canting vector

↗ · ↙ · = ↗
↙ · ↗ · = ↙
↖ · ↘ · = ↖
↘ · ↖ · = ↘

In these canting configurations the first and second configurations are the same along with third and fourth due to translation invariance. We can vary the relative phase between the laser pulse and the magnon by changing the position (in time) of the center of the laser electric field. In the first scenario the center of the pulse is chosen to be located at 16.8 fs when the Fe1y and Fe2y are at their maximum amplitude (see Fig. 6.14 (a)) and in the second case the center of the pulse is chosen to be at 8.4 fs which corresponds to the point in time when the Fe1x and Fe2x moments are at their maximum amplitude (see Fig. 6.14 (b)). These two delays in the laser pulses result in different directions of the canting vector,

Canting vector

↖ · ↘ · = ↖
↙ · ↗ · = ↙

The laser pulse used to obtain this canting is very weak with fluence=0.9537 mJ/cm^2, frequency 2.19 eV, and FWHM 2.51 fs. Unlike in the strong laser case of Fig. 6.4, where the amplitude of the Fe mode is reduced to zero, in Fig. 6.14 the Fe moments remain finite but freeze into one of the canting configurations seen above. The reason behind this must

be that the laser excitation disrupts the exchange coupling between the nearest Fe atoms, causing the magnon mode to freeze into a spin spiral configuration. Extending the delay by half a period of the magnon oscillation will result in a canting vector pointing in opposite direction.

Hence the direction of the canting vector is dependent on the time delay of the incident laser pulse. This indicates that with a careful choice of laser pulse a ferromagnetic metal can be made to be transiently non-collinear with a certain degree of control over the angle between inter-site spins.

6.3.6 Magnon frequency change

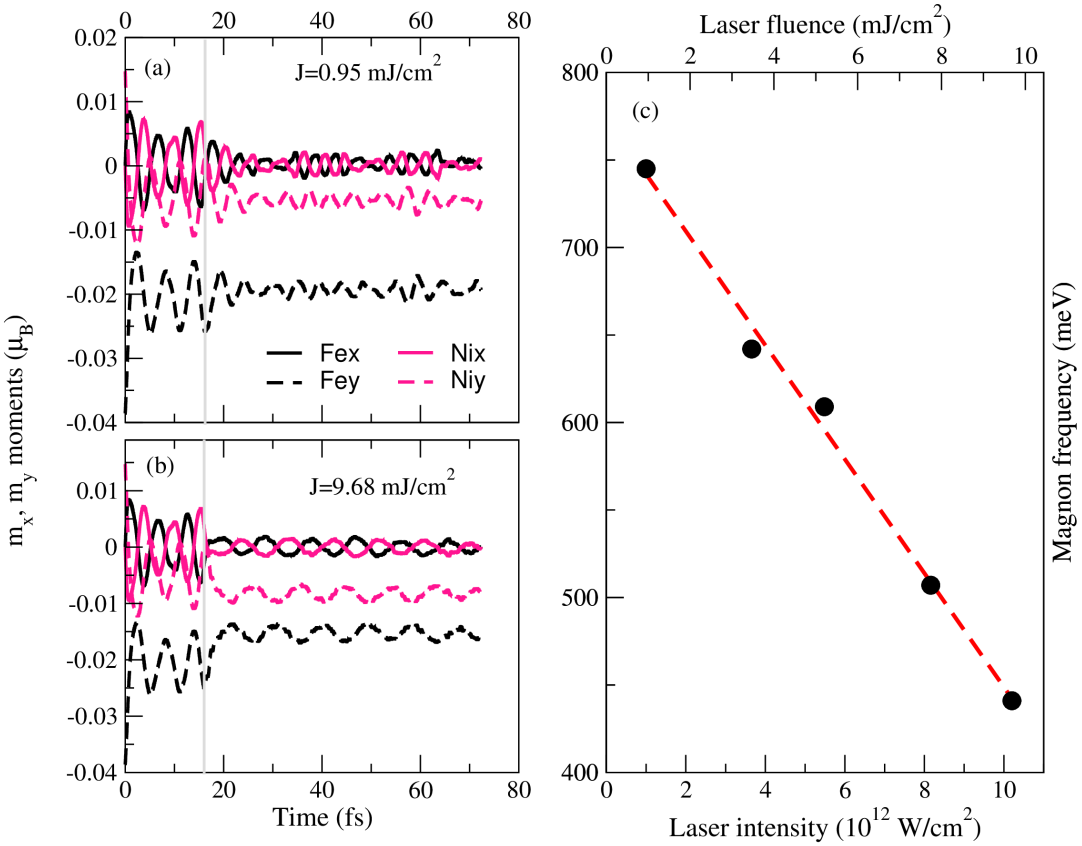

Figure 6.15: The change in magnon frequency is shown for two laser pulse of fluences (a) 0.9537 mJ/cm^2 and (b) 9.680 mJ/cm^2. (c) The magnon frequency decreases with the increase in intensity of applied laser pulse. The vertical lines corresponds to the peak of the laser.

The frequency of the magnon modes can also be manipulated by the pump-laser pulse. To demonstrate this, the optical mode is excited, and then its dynamics under the influence of pulses of differing fluences is studied. The results, for two different laser fluences (0.9537 mJ/cm^2 and 9.680 mJ/cm^2) are shown in Figs. 6.15 (a) and (b) where it is clear that the oscillations are strongly influenced by the laser. Fourier transform of the transverse moment

during these oscillations gives the new frequency of the magnon mode and this is plotted, as function of laser intensity, in Fig. 6.15 (c). The main reason behind this change in frequency is the weakened exchange field between the magnetic sub-lattices[73] due to two processes, both of which lead to increased screening– (a) excitation of electrons to high lying delocalized states and (b) transfer of localized charge from one atom to the other. This implies that the stronger this charge transfer is, the greater the change in the magnon frequency, a fact that is reflected in the linear dependence of the magnon frequency on the pump-pulse fluence (Fig. 6.15(c)). Recall that the moment transferred is also linearly dependent on the intensity, as seen in Fig. 6.3. At some higher intensity where the charge excitation process saturates, so would the change in the magnon frequency. Thus optical excitations offers a direct control of the frequency of a coupled magnon mode of two sub-lattices via tuning of the fluence of the laser pulse. Since OISTR effects are very strong on AFM coupled systems, we expect very large changes in magnon modes when pumped with lasers.

6.3.7 FWHM dependence

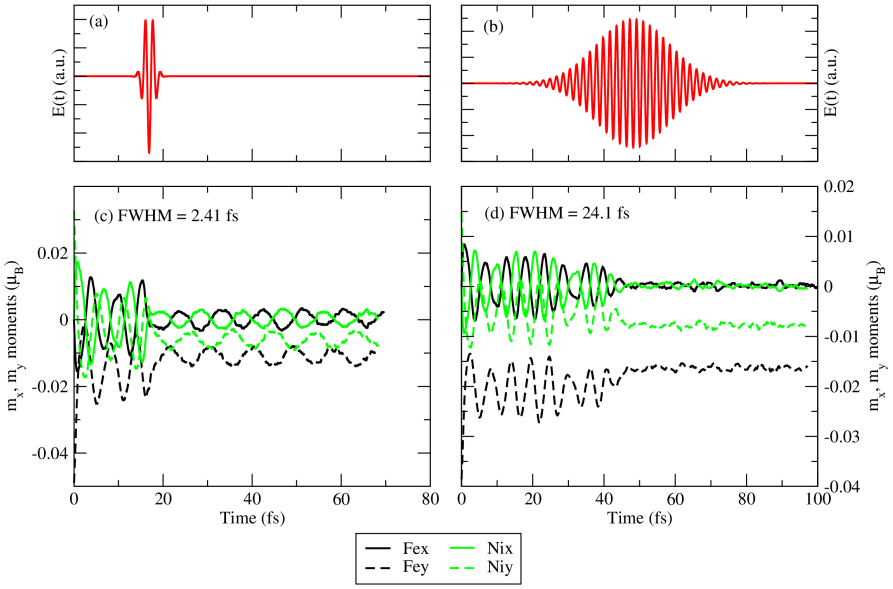

Figure 6.16: The oscillations of transverse moments of the optical magnon mode during laser excitation with pulses of fluence 9.68 mJ/cm^2 but with different duration of (a) 2.41 fs peaks at 16.8 fs and (b) 24.1 fs peaks at 48.2 fs.

In the following the section the affect of the duration of the pulse on the magnon modes is investigated. Specifically we ask if the frequency modification seen in the previous section is only a short pulse phenomena, or whether it is more general. We find that the longer laser pulse does indeed change the frequency of the optical mode. For this study a pump with a fixed fluence of 9.68 mJ/cm^2 and frequency 2.19 eV but having two different FWHMs of (a)

2.41 fs and (b) 24.1 fs was used. The results obtained by using these two pulses of different durations is shown in Fig. 6.16.

From the results it can be seen that the longer duration pulse also changes the magnon frequency which can been seen from the Fourier transform in Fig. 6.17. The short duration pulse (2.41 fs) changes the magnon frequency from 740 meV (no laser pulse) to 440 meV (green color in Fig. 6.17) while the longer duration pulse, changes the magnon frequency to 520 meV (pink color in Fig. 6.17). In the same figure there is another Fourier transform (black color) corresponding to the new magnon frequency obtained following a laser pulse with fluence 7.74 mJ/cm^2, FWHM 2.41 fs, frequency 2.19 eV. This pulse was chosen as both it and the longer duration pulse have the same amount of moment transfer. Hence, it can be inferred that the change in magnon frequency depends on the amount of z-moment change and not on individual pulse parameters.

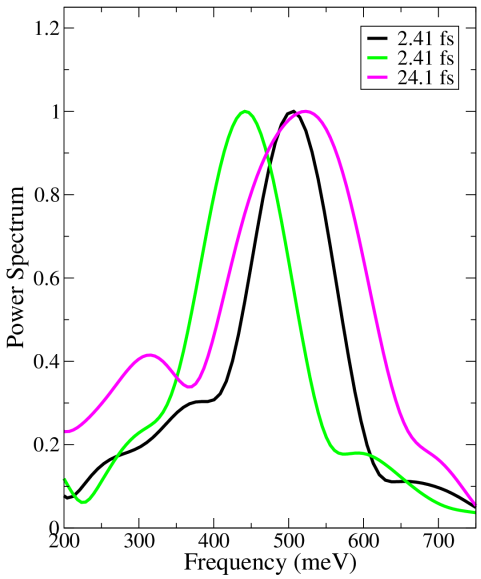

Figure 6.17: The Fourier transform of the transverse moments for pulse 9.68 mJ/cm^2 with duration of 2.41 fs peaks at 16.8 fs (green) and 24.1 fs peaks at 48.2 fs (pink). These are compared with a pump of fluence 7.74 mJ/cm^2 and width 2.41 fs (black).

To summarize, in this chapter it was shown that fundamental properties of the magnon can be controlled by applying optical laser pulse. The main results are:

- By tuning the intensity of the laser pulse one can destroy certain magnon modes. These can also be controlled by changing the frequency of the laser pulse.
- By controlling the time delay of the laser pulse the freezing of the magnon modes into non-collinear spin spiral state can be controlled.
- The optical mode frequency can be changed by changing the intensity of the laser; the frequency decreases linearly with increase in intensity.

CHAPTER 7

CONCLUSION

Stop wishing, Start Spinning ·····
- Cycling advertisement

In this work optical and magnetic excitations have been studied for extended systems within the linear and non-linear regimes, using time-dependent density functional theory. In the linear regime, the AGGA kernel was derived, implemented in the all-electron ELK code, and then applied to study excitations. Then these studies were extended to real-time TDDFT for the low lying collective magnetic excitations including their dynamics in highly out-of-equilibrium regime.

As we climb up the rung of *Jacob's ladder* the accuracy of XC functionals should increase. For example, the GGAs are known to improve over the LDA functional for predicting many physical properties. This was the motivation to derive the kernel for the GGA functionals and study excitations within LR-TDDFT. Only by implementing, assessing, and understanding the behavior of adiabatic functionals can one gain insight into the relevant features necessary for accurate XC kernels, which can guide us towards improvement or in developing new approximations in TDDFT. In chapter 3, this was derived both for collinear and non-collinear systems along with practical considerations concerning its implementation in the ELK code. An exact condition, the zero torque theorem for the kernel, was also derived.

In chapter 4, the charge and spin excitation spectra using the gradient dependent AGGA XC kernel within the linear response regime of TDDFT was studied. The calculated EELS for LiF and diamond show that the AGGA kernel performs slightly better than the ALDA kernel, although, as would be expected, neither captures excitonic effects. For magnon dispersions, AGGA, in general, does not systematically improve upon ALSDA. This is due to the fact that the GGA XC functional overestimates the exchange splitting which in turn leads to higher magnon energies. Furthermore, the intensity of the peaks is greatly suppressed in the spectra obtained by the AGGA XC kernel due to interaction of spin-waves with the Stoner continuum. This suppression is also observed in experiments, suggesting AGGA might provide better qualitative understanding than ALSDA. Heusler materials consisting of multiple magnetic sublattices were also studied, where it was found that AGGA is better at resolving higher-energy optical magnon branches.

In chapter 5, the domain of TDDFT simulations was extended to include magnon dynamics in real-time. The magnon modes found in ferromagnetic iron and $Fe_{50}Ni_{50}$ alloy were

investigated. It was found that element specific magnon modes exist in $Fe_{50}Ni_{50}$ alloy consistent with experimental observation of different spin dynamics of the iron and nickel atoms in this alloy. The real-time TDDFT simulations were mutually verified by comparing to linear response calculations. In this regard a real-time GGA calculation was performed for nickel which confirmed the findings in chapter 4, principally the overestimation of energies when compared with LDA. This shows RT-TDDFT is a powerful tool for visualizing magnons and study their dynamics.

In the last chapter, TDDFT simulations were done to study interaction of laser pulses with the magnon modes in real-time. This opens the field of laser-coupled magnonics to *ab-initio* theory. There were three major findings by which ultrafast laser pulses can control magnon dynamics: (1) selective destruction of particular magnon modes where the pure Ni and pure Fe modes could be destroyed depending on the laser intensity, (2) laser-controlled canting of Fe moments where the time delay relative to the pure Fe oscillations controlled which canted state the system evolves to, and (3) OISTR-driven renormalization of the optical magnon frequency where we found a linear dependence between the laser intensity (or moment transferred) and the decrease of the magnon frequency. In all cases the outcomes were achieved on ultrafast timescales thus demonstrating the potential of laser control of magnonics for future technology.

BIBLIOGRAPHY

[1] I. Žutić, J. Fabian, and S. Das Sarma, "Spintronics: Fundamentals and applications," *Rev. Mod. Phys.*, vol. 76, pp. 323–410, Apr 2004.

[2] S. Bader and S. Parkin, "Spintronics," *Annual Review of Condensed Matter Physics*, vol. 1, no. 1, pp. 71–88, 2010.

[3] V. Baltz, A. Manchon, M. Tsoi, T. Moriyama, T. Ono, and Y. Tserkovnyak, "Antiferromagnetic spintronics," *Rev. Mod. Phys.*, vol. 90, p. 015005, Feb 2018.

[4] J. Heidecker, "Mram technology status," 2013.

[5] G. Binasch, P. Grünberg, F. Saurenbach, and W. Zinn, "Enhanced magnetoresistance in layered magnetic structures with antiferromagnetic interlayer exchange," *Phys. Rev. B*, vol. 39, pp. 4828–4830, Mar 1989.

[6] M. N. Baibich, J. M. Broto, A. Fert, F. N. Van Dau, F. Petroff, P. Etienne, G. Creuzet, A. Friederich, and J. Chazelas, "Giant magnetoresistance of (001)fe/(001)cr magnetic superlattices," *Phys. Rev. Lett.*, vol. 61, pp. 2472–2475, Nov 1988.

[7] E. Beaurepaire, J.-C. Merle, A. Daunois, and J.-Y. Bigot, "Ultrafast spin dynamics in ferromagnetic nickel," *Phys. Rev. Lett.*, vol. 76, pp. 4250–4253, 1996.

[8] K. Vahaplar, A. M. Kalashnikova, A. V. Kimel, S. Gerlach, D. Hinzke, U. Nowak, R. Chantrell, A. Tsukamoto, A. Itoh, A. Kirilyuk, and T. Rasing, "All-optical magnetization reversal by circularly polarized laser pulses: Experiment and multiscale modeling," *Phys. Rev. B*, vol. 85, p. 104402, Mar 2012.

[9] A. A. Serga, A. V. Chumak, and B. Hillebrands, "YIG magnonics," *Journal of Physics D: Applied Physics*, vol. 43, p. 264002, jun 2010.

[10] G. Gubbiotti, S. Tacchi, M. Madami, G. Carlotti, A. O. Adeyeye, and M. Kostylev, "Brillouin light scattering studies of planar metallic magnonic crystals," *Journal of Physics D: Applied Physics*, vol. 43, p. 264003, jun 2010.

[11] V. V. Kruglyak, S. O. Demokritov, and D. Grundler, "Magnonics," *Journal of Physics D: Applied Physics*, vol. 43, p. 260301, jun 2010.

[12] T. Kampfrath, A. Sell, G. Klatt, A. Pashkin, S. Mährlein, T. Dekorsy, M. Wolf, M. Fiebig, A. Leitenstorfer, and R. Huber, "Coherent terahertz control of antiferromagnetic spin waves," *Nature Photonics*, vol. 5, 2010.

[13] R. Prasad, *Electronic Structure of Materials*. CRC Press: Taylor and Francis Group, 2014.

[14] P. Hohenberg and W. Kohn, "Inhomogeneous electron gas," *Phys. Rev.*, vol. 136, pp. B864–B871, Nov 1964.

[15] U. von Barth and L. Hedin, "A local exchange-correlation potential for the spin polarized case. i," *Journal of Physics C: Solid State Physics*, vol. 5, pp. 1629–1642, jul 1972.

[16] J. Kubler, K.-H. Hock, S. J., and A. R. Williams, "Density functional theory of noncollinear magnetism," *J. Phys. F: Met. Phys.*, vol. 18, p. 469, 1988.

[17] J. P. Perdew and K. Schmidt, "Jacob's ladder of density functional approximations for the exchange-correlation energy," *AIP Conference Proceedings*, vol. 577, no. 1, pp. 1–20, 2001.

[18] L. Goerigk and N. Mehta, "A trip to the density functional theory zoo: Warnings and recommendations for the user," *Australian Journal of Chemistry*, 2019.

[19] J. P. Perdew and Y. Wang, "Accurate and simple analytic representation of the electron-gas correlation energy," *Phys. Rev. B*, vol. 45, pp. 13244–13249, Jun 1992.

[20] D. Langreth and J. Perdew, "The gradient approximation to the exchange-correlation energy functional: A generalization that works," *Solid State Communications*, vol. 31, no. 8, pp. 567 – 571, 1979.

[21] O. Gunnarsson and B. I. Lundqvist, "Exchange and correlation in atoms, molecules, and solids by the spin-density-functional formalism," *Phys. Rev. B*, vol. 13, pp. 4274–4298, May 1976.

[22] D. C. Langreth and J. P. Perdew, "Exchange-correlation energy of a metallic surface: Wave-vector analysis," *Phys. Rev. B*, vol. 15, pp. 2884–2901, Mar 1977.

[23] K. Burke, J. P. Perdew, and M. Ernzerhof, "Why semilocal functionals work: Accuracy of the on-top pair density and importance of system averaging," *The Journal of Chemical Physics*, vol. 109, no. 10, pp. 3760–3771, 1998.

[24] J. P. Perdew, "Accurate density functional for the energy: Real-space cutoff of the gradient expansion for the exchange hole," *Phys. Rev. Lett.*, vol. 55, pp. 2370–2370, Nov 1985.

[25] J. P. Perdew, "Accurate density functional for the energy: Real-space cutoff of the gradient expansion for the exchange hole," *Phys. Rev. Lett.*, vol. 55, pp. 1665–1668, Oct 1985.

[26] G. L. Oliver and J. P. Perdew, "Spin-density gradient expansion for the kinetic energy," *Phys. Rev. A*, vol. 20, pp. 397–403, Aug 1979.

[27] M. Levy and J. P. Perdew, "Hellmann-feynman, virial, and scaling requisites for the exact universal density functionals. shape of the correlation potential and diamagnetic susceptibility for atoms," *Phys. Rev. A*, vol. 32, pp. 2010–2021, Oct 1985.

[28] M. Levy and J. P. Perdew, "Tight bound and convexity constraint on the exchange-correlation-energy functional in the low-density limit, and other formal tests of generalized-gradient approximations," *Phys. Rev. B*, vol. 48, pp. 11638–11645, Oct 1993.

[29] E. H. Lieb and S. Oxford, "Improved lower bound on the indirect coulomb energy," *International Journal of Quantum Chemistry*, vol. 19, no. 3, pp. 427–439, 1981.

[30] G. Kin-Lic Chan and N. C. Handy, "Optimized lieb-oxford bound for the exchange-correlation energy," *Phys. Rev. A*, vol. 59, pp. 3075–3077, Apr 1999.

[31] P. Elliott, D. Lee, A. Cangi, and K. Burke, "Semiclassical origins of density functionals," *Phys. Rev. Lett.*, vol. 100, p. 256406, Jun 2008.

[32] R. O. Jones and O. Gunnarsson, "The density functional formalism, its applications and prospects," *Rev. Mod. Phys.*, vol. 61, pp. 689–746, Jul 1989.

[33] J. P. Perdew and Y. Wang, "Accurate and simple analytic representation of the electron-gas correlation energy," *Phys. Rev. B*, vol. 45, pp. 13244–13249, Jun 1992.

[34] J. P. Perdew, K. Burke, and M. Ernzerhof, "Generalized gradient approximation made simple," *Phys. Rev. Lett.*, vol. 77, pp. 3865–3868, 1996.

[35] R. Armiento and A. E. Mattsson, "Functional designed to include surface effects in self-consistent density functional theory," *Phys. Rev. B*, vol. 72, p. 085108, Aug 2005.

[36] G. I. Csonka, J. P. Perdew, A. Ruzsinszky, P. H. T. Philipsen, S. Lebègue, J. Paier, O. A. Vydrov, and J. G. Ángyán, "Assessing the performance of recent density functionals for bulk solids," *Phys. Rev. B*, vol. 79, p. 155107, Apr 2009.

[37] J. P. Perdew, S. Kurth, A. c. v. Zupan, and P. Blaha, "Accurate density functional with correct formal properties: A step beyond the generalized gradient approximation," *Phys. Rev. Lett.*, vol. 82, pp. 2544–2547, Mar 1999.

[38] J. P. Perdew, S. Kurth, A. b. u. Zupan, and P. Blaha, "Erratum: Accurate density functional with correct formal properties: A step beyond the generalized gradient approximation [phys. rev. lett. 82, 2544 (1999)]," *Phys. Rev. Lett.*, vol. 82, pp. 5179–5179, Jun 1999.

[39] T. Van Voorhis and G. E. Scuseria, "A novel form for the exchange-correlation energy functional," *The Journal of Chemical Physics*, vol. 109, no. 2, pp. 400–410, 1998.

[40] E. Runge and E. K. U. Gross, "Density-functional theory for time-dependent systems," *Phys. Rev. Lett.*, vol. 52, pp. 997–1000, 1984.

[41] S. Sharma, J. K. Dewhurst, and E. K. U. Gross, "Optical response of extended systems using time-dependent density functional theory," *"First Principles Approaches to Spectroscopic Properties of Complex Materials", Eds. C. Di Valentin, S. Botti and M. Cococcioni, Topics in Current Chemistry*, vol. 347, pp. 235–257, 2014.

[42] F. Sottile, V. Olevano, and L. Reining, "Parameter-free calculation of response functions in time-dependent density-functional theory," *Phys. Rev. Lett.*, vol. 91, p. 056402, 2003.

[43] I. Campillo, A. Rubio, and J. M. Pitarke, "Ab initio calculations of the dynamical response of copper," *Phys. Rev. B*, vol. 59, pp. 12188–12191, 1999.

[44] S. Botti, N. Vast, L. Reining, V. Olevano, and L. C. Andreani, "Ab initio and semiempirical dielectric response of superlattices," *Phys. Rev. B*, vol. 70, p. 045301, 2004.

[45] S. L. Adler, "Quantum theory of the dielectric constant in real solids," *Phys. Rev.*, vol. 126, pp. 413–420, Apr 1962.

[46] N. Wiser, "Dielectric constant with local field effects included," *Phys. Rev.*, vol. 129, pp. 62–69, Jan 1963.

[47] L. Reining, V. Olevano, A. Rubio, and G. Onida, "Excitonic effects in solids described by time-dependent density-functional theory," *Phys. Rev. Lett.*, vol. 88, p. 066404, 2002.

[48] S. Botti, F. Sottile, N. Vast, V. Olevano, L. Reining, H.-C. Weissker, A. Rubio, G. Onida, R. Del Sole, and R. W. Godby, "Long-range contribution to the exchange-correlation kernel of time-dependent density functional theory," *Phys. Rev. B*, vol. 69, p. 155112, 2004.

[49] S. Sharma, J. K. Dewhurst, A. Sanna, A. Rubio, and E. K. U. Gross, "Enhanced excitonic effects in the energy loss spectra of lif and ar at large momentum transfer," *New Journal of Physics*, vol. 14, no. 5, p. 053052, 2012.

[50] S. Sharma, J. K. Dewhurst, A. Sanna, and E. K. U. Gross, "Bootstrap approximation for the exchange-correlation kernel of time-dependent density-functional theory," *Phys. Rev. Lett.*, vol. 107, p. 186401, 2011.

[51] F. Sottile, K. Karlsson, L. Reining, and F. Aryasetiawan, "Macroscopic and microscopic components of exchange-correlation interactions," *Phys. Rev. B*, vol. 68, p. 205112, 2003.

[52] J. C. Slater, "The theory of ferromagnetism: Lowest energy levels," *Phys. Rev.*, vol. 52, pp. 198–214, Aug 1937.

[53] C. Herring and C. Kittel, "On the theory of spin waves in ferromagnetic media," *Phys. Rev.*, vol. 81, pp. 869–880, Mar 1951.

[54] C. Herring and C. Kittel, "The theory of spin waves in ferromagnetic media," *Phys. Rev.*, vol. 88, pp. 1435–1435, Dec 1952.

[55] J. W. Lynn and H. A. Mook, "Temperature dependence of the dynamic susceptibility of nickel," *Phys. Rev. B*, vol. 23, pp. 198–206, 1981.

[56] F. Essenberger, S. Sharma, J. K. Dewhurst, C. Bersier, F. Cricchio, L. Nordström, and E. K. U. Gross, "Magnon spectrum of transition-metal oxides: Calculations including long-range magnetic interactions using the LSDA + u method," *Phys. Rev. B*, vol. 84, p. 174425, 2011.

[57] S. V. Halilov, A. Y. Perlov, P. M. Oppeneer, and H. Eschrig, "Magnon spectrum and related finite-temperature magnetic properties: A first-principle approach," *EPL (Europhysics Letters)*, vol. 39, no. 1, p. 91, 1997.

[58] M. Pajda, J. Kudrnovský, I. Turek, V. Drchal, and P. Bruno, "Ab initio calculations of exchange interactions, spin-wave stiffness constants, and curie temperatures of fe, co, and ni," *Phys. Rev. B*, vol. 64, p. 174402, Oct 2001.

[59] K. Yabana, T. Nakatsukasa, J.-I. Iwata, and G. F. Bertsch, "Real-time, real-space implementation of the linear response time-dependent density-functional theory," *physica status solidi (b)*, vol. 243, no. 5, pp. 1121–1138, 2006.

[60] K. Krieger, *Spin-Dynamics in Strongly Excited Ferromagnetic Systems*. PhD thesis, Martin-Luther-Universität, Halle-Wittenberg, 2016.

[61] M. Panholzer, M. Gatti, and L. Reining, "Nonlocal and nonadiabatic effects in the charge-density response of solids: A time-dependent density-functional approach," *Phys. Rev. Lett.*, vol. 120, p. 166402, Apr 2018.

[62] A. V. Terentjev, L. A. Constantin, and J. M. Pitarke, "Gradient-dependent exchange-correlation kernel for materials optical properties," *Phys. Rev. B*, vol. 98, p. 085123, Aug 2018.

[63] J. Paier, M. Marsman, and G. Kresse, "Dielectric properties and excitons for extended systems from hybrid functionals," *Phys. Rev. B*, vol. 78, p. 121201, Sep 2008.

[64] S. Refaely-Abramson, M. Jain, S. Sharifzadeh, J. B. Neaton, and L. Kronik, "Solid-state optical absorption from optimally tuned time-dependent range-separated hybrid density functional theory," *Phys. Rev. B*, vol. 92, p. 081204, Aug 2015.

[65] C. A. Ullrich and Z. Yang, "Excitons in time-dependent density-functional theory," *Top Curr. Chem.*, vol. 368, pp. 185–218, 2016.

[66] A. Marini, R. Del Sole, and A. Rubio, "Bound excitons in time-dependent density-functional theory: Optical and energy-loss spectra," *Phys. Rev. Lett.*, vol. 91, p. 256402, 2003.

[67] M. Hellgren and U. von Barth, "Exact-exchange kernel of time-dependent density functional theory: Frequency dependence and photoabsorption spectra of atoms," *The Journal of Chemical Physics*, vol. 131, no. 4, p. 044110, 2009.

[68] F. Sottile, K. Karlsson, L. Reining, and F. Aryasetiawan, "Macroscopic and microscopic components of exchange-correlation interactions," *Phys. Rev. B*, vol. 68, p. 205112, 2003.

[69] F. Sottile, V. Olevano, and L. Reining, "Parameter-free calculation of response functions in time-dependent density-functional theory," *Phys. Rev. Lett.*, vol. 91, p. 056402, 2003.

[70] V. U. Nazarov and G. Vignale, "Optics of semiconductors from meta-generalized-gradient-approximation-based time-dependent density-functional theory," *Phys. Rev. Lett.*, vol. 107, p. 216402, 2011.

[71] P. Buczek, A. Ernst, and L. M. Sandratskii, "Different dimensionality trends in the landau damping of magnons in iron, cobalt, and nickel: Time-dependent density functional study," *Phys. Rev. B*, vol. 84, p. 174418, 2011.

[72] B. Rousseau, A. Eiguren, and A. Bergara, "Efficient computation of magnon dispersions within time-dependent density functional theory using maximally localized wannier functions," *Phys. Rev. B*, vol. 85, p. 054305, 2012.

[73] F. Essenberger, S. Sharma, J. K. Dewhurst, C. Bersier, F. Cricchio, L. Nordström, and E. K. U. Gross, "Magnon spectrum of transition-metal oxides: Calculations including long-range magnetic interactions using the lsda+u method," *Phys. Rev. B*, vol. 84, p. 174425, Nov 2011.

[74] K. Karlsson and F. Aryasetiawan, "A many-body approach to spin-wave excitations in itinerant magnetic systems," *Journal of Physics: Condensed Matter*, vol. 12, no. 34, p. 7617, 2000.

[75] M. C. T. D. Müller, C. Friedrich, and S. Blügel, "Acoustic magnons in the long-wavelength limit: Investigating the goldstone violation in many-body perturbation theory," *Phys. Rev. B*, vol. 94, p. 064433, 2016.

[76] S. Y. Savrasov, "Linear response calculations of spin fluctuations," *Phys. Rev. Lett.*, vol. 81, pp. 2570–2573, 1998.

[77] D. Egli and S. R. Billeter, "Analytic second variational derivative of the exchange-correlation functional," *Phys. Rev. B*, vol. 69, p. 115106, 2004.

[78] A. Dal Corso, S. Baroni, and R. Resta, "Density-functional theory of the dielectric constant: Gradient-corrected calculation for silicon," *Phys. Rev. B*, vol. 49, pp. 5323–5328, 1994.

[79] S. Lehtola, C. Steigemann, M. J. Oliveira, and M. A. Marques, "Recent developments in libxc — a comprehensive library of functionals for density functional theory," *SoftwareX*, vol. 7, pp. 1 – 5, 2018.

[80] M. A. Marques, M. J. Oliveira, and T. Burnus, "Libxc: A library of exchange and correlation functionals for density functional theory," *Computer Physics Communications*, vol. 183, no. 10, pp. 2272 – 2281, 2012.

[81] S. Sharma, J. K. Dewhurst, C. Ambrosch-Draxl, S. Kurth, N. Helbig, S. Pittalis, S. Shallcross, L. Nordström, and E. K. U. Gross, "First-principles approach to noncollinear magnetism: Towards spin dynamics," *Phys. Rev. Lett.*, vol. 98, p. 196405, May 2007.

[82] `elk.sourceforge.net`.

[83] G. Vignale, "Center of mass and relative motion in time dependent density functional theory," *Phys. Rev. Lett.*, vol. 74, pp. 3233–3236, Apr 1995.

[84] K. Capelle, G. Vignale, and B. L. Györffy, "Spin currents and spin dynamics in time-dependent density-functional theory," *Phys. Rev. Lett.*, vol. 87, p. 206403, Oct 2001.

[85] F. G. Eich and E. K. U. Gross, "Transverse spin-gradient functional for noncollinear spin-density-functional theory," *Phys. Rev. Lett.*, vol. 111, p. 156401, Oct 2013.

[86] W. Setyawan and S. Curtarolo, "High-throughput electronic band structure calculations: Challenges and tools," *Computational Materials Science*, vol. 49, no. 2, pp. 299 – 312, 2010.

[87] S. Sharma, J. K. Dewhurst, S. Shallcross, G. K. Madjarova, and E. K. U. Gross, "Excitons in organics using time-dependent density functional theory: Ppv, pentacene, and picene," *Journal of Chemical Theory and Computation*, vol. 11, no. 4, pp. 1710–1714, 2015.

[88] D. Azhikodan, T. Nautiyal, S. Shallcross, and S. Sharma, "An anomalous interlayer exciton in mos_2," *Scientific Reports*, vol. 6, no. 37075, 2016.

[89] P. Ghosez, X. Gonze, and R. W. Godby, "Long-wavelength behavior of the exchange-correlation kernel in the kohn-sham theory of periodic systems," *Phys. Rev. B*, vol. 56, pp. 12811–12817, 1997.

[90] W. A. Caliebe, J. A. Soininen, E. L. Shirley, C.-C. Kao, and K. Hämäläinen, "Dynamic structure factor of diamond and lif measured using inelastic x-ray scattering," *Phys. Rev. Lett.*, vol. 84, pp. 3907–3910, 2000.

[91] D. L. Abraham and H. Hopster, "Spin-polarized electron-energy-loss spectroscopy on ni," *Phys. Rev. Lett.*, vol. 62, pp. 1157–1160, Mar 1989.

[92] J. Hong and D. L. Mills, "Spin dependence of the inelastic electron mean free path in fe and ni: Explicit calculations and implications," *Phys. Rev. B*, vol. 62, pp. 5589–5600, Sep 2000.

[93] R. D. Lowde and C. G. Windsor, "Generalized susceptibility of nickel," *Phys. Rev. Lett.*, vol. 18, pp. 1136–1138, Jun 1967.

[94] J. F. Cooke, "Neutron scattering from itinerant-electron ferromagnets," *Phys. Rev. B*, vol. 7, pp. 1108–1116, Feb 1973.

[95] E. Şaşıoğlu, A. Schindlmayr, C. Friedrich, F. Freimuth, and S. Blügel, "Wannier-function approach to spin excitations in solids," *Phys. Rev. B*, vol. 81, p. 054434, 2010.

[96] T. A., "Lattice parameters of binary nickel cobalt alloys," *Journal of the Institute of metals*, vol. 77, pp. 585–594, 1950.

[97] V. Iota, J.-H. P. Klepeis, C.-S. Yoo, J. Lang, D. Haskel, and G. Srajer, "Electronic structure and magnetism in compressed 3d transition metals," *Applied Physics Letters*, vol. 90, no. 4, p. 042505, 2007.

[98] F. Vincent and M. Figlarz, "A few precisions on crystalline parameters and intensity of debye-scherrer rays of cobalt cubic and cobalt hexagonal," *Weekly Records of the Academy of science series C*, vol. 264, p. 1270, 1967.

[99] M. S. edited by H. Wijn and Landolt-Börnstein, *Magnetic Properties in Metals*, vol. 3. Springer, 1986.

[100] R. Kohlhaas, P. Dünner, and S. .N, "On the temperature dependence of the grid parameters of iron, cobalt and nickel in the field of high temperatures," *Z. Angewandte Phys.*, vol. 23, p. 245, 1967.

[101] D. Bonnenberg, K. Hempel, H. W. edited by H. Wijn, and Landolt-Börnstein, *Magnetic Properties in Metals*, vol. 3. Springer, 1986.

[102] H. A. Mook and D. M. Paul, "Neutron-scattering measurement of the spin-wave spectra for nickel," *Phys. Rev. Lett.*, vol. 54, pp. 227–229, 1985.

[103] T. Balashov, *STM and STS investigation of magnetic nanostructures, inelastic magnetic excitations, magneto-electric coupling, surface science.* PhD thesis, Physikalisches Institut, Universität Karlsruhe (TH), Karlsruhe, 2009.

[104] J. W. Lynn, "Temperature dependence of the magnetic excitations in iron," *Phys. Rev. B*, vol. 11, pp. 2624–2637, 1975.

[105] A. Schindlmayr, C. Friedrich, E. Sasioglu, and S. Blügel, "First-principles calculation of electronic excitations in solids with spex," *Zeitschrift für Physikalische Chemie*, vol. 224, p. 357, 2010.

[106] A. Arno Schindlmayr, C. Friedrich, Şaşıo ğlu E., and S. Blügel, "First-principles calculation of electronic excitations in solids with spex," *Zeitschrift für Physikalische Chemie*, vol. 224, pp. 357–368, 2010.

[107] H. Kronmüller and P. S., *Handbook of Magnetism and Advanced Magnetic Materials*, vol. 1. Wiley, 2007.

[108] T. G. Perring, A. T. Boothroyd, D. M. Paul, A. D. Taylor, R. Osborn, R. J. Newport, J. A. Blackman, and H. A. Mook, "High-energy spin waves in bcc iron," *Journal of Applied Physics*, vol. 69, no. 8, pp. 6219–6221, 1991.

[109] P. Buczek, A. Ernst, P. Bruno, and L. M. Sandratskii, "Energies and lifetimes of magnons in complex ferromagnets: A first-principle study of heusler alloys," *Phys. Rev. Lett.*, vol. 102, p. 247206, 2009.

[110] C. Hordequin, J. Pierre, and R. Currat, "How do magnetic excitations behave in half metallic ferromagnets? the case of nimnsb," *Physica B: Condensed Matter*, vol. 234-236, pp. 605 – 607, 1997.

[111] E. Şaşıoğlu, L. M. Sandratskii, P. Bruno, and I. Galanakis, "Exchange interactions and temperature dependence of magnetization in half-metallic heusler alloys," *Phys. Rev. B*, vol. 72, p. 184415, Nov 2005.

[112] H. C. Kandpal, G. H. Fecher, C. Felser, and G. Schönhense, "Correlation in the transition-metal-based heusler compounds co_2MnSi and co_2FeSi," *Phys. Rev. B*, vol. 73, p. 094422, Mar 2006.

[113] R. Helmholdt, R. de Groot, F. Mueller, P. van Engen, and K. Buschow, "Magnetic and crystallographic properties of several c1b type heusler compounds," *Journal of Magnetism and Magnetic Materials*, vol. 43, no. 3, pp. 249 – 255, 1984.

[114] S. Mathias, C. La-O-Vorakiat, P. Grychtol, P. Granitzka, E. Turgut, J. M. Shaw, R. Adam, H. T. Nembach, M. E. Siemens, S. Eich, C. M. Schneider, T. J. Silva, M. Aeschlimann, M. M. Murnane, and H. C. Kapteyn, "Probing the timescale of the exchange interaction in a ferromagnetic alloy," *Proceedings of the National Academy of Sciences*, vol. 109, no. 13, pp. 4792–4797, 2012.

[115] P. Elliott, T. Müller, J. K. Dewhurst, S. Sharma, and E. K. U. Gross, "Ultrafast laser induced local magnetization dynamics in heusler compounds," *Scientific Reports*, vol. 6, no. 38911, 2016.

[116] J. K. Dewhurst, P. Elliott, S. Shallcross, E. K. U. Gross, and S. Sharma, "Laser-induced intersite spin transfer," *Nano Letters*, vol. 18, no. 3, pp. 1842–1848, 2018.

[117] D. Steil *et al.*, "Experimental evidence for optically induced ultrafast local spin dynamics in multisublattice ferromagnets," *in prep.*, 2019.

[118] J. Chen, U. Bovensiepen, A. Eschenlohr, T. Müller, P. Elliott, E. K. U. Gross, J. K. Dewhurst, and S. Sharma, "Competing spin transfer and dissipation at Co/Cu(001) interfaces on femtosecond timescales," *Phys. Rev. Lett.*, vol. 122, p. 067202, Feb 2019.

[119] F. Siegrist, J. A. Gessner, M. Ossiander, C. Denker, Y. Chang, A. Schroeder, M. C.and Guggenmos, Y. Cui, U. Walowski, J.J.and Martens, J. K. Dewhurst, U. Kleineberg, M. Muenzenberg, S. Sharma, and M. Schultze, "Petahertz spintronics," *arXiv:1812.07420*, 2019.

PUBLICATIONS

- K. Krieger, P. Elliott, T. Müller, **N. Singh**, J. K. Dewhurst, E. K. U. Gross and S. Sharma
  Ultrafast demagnetization in bulk versus thin films: an ab-initio study
  J. Phys.: Condens. Matter 29, 224001 (2017).

  This paper was chosen as 2017 highlights and was free to read for the year 2018.

- **N. Singh** and S. Sharma
  Ultrafast demagnetization dependence on layer thickness: A TDDFT calculation
  AIP Conference Proceedings 1942, 130014 (2018).

- **N. Singh**, P. Elliott, T. Nautiyal, J. K. Dewhurst, and S. Sharma
  Adiabatic generalized gradient approximation kernel in time-dependent density functional theory
  Phys. Rev. B 99, 035151 (2019)

- Jyoti Krishna, **N. Singh**, S. Shallcross, J. K. Dewhurst, E. K. U. Gross, T. Maitra, and S. Sharma
  Source-free LSDA+U functional: a complete description of magnetism in spinel vanadates
  Phys. Rev. B 100, 081102(R) (2019)

- **N. Singh**, P. Elliott, J.K. Dewhurst, and S. Sharma
  Coherent optical control of magnons: ab-initio predictions
  arXiv:1906.12270 [cond-mat.mtrl-sci]
  (In communication)

- P. Elliott, **N. Singh**, K. Krieger, E.K.U. Gross, S. Sharma, J.K. Dewhurst
  The microscopic origin of spin-orbit mediated spin-flips
  (under review JMMM (2019))

ACKNOWLEDGEMENTS

Foremost, I would like to show my gratitude toward my former supervisor Prof. Tashi Nautiyal with whom I started the journey of research. It was she who introduced me to the idea of Density Functional Theory and also to Dr. Sangeeta Sharma, who is my present supervisor. I would like to thank her for supporting me in my decisions and having faith in me. She gave me the freedom to pursue my own ideas and also created a friendly environment to work. It was enlightening to have discussions with John Kay Dewhurst and Antonio Sanna regarding their expertise in magnetism and material science.

Besides my advisor, I highly appreciate the support given to me by Dr. Peter Elliott with whom I had many fruitful discussions which lead to many new ideas of physics. I enjoyed talking to him about anything and everything as he was also my officemate. He has always been my mentor.

Next I would like to thank Tamadur Albaragtheth with whom I shared my flat for many months and will cherish the sisterly bond we developed during these months. Next the never ending list of my friends Archana, Sheetal, Manju, Sarita, Prerna, Vidushi, Chokila, Monika, Kritika, Farha, Twinkle, Thang biaklun, Ujjawal and many more whose presence in my life will always be special and close to my heart.

I always gave trouble to the computer support group of MPI, Halle and would like to thank them for providing me with the uninterrupted computational facilities. Also, the administration staff specially Ina Goffin for helping me with many problems.

Finally, I would like to thank the entire group for their support and contribution towards completion of my degree.

Declaration of Authorship

I hereby declare that the thesis I am submitting is entirely my own original work except where otherwise indicated. I am aware of the Freie Universität's regulations concerning plagiarism, including those regulations concerning disciplinary actions that may result from plagiarism. Any use of the works of any other author, in any form, is properly acknowledged at their point of use.

Student's Signature:_____

Name (in capitals): _____

Date of submission: _____